Pedro Gustavo Marchã Canhão Costa

Bachelor of Science (*B.Sc.*) Degree in Biochemistry

Towards a bioinspired 3D triculture hiPSC-derived cardiac tissue model for human heart microenvironment recapitulation and drug testing

Dissertation presented to obtain a *Master of Science* (*M.Sc.*) Degree in Biotechnology

Supervisor: Dr. Paula Marques Alves, PhD, Principal Investigator, CEO of iBET and Director of Animal Cell Technology Unit, iBET/ITQB-NOVA

Co-Supervisor: Dr. Maria Margarida de Carvalho Negrão Serra, PhD, Auxiliary Investigator, iBET/ITQB-NOVA

Jury:

President:	Dr. Rui Manuel Freitas Oliveira, FCT/UNL
Examiner:	Dr. Susana Carvalho Rosa, CNC, UC
Supervisor:	Dr. Paula Marques Alves, iBET/ITQB-NOVA
Co-Supervisor:	Dr. Margarida Serra, iBET/ITQB-NOVA

FACULDADE DE CIÊNCIAS E TECNOLOGIA
UNIVERSIDADE NOVA DE LISBOA

September, 2018

Pedro Gustavo Marchã Canhão Costa

Bachelor of Science (*B.Sc*.) Degree in Biochemistry

Towards a bioinspired 3D triculture hiPSC-derived cardiac tissue model for human heart microenvironment recapitulation and drug testing

Dissertation presented to obtain a *Master of Science* (*M.Sc*.) Degree in Biotechnology

Supervisor: Dr. Paula Marques Alves, PhD, Principal Investigator, CEO of iBET and Director of Animal Cell Technology Unit, iBET/ITQB-NOVA

Co-Supervisor: Dr. Maria Margarida de Carvalho Negrão Serra, PhD, Auxiliary Investigator, iBET/ITQB-NOVA

Jury:

President:	Dr. Rui Manuel Freitas Oliveira, FCT/UNL
Examiner:	Dr. Susana Carvalho Rosa, CNC, UC
Supervisor:	Dr. Paula Marques Alves, iBET/ITQB-NOVA
Co-Supervisor:	Dr. Maria Serra, iBET/ITQB-NOVA

FACULDADE DE CIÊNCIAS E TECNOLOGIA
UNIVERSIDADE NOVA DE LISBOA

September, 2018

Towards a bioinspired 3D triculture hiPSC-derived cardiac tissue model for human heart microenvironment recapitulation and drug testing

*This thesis is dedicated to my **mother** and also to my **buddy**, my **grandfather João**, who reminds me every day that age is no more than a state of mind:*

"Youth has no age"
(**Pablo Picasso**)

"No good fish goes anywhere without a porpoise"
(**Lewis Carroll**)

"You have to have an idea of what you are going to do, but it should be a vague idea"
(**Pablo Picasso**)

Acknowledgements

This space is dedicated to those who, in one way or another, have contributed, directly or indirectly, to the conclusion of this project. Since it is not feasible to name them all, there are, nevertheless, some whom I could not fail to express my sincere gratitude and deep recognition:

First and foremost, to my supervisor, Dr. Paula Alves, for inviting me to carry out my master's thesis project in the *Animal Cell Technology Unit*, at iBET/ITQB-NOVA, in the midst of a thought-provoking and refreshing atmosphere, where you can easily breathe science and professionalism. I would like to thank you for the opportunity and for being a strong example of leadership and perfectionism.

Also to my co-supervisor, Dr. Margarida Serra, for all the rewarding scientific debates, perpetual encouragement, support and guidance, confidence and gentle motivation words during this one-year journey. A special thank you for the knowledge you have given me and for the patience and tolerance you have had, at certain times, to deal with me, since I know that I am a very demanding person with myself and sometimes with some difficulty in relating with the fact that everything does not always go as we originally idealized. I am fully aware of this. Thank you for the challenge – fortunately, I am proud to say that I was up to it – and for having trusted me and in my work. I have always tried to give my best and to overcome every challenge. Undeniably, your contribution was vital to the extension of my growth as a young scientist and enabled me to potentiate my skills and go further.

To Bernardo Abecasis, for all the help, scientific discussions and to have eased my integration, in the context of a whole new research area for me, in addition to all the marathons we have worked together on, in the initial conception and characterization of this original and exciting 3D cardiac model.

To Henrique Almeida, for all the companionship, friendly words and, of course, for the great support provided in the development of methods that allowed us to characterize the microcapsule scaffold. Also to the "atomic force microscopy guy", Tomás Calmeiro, from CENIMAT-I3N (FCT/UNL), for the technical support provided, as a result of our collaboration, but also for the constant good disposition and sense of humour.

To all the ACTU researchers and colleagues, in particular to the *Stem Cell* team, for the sympathy, scientific discussions and knowledge sharing.

To the hosting institutions, iBET and ITQB-NOVA, for the outstanding working conditions.

To all the *Advanced Imaging Facility* staff, from *Instituto Gulbenkian de Ciência*, but, essentially, to Hugo Pereira and also to Gaby, for the endless support and help in the different types of microscopy that I worked with during this year. To Hugo, a genuine and special thanks, for the countless hours spent around the light-sheet, with the aim of developing a personalized method that would allow the characterization of my 3D cell-based models. And also for having

accompanied me in the introduction to confocal and multiphoton microscopies. Thank you for your availability, which was often beyond simple technical assistance.

Besides all the people I have worked with, during this year, I also want to acclaim FCT/UNL, because it is a hub where new ideas, knowledge and innovation are very much alive. Similarly, to all the teachers that I have met during these 5 years and who have positively enlarged my skills, both professionally and personally, a sincere thank you.

À minha mãe e à minha irmã por sempre me entusiasmarem e motivarem perante os desafios e a adversidade, assim como a fazer mais e melhor. Quero também partilhar convosco a determinação de os conseguir ultrapassar constantemente!

À Mara por estar incondicionalmente presente.

A todos os meus amigos que pacientemente me ouviram falar, durante horas a fio, sobre células estaminais, modelos 3D, esferóides cardíacos, cardiotoxicidade, biomateriais, entre outros – mesmo quando não queriam!

E para terminar, como não podia deixar de ser, um imperioso obrigado aos meus avós, Arminda e João, por tudo aquilo que me ensinaram e, acima de tudo, por serem enormes exemplos.

Mais uma vez, a todos,
os meus mais sinceros agradecimentos!

Graphical Abstract

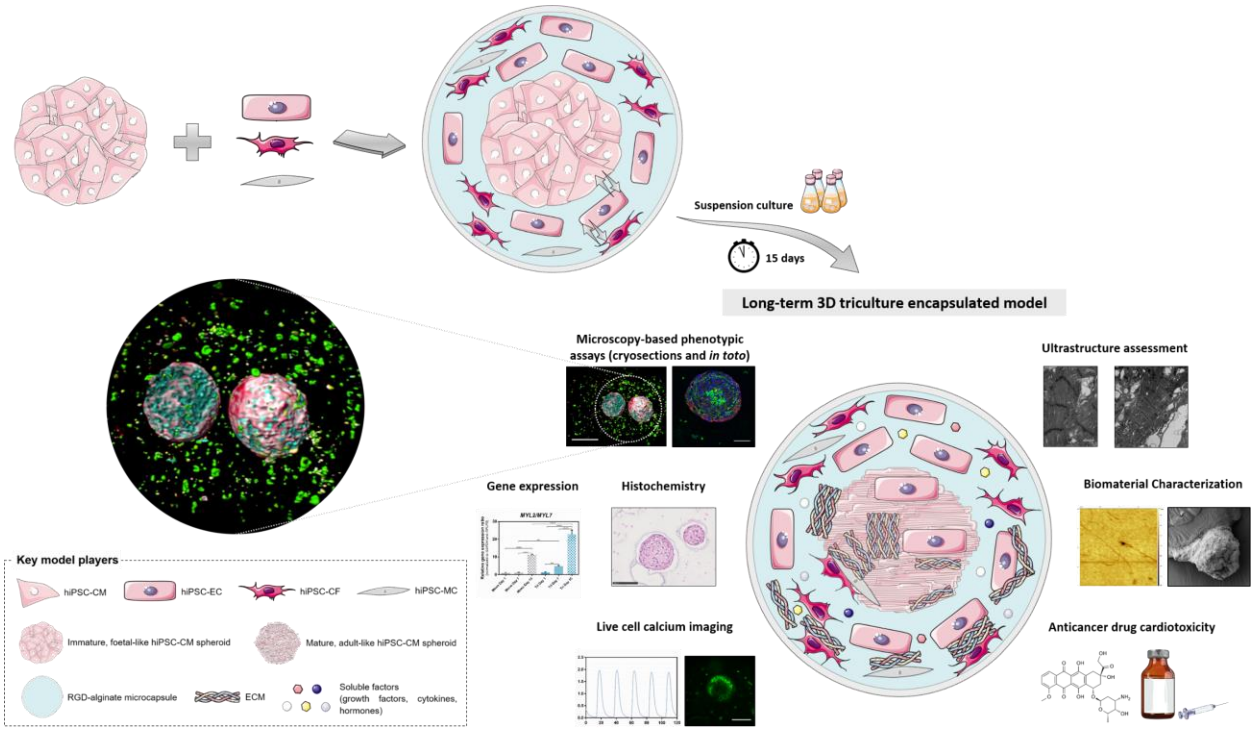

Graphical abstract caption. Schematic illustration of the long-term **bioinspired 3D triculture hiPSC-derived cardiac tissue model** complexity, in the **final day of culture**, as well as some of the major **readouts** developed for its characterization (*right panel*). The model representation (*right panel*) is not to scale. The **key model players** are also depicted (*beneath*, *left*). ***Highlighted*:** light-sheet immunofluorescence microscopy of whole 3D tricultures (*left*) immunostained for the endothelial marker VE-cadherin (green) and the mesenchymal marker Vimentin (red) and counterstained with DRAQ5 (cyan). The author wish to thank *Servier Medical Art* for their image bank used to create the illustrations.

Abstract

Background and Aim

In the human heart, cardiomyocytes (CMs), endothelial cells (ECs) and mesenchymal cells (MCs) are in close proximity and constant dialogue. Predictive models that reliably mimic the native physiology of the human heart *in vitro* would ideally incorporate this cardiomyocyte–non-myocyte crosstalk. Human pluripotent stem cells (hPSC) are an attractive candidate cell platform for *in vitro* cardiac modelling. However, the predictive power of such models is currently constrained by the immature phenotype of hPSC-CM. Hence, the generation of mature hPSC-CM is mandatory for an accurate recapitulation of the human heart microenvironment.

Herein we describe a bioinspired 3D triculture hiPSC-derived cardiac tissue model for human heart microenvironment recapitulation and drug testing.

Methodology

Cardiomyocytes (hiPSC-CM spheroids) and non-myocytes (hiPSC-EC and hiPSC-MC single cells) were differentiated from hiPSC and then microencapsulated in an alginate hydrogel-based scaffold (*tricultures*). 3D models composed only of encapsulated spheroids (*monocultures*) or, alternatively, encapsulated single cells (*co-cultures*), were also engineered.

Principal Findings

After only 15 days of culture, RT-qPCR and immunofluorescence revealed evidence of a higher structural maturation of triculture's hiPSC-CM, specifically increased *MYL2/MYL7* and *TNNI3/TNNI1* gene expression ratios and upregulation of cardiac ion channels, and overexpression of gap junction and ECM proteins. Ultrastructural analysis disclosed a remarkably organized ultrastructure in both models and confirmed improvements in sarcomere length and myofibrillar alignment in triculture. Calcium imaging exposed that hiPSC-CM were pharmacologically responsive to cardioactive drugs (norepinephrine, heptanol and propranolol). A dose-dependent response to cardiotoxic chemotherapeutic drugs (doxorubicin and paclitaxel) constitutes another sign hiPSC-CM functionality. Furthermore, AFM showed that our scaffold exhibits a suitable Young's modulus to recapitulate the human heart microenvironment, while suggesting a dynamic refashioning of the triculture's cardiac microenvironment. Lastly, we performed the upscaling of the cardiac models using perfusion stirred tank bioreactors.

Conclusions

Overall, this thesis represents a step forward in the study of myocyte–non-myocyte heterotypic communication and cardiomyocyte maturation, in a scenario that simulates essential features of the cardiac microenvironment and is compatible with the high-throughput requirements of preclinical studies.

Keywords: hiPSC-CM spheroids, hiPSC-ECMC, 3D cardiac models, alginate microencapsulation, maturation, drug testing.

Resumo

Contexto e Objectivo

Os cardiomiócitos (CMs), as células endoteliais (ECs) e as células mesenquimais (MCs) encontram-se próximas e em interacção constante no coração humano. Modelos preditivos, que mimetizem eficazmente a fisiologia nativa do coração humano *in vitro*, deverão incorporar esse diálogo entre cardiomiócitos e não-miócitos. No seguimento da modelação do microambiente cardíaco humano, surgem, como candidatos promissores, as células estaminais pluripotentes humanas (hPSC). Todavia, o poder preditivo deste tipo modelos é actualmente limitado pelo fenótipo imaturo exibido pelos hPSC-CM, pelo que a geração de hPSC-CM maturados é indispensável para uma recapitulação precisa do microambiente do coração humano.

Nesta tese é descrito um modelo cardíaco 3D de tricultura, totalmente derivado de hiPSC para a recapitulação do microambiente do coração humano e ensaios farmacológicos.

Metodologia

Diferenciações celulares com o intuito de obter cardiomiócitos (esferóides de hiPSC-CM) e não-miócitos (hiPSC-EC e hiPSC-MC, como células individualizadas), seguindo-se a microencapsulação num hidrogel de alginato, foram levadas a cabo. Modelos cardíacos respeitantes somente aos esferóides encapsulados (*monoculturas*) ou, alternativamente, às células individualizadas (*co-culturas*), foram, de igual forma, desenvolvidos.

Principais Resultados

Após 15 dias em cultura, RT-qPCR e imunofluorescência denotaram evidências de um estádio de maturação de hiPSC-CM mais avançado nas triculturas, particularmente um aumento da expressão génica de *MYL2/MYL7* e *TNNI3/TNNI1* e de canais iónicos cardíacos, bem como um incremento das junções célula-célula e de proteínas da matriz extracelular. Análises ultraestruturais revelaram uma ultraestrutura extremamente organizada em ambos os modelos e confirmaram aumentos no comprimento sarcomérico e alinhamento miofibrilar nas triculturas. A técnica de imagem de cálcio demonstrou que os hiPSC-CM possuem capacidade de responder a fármacos com afinidade cardíaca (norepinefrina, propranolol e heptanol). A capacidade de resposta a fármacos anti-cancerígenos cardiotóxicos (doxorrubicina e *paclitaxel*) constitui mais um indício da funcionalidade de hiPSC-CM. Adicionalmente, AFM demonstrou que o *scaffold* utilizado exibe um módulo elástico adequado para mimetizar o microambiente do coração humano, indiciando uma reorganização dinâmica do microambiente cardíaco na tricultura. Para ultimar, efectuou-se um aumento de escala da produção dos modelos aludidos, mediante a utilização biorreactores de tanque agitado.

Conclusões

Em suma, esta tese representa um passo em frente no estudo da comunicação celular heterotípica entre miócitos e não-miócitos e do fenómeno de maturação cardíaca, providenciando uma envolvente capaz de mimetizar aspectos-chave do microambiente cardíaco humano e apresentando compatibilidade com os requerimentos *high-throughput* de ensaios pré-clínicos.

Palavras-chave: Esferóides cardíacos, hiPSC-ECMC, modelos cardíacos 3D, microencapsulação em alginato, maturação, ensaios farmacológicos.

Preface

The work, presented in this dissertation, was carried out in the *Animal Cell Technology Unit* (ACTU) of iBET/ITQB-NOVA, within the scope of the *Fundação para a Ciência e Tecnologia* (FCT)-funded projects *CARDIOSTEM* (*Grant number*: MITP-TB/ECE/0013/2013): "Engineered cardiac tissues and stem cell-based therapies for cardiovascular applications" and *NETDIAMOND* (*Grant number*: SAICTPAC/0047/2015): "New targets in diastolic heart failure: from comorbidities to personalized medicine"; and also in the context of *iNOVA4Health* Research Unit (*Grant number*: UID/Multi/04462/2013), a program financially supported by *Fundação para a Ciência e Tecnologia*/*Ministério da Educação e Ciência*, through national funds and co-funded by *FEDER*, under the *PT2020* Partnership Agreement.

In general terms, the key objectives of these projects are as follows:

(i) Development of stem cell-based therapeutics for cardiac regeneration (cellular and non-cellular).

(ii) Establishment of an ***in vitro*** **engineered cardiac tissue model** for drug screening and toxicology assessment.

This thesis contributed fundamentally to accomplish the **objective (ii)**.

A part of this work was presented in the following **poster communications**:

Abecasis, B., **Canhão, P.G.M.**, Almeida, H.V., Gomes-Alves, P., Rosa, S., Gouveia, P.J., Ferreira, L.S., Serra, M., Alves, P.M. Development of a complex engineered cardiac tissue using human induced pluripotent stem cell derivatives. Cardiovascular Research Workshop @ Bayer, Cape Cod, Massachusetts, USA (June, 2018).

Abecasis, B., **Canhão, P.G.M.**, Almeida, H.V., Rosa, S., Gouveia, P.J., Gomes-Alves, P., Ferreira, L.S., Serra, M., Alves, P.M. Towards a microencapsulated 3D hiPSC-derived *in vitro* cardiac microtissue for recapitulation of human heart microenvironment features. 20th International Congress on *In Vitro* Toxicology (*ESTIV2018*), Berlin, Germany (October, 2018).

The results that will be discussed in this thesis are currently being compiled for the submission of an **article**.

Table of Contents

List of Figures

List of Tables

List of Abbreviations and Conventions

Abbreviation	Full form
2D	Two-dimensional
3D	Three-dimensional
AA	Ascorbic acid
AFM	Atomic Force Microscopy
Ang-1	Angiopoietin-1
ANOVA	Analysis of variance
AP	Action potential
APEL-LI	*Albumin, Polyvinylalcohol, Essential Lipids Low-Insulin* medium
ASC	Adult stem cells
AVN	Atrioventricular node
BMP	Bone morphogenetic protein
BR	Bioreactor
C	Microencapsulated 3D hiPSC-ECMC co-culture
Ca^{2+}	Calcium(II) cation
CACNA1C	Calcium, L-type voltage-gated channel, *alpha* 1C subunit, encoding the calcium channel $Ca_v1.2$
CAM	Cell adhesion molecule
CD31	Cluster of differentiation 31
CF	Cardiac fibroblast
CLSM	Confocal Laser Scanning Microscopy
CM	Cardiomyocyte
CM/ECMC	Triculture model consisting of cardiomyocyte spheroids mixed with a co-culture of endothelial and mesenchymal cells, grown in monolayer
Coll I	Collagen type I
Coll IV	Collagen type IV
CPC	Cardiac progenitor cell
C_T	Threshold cycle values
cTnI	Troponin I, cardiac muscle isoform
cTnT	Cardiac troponin T
CVD	Cardiovascular disease
Cx43	Connexin 43
d	day
DAPI	4',6-diamidino-2-phenylindole
DDR2	Discoidin domain receptor tyrosine kinase 2
DMEM	*Dulbecco's Modified Eagle* medium
DO	Dissolved oxygen
DPBS	Dulbecco's Phosphate Buffered Saline
EB	Embryoid body
EC	Endothelial cell

ECGM2	Endothelial Cell Growth Medium 2
ECM	Extracellular matrix
ECMC	Co-culture model consisting of endothelial and mesenchymal cells, grown in monolayer
EGF	Epidermal growth factor
EHT	Engineered heart tissue
EMT	Epithelial-to-mesenchymal transition
ESC	Embryonic stem cells
F/F_0	Fluorescence (F) normalized to baseline fluorescence (F_0)
FB	Fibroblast
FBS	Fetal bovine serum
FC	Flow Cytometry
FGF	Fibroblast growth factor
FGFR	Fibroblast growth factor receptor
FS-AFM	Force Spectroscopy mode-Atomic Force Microscopy
GAG	Glycosaminoglycan
GAPDH	Glyceraldehyde-3-phosphate dehydrogenase
GSK-3β	Glycogen synthase kinase-3 *beta*
h	hour
H&E	Hematoxylin and eosin
HA	Hyaluronic acid
hCM	Human cardiomyocyte
hESC	Human embryonic stem cells
hESC-CM	Human embryonic stem cell-derived cardiomyocytes
HF	Heart failure
hiPSC	Human induced pluripotent stem cells
hiPSC-CM	Human induced pluripotent stem cell-derived cardiomyocytes
hiPSC-CM/ECMC	Human induced pluripotent stem cell-based triculture model, consisting of cardiomyocyte spheroids mixed with a co-culture of endothelial and mesenchymal cells, grown in monolayer
hiPSC-EC	Human induced pluripotent stem cell-derived endothelial cells
hiPSC-ECMC	Human induced pluripotent stem cell-based co-culture model, consisting of endothelial and mesenchymal cells, grown in monolayer
hiPSC-MC	Human induced pluripotent stem cell-derived mesenchymal cells
hPSC	Human pluripotent stem cells
HTS	High-throughput screening
HUVEC	Human umbilical vein endothelial cell
ICM	Inner cell mass
IF	Immunofluorescence
IGF-1	Insulin-like growth factor 1
iPSC	Induced pluripotent stem cells
LSFM	Light-Sheet Fluorescence Microscopy
M	Microencapsulated 3D hiPSC-CM monoculture
MC	Mesenchymal cell

MHC-*α*	Cardiac *alpha*-myosin heavy chain protein isoform
MHC-β	Cardiac *beta*-myosin heavy chain protein isoform
MI	Myocardial infarction
min	minute
MLC-2*a*	Myosin light chain, atrial protein isoform
MLC-2*v*	Myosin light chain, ventricular/cardiac muscle protein isoform
MPLSM	Multiphoton Laser Scanning Microscopy
MT	Masson trichrome
MYH6	Myosin heavy chain 6, encoding the cardiac *alpha*-myosin heavy chain protein isoform (frequently referred to as MHC-α)
MYH7	Myosin heavy chain 7, encoding the cardiac *beta*-myosin heavy chain protein isoform (frequently referred to as MHC-β)
MYL2	Myosin regulatory light chain 2, encoding the ventricular/cardiac muscle protein isoform (frequently referred to as MLC-2*v*),
MYL7	Myosin regulatory light chain 7, encoding the atrial protein isoform (frequently referred to as MLC-2*a*)
n.a.	not applicable
NA	Numerical aperture
Norepi	Norepinephrine
NRG	Neuregulin (also known as neuroregulin)
ns	not significant
o.n.	Overnight
P	*p*-value
PAS	Periodic acid-Schiff
PC	Pericyte
PDGF	Platelet-derived growth factor
PECAM-1	Platelet–endothelial-cell adhesion molecule-1, encoding the cluster of differentiation 31 (frequently referred to as CD31)
PFA	Paraformaldehyde
PPL	Propranolol
PSC	Pluripotent stem cells
PSR	Picrosirius red
RGD	Extracellular matrix protein-derived tripeptide sequence: arginine-glycine-aspartate
ROCK	Rho-associated protein kinase
RPLP0	Ribosomal protein lateral stalk subunit P0
RPMI	*Roswell Park Memorial Institute* 1640 medium
RT	Room temperature (18–20 ^{o}C)
RT-qPCR	Real-Time Reverse Transcription-Quantitative Polymerase Chain Reaction
RyR	Ryanodine receptor
SAN	Sinoatrial node
SCN5A	Sodium voltage-gated channel, *alpha* subunit 5, encoding the cardiac sodium channel $Na_v1.5$
SD	Standard deviation

SDCM	Spinning Disk Confocal Microscopy
sec	second
SEM	Scanning Electron Microscopy
SEM	Standard error of the mean
SF	Shake flask
SR	Sarcoplasmic reticulum
ssTnI	Troponin I, slow skeletal muscle isoform
STBR	Stirred tank bioreactor
T	Microencapsulated 3D hiPSC-CM/ECMC triculture
TB	Toluidine blue
TEM	Transmission Electron Microscopy
TGF-β	Transforming growth factor *beta*
TNNI1	Troponin I1, encoding the slow skeletal muscle isoform (frequently referred to as ssTnI)
TNNI3	Troponin I3, encoding the cardiac muscle isoform (frequently referred to as cTnI)
VEGF	Vascular endothelial growth factor
VSMC	Vascular smooth muscle cell
VWF	von Willebrand factor
WB	Washing Buffer
WHO	World Health Organization
Wnt	Wingless/INT protein
ZO-1	Zonula occludens-1, also known as tight junction protein-1
α-SMA	*Alpha* smooth muscle actin

List of Models

Given that several experiments were carried out, leading to models with different degrees of complexity, we have established a reaction code (recurrently used during the course of this dissertation), which systematises, in an easily perceptible way: **(i)** the model identification, **(ii)** the connexion between two models (biological replicates, or not), **(iii)** whether they are microencapsulated models or not, and, if so, which conditions were encapsulated and, lastly, **(iv)** the implemented culture strategy (shake flask or small-scale stirred-tank bioreactor culture). Each one of these codes unambiguously identifies one, and only one, of the prepared models.

The identification of the three-dimensional models follows the alphanumeric system: ***Designation of the Model* (#number-*letter*) – *Encapsulated Conditions* – *Culture Strategy***.

Exemplifying for a specific example: **Model #1-*a*-MCT-SF** and **Model #1-*b*-MCT-SF** constitute two **biological replicates**, identified by the letters ***a*** and ***b*** (the only difference in the designation of the two replicas), in which **mono-** (**M**), **co-** (**C**) and **tricultures** (**T**) were **encapsulated**, being always cultivated in **shake flask** (**SF**). For simplicity and merely for the bioreactor-based experiments, **Model #2-*a*-BR-1** and **Model #2-*b*-MT-BR-2**, will be referred to as **BR-1** and **BR-2**, respectively.

3D Model	Description	Schematic illustration
	Shake flask-based cultures	
Pilot Model–M-SF	Single pilot experiment, leading to the microencapsulation of only monocultures (M) of hiPSC-CM spheroids (*culture strategy*: shake flask).	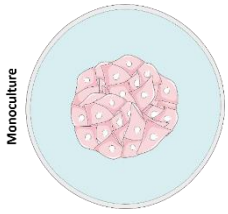
Model #1-*a*-MCT-SF	Microencapsulation of hiPSC-CM mono- (M), hiPSC-ECMC co- (C) and hiPSC-CM/ECMC tricultures (T) (first of two independent experiments; *culture strategy*: shake flask; *relevant features*: higher average microcapsule diameter and lower spheroid size, meaning an additional empty space within the capsule, when compared to the biological replicate.	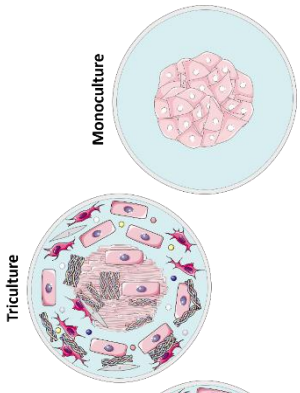
Model #1-*b*-MCT-SF	Microencapsulation of hiPSC-CM mono- (M), hiPSC-ECMC co- (C) and hiPSC-CM/ECMC tricultures (T) (second of two independent experiments; *culture strategy*: shake flask; *relevant features*: lower average microcapsule diameter and higher spheroid size, suggesting a reduced empty space inside the capsule, when compared to the biological replicate.	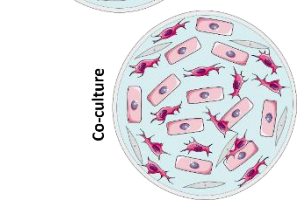

Small-scale stirred-tank bioreactor-based cultures		
Model #2-*a*-BR-1	Single exploratory experiment with the aim of optimizing hiPSC-CM aggregation in small-scale stirred-tank bioreactors (*culture strategy*: bioreactor-based; *relevant features*: none of the abovementioned conditions was microencapsulated; large spheroid size dispersion.	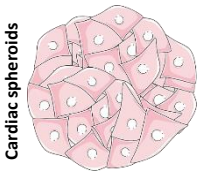
Model #2-*b*-MT-BR-2	Microencapsulation of hiPSC-CM mono- and hiPSC-CM/ECMC tricultures (T) (one independent experiment; *culture strategy*: bioreactor-based; *relevant features*: fine aggregation and microencapsulation processes; large spheroid size dispersion.	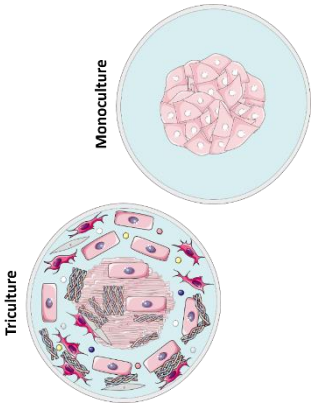

Main abbreviations: M – Microencapsulated 3D hiPSC-CM **Monoculture**, **C –** Microencapsulated 3D hiPSC-ECMC **Co-culture**, **T –** Microencapsulated 3D hiPSC-CM/ECMC **Triculture**, **SF –** Shake Flask, **BR –** Bioreactor (for the remaining ones, consult **List of Abbreviations and Conventions**). Model representations (*right panel*) are not to scale.

1. Introduction

1.1. State-of-the-*heart*

1.1.1. Motivation – *in vitro* myocardial cell-based models in the landscape of cardiovascular preclinical research

Cardiovascular disease (CVD)[1–7] and heart failure (HF)[1–3,5,7–9] are today a global epidemic and still represent the major causes of mortality and morbidity in the Western world[1–4,8]. CVD and HF can derive primarily from myocardial infarction (MI)[1–3,7,9,10], chemotherapy-induced cardiotoxicity[1,3,7,10–13] and inherited abnormalities affecting cardiac function[1–3,10].

According to data published in the latest annual *World Health Statistic* report of the *World Health Organization* (WHO, June 2016), the number of deaths arising from CVD is already 17.7 million per year[1,2,7], thereby representing a shocking number of 30% of all global deaths[2].

Furthermore, notwithstanding the new scientific and medical progresses, the number is unfortunately projected to rise to more than 23.6 million per year until 2030[2]. Hence, it is unquestionably clear that CVDs represent a massive problem in our contemporary society[1–7], even from an economic point of view[1,5,14], with a cost to the world healthcare sector estimated at about eight hundred and sixty billion dollars per year[5,15]. Thus, there is an imperative and urgent need to discover innovative, efficient, personalized and cost-effective cardiac therapies that allow this problem to be reached on a global scale[1–6,14,15].

Similarly, contributing to the abovementioned scenario, is the fact that drug discovery and development is a very challenging road, with high failure rates[14,16], along with the cost-ineffectiveness[14] and inadequacy[14] of the prevailing methods, used to estimate their safety[2,7,14,17], efficacy[2,7,14,17] and mode of action[2,17]. In this context, mention should be made of the example stated by **Mathur (2016)** and **Zeevi-Levin (2012)**, concerning that the average period between the discovery and actual commercialization of a drug varies between 10 to 15 years, with median costs exceeding $5 billion[14,18].

1.1.1.1 Cardiotoxicity paves the way for more predictive *in vitro* cardiac models

Cardiovascular toxicity[3,11,14,19] (**Fig.1.1**), which leads to numerous cardiovascular adverse pharmacological events (**Fig.1.1*a***), is one of the major causes of drug recalls[3,14], post-approval withdrawals[3,14,16] (**Fig.1.1*b***) and regulatory approval delays[3,14] during preclinical and clinical development[3,11,14,16,19]. Cardiotoxicity is especially crucial for chemotherapeutic drugs[3,11,14,16,19–21] (or simply anticancer drugs) (**Fig.1.1*b***), although it is also observed with other drug classes[7,16,19,21] (**Fig.1.1*b***), such as antimicrobials[16] (**Fig.1.1*b***), antihistamines[16] (**Fig.1.1*b***), antidiabetics[7], antidepressants[16] and antipsychotics[16] (**Fig.1.1*b***).

Recently, several non-cardiovascular drugs, including the first non-sedating antihistamine, *terfenadine*[3,16] (***Triludan***, in the United Kingdom), famous nowadays for the fact that 100 million people used it before its risks were entirely recognised, have been withdrawn from the major markets because of cardiotoxicity concerns[3,16]. This is just a single example, with a list of *a priori* withdrawn drugs or modified to re-enter the market, rather extensive[3,11,16,21].

This phenomenon can be mostly attributed to several obstacles that currently hinder human drug investigation[3,14].

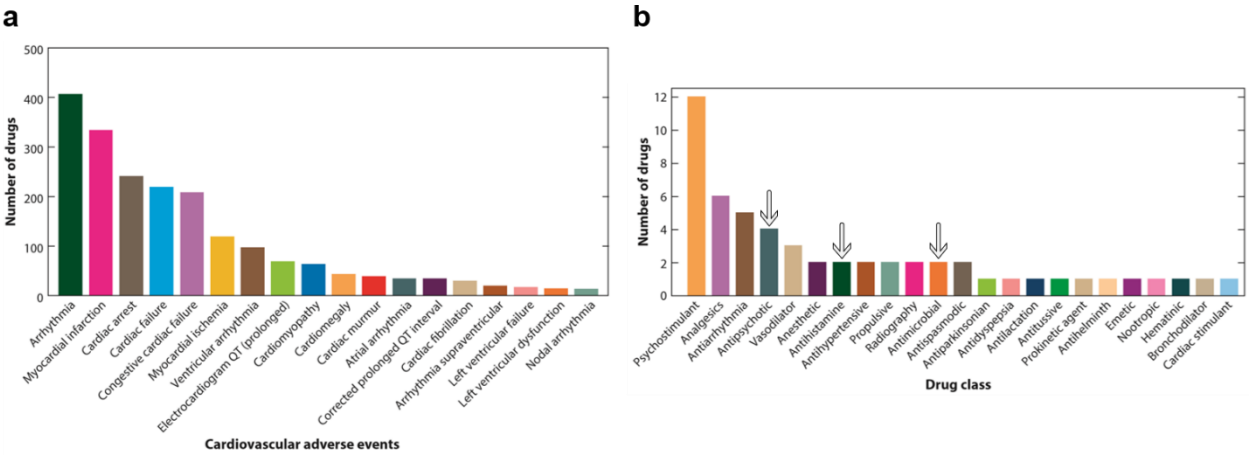

Figure 1.1 | Current picture of cardiovascular toxicity [adapted from **Magdy *et al*. (2018)**[21]].

(***a***) Summary of the prevailing drugs on the market, as well as the related cardiovascular adverse pharmacological events.

(***b***) Drug discovery and development in the cardiovascular context: withdrawal from the market of sixty-three drugs, in different pharmacological classes, between 1953 and 2013, as a result of severe cardiotoxic effects. **Highlighted** (light grey arrows): *from left to right*, **antipsychotics**, **antihistamines** and **antimicrobials**.

On one side of the coin, *in vivo* human experimental interventions pose unnecessary and unacceptable risks to the person undergoing clinical trials[1,3], in addition to displaying a restricted applicability[3] (owing to the requirement of a necessarily small sample of individuals) and intraspecies genetic and phenotypic differences[3,10,11,21].

On the other side of the coin are animal models[3,14,22], which fail to adequately recapitulate the human physiology (including that of the human heart)[3], due to notorious interspecies differences[3,10,14,22], with respect to key biochemical pathways[14], ion channels[14] and pharmacokinetic and pharmacodynamic behaviour[14]. Differences in cardiac structure[3,22] and electrophysiological properties[3,22] between human cardiomyocytes (hCM) and animal cardiomyocytes are also vital factors that, in agreement with **Feric and Radisic (2016)** and **Sharma *et al*. (2017)**, restrict the relevance of the latter in preclinical animal studies[3,22].

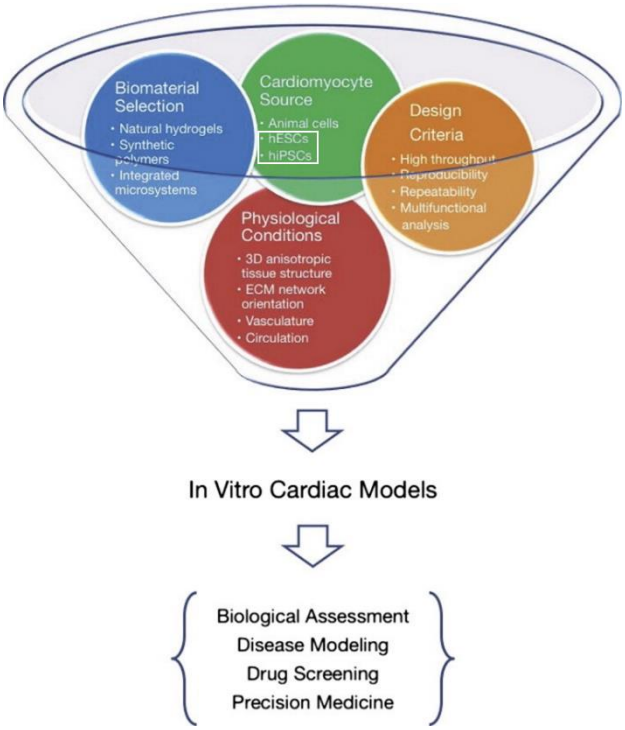

Figure 1.2 | Schematic overview of the conditions to be considered in the design of novel *in vitro* cardiac tissue models and its main current applications [adapted from **Mathur *et al*. (2016)**[14]].

Conditions (circles in the inverted cone): **biomaterial**, **physiological**, **CM source** and **design criteria**. **Applications**, concerning **basic science** and **translational research**: biological assessment, disease modelling, drug discovery and development, drug screening and precision medicine are just some of the many potentialities that are already beginning to emerge in this sort of models. **Highlighted** (white rectangle): human pluripotent stem cells (hPSC), *viz*. human induced (hiPSC) and human embryonic stem cell (hESC) sources.

Therefore, it is critical to develop novel human *in vitro* cell-based cardiac tissue models (**Fig.1.2**) that recapitulate certain physiological functions and reproduce key details of the heart anisotropic 3D architecture (**Fig.1.2**), so that they can be applied in preclinical and clinical settings[2,3,14,17] (**Fig.1.2**). In other words, the solution that this thesis intends to explore are three-dimensional (3D) *in vitro* human induced pluripotent stem cell (hiPSC)-derived cardiac tissue models.

Hopefully this will simplify cardiotoxic effects' identification, when evaluating the efficacy and safety of drug candidates, as well as studying and understanding the mode of action and pharmacokinetic and pharmacodynamic properties of the therapeutic agents. Regardless of being a difficult task to mimic the structure and functionality of the human heart[2,17] and even though these models also have limitations[17], they are a viable alternative to the foregoing state-of-the-art strategies, as will be later discussed.

1.1.2. *In vivo* cardiac microenvironment – getting to the *heart* of the matter

Since this dissertation focuses on the establishment of 3D *in vitro* hiPSC-derived cardiac models, it is similarly relevant to address the *in vivo* scenario, regarding (i) the cellular composition and interactions between the key *in vivo* players (myocytes and non-myocytes) and, particularly, between (ii) the cardiomyocyte-endothelial cell duo, (iii) structure and physiology of the human heart and (iv) estimated cell numbers of the different cardiac populations, as those models attempt to faithfully recapitulate key aspects of its physiology and tissue-specific architecture. However, in this context, they should be understood not as a medicinal product, but as a drug testing platform. Besides, modelling human cardiac physiology *in vitro* is a difficult task, not yet attained with any type of cellular or tissue-based system.

1.1.2.1. Cellular composition and cardiomyocyte–non-myocyte interactions

The heart is a multicellular[23] organ composed of three layers[24,25]: i) myocardium[17,24–26], ii) endocardium[24–26] and iii) the epicardium[1,2,24,25], enclosed by an endomysial collagen network[24,27]. Within these layers, there is a complex arrangement of cells, organized into different functions and with distinct properties, including cardiomyocytes (CMs)[17,24–26,28] and nonmyocytes[17,24–26,28] (**Fig.1.3**), which comprise endothelial cells[17,24–26] (ECs), pericytes[17,24,25] (PCs), cardiac fibroblasts[17,24–26] (CFs), vascular smooth muscle cells[17,24–26,29] (VSMCs), epicardial cells[17,24,25], neurons[24,25] and a transient population of immune cells[24,25,27].

CMs are the cardiac muscle cells[23,25,27], responsible for all the mechanical contractile force[23,25,27] generation in the heart and are located in the myocardium[24,25], constituting approximately only 25 to 35%[17,25,26,30] of its total cells. There are several CM subtypes, specifically nodal[31], ventricular[17,31] and atrial[17,31]. These subtypes arise from different cardiac mesodermal populations[31] (which emerge from the anterior region of the primitive streak during gastrulation[32,33]) and are inherent in different locations[31,34] – ventricular and atrial CMs, as indicated by their designation, in the ventricles and atria[31,34], respectively, while the nodal CMs are found in the sinoatrial node (SAN)[31,34].

Albeit the most renowned, CMs are not, as formerly stated, the only population residing in the heart and, during development stage and normal homeostasis, interact with other cell types[17,28,35]. For instance, as recently stated by **Dunn and Palecek (2018)**, epicardial cells (cells covering the outer layer of the heart)[33] undergo epithelial-to-mesenchymal transition (EMT)[2,25,28], throughout the phases of cardiac development and repair[25], so as to produce VSMCs, CFs and plausibly ECs[25].

The latter (VSMCs, CFs and ECs non-myocytes) interact with CMs (**Fig.1.3**), in the myocardium, and influence their functionality and survival[23,25,26,28].

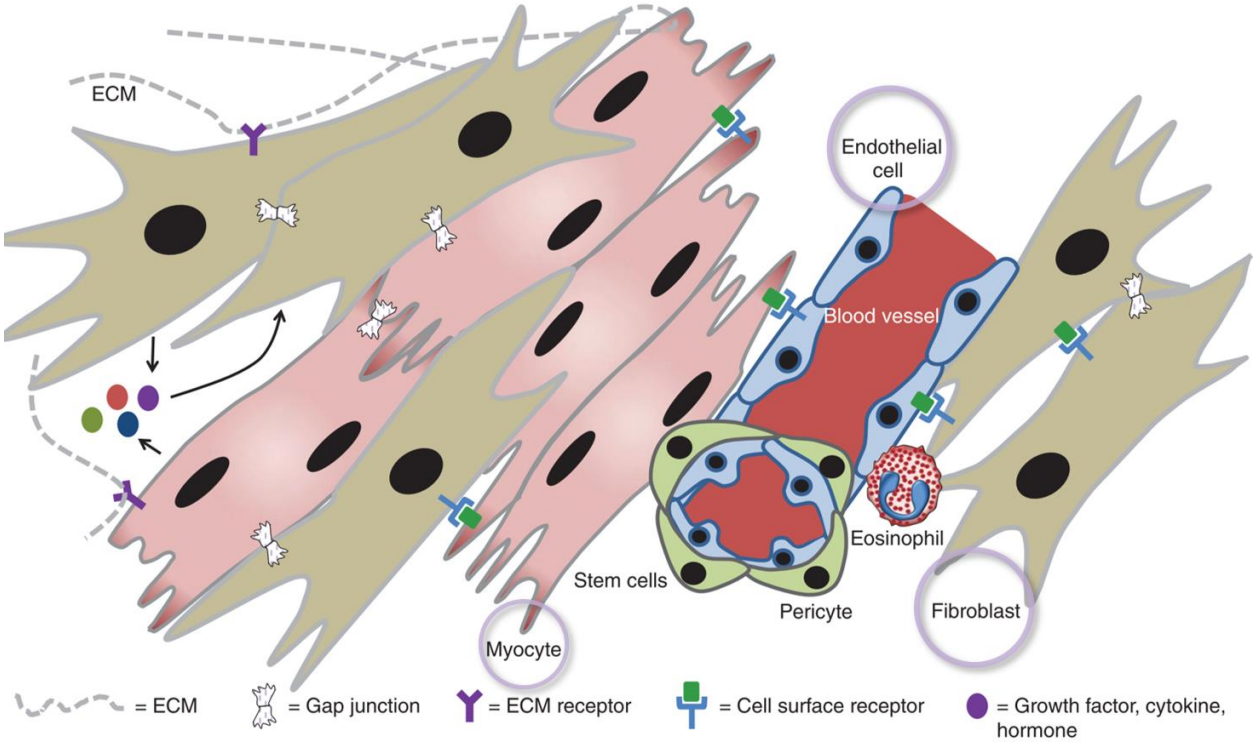

Figure 1.3 | Simplified scheme of the organization and interactions between cellular key players in the *in vivo* mammalian heart microenvironment [adapted from **Dostal *et al.* (2015)**[24]].

Myocytes and non-myocytes – **highlighted** (blue circles): **cardiomyocytes**, **endothelial cells** and **cardiac fibroblasts** – may interact through **cell surface receptors** and cell adhesion molecules (CAMs), such as cadherins, homo- or heterotypic **gap junctions** (which are comprised of one or more types of connexins) and ions and **molecules** (growth factors, cytokines or hormones), that can act via paracrine and/or autocrine signalling. Cardiomyocytes–non-myocyte **crosstalk** may lead to the activation or silencing of certain cell signalling pathways and consequently induce dramatic changes in gene and protein expression.

CFs have a structural role[36], contributing for the deposition of extracellular matrix (ECM) in the heart[24,25,36]. VSMCs assist the coronary arteries[29,34] and regulate the inflow and outflow microvasculature[25,29,33,34].

In the case of ECs, they delineate this microvasculature[34], establishing the endocardium and the interior of blood vessels and cardiac valves[33,34], and also aid in delivery of nutrients and removal of toxicants and waste[25]. They can be of two types: (i) endocardial ECs[25,26], that delineate heart chambers and (ii) myocardial ECs[25,26], which comprise the capillaries that interact dynamically with CMs.

More importantly, this dynamic crosstalk between CMs and non-myocytes (**Fig.1.3**) is critical in cardiac development[31,33,34] and regulation of postnatal morphology[28,37] phases and vital to support the biochemical, structural, mechanical and electrical properties of a functional heart[23,25,26,28,34].

1.1.2.2. Cardiomyocyte-endothelial cell duo – interactions and signalling pathways

Regarding the crosstalk between CMs and non-myocytes, we will now address the interactions amongst the endocardium and the myocardium[26,28,38] (**Fig.1.4**). Understanding how ECs and CMs communicate is a vital starting point for the creation of *in vitro* cardiac models, that favour normal structural and functional aspects of CMs, in the long term, and that can ultimately be used in cardiac regeneration applications.

Communication between ECs and CMs controls not only aspects of early cardiac development[28,35,38,39], but also adult CMs' function[35,38,39], survival[35,38,39] and proliferation[35,38,39], including cardiac growth[26], contractile performance[26] and rhythmicity[26]. Besides, CMs depend on ECs not only for oxygenated blood

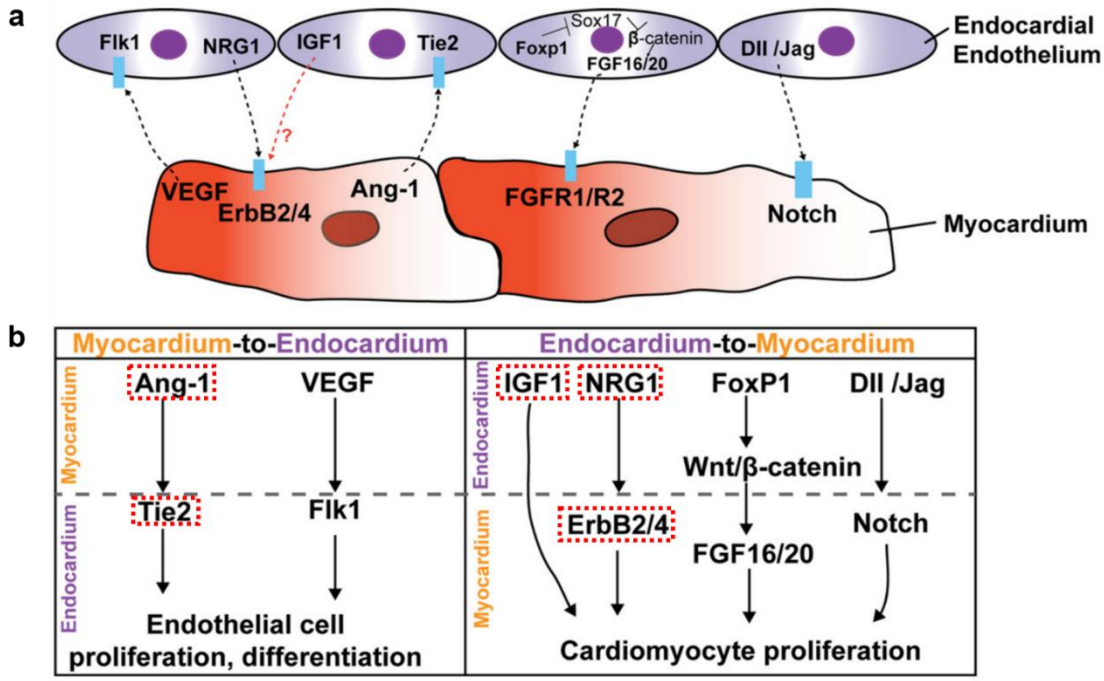

Figure 1.4 | Schematic model of reciprocal myocardial-endocardial interactions and major signalling pathways involved in cardiac development, proliferation and maturation [adapted from Tian and Morrisey (2012)[28]].

(*a*) Mutual signalling during the formation of myocardial *trabeculae*.

(*b*) (*left panel*) **myocardial (CM)-endocardial (EC) signalling:** CMs may secret signalling mediators modulating ECs survival, proliferation, differentiation and assembly (Ang-1 and VEGF-A); (*right panel*) **endocardial (EC)-myocardial (CM) signalling:** reciprocally, ECs may also promote CMs survival and proliferation, via IGF-1 and NRG-1. **Highlighted** (red rectangles): (*left panel*) **Ang-1/Tie-2**; (*right panel*) **NRG-1/ErbB2/ErbB4** and **IGF-1.**

supply, but also because of local protective signals[38,40] that promote CM organization and survival[28,35,38,40]. However, this interaction is mutual: whilst ECs secrete certain factors, CMs respond, reciprocally secreting factors that have a decisive impact on EC function[24,28,35,38–41] (**Fig.1.4**).

NRG-1/*ErbB2*/*ErbB4*, *IGF-1*, *Notch*, *Ang-1*/*Tie-2* and *FGF* are some of the signalling pathways involved in the endocardium role of orchestrating the function and maturation of myocardial cells[28,38–41].

Neuregulins or neuroregulins (NRG) are a family of four structurally related growth factors, EC-synthesized, that are part of the epidermal growth factor (EGF) family[28,35,38,42]. These proteins have several functions in the development of the nervous system[35] and have been shown to play an important role in the embryogenesis of vertebrates[35], including in cardiac development[35].

Particularly, it is described that NRG-1 has the capacity to promote cell survival and growth[28,35,38], via activation of ErbB receptors[28,35,38], in the *neuregulin-ErbB* signalling pathway[28,35,38] (**Fig.1.4**). NRG-1 is expressed in the endocardium, where it is released as a paracrine signal that activates the tyrosine kinase receptor ErbB4 and its co-receptor, ErbB2, expressed on adjacent CMs[26,28,35,38,41,43]. *NRG-1*-induced paracrine communication, between ECs and CMs, has been confirmed in *in vitro* co-culture studies[26,35], with impact on the cardiovascular function regulation[26,35]. Also, it has been recently demonstrated that the *NRG-1/ErbB4* pathway promotes the proliferation of already differentiated CMs[28,34,38].

Furthermore, NRG-1 induces the proliferation[43], survival[43] and hypertrophic growth[43] of cultured neonatal CMs[43] and, therefore, this is why the activation of the *ErbB2/ErbB4* heterodimeric receptor complex (NRG-1-mediated) is one of the factors required for the formation of myocardial *trabeculae*[28,38,43] (**Fig.1.4**) and cardiac cushions[38,43].

Insulin-like growth factor 1 (IGF-1), also termed somatomedin C, is a protein that is also secreted by the endocardium[28]. IGF-1 interrelates synergistically with NRG-1 and potentiates the proliferation and maturation of ventricular CMs[28,35] (**Fig.1.4**). Moreover, IGF-1 signalling is also linked with adaptive and cardioprotective response[28,35].

Another quite important pathway is *Notch* signalling[28,44], which is likewise associated with CM proliferation[28] (**Fig.1.4**), being responsible for ventricular chamber morphogenesis and development[28,44].

On the other hand, with regard to myocardial repercussion in endocardium, it is important to highlight Tie-2 (previously known as TEK), which is a tyrosine kinase receptor expressed in endocardial cells[26,28]. When its ligand, angiopoietin-1 (Ang-1), expressed in the myocardium, binds to Tie-2 receptor, in the endocardium, differentiation and proliferation of the endocardium are triggered[26,28] (**Fig.1.4**).

Lastly, fibroblast growth factors (FGFs) are also essential in the regulation of cardiac development[28,34,45,46], via the paracrine activity of ligands expressed in the endocardium[25,28,45,46].

FGF-9, FGF-16, and FGF-20 are all expressed in the endocardium during cardiac development[25,45,46]. These FGFs signal the myocardium through specific receptors, FGFR1 and FGFR2, thus stimulating the proliferation and differentiation of CMs[25,45,46]. Contrariwise, FGF-1 and FGF-2 induce EC proliferation and their physical organization into tube-like structures[45,46]. Therefore, FGF-1 and FGF-2 promote angiogenesis and the formation of novel blood vessels from the pre-existing microvasculature[45,46]. They are also more potent angiogenic factors than vascular endothelial growth factor (VEGF) or platelet-derived growth factor (PDGF)[45,46].

Altogether, these signalling pathways demonstrate that there is a reciprocal regulation between CMs and ECs, mostly in a paracrine way (**Fig.1.4**).

1.1.2.3. Fundamentals of heart structure and physiology

As schematically depicted in **Fig.1.5**, structurally, the heart, in all mammals, is constituted of four separate chambers[2,34,47] – the left and right atria[2,47] and, correspondingly, the left and right ventricles[2,47] – in addition to components of the conduction (or *pacemaker*)[2,34,47] system, that certify the heart's muscle contraction[2,34]. Cardiac rhythmicity (contraction/systole together with relaxation/diastole cycles) ensures the supply of blood and nutrients throughout the body[2,47].

The left ventricle is in charge of pumping blood to the entire body (systemic circulation)[2,47], culminating in the aorta artery[47] (**Fig.1.5**), whereas the right ventricle only to the lungs[2,47], via the pulmonary artery[47]. Intuitively, this means that left ventricular CMs should

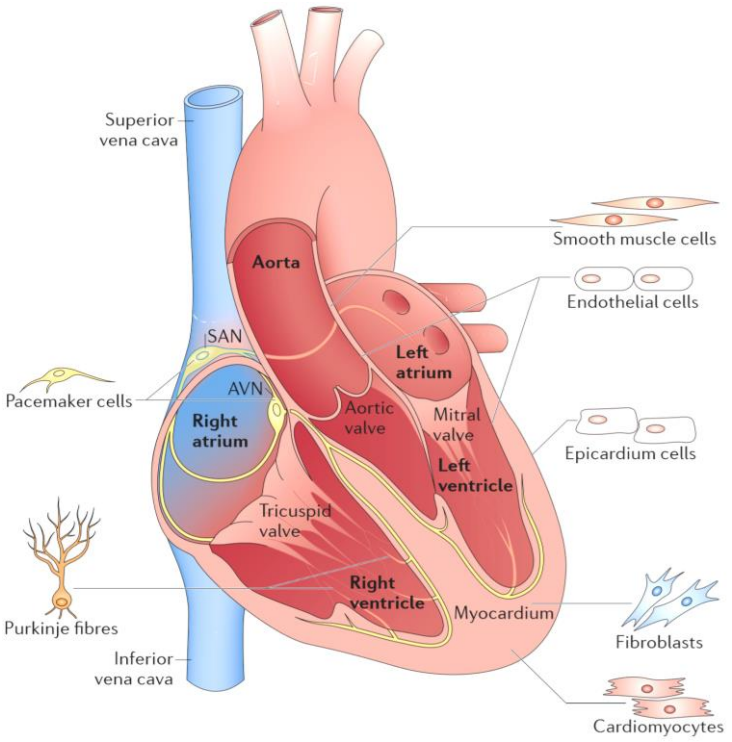

Figure 1.5 | Schematic depiction of structural features and major cell types of the heart [adapted from **Xin *et al.* (2013)**[34]]. **Abbreviations: AVN –** Atrioventricular node and **SAN –** Sinoatrial node.

produce superior contraction forces and require a greater supply of both oxygen and nutrients[25,47]. On the other hand, atrial CMs will require less force generation to pump the blood from the atria into the ventricles[25,47].

Heart contraction is mediated by the cardiac *pacemaker*[2,17,25,34], which involves sinoatrial node CMs[2,25,34], positioned at the entrance of the right atrium[34] (**Fig.1.5**). These cells are responsible for monitoring the rhythmicity of the heart beat and are then called *pacemaker* cells[2,25,34] (**Fig.1.5**).

A given electrical impulse, produced by the sinoatrial node CMs, spreads to the atria, leading to its contraction[34]. The electric impulse then travels to the atrioventricular node (AVN) (**Fig.1.5**), where it is decelerated, allowing enough time for the atria to contract[2,34]. Afterwards, the electrical activity is conducted to the Purkinje network[2,26,34] (also termed His-Purkinje) (**Fig.1.5**), which are conduction fibres[26,34] located in the inner ventricular walls of the heart[26,34], just beneath the endocardium[26], in a space called the subendocardium[26]. In turn, those fibres innervate the muscular walls of the ventricles[2,26,34] (**Fig.1.5**), now leading to their contraction and consequential blood ejection into the systemic (left ventricle-mediated) or pulmonary (right ventricle-mediated) circulations[2,26,34].

In practice, this allows the electrical activity, which is recorded as an action potential, to unmistakeably identify the CM subtype[2,26], as it will be noticeably different[2,26] in the SAN, atria, AVN, ventricles and Purkinje network, ultimately leading to dissimilar Ca^{2+} handling kinetics[1–3,17,23,26] and electrophysiological properties[17,25,26]. Any trouble in this rhythm, precisely orchestrated by sinoatrial node CMs (the orchestra master) can conduct to fatal arrhythmias[2,23].

1.1.2.4. Cardiac cell numbers – a controversial question

Notwithstanding non-myocytes being important for normal heart's homeostasis[26,28,38], either through cellular communication pathways[26,28,38] (ECs), or in terms of vascular supply[26,28,38] (ECs and VSMCs), impact on myocyte survival[26,28,38] (ECs) or ECM deposition[24,26,28,38] (CFs), there is still some misunderstanding and controversy about the cell numbers (**Fig.1.6**) of each of these populations in the mammalian heart[48,49] .

As mentioned in the former topic, CMs make up about 25 to 35%[17,25,26,30,49] of the cells in the heart of mammals, which means that they have 65 to 75% remaining for the other populations and this is where the debate begins.

Fundamentally, this is attributable to two aspects: i) dispersion of the methodologies used[48] to assess those numbers and ii) absence of specific markers for some mesenchymal populations[24,29,48], such as CFs and VSMCs.

Although the number of CMs remains constant during the human lifespan[49], ECs and mesenchymal cells (MCs), in the myocardium, increase in number into adulthood[49] and show high turnover[49]. Thus, the myocardial intrinsic plasticity[26,28,49], which translates into the fact that the human heart does not have a static cellular composition as it ages[49], allied to the differential and dynamic turnover[49] of the involved populations, are also contributing factors to this lack of definition[48,49].

A study recently published by **Bergman *et al*. (2015)**, with the aim of quantifying the cell populations of human hearts, via stereological methods and flow cytometry (FC), came somehow to uncover the curtain to this problem[49] (**Fig.1.6**). Stereological examination of histological sections estimated the frequency of CMs, ECs and MCs at 18, 24 and 58% (**Fig.1.6**), respectively[49]. On the other hand, by flow cytometry of isolated cell nuclei, it was possible to determine frequencies of 33, 24, and 43% (**Fig.1.6**), correspondingly[49].

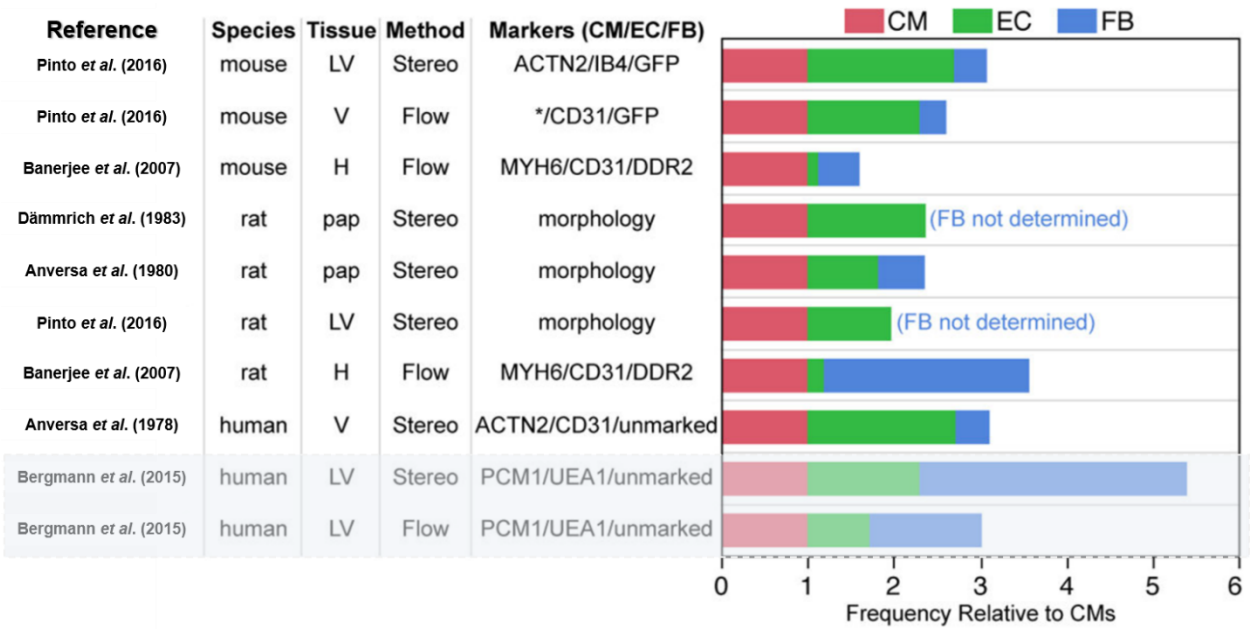

Figure 1.6 | Cell numbers in the mammalian heart [adapted from **Zhou and Pu. (2016)**[48]].

A summary of the studies that measured the proportion of CMs, ECs and fibroblasts (FBs), in the mammalian heart, using stereological methods or flow cytometry, is gathered in this figure. In order to allow a comparison between studies, the results are expressed as the relative proportion of cells, with CMs fixed in a value of one, and assuming that most MCs are FBs. **Highlighted** (cyan box): *CM:EC:FB* ratios evaluated by **Bergman *et al.* (2015)**. Flow cytometry values (*bottom*, last line) were the starting point for the development of the 3D hiPSC-based cardiac models that will be discussed in later sections. **Abbreviations: CM** – Cardiomyocyte, **EC –** Endothelial cell, **FB –** Fibroblast, **H –** Whole heart, **LV –** Left ventricle, ***pap*** **–** papillary muscle. ***** fraction of CMs not determined (based on stereology study of the indicated reference).

Thus, despite the dissimilarities, especially with respect to CM and EC populations, and assuming that most MCs are actually CFs[48,49], these findings corroborate the hypothesis that CFs are the predominant cell type in the mammalian heart[48], which is in line with the results of other analogous studies[50].

These differences are, in a broader sense, intrinsic to the limitations of the techniques used[48,50]. Current state-of-the-art used methods relate to stereology[48], flow cytometry[48,50], heart dissociation followed by immunostaining and flow cytometric analysis[48,50] and stereological analysis combined with flow cytometry[48].

Even though flow cytometry is an objective, quantitative, reliable and not sampling-biased method, it requires a dissociation step[48] (typically chemical or enzymatic), which may lead to an excessive cell death[48] or incomplete dissociation[48], inducing errors in the results[48].

In contrast, stereological methods avoid the tissue dissociation[48] step and incorporate important information regarding cell polarity and morphology[48]; however, histological analysis is generally susceptible to sample bias[48], so making an identification based only on this method may equally be prone to error[48].

Beyond all this, both of the techniques require labelling[48,50] with antibodies or genetic tags, which may not be specific[48] (challenging especially in the case of mesenchymal populations) or incompletely labelling[48] the desired cell type.

1.2. Harnessing human pluripotent stem cells (hPSC) as an attractive candidate cell platform for *in vitro* cardiac modelling

1.2.1. Human pluripotent stem cells (hPSC) – characteristics, sources and applications

Pluripotent stem cells (PSC)[10,15,18,33,51], and in particular human pluripotent stem cells (hPSC)[10,15,18,33,51], are capable to grow unlimitedly (self-renewal)[15,33,51–54] and have the intrinsic ability to differentiate into any type of somatic cell (pluripotency)[1,4,18,33,51–57] and, therefore, in all the tissues of the three germ layers[58–60]: endoderm, mesoderm and ectoderm – which establish the precursor layers of the cells in adult organisms and form during embryogenesis[59,61]. They do not, however, differentiate into extra-embryonic tissue[58–60].

hPSC include (i) human embryonic stem cells (hESC)[10,15,18,33,51,53], isolated from the embryo's inner cell mass[58,62–68] (ICM) at the blastocyst stage[58,62–68], after *in vitro* fertilization or somatic nuclear transfer[58,62–68] (with the cells forming its outer layer being called trophectoderm[58,64]); and (ii) human induced pluripotent stem cells (hiPSC)[10,15,18,33,51,53], reprogrammed from somatic cells via the ectopic expression of a set of defined transcription factors[1,10,15,53].

Owing to these refined characteristics, hPSC are considered the most powerful cell type for tissue engineering[2,51], disease modelling[2,56] (**Fig.1.7**), personalized drug screening[11,20–22,56,69] (**Fig.1.7**) and cell therapy (**Fig.1.7**) and regenerative medicine applications[51,56].

However, their unrestricted capacity for self-renewal also brings up safety barriers, due to the possible formation of teratomas[8,33,57] and to the instability of their genetic material[33,57]. One of the major challenges to the application of hPSC in therapy is incontestably eradicating these risks in preclinical studies before the initiation of clinical trials[8,33,57]. Thus, the efficacious application of hPSC in clinical therapy will require control of their pluripotency phenotype and self-renewal ability, which can be

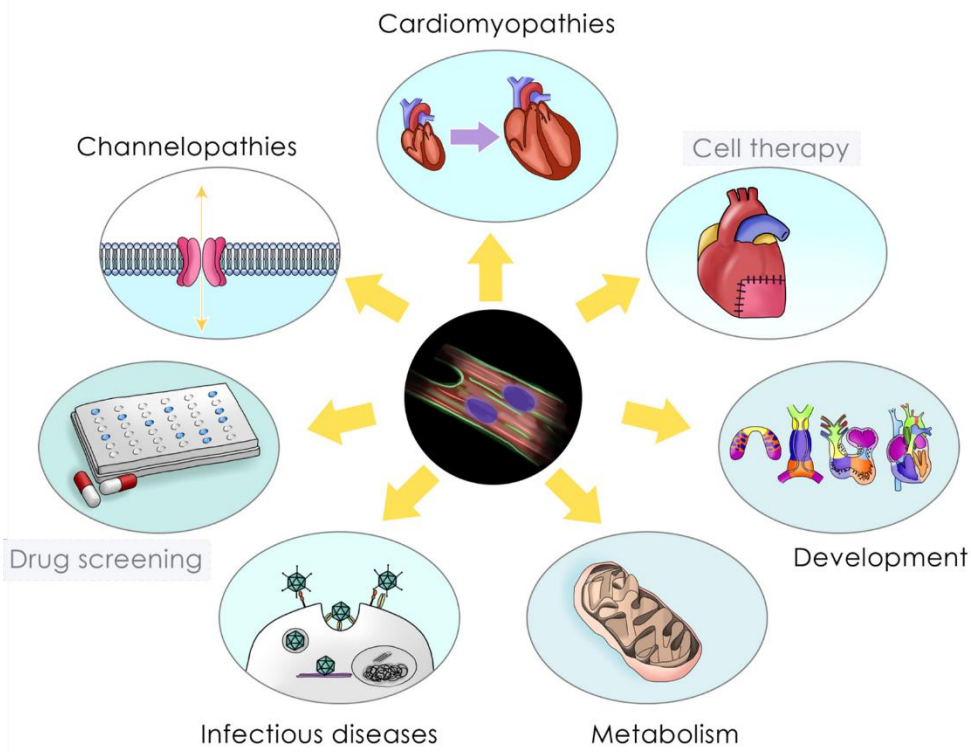

Figure 1.7 | hPSC as an ideal cell platform in the cardiovascular landscape: emerging applications [adapted from **Karakikes *et al.* (2016)**[56]].

Current **applications** of human pluripotent stem cell-derived cardiomyocyte (**hPSC-CM**) platform. **Highlighted** (cyan boxes): **drug screening** and **cell therapy**.

attained when they are cultured in maintenance media containing self-renewal factors[33]; howsoever, the removal of these factors triggers hPSC spontaneous differentiation into a cell mixture representative of the three germ layers[33].

The first derivation of hESC from pre-implantation embryos was described by **Thomson *et al*. (1998)** and occurred more than a decade ago[70]. These PSC can be isolated and maintained through well-established protocols[51,52], with scalable options[18,71–73] and indefinite proliferation associated with their ability to differentiate into virtually any cell of the human body[18,32].

Another breakthrough arose when **Takahashi and Yamanaka (2006)**[66] found that, through the ectopic overexpression of four retrovirally transduced transcription factors, *OSKM* (*OCT4*, *SOX2*, *C-MYC* and *KLF4*), in mouse dermal fibroblasts grown in conditions favouring the ESC expansion, they had the ability to generate induced pluripotent stem cells (iPSC)[62,65–67].

The promise of applying this technology to human cells did not take too long and a first generation of human induced pluripotent stem cells (hiPSC) was obtained from human fibroblasts[74], using the same combination of *OSKM* transcription factors[74] or a slightly different lentivirally transduced gene cocktail (*OCT4*, *SOX2*, *NANOG* and *LIN28*)[74], in which the proto-oncogenes *C-MYC* and *KLF4* were substituted by *NANOG* and *LIN28*. The iPSC field remains to grow very quickly and pluripotency has now been induced with non-integrating viruses[55,75] (*e.g*. recombinant lentiviruses and adenoviruses), excisable transposon-based systems[55,75], recombinant proteins[18,55], transfection of modified RNAs[18,55,75] and small organic molecules[18,55], in numerous cell types.

Additionally, hiPSC do not entail ethical issues[15,55] (contrasting with hESC, resulting from early embryos) and can be derived from patient- and disease-specific somatic cells[10,15,53,55,56], which allows them to be used in several fields, especially in the cardiovascular[10,15,51,55,56,76] (**Fig.1.7**) and neuroscience areas[51,77]. This is not possible in the case of hESC, because they do not harbour the desired mutations[15,53].

Nevertheless, apart from the ethical question[15,55] and some subtle differences in epigenetic modifications and gene expression signatures[15], hiPSC and hESC are quite similar in their capacity of unrestricted self-renewal and differentiation into any type of somatic cell[1,15]. Also, they are comparable in terms of cell morphology, growth profiles, expression of stemness-related markers, DNA methylation mode, chromatin status, among others[15].

In this context, one of the areas uppermost in the list of hiPSC-based research arena is the *in vitro* recapitulation of the human heart microenvironment (**Fig.1.7**), either for fundamental or translational research, as well as cell-based cardiac disease models for studying disease progression and treatment (**Fig.1.7**). For this, it is crucial to resort to cardiac hiPSC-derivatives.

1.2.2. Human pluripotent stem cell-derived cardiomyocytes (hPSC-CM)

1.2.2.1. Strategies for the cardiac differentiation of hPSC

The first hPSC-based cardiac differentiation protocol was reported by **Kehat *et al*. (2001)**[78] and involved the formation of embryoid bodies (EBs)[4,18,33,53,55,78,79], which are 3D spheroid-like aggregates that produce cells from all the three germ layers[4,53,78]. This strategy depends on the formation of EB spontaneous contraction[4,25,53], which has a variable efficiency, oscillating between 5 and 15%[4,25,53]. Protocols for generating these EBs were initially developed using fetal bovine serum (FBS) supplemented culture media[4,10,55], although defined media formulations are already regularly used[4,10,55].

Beyond this method, two were later established: i) a co-culture of hESC with visceral endoderm-like cells (END-2)[1,4,18,53,79,80], derived from mouse P19 embryonal carcinoma cells[10,53,80], described by

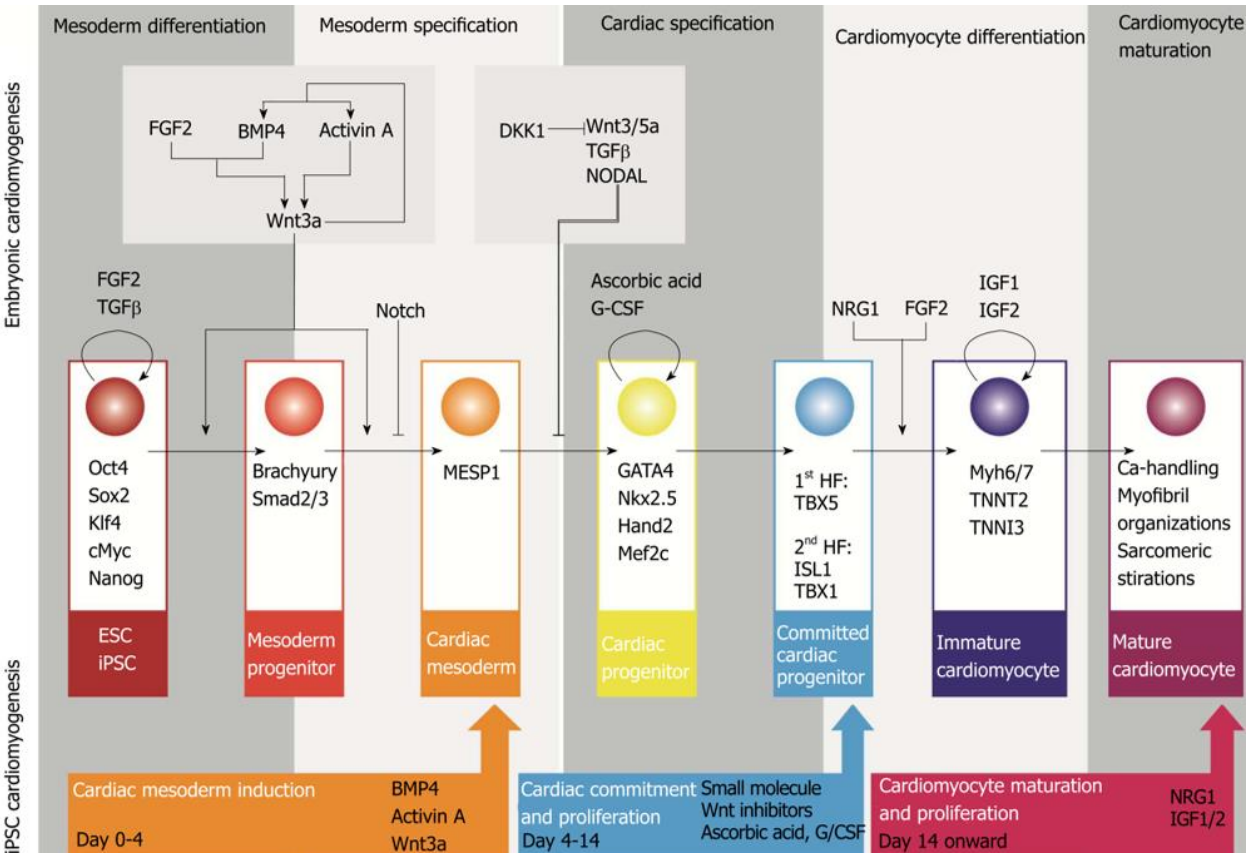

Figure 1.8 | Diagram of the pivotal steps and key signalling pathways enrolled in hPSC cardiac differentiation [adapted from **Kamps and Krenning (2016)**[89]].

Factors that influence the advance over the **five pivotal steps** of **hPSC-CM differentiation**: (*from left to right*) (i) **mesoderm differentiation**, (ii) **mesoderm specification**, (iii) **cardiac specification**, (iv) **cardiomyocyte differentiation** and (v) **cardiomyocyte maturation**. (*below*) The major markers associated with each one of the seven cell types during differentiation are listed in the corresponding boxes.

Mummery *et al*. (2003)[80]; and, as an alternative, (ii) differentiation in 2D monolayer cultures[1,10,18,79,81,82], used in many labs (including ours[83,84]), firstly reported by **Laflamme *et al*. (2007)**[81].

Among those three strategies, monolayer differentiation is the gold method, since it offers a superior differentiation efficiency and ease of monitoring[53,76]. Refinements, over the last decade, make it possible to generate cultures containing 85% of human pluripotent stem cell-derived cardiomyocytes (hPSC-CM)[53,76]. In addition, several methods, in which these populations can be enrich up to 95%, using, for example, sodium lactate containing medium[85,86], or based on cell surface markers[87,88], such as SIRPα/β and VCAM-1, have been described. But, in practice, how does the cardiac differentiation work?

1.2.2.2. How to make a cardiomyocyte: understanding the pivotal steps in cardiac differentiation

The principle of hPSC-CM differentiation is to mimic, *in vitro*, the pivotal steps (**Fig.1.8**) in embryonic cardiogenesis, via the supplementation of hPSC with key stage-specific small molecules that efficiently direct them to the cardiac lineage[89,90] (**Fig.1.8**).

In the embryo of vertebrates, the heart is one of the first organs to be formed, which occurs from the appearance of the mesoderm, that arises from the primitive streak during gastrulation[1,33,34,76,89]. At embryonic day 5, mesoderm forms with *Nodal* signalling in the proximal epiblast, maintaining BMP-4 (bone morphogenic protein 4) expression in the extra-embryonic ectoderm[1,32,34]. Other signalling

pathways (*e.g*. Dkk1, Cer1, and Lefty1) are responsible for the *Nodal* and *Wnt* (homologous of Drosophila *Wingless* gene) signalling restriction to the posterior epiblast[1,32,34,91].

Hence, a sequence of signals, spatially and temporally regulated, fundamentally bone morphogenetic proteins[1,55,89,90,92] (BMPs), *Wnt*[1,55,89,90,92] proteins, *Nodal/Activin*[1,55,89,90,92] pathway molecules and FGFs[1,55,89,90,92], are crucial for endorsing the *in vitro* myocardial fate specification[1,55,89,90,92] (**Fig.1.8**). Built on this premise, there are many protocols that induce cardiomyogenesis in hPSC, via activation and inhibition of these signalling pathways[53,76,85,92].

In this context, we can mention, as an example, the stimulation of extra-embryonic ectoderm[32,90], through BMP-4 and activin A, and posterior primitive streak[1,32,53,90], via *Wnt* signalling activation (specifically *Wnt3a*), by CHIR99201, during the first 24h of cardiac differentiation, promoting the exit of the pluripotency state and induction of cardiac mesoderm[53] (**Fig.1.8**). Particularly, CHIR99021 is a potent inhibitor of the glycogen synthase kinase-3 *beta* (GSK-3β), activity[5,25,53], functioning as a *Wnt* activator[5,25,53], since it blocks the enzyme activity[1], preventing β-catenin degradation[1], that is thereby able to move from the cytoplasm to the nucleus, where it activates the Wnt target genes[1].

Then, to induce the cardiac specification, *Wnt* signalling pathway must be inhibit[1,32,89] (**Fig.1.8**) to allow the heart development from the *Mesp-1*$^{+}$ cells in the anterior mesoderm[1,32], being *Mesp1* the "master regulator" of cardiac progenitor specification[1,32].

Wnt signalling small molecule inhibitors, such as IWR-1[4,32,53], IWP-3[53], IWP-4[4] and XAV939[53], have been shown to have the ability to induce the formation of cardiac progenitor cells (CPCs), when added after mesoderm formation[4,32,53,89]. SB-431542, an inhibitor of the TGF-β pathway, has a similar effect, when its addition occurs at this stage[5]. Media supplementation with these inhibitors recaps the actions of Dkk1-mediated inhibition of *Wnt* signalling, during embryology[89].

At this stage, the addition of ascorbic acid (AA) (**Fig.1.8**) boosts CM differentiation, by increasing collagen synthesis[93], enhancing the proliferation of CPCs[89,93] and upregulating late stage markers of cardiomyogenesis[93]. Furthermore, CPC-derived cultures may still undergo an additional maturation round[94] in the presence of NRG-1 and IGF-1[28,35,38,89] (**Fig.1.8**), as discussed in former sections.

1.2.2.3. Developmental status and challenges – immaturity concerns

Overall, hPSC-CM, obtained from these culture methods, contract spontaneously[53], express sarcomeric proteins and ion channels[18,53,56] and exhibit actions potentials[4,33,53] (APs) and Ca^{2+} transients[53,95,96]. Also, they display functional properties comparable to those of the CMs during cardiac development[1,53], including dose-dependent response to cardiac affinity drugs[3,19,53,97], to agonists and antagonists of β-adrenergic receptors[1,3,17,23,53,97] and to cardiotoxic drugs[11,20–22,98].

Differentiation and purification of hPSC-CM have been gradually optimized, but there are some hurdles with respect to: (i) reproducibility of cardiac differentiation between individual hPSC lines[10,53,85], (ii) cost-inefficiency of reagents[25,32,53,76], (iii) *batch-to-batch* variability[10,53,85], (iv) hPSC-CM yield and purity[53,85] and (v) the immature phenotype displayed[1,3,5,10,17,53,83].

Concerning the latter, the maturation efficacy of hPSC-CM is one of the topics that has visibly escaped the field: hPSC-CM exhibit immature phenotypes, evinced by a reduced sarcomeric alignment, small APs, in electrophysiological characterizations, and fetal transcriptome and metabolome profiles[4,25,33,53].

The challenge of cardiac maturation has been mitigated with a number of different methodologies, which will be covered in sections **1.3.1** and **1.5**, yet still far from cracking this issue.

1.2.3. Human pluripotent stem cell-derived endothelial cells (hPSC-EC)

In a similar fashion to what has been described for hiPSC-CM, there are basically two methodologies for generating human pluripotent stem cell-derived endothelial cells (hPSC-EC): (i) 3D EB-mediated differentiation[99,100] and (ii) 2D monolayer-based differentiation[99–101].

As stated in a preceding topic (**1.2.2.2**), when mesoderm polarization occurs, several types of cells are generated in the cardiovascular system[101], including CMs (**Fig.1.9**), along with those from the endocardium (**Fig.1.9**), vascular endothelium (**Fig.1.9**) and hematopoietic system[101] (**Fig.1.9**). So, similarly to what happened with CMs, hPSC are also, in this case, differentiated into mesodermal lineages[101] (**Fig.1.9**).

The main strategy is the sequential addition of growth factors, such as BMP4 and vascular endothelial growth factor A (VEGFA)[99,100]. In EB-based cultures, this method generated low differentiation yields, ranging from 2 to 15% of $CD31^+$ cells[99] (a surface marker extensively described for definitive endothelial phenotype).

Moreover, in this case, it is also possible to modulate the *Wnt* signalling pathway[99,100], through selective small molecule inhibitors of GSK-3β[100] (consult **1.2.2.2**), in conjunction with BMP4[99,100], translating in 25% to >40% of $CD31^+$ cells[102]. Further defined differentiation conditions, based on monolayer cultures coupled with the addition of growth factors and small molecules (*e.g.* *Wnt* activators and cAMP-elevating agents)[99] resulted in higher differentiation yields, ranging from 20 to 80% of $CD31^+$ cells[103].

Other studies have revealed that in combinations with VEGFA, SB-431542 (small molecule inhibitor of TGF-β) or forskolin lead to higher CDH5 (VE-Cadherin) expression in hPSC-EC[100]. This expression is even more pronounced when CHIR99021 is combined with DLL4 (*Notch* ligand that inhibits the hematopoietic-lineage differentiation) and with a low concentration of VEGFA[104].

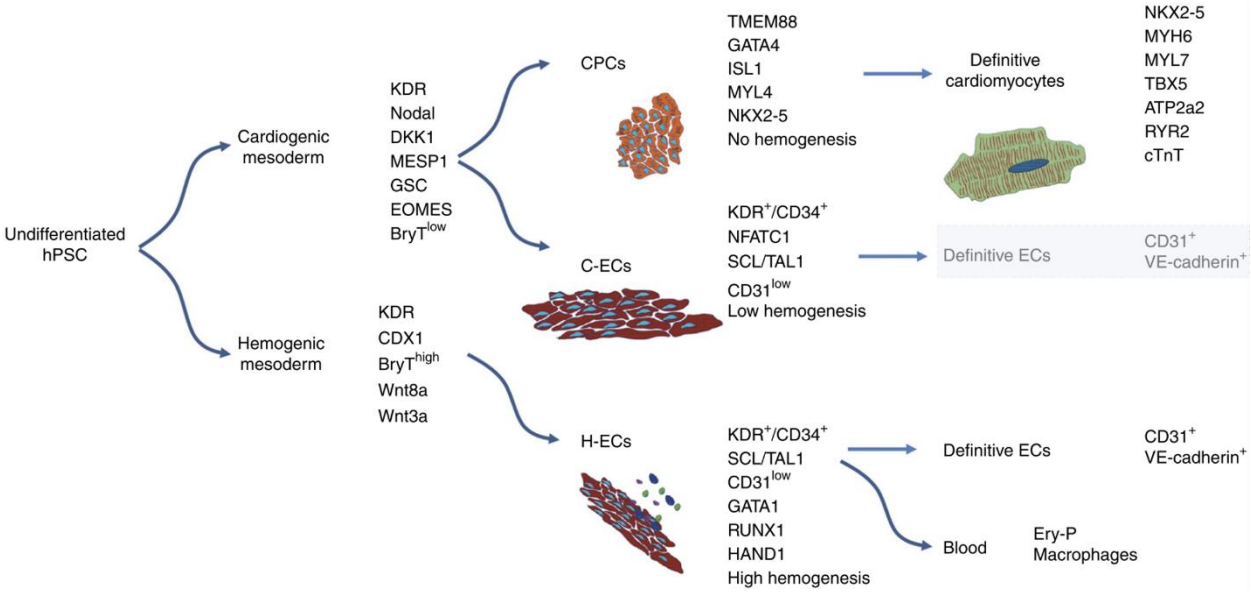

Figure 1.9 | EC fate decision and related molecular markers [adapted from **Palpant *et al.* (2017)**[101]].

Schematic overview of the fundamental **cell-fate choices** from the pluripotent state (undifferentiated hPSC) to the **vascular** (**hPSC-EC**) and cardiac (hPSC-CM) destinations. Molecular markers are identified for each of the populations. **Highlighted** (cyan box): **markers** for **definitive endothelial** phenotype (**PECAM-1/CD31** and **CDH5/VE-Cadherin**). **Abbreviations**: **CECs –** Cardiogenic-mesoderm-derived endothelial cells, **CPCs –** Cardiac progenitor cells, **EryP –** Primitive erythroid, **H-ECs –** Hemogenic-mesoderm-derived endothelial cells (for the remaining, consult **List of Abbreviations and Conventions**).

The last step is to select EC lineage via specific surface markers: whereas KDR and CD34 are selective for EC progenitors, PECAM-1 (CD31) (**Fig.1.9**), CDH5 (VE-Cadherin) (**Fig.1.9**) and von Willebrand factor (VWF) are those used to isolate mature ECs[99–101] (**Fig.1.9**).

Some of the major drawbacks of the differentiation protocols towards the endothelial lineage are the fact that they are hardly scalable[99], the low differentiation yields[99,104], dependence on undefined supplements[104], existence of heterogeneous cell aggregates[104] and lack of reproducibility[99,100,104]. Therefore, methods that improve the scalability, reproducibility and fidelity of differentiation towards the endothelial fate, are desired.

1.3. State-of-the-*heart* tissue models

1.3.1. Maturity issues boost the creation of more robust and faithful *in vitro* cardiac models

Before discussing the various approaches to assemble a heart *in vitro*[2,105], it is important to underline that the need for such models arises essentially from the immature phenotype exhibited by hPSC-CM[4,32] (**Fig.1.10**), which prevents the use of this cellular platform in translational applications[4,32].

hPSC-CM maturation is a very complex arena, subordinate to the domain of several cues, including biochemical[2,23,106,107] (*e.g*. thyroid hormone stimulation[106,107], **Fig.1.10**), mechanobiological[108,109], topographical[23], electrical[23] (**Fig.1.10**) and important homo- and heterotypic interactions[4,17,23,30,110,111] (**Fig.1.10**).

Hence, an ideal bioinspired, *in vitro*, cardiac model should be able to faithfully recapitulate the physiological (heart in its inherent state) or pathophysiological (disease progression) conditions of the human heart, including the 3D anisotropic tissue structure together with cell-cell and cell-extracellular environment interactions, ECM orientation and composition, vascularization and circulation[14,23,32,105]. These aspects are summarized in **Fig.1.11**.

However, even though several caveats persist, it is only conceivable to recapitulate *in vitro* a subset of the *in vivo* phenotype (**Fig.1.11**).

1.3.2. Shifting the paradigm: conventional 2D monolayers toward 3D cultures

Under physiological conditions, cells are part of a versatile and dynamic network that cannot be entirely recapitulated in a 2D monolayer system[110]. Conventional 2D culture systems do not satisfactorily mimic the *in vivo* developmental microenvironment of the human heart[14,25,105].
Also, their inherent uncontrollability, heterogeneity, low production yields and poor scalability make these systems inapt for clinical applications[51,112]. Yet, they can be quite useful, as a starting point, by providing important evidence regarding basic cell-cell interactions and ECM composition[14,105].

Cells in a 3D environment behave fundamentally differently from cells in a 2D monolayer culture[14,23,32,105] and, therefore, in order to understand the complete picture, we will have to resort to more complex models (**Fig.1.11**).

When compared to 2D monolayers, 3D culture systems potentiate cell-cell[14,23,25,32,105] and cell-ECM interactions[14,23,25,32,105], establish molecular concentration gradients[23,32] and may disregard the need for unnaturally stiff and adherent substrates[23,32].

Furthermore, the main benefit of 3D models is to offer a cellular context analogous to that occurring in the native tissue[2,17,23,51] (in this case, the heart) (**Fig.1.11**), driving an increase in cell viability and

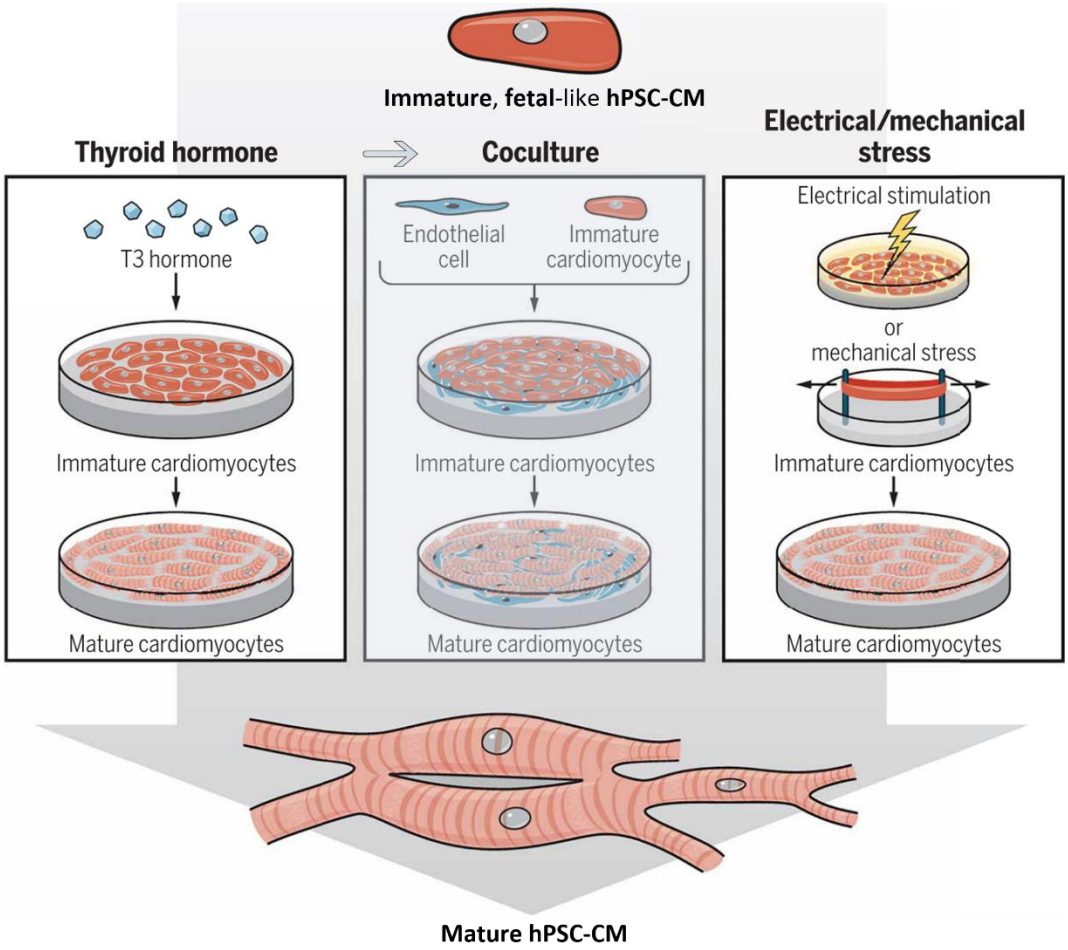

Figure 1.10 | Key strategies to induce hPSC-CM maturation *in vitro* [adapted from **Devalla and Passier (2018)**[2]]. The structural, functional and metabolic characteristics of hPSC-CM are consistent with an **immature phenotype**. Some **cues**, including (i) **biochemical**, such as (*left panel*) the addition of **tri-iodo-L-thyronine** (**T3**) to the culture medium, (ii) **heterotypic cellular communication**, based on (*middle panel*) **co-cultures** with **non-myocyte populations** (*e.g.* **ECs**), or (iii) built on **electrical stimulation** or cycles of **mechanical stress**, can drive hPSC-CM toward a more **definitive** and **mature phenotype**. **Highlighted** (blue arrow and box): **co-culture strategy** (as a starting point for the work carried out and discussed in the course of this dissertation).

functionality[51], whereas, at the same time, offer a higher degree of efficiency[51], robustness[51], consistency[51] and predictability[51].

1.3.3. 3D models: steering the complex architecture of the cardiac tissue

Options for 3D model systems comprise: (i) scaffold-free approaches[14,113], such as cells cultured as organoids[2,14,84,113–115] (*e.g.* 3D cardiac spheroids, also named microtissues) and (ii) scaffold-based models[2,14,17,32,105], such as cells encapsulated in hydrogels[2,17,105] composed of natural products[2,17,105], cells in combination with synthetic materials[14,17,105], cells in peptide-modified scaffolds[116], cells in biological scaffolds[2,17,105] (*e.g.* decellularized hearts), 3D-bioprinted structures[2,17,23], microfluidic devices[2,117], among others.

Scaffold-free approaches promote and rely on cellular self-assembly and organization, while scaffold-derived approaches offer natural and/or synthetic matrices as a structural template for cells to attach to[14,17,23]. In practice, this means that in scaffold-free approaches cell-to-cell are the predominant interactions, contrasting with scaffold-based models, in which cell-to-scaffold interactions prevail[17,23].

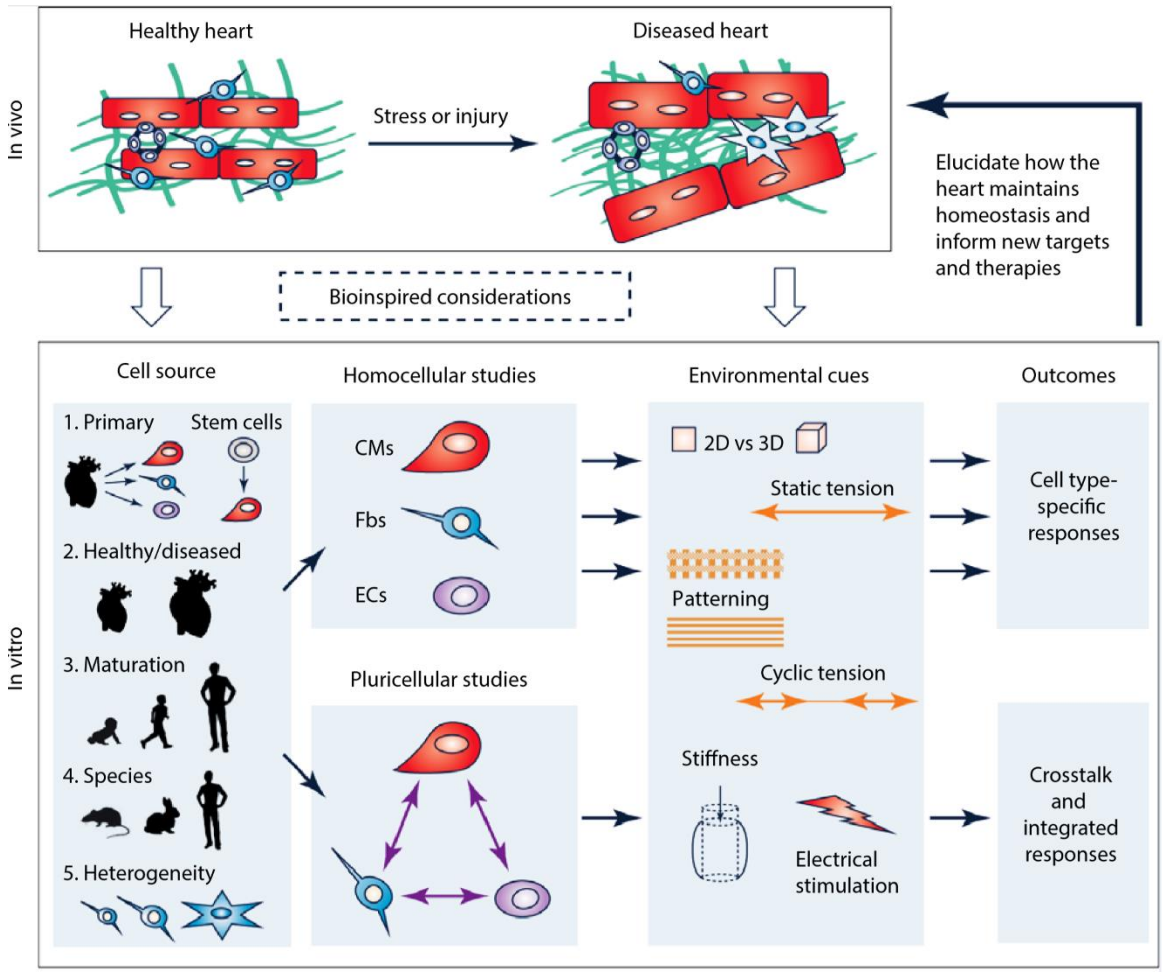

Figure 1.11 | Considerations for creating bioinspired *in vitro* cardiac models [reproduced from **Kofron and Mende (2017)[23]**].

In vitro platforms should consider (*upper panel*) (i) the **model purpose** (recapitulate **physiological** or **pathophysiological** conditions) and (*lower panel*, *from left to right*) (ii) the **cell source** (*e.g.* **hPSC**), (iii) **crosstalk** between **myocytes** and **non-myocytes** (*e.g.* **ECs** and **FBs**) and (iv) **environmental cues** (*e.g.* **3D organization**, mechanics and electrical stimulation). *Outcome*: in comparison with 2D, pluricellular **3D studies** will always favour **cellular crosstalk** and **integrated responses**, rather than those associated with a single cell type.

1.3.3.1. Scaffold-free cell spheroids

Spinner flasks, rotation systems, hanging drops, microfluidic devices and non-adhesive substrates are some of the examples used to self-assemble cardiac cells into spheroid-like 3D tissues *in vitro*[105,112].

Homo- or heterotypic organoids are one of the most common and versatile example of *in vitro* cardiac models in the cardiovascular context[2,83,110,112,114]. The referred self-assembly methods allow the generation of homotypic organoids[83,84], typically comprising several CM subtypes[2], or heterotypic[2,105,110,114], adding, along with CM, non-myocyte populations[2,105], such as ECs[2,105], VSMCs[2,105] and CFs[2,105]. Hence, they are perhaps one of the most relevant cell-based platforms for understanding interactions between different cell types[2,105].

Since hPSC cultured as EBs, in the presence of certain growth factors (consult **1.2.2.1** and **1.2.2.2**), generate a mixture of atrial, ventricular and nodal cells, it is thus possible to generate cardiac organoids as 3D aggregates[2].

The advantages of 3D spheroids' self-assembly are organotypic density and architecture, maximization of cell-to-cell communication and movement among the different cell types, self-produced ECM and

adrenergic responses similar to those *in vivo*[14,23,32,110]. Outstandingly, hPSC-CM demonstrate an increased cardiac maturation when grown as 3D aggregates, compared to 2D monolayer cultures[83,118,119]. The *in vitro* exogenous electrical stimulation of nanowired hiPSC cardiac spheroids allows to further improve cellular maturation and function[120,121].

In addition, as shown by **Garzoni *et al*. (2009)**[114] and **Stevens *et al*. (2009)**[115], they self-organize with ECs and CFs to form vascular networks without the need for exogenous materials[114,115]. Also, the inclusion of non-myocyte populations in the spheroids promotes the sarcomeric organization and an increased Cx43 expression[122].

Recently, **Giacomelli *et al*. (2017)** established conditions for the simultaneous differentiation of CMs and ECs from hPSC, then enriched and recombined to generate 3D cardiac spheroids[110]. This study showed an increased expression of cardiac genes[110], encoding ion channels[110], and Ca^{2+} handling proteins[110], as well as human dose-response to β-adrenoceptor stimulation[110], consistent with cardiac maturation. Also, this study contributes to understanding non-myocytes' role (*e.g*. ECs) in the functionality and maturation of CMs.

Despite the numerous advantages, this strategy also entails some hindrances, relating to the difficulty in controlling spheroid size[51] and in performing their harvesting[51], which is usually accompanied by some associated cell death[51], owing to the dissociation agents used.

1.3.3.2. Scaffold-based strategies

The native heart matrix is a well-organized anisotropic structure that supports CMs and nonmyocytes[17,23,24]. The ECM of the adult heart is composed mostly of collagen[7,14,24,32,123], but also includes fibronectin[24,32,123], laminin[32,123], vitronectin[32,123] and elastin[7,123], all of which contribute to cell adhesion[14,123] and load-bearing capacity of the heart[123].

Biomaterial scaffolds should offer a 3D microenvironment for cells to attach, interact with each other, transmit load and conduct electrical signals[17,23]. They should also induce alignment, provide adequate stiffness for the cells to generate mechanical strength and have the ability to enzymatically degrade over time, to be swapped by cell-secreted ECM, so that a remodelling of the cardiac microenvironment may occur within the scaffold[14,17].

A wide variety of scaffolds and matrices[2,14,23,25,105] have been used for the purpose of assembling the human heart milieu, *in vitro*, from different cell sources, including murine and hPSC-cardiac derivatives (the latter being those in which we will concentrate more attention). There are two major groups of scaffolds for the *in vitro* development of engineered heart tissues (EHTs): (i) natural[2,14,23,25,105] and (ii) synthetic[2,14,23,25,105].

1.3.3.2.1. Naturally occurring hydrogel-based EHTs

The most widely studied constructs for the seeding of the aforementioned cardiac populations are hydrogel systems[2,17,105,116] (**Fig.1.12**).

This method comprises three components[105]: (i) solutions of natural gelling products[2,17], such as alginate[105,116], *Matrigel*[14,17,32,105,116], collagen[105], fibrin[14,105], gelatine[105,116], hyaluronic acid (HA) [105], or mixtures of them[105]; (ii) casting molds[105]; and (iii) and anchoring constructs[105]. The hydrogel entraps cells in a 3D space during gelling, the mold confers the 3D shape and, lastly, the anchors allow the tissue to grow in a controlled space[105].

Hydrogels formed from such materials are particularly suitable for tissue engineering applications, because their biomechanical properties can be tuned to the values found in the native heart matrix

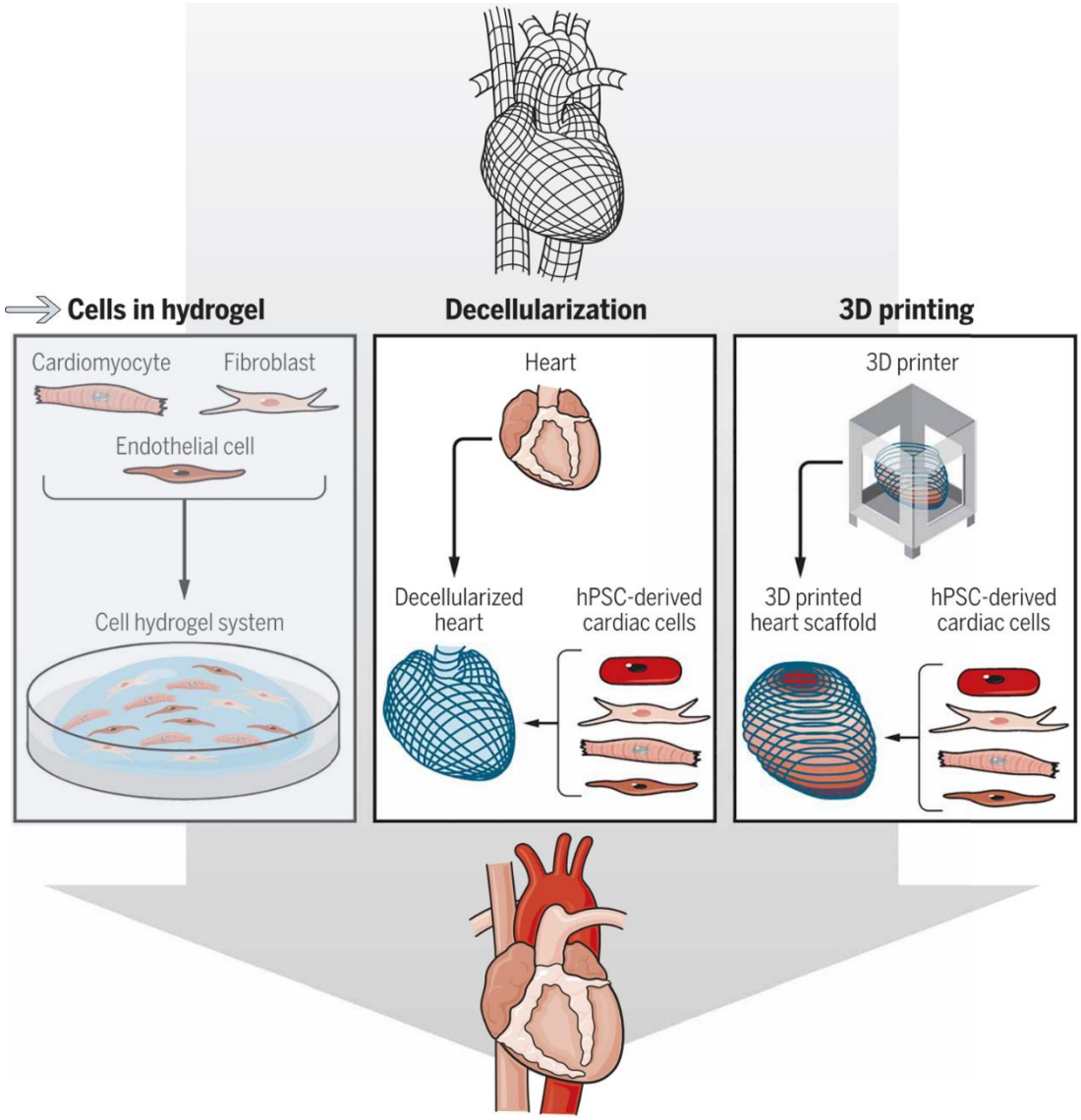

Figure 1.12 | Important scaffold-based tissue engineering strategies to assemble a human heart *in vitro* [adapted from **Devalla and Passier (2018)**[2]].

Human EHTs can be generated by: (*left panel*) (i) combination of hPSC-cardiac derivatives in naturally occurring **hydrogels**, (*middle panel*) (ii) **decellularization** of animal or human hearts, that function as "biological" scaffolds and can be subsequently repopulated with hPSC-cardiac derivatives, or (*right panel*) (iii) **bioprinting** of hPSC-cardiac derivatives onto a 3D heart scaffold, thereby generating a highly robust model of the human heart. . **Highlighted** (blue arrow and box): **hydrogel strategy** (as a starting point for the work carried out and discussed in the course of this dissertation).

(approximately 5 kPa)[17]. Another plus of this type of system is that it enables the miniaturization[2] and automation[2] of cardiac tissue generation, which is particularly relevant for high-throughput drug screening[2,105]. In addition, naturally occurring hydrogels stimulate cells to spread and form intercellular connections[17,105].

In the cardiac context, hydrogel encapsulation has been used to study heterotypic interactions between myocytes and non-myocytes (**Fig.1.12**). **Narmoneva *et al*. (2004)** reported the use of a peptide hydrogel, seeded with of murine cardiac cells, in three distinct configurations: CMs alone[124], CMs mixed with ECs (co-culture)[124] and CMs seeded on preformed (prevascularized) EC networks[124]. It was found that the co-culture was the condition that minimized the CM apoptosis and necrosis, which were far superior in the remaining conditions[124]. Similar studies, nonetheless with hiPSC-cardiac derivatives, were also carried out[125,126].

More recently, hydrogel-based engineered heart tissues (EHTs) demonstrated enhanced ultrastructural organization, with defined sarcomere striation patterns[17], mRNA expression of specific cardiac markers[17] and synchronous contractile behaviour[17], in addition to functional properties consistent with a mature phenotype[17].

Moreover, cell or aggregate microencapsulation in hydrogels provides a shear stress-free microenvironment, avoiding excessive clumping of aggregates in culture[51]. Thus, this 3D strategy turns out to be quite attractive for use in large-scale bioprocesses and provides a finer control of the cultures and higher cell yields, when compared to non-encapsulated cultures[51].

1.3.3.2.2. Synthetic scaffold-based EHTs

In contrast, the synthetic materials used may be based on two major classes: (i) polyesters, such as PLLA (poly-L-lactic acid)[14,17,105], PGA[14,17,105] (polyglycolic acid), PLLA/PGA[14,17,105] (poly-L-lactic acid/polyglycolic acid) composites, polylactones[14,17,105], polyurethanes[14,17,105] and PGS[2,7,14,17,97,105], poly(glycerol sebacate), a biodegradable elastomer; or in (ii) polyethers[116].

An obvious advantage of synthetic scaffolds, when compared to the other techniques, is that they may be fully customized[17]; however, they are more restricted in terms of functional interactions and, because of that, are normally modified to incorporate adhesion peptides or molecules[17].

As an example, we can highlight the study of **Caspi *et al*. (2007)**, in which multicellular biodegradable scaffolds[127], consisting of 50% PLLA/50% PLGA[127], were constructed: hESC-CM were combined with hESC-EC or human umbilical vein ECs (HUVECs), with or without embryonic fibroblast (EmFs)[127]. Again, the co-culture condition resulted in an enhanced CM proliferation, without affecting elongation, orientation or alignment[127].

1.3.3.2.3. Peptide-modified scaffolds

Typically, to increase cell survival and organization in the aforementioned scaffolds, cardiac cells are often seeded mixed with *Matrigel* (*e.g*. hybrid constructs) to enable cell adhesion[17,32,116]. However, since *Matrigel* is an undefined gelatinous protein mixture[32,116], derived from a mouse cell line carcinoma[32,116], contains unknown growth factors and proteins[32,116], which limits its attractiveness for cell therapy and regenerative medicine applications, as they require very precise conditions[116].

In this context, recent research in biomaterials, organic chemistry and chemical biology (*e.g*. click chemistry)[128] has advanced to design, synthesize and modify materials, in a way that they interact selectively and spatially with the cells through very specific biomolecular recognition events[116,129].

One of these examples is the functionalization of materials[116,130,131], natural or synthetic, or the preparation of pseudopeptide compounds[128], with RGD motifs[116,128,130,131].

RGD is one of the most physiologically ubiquitous binding motifs attached to scaffolds[116]. Corresponds to the *arginine-glycine-aspartate*[116,130,131] peptide sequence, derived from ECM proteins[116,130,131], such as fibronectin[116,131], collagen[116,131], vitronectin[116,131] and laminin[116] and is the link between the intracellular cytoskeleton and ECM, via cellular integrins[116,131]. It is ultimately responsible for initiating cell signalling for cell survival and proliferation[116,131].

However, very few examples exist in the literature reporting the existence of RGD peptide-modified scaffolds for the *in vitro* generation of cardiac models. An important example in the field is that of **Shachar *et al*. (2011)**, which demonstrated that the presence of RGD peptide, immobilized in an alginate scaffold, was able to promote neonatal rat CMs' adhesion, preventing apoptosis and accelerating tissue regeneration[116].

1.3.3.2.4. Biological tissue-scaffolds: decellularized whole hearts

In addition to strategies based on the self-assembly of cardiac spheroids or in compatible biomaterials, several groups have been reporting the use of biological tissues as scaffolds for developing EHTs[2,17] (**Fig.1.12**).

The principle of tissue decellularization is the removal of all the cellular elements, leaving the ECM "undamaged"[2,105].

Proof that it is possible to use decellularized whole hearts, leaving the microvasculature intact, is given by **Ott *et al*. (2008)**'s study, which reports the production of EHTs in decellularized rat hearts[132]. More recently, this has also been successively shown for human EHT[133], in which an acellular human heart scaffold has been repopulated with hiPSC-CM to create an *in vitro* human EHT[133].

This method has the advantage of providing a combination of local control[17] (conserved through protein content and native mechanical properties) and long-range signalling[17] (through the preservation of the anisotropic structure and ECM topology).

1.3.3.2.5. Emerging strategies – 3D bioprinting and microfluidics

Finally, highlight two methods that together can alter the way we conceptualize *in vitro* cardiac models (**Fig.1.12**).

The first has already revolutionized the medicine field, with the production of some medical devices, such as implants and prostheses[2,23]; we are referring to 3D printing. More recently, a variant of this technique, termed 3D bioprinting (**Fig.1.12**), has been successfully used to print living tissue. A thermoreversible support bath was used to allow hydrogel-based bioprinting of a 3D chicken heart[134].

The prospects are that in the future, hPSC-CM can be bioprinted and layered to reproduce the 3D architecture of the heart. If we combine this method with microfluidics, which can be used to simulate blood flow[2,117,135] in the bioprinted cardiac tissue, we come to a highly robust model of the human heart.

1.4. Reaching clinically significant cell numbers in bioreactors

Bioreactors have been broadly used in chemical and biological industries for the production of antibodies[51,73] and recombinant proteins[51,73], in addition to other products[51,73]. More recently, applications with hPSC, in which hPSC itself or their cardiac derivatives are the major products, have also been reported[51,72,73,99,136,137].

Many of these applications, both clinical and industrial, involve the use of hPSC-cardiac derivatives, and depend on the constant and controlled production of billions of cells[54,73,136]: note that the human heart encompasses about 4 billion CMs[138].

The estimated cell requirements for heart and liver repair, as well as for the treatment of diabetes, relate to 10^9-10^{10} hPSC-derived progenies per patient[54,71]. This implies a mandatory significant upgrading in the bioprocesses, as well as further scale-up[72,73].

Furthermore, unlike, for instance, the production of recombinant proteins in mammalian cell lines, in a relatively easy manner, the challenge, in the case of hPSC, is much more complex, requiring more sophisticated and innovative bioprocesses[51,73] (**Fig.1.13**). Thanks to their intrinsic potential, hPSC may switch (uncontrollably) from pluripotency toward an undesired differentiated state during the cell expansion phase[73]; besides, the differentiation into the desired lineage is highly complex, including the effects of the previous expansion[73].

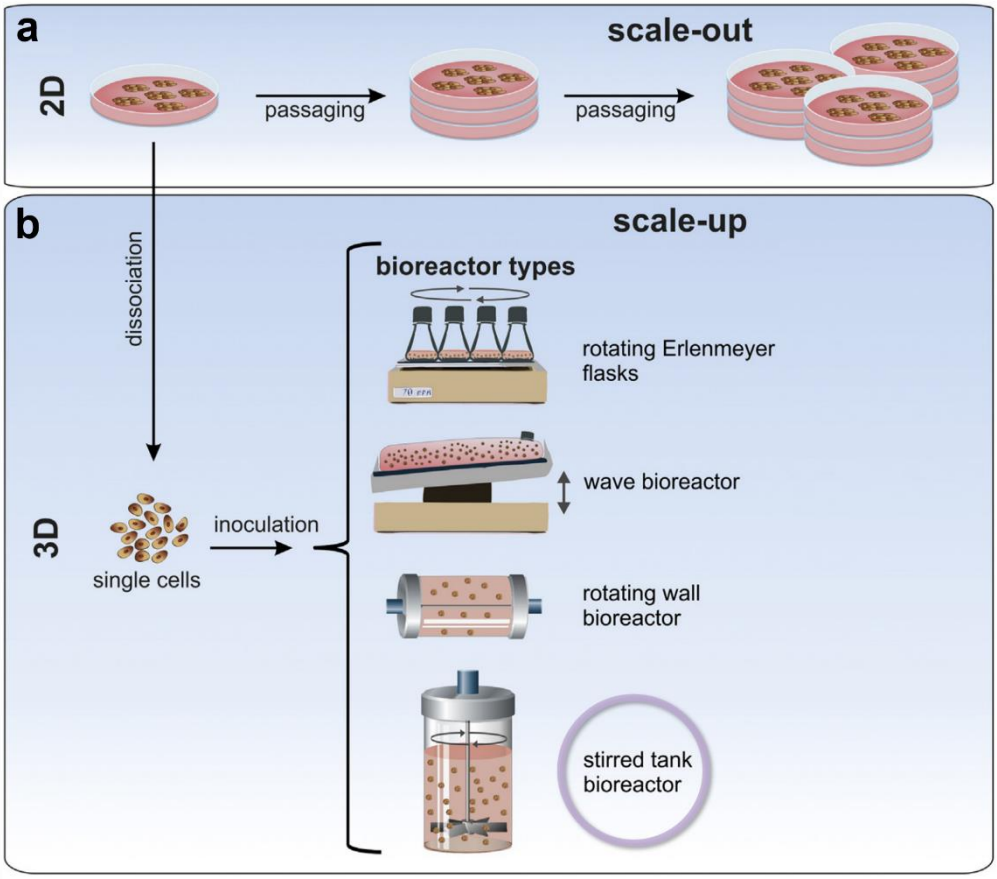

Figure 1.13 | Expansion strategies for hPSC and hPSC-cardiac derivatives [adapted from **Kropp *et al.* (2017)**[73]]. (***a***) (*upper panel*) **"Scale-out"** approaches of the conventional **2D** culture methods via increasing the number of cultivation vessels. (***b***) (*lower panel*) **Scale-up** approaches using **3D** culture methods within **bioreactor systems** (*e.g.* rotating Erlenmeyer flasks, in addition to wave, rotating wall or **stirred tank bioreactors**), which allow to increase the entire manufacturing scale. **Highlighted** (blue circle): stirred tank bioreactors.

Bearing in mind this scenario, instead of the conventional "scale-out" (of the 2D approaches) (**Fig.1.13*a***), which is relatively cost-[73], space-[73], and labour-intensive[73], the establishment of bioreactor systems (**Fig.1.13*b***) provides a technology capable of meeting these needs in the cardiovascular context[136,139]. By combining bioprocess automation[51,71,73], monitoring[51,71,73], molecular and fluidic control[32,51,71,73] and scalability[51,71,73], bioreactor systems allow a reduced operator-dependent variability[73], opening the doors for more robust and cost-effective bioprocesses[51,73].

The use of bioreactor systems simplifies the establishment of suspensions of dynamic and homogenous cultures, thereby overcoming the heterogeneity, typical of 2D static conditions[51,54,71,73,139]. Moreover, they offer a non-destructive sampling[51] (beneficial for continuous monitoring and control).

There are numerous types of bioreactor systems (**Fig.1.13*b***): wave bioreactors, stirred tank, packed bed, hollow fibre, bubble-column and airlift bioreactors are the some of the examples[51,71–73,136,139–141]. Amid all these, we will focus on stirred tank bioreactors (STBRs) as a tool for cellular aggregation in a controlled microenvironment.

STBRs are equipped with integrated probes that allow a tight and tuned monitoring and control of the culture environment, including parameters such as temperature, pH, DO, nutrient (*e.g.* glucose), metabolite (*e.g.* lactate, ammonia) concentrations, gas composition (*e.g.* O_2 and CO_2) and vital biomass assessment[51,73,136].

Hence, STBR technology allows a relatively linear and straightforward *up-scaling* process[142] and supports distinct bioreactor operation modes[73], categorized into four classes[73]: (i) *batch*, (ii) repeated *batch*, (iii) fed *batch* and (iv) perfusion (continuous feeding with cell retention).

However, it also presents downsides, such as the hydrodynamic shear stress caused by stirring, which can adversely affect 3D spheroid cultures and cell differentiation[143].

1.5. Towards an integrated characterization toolbox for 3D *in vitro* cardiac models

As revealed in the above sections (**1.2.2.3** and **1.3.1**), the lack of a mature, adult-like phenotype in hPSC-CM, countered, in part, by the creation of more faithful and robust 3D cardiac cell-based models that recapitulate *in vitro* certain aspects of the physiology and architecture of the human heart *in vivo* (**1.3**), is one of the core limiting factors that averts the advance of these models towards clinical settings.

However, since there is such a miscellaneous array of models, an equally robust characterization toolbox must be developed to study and characterize them, in depth.

This section briefly outlines some of the current state-of-the-art methodologies, used to characterize these models, covering (i) structural and ultrastructural features, molecular profiling (gene and protein expression) and calcium handling; (ii) mechanobiological approaches, particularly atomic force microscopy; and, lastly, (iii) microscopy-based phenotypic approaches.

1.5.1. Structural and ultrastructural features

Structurally, hPSC-CM are small[25,144], round[25,144] or multi-angular[144] cells (**Fig.1.14**), resembling embryonic CMs[25,56], with a single nucleus and chaotic myofibrillar alignment[18,144] (**Table 1.1**). Ultrastructurally, they display disorganized and small sarcomeres (with a length of about 1.6 µm[144]) and absence of T-tubules[2,18,25,56] (**Table 1.1**). Typically, it is only possible to detect Z-discs and I-bands, via transmission electron microscopy (TEM) characterizations[25,56,144] (**Table 1.1**).

Conversely, adult CMs or mature hPSC-CM exhibit a much more elongated[25,56,144], rod-like shape[25,56,144] and about 30-35% of them are multinucleated[25,53] (**Fig.1.14**, **Table 1.1**) (this percentage does not fluctuate meaningfully throughout life[53]).

In addition, several alterations affecting CM contractility occur in sarcomere and myofibril organization during maturation[18,25] (**Fig.1.14**). Specifically, they have highly organized sarcomeres (with a length of approximately 2.2 µm; higher than in immature CMs) with longitudinal myofibrillar alignment and scattered presence of T-tubules[2,53,144] (**Table 1.1**). TEM ultrastructural analysis demonstrate CM anisotropy[53] and normally detect Z-discs, together with I-, H-, A-bands[25,56,144] (**Fig.1.14**), albeit the presence of M-bands is not clear[56] (**Table 1.1**). This anisotropic alignment of adult CMs is also important to allow an efficient propagation of electrical signals[25,53], which are supported by the formation of connexin-43 (Cx43), holding gap junctions between cells[145].

Via TEM it is additionally possible to perceive that, in adult CMs[144], mitochondria are located along the cell[144], occupying 20-40% of its total volume[144], whereas in hPSC-CM[144] these numbers are noticeably lower and associated with a perinuclear location[144] (**Table 1.1**).

With this in mind, TEM, enabling a high subcellular imaging resolution[53,146–148], to access ultrastructure[53,146,147], and scanning electron microscopy (SEM), allowing for topographical imaging (*e.g.* 3D spheroids or complex 3D cardiac models) and providing data on the cellular organization and

Table 1.1. Comparison of phenotypic features between adult and hPSC-CM, in terms of structure, sarcoplasmic reticulum (SR), gene expression, metabolism, electrophysiology and calcium handling kinetics [adapted from Denning *et al.* (2016)[144]]. **Highlighted** (cyan boxes): structure, SR, gene expression and calcium kinetics properties.

		Adult-CM	hPSC-CM
Structure	Structure	Rod-shaped	Round or polygonal
	Alignment	Longitudinally aligned	Chaotically organised
	Nucleation	~30% cells bi- or poly-nuclear	Very limited bi-nucleation
	Sarcomere organisation	Highly organised	Disorganised
	Aspect ratio	5–9.5:1	2–3:1
	Banding	Z-discs, I-, H-, A- and M-bands	Mainly Z-discs and I-bands
	Sarcomere length	2.2 μm	1.6 μm
SR	Sarcoplasmic reticulum	Well developed	Mixed response: caffeine, Thapsigargin & ryanodine
	SR proteins	e.g. CSQ, PLN, RYR2, SERCA/ATP2A2	Expression lower than adult
	T-Tubules	Yes	No
Expr.	Gene expression	MYH7 (β-MHC) > MYH6 (αMHC)	MYH6 (αMHC) > MYH7 (βMHC)
		TNNI3 (cTnI) > TNNI1 (foetal ssTnI)	TNNI1 (foetal ssTnI) > TNNI3 (cTnI)
		MYL2 (MLC2v) > MYL7 (MLC2a)	MYL2:MYL7 ratio not determined
		Titin isoform N2B predominates	Titin isoform N2BA predominates
		ADRA1A (α-adrenoceptor) expressed	ADRA1A (α-adrenoceptor) not expressed
Energy & force	Metabolism	Mainly fatty acids	Glucose and lactate but can use fatty acids
	Energy production	Mainly oxidative phosphorylation	Mainly oxidative phosphorylation
	Mitochondria	Throughout cell; occupies 20–40% of cell volume	Near nuclei; numbers increase during differentiation
	Beating	Quiescent	Many cells spontaneous
	Force	40 to 80 mN/mm^2 (muscle strips)	0.08–4 mN/mm^2 (3D constructs)
		~μN range (single cells)	~200 nN (single cells)
Conduct	Capacitance	150 pF	20–50 pF
	Resting mem potential	−80 to −90 mV	−20 to −60 mV
	Upstroke velocity	150–350 V/s	10–50 V/s
	Conduction velocity	60 cm/s	10–20 cm/s
	Location of gap junctions	Intercalated discs	Circumference of cells
Ca^{2+} kinetics	Cycle Length	0.8–1 s	0.8–2 s
	T-rise	2.5 ms	3.5-10 ms
	Triangulation	45 ms	45-120 ms

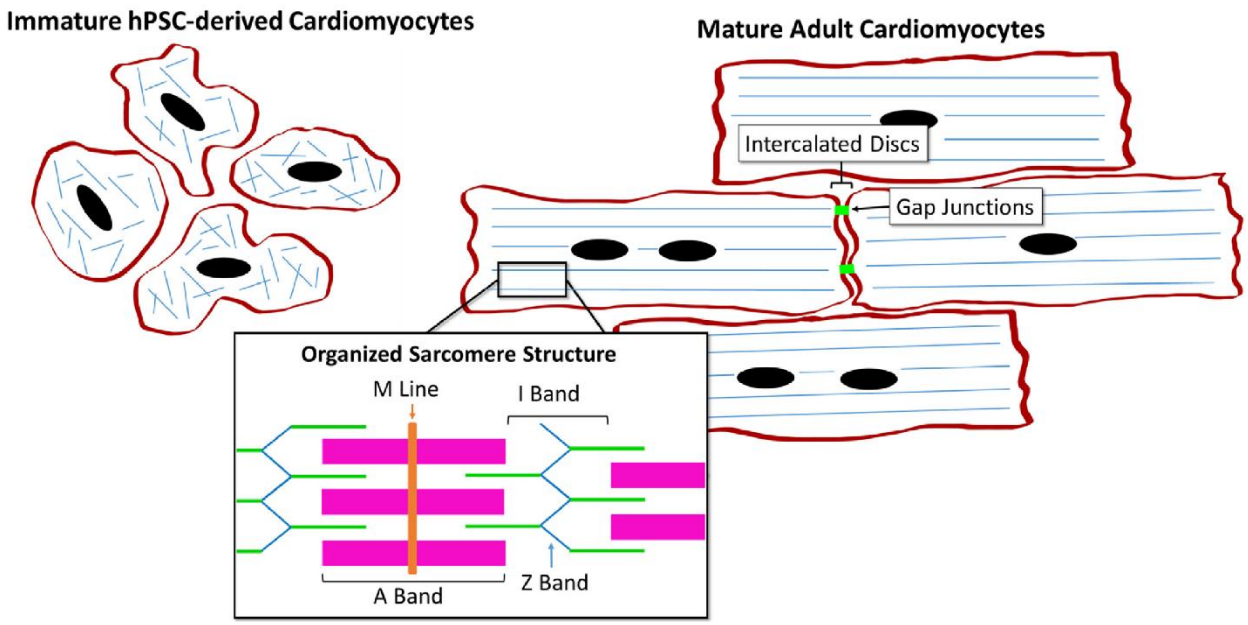

Figure 1.14 | Structural and ultrastructural differences between immature hPSC-CM and mature adult CMs, that occur during the maturation process [adapted from Dunn and Palecek (2018)[25]].

(*left*) **Immature hPSC-CM:** small, round or multi-angular shape, mononucleated and chaotic myofibrillar alignment.

(*right*) **Mature adult CMs:** more elongated, rod-like shape, bi- or multinucleated, with highly organized sarcomeres displaying a longitudinal myofibrillar alignment. The inset indicates a high magnification image of the corresponding black rectangle: adult CMs' ultrastructural analysis detecting Z-bands, together with I-, A- and M- bands.

architecture of specific structures[114,149], are the state-of-the-art methodologies for studying ultrastructural and structural features.

The main structural and ultrastructural properties that have been described, for both immature and adult CMs, in addition to aspects related to molecular profiling and calcium handling kinetics, which will be discussed beneath, are summarized in **Table 1.1**.

1.5.2. Molecular profiling: gene and protein expression

Several CM genes are more expressed in adult CMs than in hPSC-CM[25,144] (whose expression is similar to that found in the first trimester fetal heart[144]) (**Table 1.1**).

These genes encode ion channels[2,4,18,25,56,144] (*e.g*. *L*-type calcium: *CACNA1C* and *CACNA1D*; sodium: *SCN5A*; potassium: *KCNH2* and *KCNQ1*; and sodium/potassium: *HCN4*), critical regulators of calcium cycling machinery and sarcoplasmic reticulum (SR) transporters[2,4,18,25,56,144] (*e.g*. *IPTR3*, *RYR2*, *SERCA2*, *CASQ2*, *CALR*, *JPH2*, *PLN*, *NCX1* and *TRDN*), sarcomeric proteins[2,4,18,25,56,144] (*e.g*. *MYL2*, *MYL3*, *TNNI3*, *ACTN2*, *MYH7*, *MYL3*, *TNNC1*, *TNNT2*)[2,4,18,25,56,144] and other cardiac specific proteins[4,18,78] (*e.g*. atrial natriuretic factor, *ANF*).

More importantly, the expression of different sarcomeric protein isoforms switches during CM maturation[25,53,144], denoting a transition from fetal to postnatal development[53].

For instance, immature CMs express the slow skeletal isoform of troponin I (*TNNI1*)[25,53,144] and titin isoform *N2BA*[144], whilst more mature CMs express the cardiac isoform (*TNNI3*)[25,53,144] and titin isoform *N2B*[144]. In the same way, ventricular CMs express MLC-2*a* and MHC-α (encoded by *MYL7* and *MYH6* genes, respectively), early in development, but upregulate MLC-2*v* and MHC-β (encoded by *MYL2* and *MYH7* genes, correspondingly), as they mature[4,53,56,144].

Hence, real-time reverse transcription-quantitative polymerase chain reaction (RT-qPCR) and flow cytometry (FC) arise as the gold methods to recognise and quantify changes in gene and protein expression, respectively[91,144].

1.5.3. Calcium handling: functional but immature Ca^{2+} handling apparatus

The aptitude for the *in vitro* development of a functional Ca^{2+} handling apparatus, ion channels and calcium regulatory proteins is an important feature for a mature phenotype of repolarization[18,95,96].

In adult ventricular CMs, Ca^{2+} handling exhibits an arrangement of well-defined events[95,96,150,151].

Briefly, a small Ca^{2+} influx into the cells, through depolarization-activated *L*-type Ca^{2+} channels, during systole, triggers a calcium release from the internal calcium store, sarcoplasmic reticulum (SR), via ryanodine receptors (RyRs)[95,96,150,152,153]. This process is known as Ca^{2+}-induced Ca^{2+} release (CICR)[95,96,150,152,153] and constitutes the primary mechanism linking electrical excitation and mechanical contraction in CMs[95,96,150,152,153]. Instead, during diastole, repolarization occurs and calcium is actively (with ATP expenditure) removed from the cytosol, mostly via SR calcium-ATPase (SERCA) back into SR and sodium/calcium exchanger out of cells[153].

However, as expected, hPSC-CM Ca^{2+} handling properties (*e.g*. smaller peak amplitude and slower kinetics) resemble those of fetal left ventricular (LV) CMs and are significantly different from adult LV CMs[95,109] (**Table 1.1**). RyRs are expressed in hPSC-CM, but lack the organizational pattern observed in adult CMs, owing to the lack of T-tubules[95]. Also, regulatory proteins such as triadin (TRDN), calsequestrin (CSQ) and junctin (JCTN), that are common in adult CMs, are rarely expressed in hPSC-CM[4,56,95].

Overall, hPSC-CM exhibit an immature calcium machinery, due to the underdeveloped SR and fetal expression profiles of important calcium handling proteins[95,109,150,152].

Calcium sparks, waves or transients can be imaged and quantified using fluorescent Ca^{2+} indicators[10,126,154,155] (*e.g*. *Fluo*, *Fura*, *Indo 1* and *Oregon-Green*), which enhance their fluorescence intensity in the presence of Ca^{2+} ions[155], allowing the study of CM functionality[91,95,96,152].

1.5.4. Mechanobiological dynamic characterization: atomic force microscopy

Atomic force microscopy (AFM) is a 3D topographic method that allows for surface roughness measurement with superior atomic resolution[156]. It belongs to scanning probe microscopies and its principle is based on the interaction between a sharp *tip* and the atoms on the sample surface[156].

Importantly, it can be used in biological applications[108,109,148,156] (*e.g*. Alzheimer's disease process and cell-based biosensing of drug responses) under native conditions[157] (*e.g*. liquid environments).

Moreover, by modifying AFM scanning probe (the *tip*), additional surface properties, such as friction, adhesion force, hardness, stiffness, Young's modulus and even magnetic or electrostatic features, can be determined[108,109] and quantified[158].

The use of AFM to study mechanobiological properties may be particularly useful in the cardiovascular context, although few examples are reported in the literature[108,109,159].

One of these, reported by **Lieu *et al*. (2009)**, relates to the use of AFM in synergy with calcium imaging[160], in order to demonstrate the lack of T-tubules in hESC-CM[160], which, as mentioned in the previous topic (**1.5.3**), are vital for a normal CICR mechanism in adult CMs. In addition, fascinatingly, cardiac microenvironment remodelling can be correlated with AFM measurable-biomechanical parameters (*e.g*. Young's modulus, stiffness, hardness, amid others), that can ultimately be used to discriminate between healthy and hypertrophic hPSC-CM lines[109].

1.5.5. Microscopy-based phenotypic approaches: from conventional widefield to the cutting-edge 3D reconstructions

Most imaging in cell biology is performed with widefield microscopy, in which the microscope basically creates an image of the sample on the camera, without any further optical manipulation[161].

A number of experimental and technical challenges, however, have to be unravelled before researchers can take full benefit of the cutting-edge 3D models[161–163].

Providing insight into the internal morphology of large and compact spheroids has, undoubtedly, been a challenge[164] (**Fig.1.15**). The traditional preparation technique for immunofluorescence microscopy purposes is the physical sectioning of paraffin-embedded or frozen spheroids[164,165]. Then, the (cryo)sections are generally analysed in a conventional fluorescence microscope[164,165] (**Fig.1.15**). However, following sectioning, it is challenging and laborious to reconstruct the 3D information[164], in addition to these techniques being restricted to fixed samples only[165].

Bearing in mind that conventional wide-field fluorescence microscopy does not allow a faithful visualization of 3D cellular spheroids[161], mainly owing to their inhomogeneity[162,163,166] and low transparency[162,163,166], one of these challenges is finding improved imaging techniques that can penetrate the depth of thick and highly scattering samples with negligible photodamage[162,163,166].

Furthermore, a dynamic quantitative analysis of a 3D biological structure requires the satisfaction of several crucial factors[162–167]: (i) excellent *signal-to-noise* ratio, (ii) optical sectioning capability, (iii) large field of view, (iv) good spatial resolution, (v) a desirable fast image stack recording rate and (vi) low sample fluorophore excitation level.

The options available for such imaging techniques will now be briefly discussed.

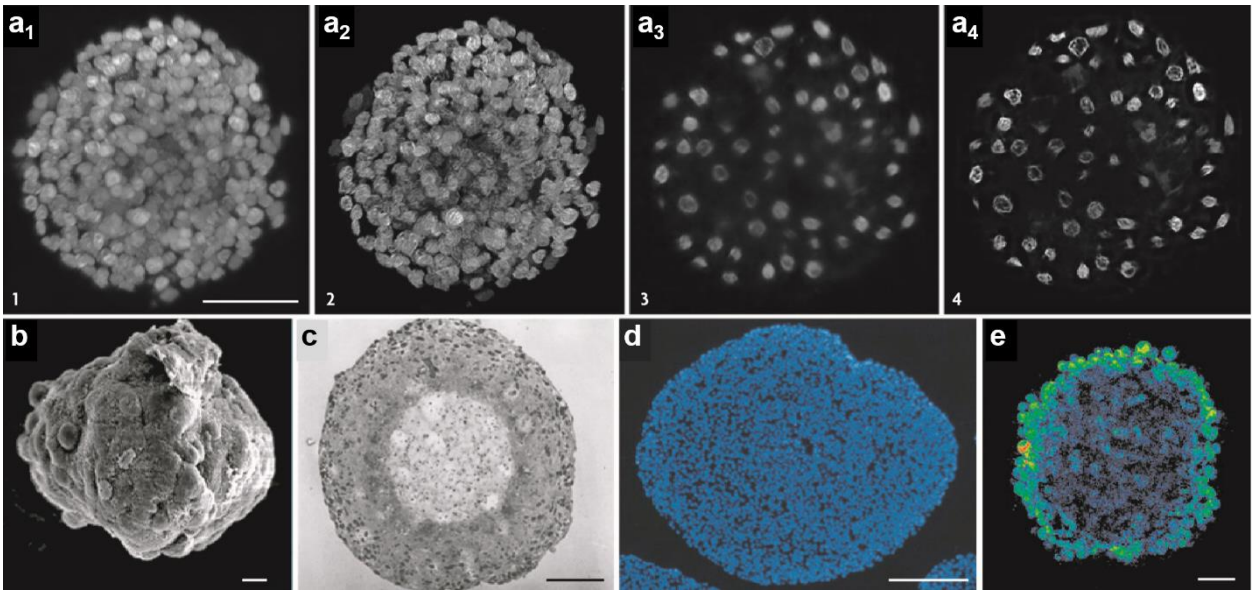

Figure 1.15 | Microscopy-based phenotypic approaches for characterizing large and thick 3D spheroids [adapted from **Pampaloni *et al*. (2007)**[163]]. Examples of 3D cellular spheroids imaged with several microscopic techniques. **(*a*)** Compilation of **LSFM images** of a spheroid composed of *BxPC-3* human pancreatic cancer cells. Scale bars, 50 µm. **(*a*$_1$)** Nuclei of the spheroid, stained with *Draq5* dye. Maximum projection of a stack obtained from a **multi-view reconstruction** of twelve stacks recorded along different angles (0 to 330º) with an incremental step of 30º. **(*a*$_2$)** Maximum projection of the same dataset exhibited in **(*a*$_2$)**, **after deconvolution**. **(*a*$_3$)** **Cross-section** of the same spheroid. **(*a*$_4$)** Same image in **(*a*$_3$)** **after deconvolution**. **(*b*)** Scanning electron microscopy (**SEM**) **micrograph** of a human hepatoma cell line. Scale bar, 10 µm. **(*c*)** Transmission electron microscopy (**TEM**) **cross-section** of a *V79* Chinese hamster lung cell spheroid. Scale bar, 250 µm. **(*d*)** **Immunohistochemical staining** of the nuclei of a *Rat1-T1* spheroid. Scale bar, 250 µm. **(*e*)** **Multiphoton** microscopy autofluorescence **images** of a multicellular tumour spheroid. Scale bar, 100 µm.

1.5.5.1. Confocal microscopy

Fluorescence confocal laser scanning microscopy (CLSM) represents the commercially available imaging method of moderately thick specimens, such as 3D spheroids[161].

In confocal microscopy, the sample is illuminated by a focused laser beam at a single point in the sample focal plane[161,168]. Summarily, the light from this point is detected after passage through a pinhole, so that only the light emitted from the focal plane passes through the pinhole and is recorded on the photodetector[161,168]. Light from *out-of-focus* planes is blocked by the pinhole and, therefore, the confocal modality only records light from the focal plane of the sample[161,168].

Thus, it is an imaging modality that allows a high *signal-to-noise* ratio, optical sectioning capability and good spatial resolution[161,168].

However, as in traditional wide-field fluorescence, in confocal imaging the excitation light illuminates the entire object, unwittingly extending photobleaching and phototoxic effects to all planes[161,163,168,169]. Also, a shortcoming of confocal is the limited penetration depth, when using high numerical aperture (NA) lenses[169]. These two limitations limit a regular application of confocal microscopy to *in toto* studies of large and thick 3D spheroids[161,163,168,169].

1.5.5.2. Multiphoton microscopy

A related technique is multiphoton or two-photon laser scanning microscopy (MPLSM)[170], which emerges as an attractive platform when observing large species (usually >200 µm)[161], mainly due to its twofold penetration depth, in comparison with confocal microscopy[161,163].

Another advantageous feature of multiphoton microscopy is the use of pulsed lasers that allow for second harmonic generation imaging of collagen fibres (major component of the native matrix of the human heart), flavoproteins and non-centrosymmetric polymers, without sample labelling[171,172].

Hence, multiphoton microscopy is usually recognized as the technique of choice for 3D imaging[169] and, particularly, for spheroid analysis[173] (**Fig.1.15**).

Notwithstanding, it offers low resolution and requires huge light intensities, causing bleaching and phototoxic effects in the focal plane[163]. Since it is a very sampling-destructive method, multiphoton may be particularly valuable when used in combination with other techniques[168].

1.5.5.3. Spinning disk confocal microscopy

Spinning disk confocal microscopy (SDMC) combine ease of use and high speed (up to hundreds of frames per second) and sensitivity and, thereby, has become widely used in cell biology[161].

For very compact samples (thicker than about 30 µm), SDMC is, however, more inefficient at rejecting *out-of-focus* light than confocal, but this is not a limitation for imaging the majority of tissue models[161,168]. The high scan speed does not only improve image acquisition rate, but also minimizes the light density required for the excitation peak, consequently increasing the fluorescence efficiency and decreasing photobleaching and photodamage effects, in comparison with regular confocal microscopy[168].

Owing to these advantages, spinning disk confocal is more live cell-friendly than widefield or confocal microscopy, being proper for live imaging[161,168] (*e.g*. protein or microtubules imaging, organelle dynamics, among others).

An interesting application, according to the background of this work, is the use of SDCM in live cell calcium imaging, with the aim of studying calcium handling machinery and kinetics[174] (in 2D monolayers or in 3D aggregates of hPSC-CM).

1.5.5.4. Light-sheet fluorescence microscopy: heralding a *whole picture* revolution in 3D microscopy

Progress in optical microscopy has overcome challenges that prevent high-resolution imaging of thick and highly scattering samples, such as 3D spheroids[162,163,166,169].

A revolution in microscopy befell with the development of light-sheet fluorescence microscopy (LSFM)[175] (**Fig.1.16**). These microscopes illuminate the sample from a plane orthogonal to the imaging plane[161] (**Fig.1.16*b*** and **Fig.1.16**, *lower left corner*). This eliminates the problem of *out-of-focus* light because only light from the focal plane or very close to it is excited[165–167] (**Fig.1.16*b*** and **Fig.1.16**, *lower left corner*).

Due to the high imaging speed and relatively good penetration depth with remarkably low photobleaching and phototoxicity (by virtue of the selective illumination)[162,163,165,166,169,176], LSFM is suitable for imaging large spheroids[165,167,177] and 3D complex models[178–181] (**Fig.1.16*a***) (*e.g*. alginate microcapsules containing spheroids and/or single cells). The combination with optical clearing methods may further increase the penetration depth by rendering the spheroid transparent[164].

In whole mount immunofluorescence techniques, the use of IgG antibodies (with a molecular weight of approximately 150 kDa) leads to poor penetration into 3D species and, consequently, inhomogeneous staining[164]. Imagine a spheroidal 3D structure: ordinarily, a good staining quality is only attained for the peripheral cells, whereas the staining quality quickly fades for cells in deeper regions.

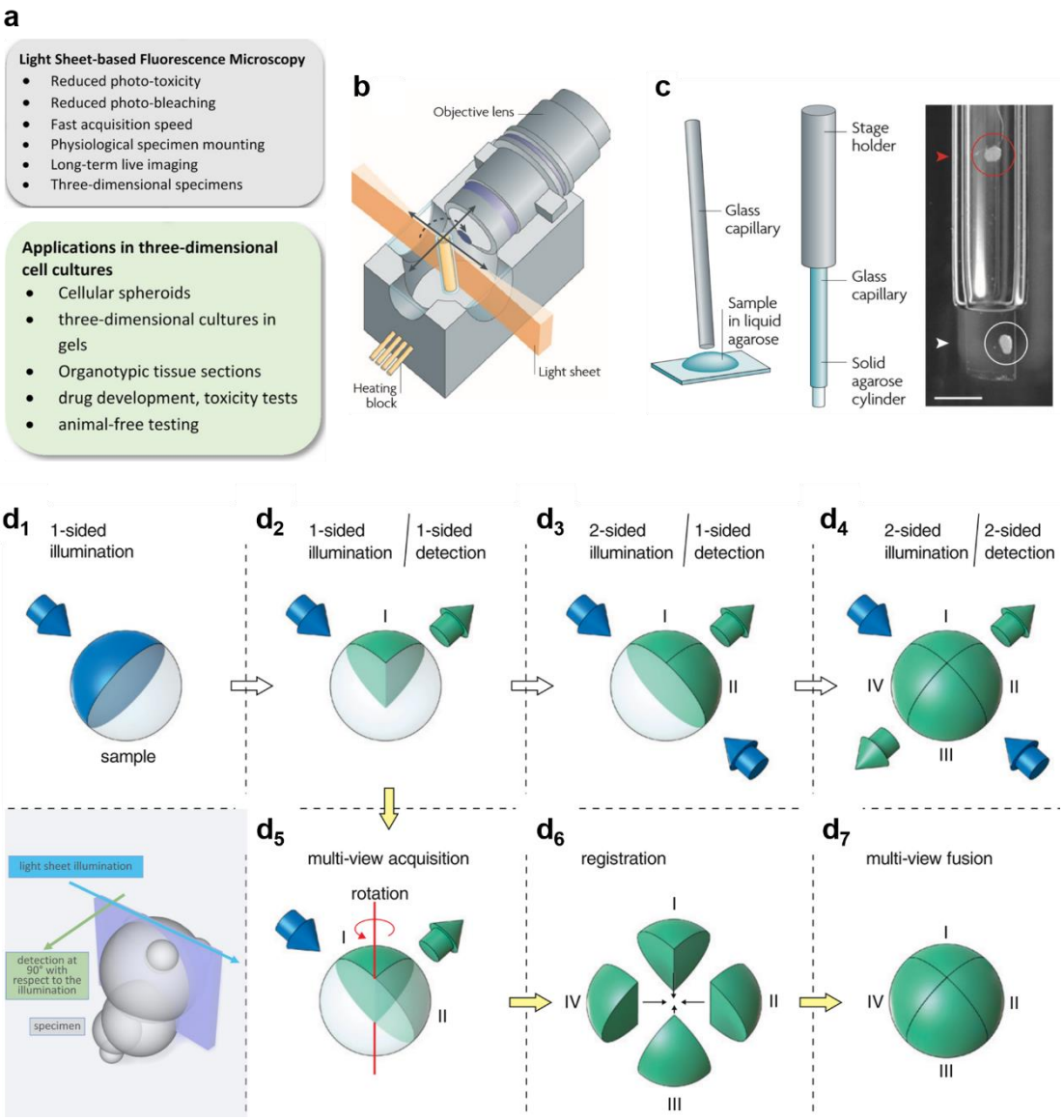

Figure 1.16 | Heralding a *whole picture* revolution in 3D microscopy with LSFM [adapted from **Pampaloni *et al*. (2015)[166]**, **Pampaloni *et al*. (2007)[163]** and **Weber and Huisken (2011)[175]**].

(*a*) **Relevant characteristics and major applications of LSFM, in 3D cell culture.** (*b*) **Autoclavable cell culture chamber for single plane illumination microscopy (SPIM).** The temperature is maintained at 37 ± 0.1 ºC and the objective lens is immersed into the culture medium. (*c*) **Mounting of 3D cellular spheroids for LSFM imaging.** The spheroid is suspended into a droplet of low-gelling agarose, at 37-40 ºC, and sucked into a thin glass capillary. Once the agarose has polymerized and hardened, the sample is pushed out of the capillary and imaged. (*right*, *white arrow and circle*) image of a cellular spheroid outside the capillary; (*right*, *red arrow and circle*) a second image of the same spheroid, but inside the capillary, is noticeable. (*d*) **Concept of 3D multi-view reconstruction in LSFM.** (*d_1*) In a scattering sample the light illumination will only penetrate part of the sample. (*d_2*) Likewise, fluorescence only penetrates the side facing the detection optics, so that only the quadrant facing illumination and detection will be well imaged. (*d_3*) By adding a second illumination source, quadrant II can be illuminated and imaged as well. (*d_4*) Lastly, by adding a second detection unit, quadrants III and IV can be imaged. (*d_5*) Instead, in **LSFM**, the sample can merely be **rotated**, making **all quadrants reachable**, even with a single set of illumination and detection. (*d_6*) Datasets are individually **recorded** and, then, (*d_7*) are **fused** to generate a faithful **3D volume reconstruction** of the **whole sample**, termed ***multi-view reconstruction***. **Highlighted** (*lower left corner*, blue box): Laser light sheet illumination and orthogonal detection (at 90 ºC with respect to illumination) provides optical sectioning, disregarding the *out-of-focus* issues.

Hence, LSFM is also an appropriate technique for *in toto* immunostaining[162–164,166,167,169,180], since, besides all the aforesaid advantages, it is able to counter this hindrance, via the possibility of obtaining multi-views of the sample (**Fig.1.15**), by rotating it, with isotropic resolution[161], so that the hidden parts

become visible[162,163,165–167,169,180] (**Fig.1.16*d***, ***d*$_1$-*d*$_7$**). This feature is not offered in the formerly referred multidimensional microscopy imaging systems (*e.g*. confocal and multiphoton) and allows to obtain a realistic 3D volume reconstruction, not accomplished by any other type of microscopy technique[165,167,180].

So far this technique has been successfully used to image cell aggregates and zebrafish, not only for fixed samples, but also live monitoring of cellular events, like apoptosis and calcium signalling[165,167,180].

Albeit these microscopes start to be commercialized, they are not yet readily available in the market, and are usually customized systems[161,166,169,180] (**Fig.1.16*b*** and **Fig.1.16*c***). The widening of their obtainability, together with the development of other personalized designs may, in a near future, herald a *whole picture* revolution in 3D microscopy.

2. Aims and Scope of the Thesis

The **scope** of this thesis was the **establishment of a bioinspired 3D hiPSC-derived cardiac tissue model** (***main aim***, **Fig.2.1**) that recapitulates *in vitro* certain features of the *in vivo* physiology and architecture of the human heart. Specifically, for the development of this model, cardiomyocytes and, separately, non-myocyte populations (endothelial cells and mesenchymal cells) were differentiated from hiPSC; afterward, hiPSC-CM were aggregated into 3D homotypic spheroids and microencapsulated in a biocompatible hydrogel, together with the non-myocyte populations (hiPSC-EC and hiPSC-MC), in order to generate a *scaffold*-based *in vitro* 3D triculture model, fully derived from hiPSC. As controls, 3D models composed only of encapsulated hiPSC-CM spheroids (*monocultures*) or, alternatively, encapsulated hiPSC-ECMC single cells (*co-cultures*), were also developed.

Considering the problem of the hiPSC-CM immature phenotype, **interrogating heterotypic cellular communication** between **myocytes** and **non-myocytes** (***specific aim* i**, **Fig.2.1**), especially that between hiPSC-CM and hiPSC-EC, and its **role in cardiac maturation**, is the first of the specific aims.

Given the massive difficulty in characterizing the internal morphology of compact and highly scattering spheroids, in addition to the fact that they were encapsulated in a microbead, **imaging-based phenotypic assays** were also **implemented**, based on confocal, spinning disk confocal, multiphoton and LSFM (***specific aim* ii**, **Fig.2.1**).

Another of the thesis' aims was to **challenge the models with cardioactive drugs** (*e.g*. norepinephrine, propranolol and heptanol) or **cardiotoxic anticancer drugs** (*e.g*. doxorubicin and paclitaxel) and evaluate the pharmacological responses and their ability to be used in drug screening and toxicology assessment (***specific aim* iii**, **Fig.2.1**).

Mechanical dynamic characterization, based on **AFM**, was also implemented, in order to study the hydrogel **scaffold** (in the absence of cells), **mono-** and **triculture mechanobiological behaviour** (***specific aim* iv**, **Fig.2.1**). It was also sought to study cell-ECM interactions (particularly those involving mesenchymal cells) and their impact on the remodelling of the cardiac microenvironment.

A preliminary study in **stirred-tank bioreactors** (STBRs), operating in perfusion, in order to perform the ***scale-up*** of the models, initially generated in shake flask, closes the final aim (***specific aim* v**, **Fig.2.1**).

Hence, the establishment of such a multifaceted model led to a correspondingly **robust characterization toolbox**. In addition to the stated strategies: (i) cryosections (using widefield and confocal microscopy) and whole mount (through multiphoton and LSFM) **immunofluorescence** microscopy, (ii) **gene expression** and **flow cytometry**, (iii) histological/**histochemistry**-based methods, (iv) live cell **calcium imaging** (using spinning disk confocal microscopy), (v) **ultrastructural** assessment via TEM, (vi) **characterization** of the **biomaterial**-based ***scaffold*** via AFM and SEM and, finally, (vii) **anticancer drug cardiotoxicity evaluation**, based on metabolic activity quantification, via *PrestoBlue* resazurin-based dye assay, were some of the major readouts used to in depth characterize it.

The **aims** of this thesis (**main** and **specific**), as well as the **major readouts** used, are summarized in **Fig.2.1**. This figure also displays a schematic depiction of the 3D triculture hiPSC-derived cardiac tissue model, together with the key model players (cardiomyocytes and non-myocytes, the biomaterial scaffold, self-produced ECM, soluble factors, among others) at the endpoint of the model.

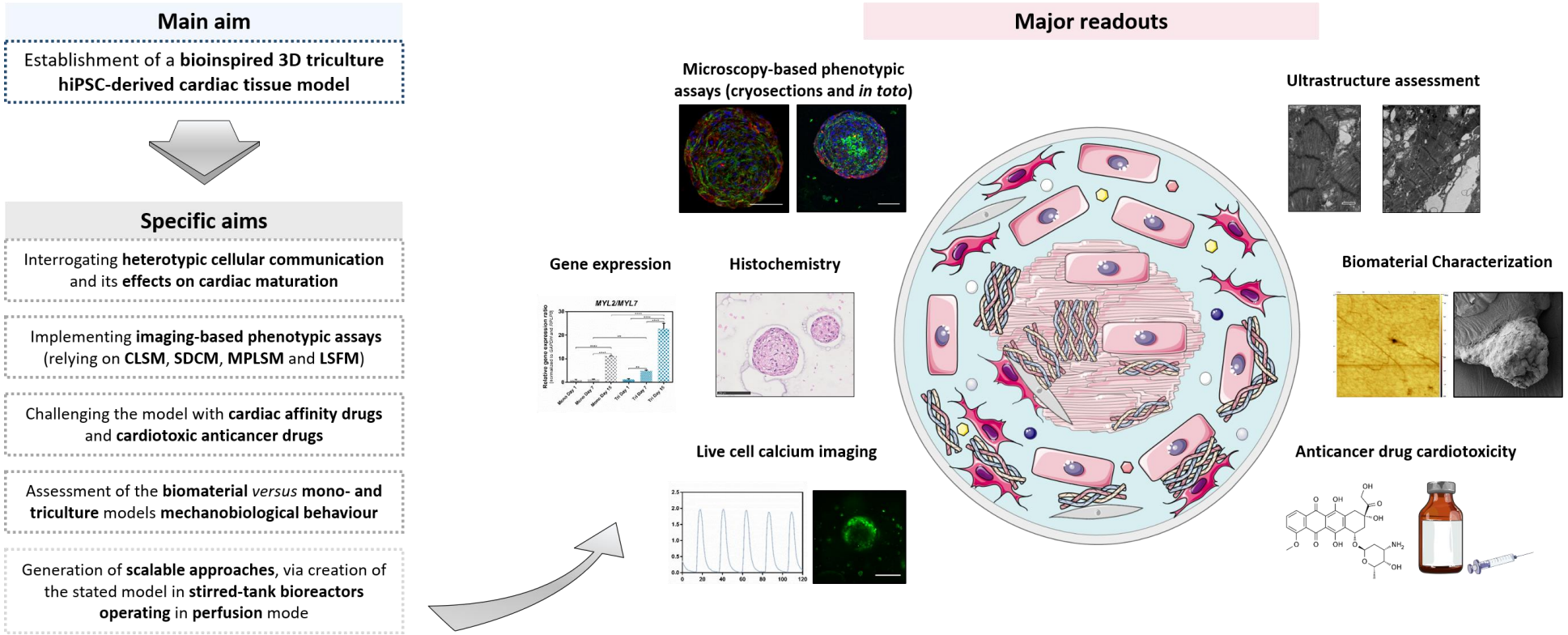

Figure 2.1 | Schematic overview of thesis rational. (*left panel*) **Main** (**blue**) and **specific** (light grey) **aims** of the dissertation project and (**right panel**) representative scheme of the **3D triculture** hiPSC-derived **cardiac** tissue **model** complexity, in the final day of culture, highlighting some of the **major readouts** developed for its characterization. The model representation (*right panel*) is not to scale. The **key model players** are also exhibited (*beneath*, *centred*). **Abbreviations** of the **techniques** used: **CLSM –** Confocal Laser Scanning Microscopy, **SDCM –** Spinning Disk Confocal Microscopy, **MPLSM –** Multiphoton Laser Scanning Microscopy and **LSFM –** Light Sheet Fluorescence Microscopy (for the remaining ones, consult **List of Abbreviations and Conventions**). The author wish to thank *Servier Medical Art* for their image bank used to create the illustrations.

3. Materials and Methods

3.1. Cell culture

3.1.1. Human iPSC culture

Only one human iPSC line was used: hiPSC *DF19-9-11T.H* (***WiCell***, Madison, WI, USA), between passages 39 and 47.

This human iPSC line was routinely propagated in 2D static adherent conditions (6-well plates), on *Matrigel*™ (***Corning***, New York, MA, USA; 1 mL/well) *Matrix hESC-Qualified*-coated plates (prepared according to the manufacturer's instructions), in *mTeSR*™1 medium **(*STEMCELL Technologies***, Vancouver, BC, Canada; 2 mL/well), and kept at 37 °C, in a humidified atmosphere composed of 5% CO_2 and 95% air.

Culture medium was daily exchanged and cells were non-enzymatically passaged, via incubation, at 37 °C, for 7-8 min, with, *Versene*™ (***Thermo Fisher Scientific***; 1 mL/well) cell dissociation reagent. 1h before the passage, the exhausted *mTeSR*™1 medium, in the wells, was supplemented with 5 µM of rho-associated protein kinase, ROCK, signalling pathways' inhibitor (*Y-27632*, ***Merck Millipore***, Kenilworth, NJ, USA; 2 µL/well). Subculturing was performed whenever the cells reached 80-90% confluence (typically every 2-3 days).

As described by **Correia *et al*. (2018)**[83], when the desired cell concentrations and a confluence of 80-90%[83] were attained, differentiation was induced toward CMs or non-myocytes (ECs and MCs), using the corresponding protocols, described underneath.

3.1.2. Directed differentiation of hiPSC toward CMs

Directed differentiation of hiPSC into CMs was started when cell confluence reached 80-90%.

Briefly, at day 0, cardiac mesoderm was induced by exchanging *mTeSR*™1 expansion medium to RPMI 1640 (*Roswell Park Memorial Institute* 1640) medium (***Thermo Fisher Scientific***), supplemented with *B-27*™, without insulin (hereinafter referred to as *RPMI/B27−ins*; ***Thermo Fisher Scientific***), 12 µM GSK-3β inhibitor/*Wnt* activator CHIR99021 (***Tocris Bioscience***, Madrid, Spain), 80 ng/mL activin A (***PeproTech***, Peterborough, UK) and 50 µg/mL ascorbic acid, AA (***Sigma-Aldrich***, St. Louis County, MO, USA). At day 1 (approximately 24h – 24 ± 1h – after differentiation induction), medium was replaced by *RPMI/B27−ins* supplemented with 5 µM of a *Wnt* signalling small molecule inhibitor (IWR-1, ***Sigma-Aldrich***) and 50 µg/mL AA (***Sigma-Aldrich***). At day 3 (72h post-differentiation induction), medium was exchanged for *RPMI/B27−ins* supplemented only with 5 µM IWR-1 (***Sigma-Aldrich***). At day 7 (when more than 80% of the cells spontaneously contract in culture), cells were enzymatically dissociated[*N1*] via incubation with *TrypLE Select* (5 min at 37 °C)[83] (***Thermo Fisher Scientific***), followed by culture medium (*RPMI/B27−ins*) addition and centrifugation (220 x *g* for 5 min).[1]

3.1.2.1. Microwell establishment of 3D cardiac homotypic spheroids

Most of the cells, harvested at day 7 (already cardiac progenitor cells, CPCs), were seeded into microwells (*AggreWell*™ 400Ex, ***STEMCELL Technologies***), at a cell density of 1500 cell/microwell (chosen based on **Nguyen *et al*., 2014**[118] and **Correia *et al*., 2018**[83] studies, regarding hPSC-CM aggregation), centrifuged (100 x *g* during 3 min), and then cultured in *RPMI/B27−ins*.

[*N1*] Similarly to what has been described for human iPSC culture, 1h before the CMs passage, at day 7 the exhausted *RPMI/B27-ins* medium, in the wells, was supplemented with 5 µM of rho-associated protein kinase, ROCK, signalling pathways' inhibitor (*Y-27632*, ***Merck Millipore***, Kenilworth, NJ, USA).

After 48 h (at day 9), the spheroids were transferred to rotary orbital suspension culture (*i.e*. shake flasks), with a stirring rate of 90 rpm (selected based on *in-house* preceding studies performed with PSC spheroids[139], with an average diameter oscillating between 100 and 300 µm, which evidenced that this stirring rate was suitable for keep cells in suspension without deleteriously affecting them or causing diffusional limitations).

Lastly, hiPSC-CM were kept in suspension culture for further 6 days under the aforesaid conditions (*total culture time*: 15-18 days). Medium was refreshed every two days, yielding the desired cellular product, which was designated as **3D hiPSC-CM**.

3.1.2.2. 2D monolayer culture: control condition

Conversely, the other portion of the cells, dissociated at day 7 with *TrypLE Select* (***Thermo Fisher Scientific***), were replated in 2D static culture plates, in order to function as a cellular control for the 3D cardiac spheroid differentiation. Accordingly, the harvested cells were inoculated at 2 x 10^5 cells/cm^2 on *Matrigel*™ *Matrix* (***Corning***, New York, MA, USA; 1 mL/well) *hESC-Qualified*-coated plates (prepared according to the manufacturer's instructions) and cultured in *RPMI/B27–ins*. Medium was replaced 24h later and, then, every two days, until day 15, yielding the desired cellular product, which was termed as **2D hiPSC-CM**.

3.1.3. Simultaneous differentiation of hiPSC toward ECMCs in a 2D co-culture

Concomitant differentiation in endothelial and mesenchymal cell (ECMC) lineages was induced in a 2D monolayer co-culture, based on an adaptation of the methodology described by **Giacomelli *et al*. (2017)**[53].

Summarily, hiPSC were seeded on 6-well plates at 0.0125 x 10^6 cells/cm^2 (roughly 0.04 x 10^6 cells/mL). At day 0, cardiac mesoderm formation was favoured by exchanging *mTeSR*™1 to *APEL*™2-LI (*Albumin, Polyvinylalcohol, Essential Lipids Low-Insulin*) differentiation medium (***STEMCELL Technologies***), supplemented with a mixture of cytokines, *viz*. 20 ng/mL BMP-4 (***PeproTech***, Peterborough, UK), 20 ng/mL activin A, (***PeproTech***, Peterborough, UK) and 1.5 µM GSK-3β inhibitor/*Wnt* activator CHIR99021 (***Tocris Bioscience***, Madrid, Spain). At day 3, cytokines were removed and 50 ng/mL VEGF (***PeproTech***, Peterborough, UK) was added.

APEL™2-LI medium supplemented with VEGF was refreshed every 3 days, until day 10 of ECMC differentiation (*total culture time*: 10-12 days), yielding the desired cellular product, which was designated as **2D hiPSC-ECMC**.

3.2. Generation of wholly hiPSC-derived hydrogel-based 3D cardiac tissue models

For the generation of the biomaterial-based 3D hiPSC-derived cardiac tissue models, a microencapsulation approach, using a biocompatible hydrogel, was used[178,179,182].

3D hiPSC-CM spheroids were collected from the shake flasks and approximately 5.2 x 10^6 cells were dispersed in 1 mL of 1.1% (w/v) of an equimolar mixture (*i.e*. 1:1) composed of conventional non-RGD alginate and a commercially available RGD peptide-coupled alginate, *viz*. ultrapure MVG alginate (*Ultrapure MVG*, ***NovaMatrix***, PRONOVA™, Oslo, Norway) and NOVATACH MVG G**RGD**SP peptide-coupled alginate (*GRGDSP-coupled with a high G-content*, *high MW alginate*, ***NovaMatrix***, PRONOVA ™, Oslo, Norway), dissolved in NaCl 0.9% (w/v) solution (***Merck Millipore***).

Spheroids (consult **3.1.2.1**) were microencapsulated either alone, or together with hiPSC-ECMC (consult **3.1.3**), in a 1:2 ratio (about 10.4 x 10^6 ECMC), for an approximate total of 15.6 x 10^6 CM/ECMC.

The cardiac model regarding the microencapsulated hiPSC-CM spheroids, as well as the one contemplating the spheroids plus the hiPSC-ECMC monolayer of non-myocyte populations, will henceforth be referred to as **3D hiPSC-CM monoculture** and **3D hiPSC-CM/ECMC triculture** (or simply **monoculture** and **triculture**, correspondingly). hiPSC-ECMC monolayers (consult **3.1.3**) were also microencapsulated (approximately 10 x 10^6 cells) and maintained as controls. Hereinafter, they will be termed as **3D hiPSC-ECMC co-culture** (or just **co-culture**).

As regards the alginate microencapsulation process itself, it was carried out using an electrostatically driven bead generator[178,179,182] (*VarV1*, *Nisco Encapsulation Unit*, Zurich, Switzerland), to generate microbeads with an average diameter of approximately 1500 µm (**Model #1-*a*-MCT-SF**; consult ***List of Models***, for further information on the designations and specificities of each of the models) or ranging from 700 to 800 µm (**Pilot Model-M-SF**, **Model #1-*b*-MCT-SF** and **Model #2-*b*-MT-BR-2**).

Alginate polymerization was attained with a solution of 100 mM $CaCl_2$/10 mM HEPES (pH 7.4) (*Merck Millipore* and *Sigma-Aldrich*, respectively). The **calcium alginate microcapsules** were further washed three times in a 0.9% (w/v) NaCl (*Merck Millipore*) solution and, finally, equilibrated in culture medium, before being transferred to shake flasks. Conversely, when needed, alginate microbeads' disruption was accomplished via incubation (5 min at room temperature, *RT*, 18–20 °C) in a solution of 50 mM $Na_3C_6H_5O_7$/104 mM NaCl (*Sigma-Aldrich* and *Merck Millipore*, respectively).

The microencapsulated 3D hiPSC-derived cardiac models (mono-, co- and triculture) were then transferred to rotary orbital suspension culture (*i.e*. shake flasks), with a stirring rate of 90 rpm. They were maintained in culture at 37 °C, in a humidified atmosphere, with 5% CO_2 in air, in a 1:1 mixture of *RPMI/B27-ins* and *ECGM2* (*Endothelial Cell Growth Medium 2*, *PromoCell GmbH*, Heidelberg Germany). A 100% medium exchange was performed every 2-3 days, for, at least, 15 days (*total culture time*: 31-37 days, from the beginning of hiPSC-CM differentiation).

3.3. Model characterization

3.3.1. Viability and cell concentration

Two methods were used to estimate cell viability. Samples were collected periodically and used for monitoring of cell viability via (i) a fluorescent cell membrane integrity assay (FDA-PI live/dead double staining) and (ii) *Trypan Blue* exclusion method.

3.3.1.1. Cell membrane integrity assay: FDA-PI live/dead double staining

A qualitative assessment of 3D hiPSC-based cardiac tissue models' (mono-, co- and tricultures) cell viability over time (after microencapsulation) was performed using the enzyme substrate fluorescein diacetate (FDA, *Sigma-Aldrich*), which stains viable cells, and the DNA-binding dye propidium iodide (PI, *Sigma-Aldrich*), that labels dead cells, as described in the literature[183]. FDA is taken up by cells which convert the non-polar and non-fluorescent FDA into a bright green fluorescent metabolite, fluorescein[184]. The measured signal is the result of *FDA to fluorescein* conversion via the intracellular esterases of viable cells. In contrast, the nuclei staining dye, PI, cannot pass through a viable cell membrane, since it is polar[184]. It reaches the nucleus by passing through disordered areas of dead cell membranes and intercalates within the DNA double helix[184], thereby labelling the dead cell nuclei in red.

Briefly, cells were incubated with 20 µg/mL FDA and 10 µg/mL PI, in DPBS (*Thermo Fisher Scientific*), for 2-3 min and then visualized using a conventional widefield fluorescence microscope (*DMI6000*, *Leica Microsystems GmbH*, Wetzlar, Germany).

3.3.1.2. *Trypan Blue* exclusion method

For the *Trypan Blue* exclusion method, hiPSC-CM spheroids (before microencapsulation) were centrifuged at 300 × *g* for 5 min and enzymatically dissociated via incubation with *TrypLE Select* for 5 min at 37 °C with agitation (*ThermoMixer*, ***Eppendorf***). Viable cell concentration was determined by mixing the resulting cell suspension with 0.1% (v/v) *Trypan Blue* dye (***Thermo Fisher Scientific***), in DPBS, and subsequent counting in a *Fuchs-Rosenthal* haemocytometer chamber (***Brand***) (colourless cells — viable; blue cells – non-viable)[52,182]. The concept is the same as in the previous assay: viable cells do not take up impermeable dyes (*e.g*. *Trypan Blue* or PI), instead of dead cells, that are permeable and take up the dye.

3.3.2. Metabolic activity quantification: *PrestoBlue* resazurin–based dye assay

Metabolic activity was quantified in the different 3D cardiac tissue models over culture time (after microencapsulation), using a *PrestoBlue*™ (#A13262, ***Life Technologies***) resazurin–based dye assay, following manufacturer's recommendations.

Samples of 2 to 5 microcapsules were taken from culture into a 96-well plate and then incubated with 1X *PrestoBlue*™ *Cell Viability Reagent* (diluted in a 1:1 mixture of *RPMI/B27-ins* and *ECGM2*) for 3h at 37 °C, with gentle agitation, in the dark. Fluorescence was measured at the excitation and emission wavelengths of 560 and 590 nm, respectively, using the micro plate reader *Infinite*® 200 PRO (*NanoQuant*, ***Tecan Trading AG***) and fluorescence intensity values (*RFU*, relative fluorescence units) were normalized to the number of capsules, counted per well, and to the maximum of fluorescence intensity, verified in the timepoints considered. Analyses consisted of three technical replicas. Controls (subtracted from the mean of the three technical replicas) were also read and correspond to 1X *PrestoBlue*™ diluted in the culture media mixture. The increase in fluorescence intensity is a result of *PrestoBlue*™ (which is a resazurin-derived blue non-toxic and non-fluorescent reagent) reduction, to resorufin, a red fluorescent compound, solely via metabolically viable cells. Therefore, *PrestoBlue*™ assay provides a quantitative measure of cell viability and metabolic activity.

3.3.3. Spheroid and microcapsule concentration and distribution of spheroids per microcapsule

The concentration of CM spheroids or microcapsules was determined over the culture time, in a 1 mL sample, distributed among 5 wells (200 µL per well) of a 96-well plate. The number of aggregates or microcapsules was manually counted in each well, using an inverted microscope (*DMI6000*, ***Leica Microsystems GmbH***; or CKX31, ***Olympus***). The corresponding concentrations, in addition to spheroids per microcapsule distribution, were calculated thereafter.

3.3.4. Spheroid and microcapsule size determination

CM spheroid size determination was performed using an inverted-microscope (*DMI6000*, ***Leica Microsystems GmbH***). The acquired images were analyzed via *Fiji* open source software[185]. In brief, the contrast threshold of non-consecutive images was manually adjusted, in order to define the spheroid boundaries. Average spheroid diameter was then measured using *Feret's* diameter measurement algorithm.

Average microcapsule diameter was estimated by measuring two perpendicular diameters per microcapsule, resorting to non-consecutive images acquired with the mentioned microscope.

3.3.5. Flow cytometry-based phenotypic analysis

3.3.5.1. hiPSC

For flow cytometric (FC) analysis of common pluripotency stem cell (Oct-3/4, SSEA-4 and TRA-1-60) and early differentiation (SSEA-1) markers, before the beginning of the differentiations toward CMs and ECMCs, hiPSC were harvested from culture via enzymatically dissociation with *TrypLE Select* (***Thermo Fisher Scientific***), for 5 min at 37 ºC.

Cell suspensions of hiPSC (0.5 x 10^6 cell/marker) were centrifuged (300 x *g* for 5 min), resuspended twice in *Washing Buffer*, WB (DPBS with 5% (v/v) FBS), and incubated, for 1 h at 4 ºC, in the dark, with one of the subsequent conjugated primary antibodies: 1:10 **anti-TRA-1-60** mouse monoclonal IgM (*sc-21705*, ***Santa Cruz Biotechnology***; diluted in *WB*), 1:5 **anti-SSEA-4**–FITC conjugate mouse monoclonal IgG3,*k* (clone MC813-70, *560126*, ***BD Biosciences***; diluted in *WB*) and 1:10 **anti-SSEA-1**–FITC conjugate mouse monoclonal IgM,*k* (clone MC480, *560127*, ***BD Biosciences***; diluted in *WB*); or isotype controls: 1:40 mouse monoclonal IgG3,*k*–FITC conjugate (clone J606, *555578*, ***BD Biosciences***; diluted in *WB*) and 1:400 mouse IgM,*k*–FITC conjugate (clone G155-228, *553474*, ***BD Biosciences***; diluted in *WB*).

In parallel, for the detection of intracellular markers, cells were fixed and permeabilized with *Inside Stain Kit* (#130-090-477, ***Miltenyi Biotec***), according to the manufacturer's instructions, and stained intracellularly with 1:5 **anti-Oct-3/4**–*AlexaFluor*® 488 conjugate mouse monoclonal IgG1*,k* (clone 40, *560253*, ***BD Biosciences***; diluted in *Inside Perm*) and 1:1.19 mouse IgG1,*k*–*AlexaFluor*® 488 conjugate, isotype control (clone MOPC-21, *557721*, ***BD Biosciences***; diluted in *Inside Perm*), for 10 min at *RT*, in the dark.

Cells were washed with buffer (tubes stained with membrane markers – anti-TRA-1-60, anti-SSEA-4 and anti-SSEA-1 – were washed and diluted in *WB*, whereas those stained with intracellular markers – anti-Oct-3/4 – were diluted in *Inside Perm*). Subsequently, the non-conjugated marker anti-TRA-1-60 was incubated with the corresponding secondary antibody, namely 1:200 goat anti-mouse IgM *AlexaFluor*® 488 (*A21042*, ***Thermo Fisher Scientific***; diluted in *WB*), for 10 min at *RT*, in the dark.

Finally, at least ten thousand events per sample were registered with the *CyFlow*® space (***Partec GmbH***, Görlitz, Germany) instrument, equipped with blue (488 nm), yellow (561 nm) and red (638 nm) lasers. Data were analysed using *FlowJo* (***Tree Star***). Appropriate scatter gates were applied, in order to circumvent cellular debris and also to allow direct comparisons between different experimental groups. The percentage of positive cells is given by events in which the measured fluorescence intensity surpasses the signal obtained in the isotype or unstained cells' control.

3.3.5.2. hiPSC-CM

For flow cytometric analysis of cardiac differentiation efficacy at day 15 of differentiation, hiPSC-CM spheroids were harvested from culture and enzymatically dissociated into single cells, with *TrypLE Select* (***Thermo Fisher Scientific***), for 5 min at 37 ºC.

Cell suspensions of hiPSC-CM (0.5 x 10^6 cell/marker) were centrifuged (300 x *g* for 5 min), resuspended twice in *Washing Buffer*, WB (DPBS with 5% (v/v) FBS), and incubated, for 1 h at 4 ºC, in the dark, with one of the subsequent conjugated primary antibodies: 1:20 **anti-SIRPα/β**–PE conjugate mouse monoclonal IgG1,*k* (anti-CD172α/β–PE conjugate, clone P84, *323805*, ***BioLegend***; diluted in *WB*), 1:5 **anti-VCAM-1**–PE conjugate mouse monoclonal IgG1,*k* (anti-CD106–PE conjugate, clone 51-10C9, *555647*, ***BD Biosciences***; diluted in *WB*) and 1:5 mouse monoclonal IgG1,*k*–PE conjugate, isotype control (clone MOPC-21, *555749*, ***BD Biosciences***; diluted in *WB*).

In parallel, for the detection of intracellular markers, cells were fixed and permeabilized with *Inside Stain Kit* (#130-090-477, ***Miltenyi Biotec***), according to the manufacturer's instructions, and stained intracellularly with 1:200 **anti-cardiac troponin T** mouse monoclonal IgG1 (clone 13-11, *MS-295-P1*, ***Thermo Fisher Scientific***; diluted in *Inside Perm*) and 1:1.5 mouse monoclonal IgG1, isotype control (*sc-3877*, ***Santa Cruz Biotechnology***; diluted in *Inside Perm*), for 10 min at *RT*, in the dark. Cells were washed with buffer (*Inside Perm*) and incubated with the secondary antibody, 1:200 goat anti-mouse IgG *AlexaFluor*® 488 (*A11001*, ***Thermo Fisher Scientific***; diluted in *Inside Perm*), for 10 min at *RT*, in the dark. Afterwards, two more washes with *Inside Perm*, followed by centrifugations (300 x *g* for 5 min), were carried out.

Data were acquired and analysed as described in **3.3.5.1**. The results obtained via this analysis constitute an indirect measure of the efficiency of hiPSC-CM differentiation, symbolizing the purity level of the culture on the day immediately prior to microencapsulation.

3.3.5.3. hiPSC-ECMC

At day 10 of differentiation, hiPSC-ECMC were harvested from culture via enzymatically dissociation with *TrypLE Select* (***Thermo Fisher Scientific***), for 5 min at 37 ^{o}C.

Cell suspensions of hiPSC-ECMC (0.5 x 10^6 cell/marker) were centrifuged (300 x *g* for 5 min), resuspended twice in *Washing Buffer*, WB (DPBS with 5% (v/v) FBS), and incubated, for 1 h at 4 ^{o}C, in the dark, with one of the subsequent conjugated primary antibodies: 1:50 **anti-CD31** mouse monoclonal IgG1 (clone JC70A, *M0823*, ***Agilent Technologies/DAKO***; diluted in *WB*) and 1:13 **anti-VE-cadherin** goat polyclonal IgG (*AF938*, ***R&D Systems***; diluted in *WB*).

In parallel, for the detection of intracellular markers, cells were fixed and permeabilized with *Inside Stain Kit* (#130-090-477, ***Miltenyi Biotec***), according to the manufacturer's instructions, and stained intracellularly with 1:100 **anti-α-smooth muscle actin** mouse monoclonal IgG2*a* (clone 1A4, *M085129-2*, ***Agilent Technologies/DAKO***; diluted in *Inside Perm*) and 1:100 **anti-vimentin** rabbit monoclonal IgG1 (clone v9, *ab16700*, ***abcam***; diluted in *Inside Perm*), for 10 min at *RT*, in the dark.

Cells were washed with buffer (tubes stained with membrane markers – anti-CD31 and anti-VE-cadherin – were washed and diluted in *WB*, whereas those stained with intracellular markers – anti-α-smooth muscle actin and anti-vimentin – were diluted in *Inside Perm*) and, then, incubated with the corresponding secondary antibodies, particularly 1:200 goat anti-mouse IgG *AlexaFluor*® 488 (*A11001*, ***Thermo Fisher Scientific***; diluted in *WB*), 1:200 goat anti-mouse IgG *AlexaFluor*® 488 (*A11001*, ***Thermo Fisher Scientific***; diluted in *Inside Perm*), 1:200 chicken anti-goat IgG *AlexaFluor*® 488 (*A21467*, ***Thermo Fisher Scientific***; diluted in *WB*) and 1:200 goat anti-rabbit IgG *AlexaFluor*® 488 (*A11008*, ***Thermo Fisher Scientific***; diluted in *Inside Perm*), for 10 min at *RT*, in the dark.

Data were acquired and analysed as described in **3.3.5.1**.

3.3.6. Microscopy-based phenotypic assays

3.3.6.1. Immunofluorescence in 2D cell monolayers

At day 10 of hiPSC-ECMC differentiation (prior to microencapsulation), culture samples were collected and then transferred onto *µ-Slide 4 Well* or *µ-Slide 8 Well* (***Ibidi***). Culture wells were fixed in 4% (w/v) paraformaldehyde (PFA, ≥95%, ***Fluka***) with 4% (w/v) sucrose (≥99.5%, ***Sigma-Aldrich***), in DPBS (***Thermo Fisher Scientific***), for 20 min at *RT*.

ECMC monolayers were simultaneously permeabilized and blocked in 0.1% (w/v) Triton X-100 (TX-100, ***Sigma-Aldrich***)/0.2% (w/v) cold water fish skin gelatine (FSG, ***Sigma-Aldrich***), in DPBS (***Thermo Fisher***

Scientific), for 30 min at *RT*. Subsequently, cells were incubated with the respective primary antibodies, diluted in the same solution used for permeabilization and blocking, for 2h at *RT*. After the 2-hour incubation period, they were washed three times with DPBS and incubated with the corresponding secondary antibody, in the same solution, for 1h at *RT*. After three washes with DPBS, nuclei were counterstained with DAPI (*Thermo Fisher Scientific*). Samples were visualized using a conventional widefield fluorescence microscope (*DMI6000*, *Leica Microsystems GmbH*, Wetzlar, Germany).

Details on the characteristics and dilutions of primary and secondary antibodies, as well as the counterstain, are fully provided in **Annex 1.1**, **Table S1** and **Table S2** (consult the last column of the table – *Dilution and Analytical Method* – and identify *2D IF*).

3.3.6.2. Confocal immunofluorescence in cryosections

At the endpoint (day 15 *post*-microencapsulation) of the microencapsulated 3D hiPSC-CM mono- and 3D hiPSC-CM/ECMC triculture cardiac tissue models, culture samples were collected and fixed in 4% (w/v) paraformaldehyde (*Fluka*) with 4% (w/v) sucrose (*Sigma-Aldrich*), in DPBS (+Ca^{2+}/+Mg^{2+}) (*Thermo Fisher Scientific*), for 30 min at *RT*, under gentle agitation. After washing with DPBS (+Ca^{2+}/+Mg^{2+}) , they were then, overnight (*o.n.*) at 4 °C, dehydrated in 30% (w/v) sucrose (*Sigma-Aldrich*) in DPBS, embedded in *Tissue-Tek*® O.C.T.™ (*Sakura*, Alphen aan den Rijn, Netherlands) and frozen at –80 °C, until cryosectioning. The frozen samples were sliced with a thickness of 10 µm in a cryostat (*Cryostat CM 3050 S*, *Leica*, Wetzlar, Germany).

In brief, the cryosections were permeabilized with 0.1% (w/v) Triton X-100 (TX-100, *Sigma-Aldrich*), for 10 min at *RT*, followed by blocking, for 30 min at *RT*, with 0.2% (w/v) cold water fish skin gelatine (FSG, *Sigma-Aldrich*), in DPBS with Ca^{2+} and Mg^{2+}. Primary antibodies were diluted in 0.2% (w/v) FSG, in DPBS (+Ca^{2+}/+Mg^{2+}), and incubated for 2h at *RT*, whereas secondary antibodies were diluted in 0.125% (w/v) FSG, in DPBS (+Ca^{2+}/+Mg^{2+}), and incubated only for 1h, also at *RT*. Cryosections were mounted under glass coverslips using *ProLong™ Gold Antifade Reagent* containing DAPI (*Thermo Fisher Scientific*) and visualized either in a confocal laser scanning microscope, CLSM (*SP5 Live Upright*, *Leica*) or, for routine control, in a conventional widefield fluorescence microscope (*DMI6000*, *Leica Microsystems GmbH*, Wetzlar, Germany).

Details on the characteristics and dilutions of primary and secondary antibodies are fully provided in **Annex 1.1**, **Table S1** and **Table S2** (consult the last column of the table – *Dilution and Analytical Method* – and identify *CLSM*, which was the preferred microscopy to visualize the cryosections).

3.3.6.3. Whole mount immunofluorescence

3.3.6.3.1. Multiphoton and LSFM: *in toto* immunofluorescence protocol

At the endpoint (day 15 *post*-microencapsulation) of the microencapsulated 3D hiPSC-CM mono- and 3D hiPSC-CM/ECMC triculture cardiac tissue models, culture samples were collected and fixed in 4% (w/v) paraformaldehyde (*Fluka*) with 4% (w/v) sucrose (*Sigma-Aldrich*), in DPBS (+Ca^{2+}/+Mg^{2+}) (*Thermo Fisher Scientific*), for 30 min at *RT*, under mild agitation conditions.

Briefly, whole microcapsules were simultaneously permeabilized and blocked in 1% (w/v) Triton X-100 (TX-100, *Sigma-Aldrich*)/0.2% (w/v) cold water fish skin gelatine (FSG, *Sigma-Aldrich*), in DPBS (+Ca^{2+}/+Mg^{2+}) (*Sigma-Aldrich*) with 0.01% sodium azide, for 2h at *RT*, with agitation.

Primary antibodies were diluted in 0.1% (w/v) TX-100/0.2% (w/v) FSG, in DPBS (+Ca^{2+}/+Mg^{2+}) with 0.01% sodium azide, and incubated *o.n.* at 4 °C, with mild agitation, for two days. Microcapsules were then washed three times with DPBS (+Ca^{2+}/+Mg^{2+}) and incubated with the secondary antibodies, diluted in

0.1% (w/v) TX-100/0.125% (w/v) FSG, in DPBS (+Ca^{2+}/+Mg^{2+}) with 0.01% sodium azide, *o.n*. at 4 °C, with mild agitation. After three washes with DPBS (+Ca^{2+}/+Mg^{2+}), nuclei were counterstained with DAPI (***Thermo Fisher Scientific***) and DRAQ5 (***Cell Signalling Technology***). Samples were visualized either in a multiphoton laser scanning microscope, MPLSM (*Ultima*, ***Prairie Technologies***), or, alternatively, in a custom-made light-sheet fluorescence microscope, LSFM (*OpenSpin*, *Cell Imaging Unit*, IGC, Oeiras, Portugal).

Details on the characteristics and dilutions of primary and secondary antibodies are fully provided in **Annex 1.1**, **Table S1** and **Table S2** (consult the last column of the table – *Dilution and Analytical Method* – and identify *MPLSM* or *LSFM*, which were the preferred microscopy modalities to *in toto* visualize the whole 3D models).

3.3.6.3.2. LSFM: image acquisition and light-sheet setup

The 3D reconstructed images were acquired with a home-made light-sheet fluorescence microscopy (LSFM) system, based on an open software and hardware approach[165,180,186], the ***OpenSpin*** project (not yet published) (*Cell Imaging Unit*, *Instituto Gulbenkian de Ciência*, IGC; for additional information, consult http://facilities.igc.gulbenkian.pt/microscopy/microscopy-dslm.php).

Light-sheet fluorescence microscopy setup is depicted in **Fig.3.1**.

Images were acquired consecutively, as the samples cross the light-sheet plane (**Fig.3.1*a***, **Fig.3.1*b*** and **Fig.3.1*c***). The illumination block consists of a custom-made laser combiner, including three laser lines: 473 nm (DPSSL MBL-III-473-50), 561 nm (Coherent OBIS 561-50 LS) and 638 (*LuxX 638-150*, ***Omicron Laserage***), selected using an *Arduino*. Laser scanning is carried out in the vertical axis using two *Arduino* controlled galvanometric mirrors (*GVS201*, ***Thorlabs***), in which the optical plane is conjugated with the back focal aperture of two objective lens (10x, 0.3*NA*, WD 16.3 mm, ***Plan Fluor***) using a 4x telescope system. For detection, a water immersion objective (16x, 0.8*NA*, WD 3.0 mm, ***Nikon***), placed perpendicularly to the excitation plane, is used to collect fluorescence emission. Excitation light is rejected using emission filters placed in infinity space before the camera. Finally, a 200 mm tube lens creates the image on the chip of the *sCMOS* cameras (*Orca-Flash4*, ***Hamamatsu***) (**Fig.3.1*e***). Each sample is moved across the plane of light created and virtually sectioned for eight different angles. Rotation is controlled through custom *Java* plugin (*OPenSpin*) for *Micromanager* (**Fig.3.1*f***).

After image acquisition, images were aligned and reconstructed using the different tools available in *Fiji*'s open source plugin *BigStitcher*[185].

3.3.6.3.3. LSFM: sample mounting

Fixed samples (consult **3.3.6.3.1**) were embedded on 2% *Phytagel*™ (***Sigma-Aldrich***) inside a FEP tube (O.D. 5 mm) (**Fig.3.1*d***). FEP tubes are ideal for light-sheet fluorescence microscopy, since their refractive index is very close to that of water, reducing the optical aberrations and thereby providing a better environment to the samples with high optical clarity[166,187]. This is critical in thick, highly scattering and inhomogeneous samples (*e.g*. 3D hiPSC-CM/ECMC triculture model), being a fitting strategy for the generated 3D cardiac models[165,166,169,179,180]. The tube is then inserted in a rotational stepper motor for sample rotation, which is attached to a linear stepper motor for sample scanning through the light-sheet.

Datasets were individually recorded and, then, fused to generate a faithful **3D volume reconstruction** of the **whole models**. In order to perform **multi-view reconstructions**, we acquired eight different angles per sample (0° to 360°), with an incremental step of 45°.

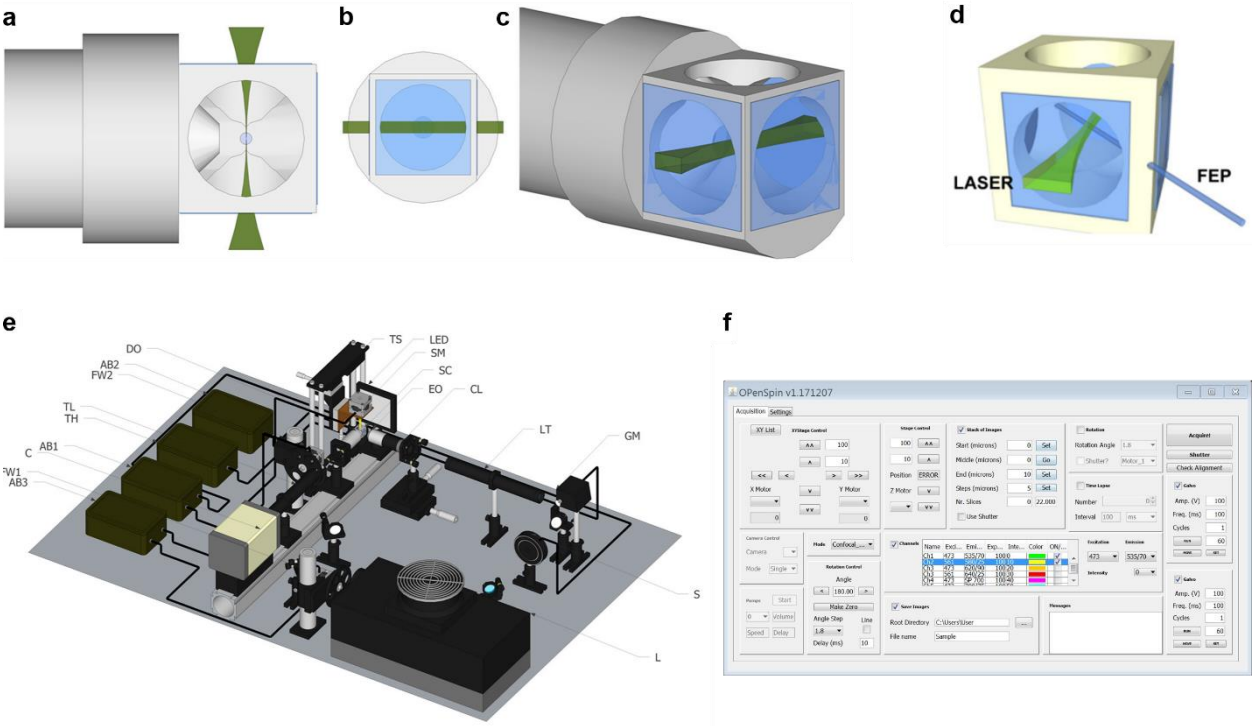

Figure 3.1 | Light-sheet fluorescence microscopy experimental setup [adapted from Gualda *et al.* (2014)[165] and Gualda *et al.* (2015)[180].

(*a*) **Top view of the light-sheet**, including the objective and cell culture chamber for single plane illumination microscopy (SPIM). (*b*) **Front view of light-sheet.** (*c*) **Perspective view of the light-sheet.** (*d*) **Diagram of the sample chamber**, where a FEP crosses at 45 º. Laser illumination is represented in green and FEP tube in blue. (*e*) **Schematic depiction of the LSFM experimental setup.** Key elements comprise: Argon/Krypton laser (L), excitation filter wheel (FW1), shutter (S), galvanometric mirror (GM), excitation objective (EO), 3.5x lens telescope (LT), detection objective (DO), *sCMOS* camera (C), tube lens (TL), emission filter wheel (FW2), translational stage (TS), stepper motor to rotate the sample (SM), *Arduino* board (AB) and a sample chamber (SC) for water immersion objectives. (*f*) **Front panel of the custom *Java* plugin (*OPenSpin*) for *Micromanager*.** It allows a full control of the light-sheet fluorescence microscope with a single window.

3.3.6.3.4. LSFM: fibronectin quantification

Since it was possible to obtain realistic 3D volume reconstructions of the 3D hiPSC-CM mono- and 3D hiPSC-CM/ECMC triculture microcapsules, as *proof-of-concept*, an extracellular matrix protein, fibronectin, was quantified in both models.

In first place, data were sorted by image intensities, using *Fiji*'s "Histogram" tool, in order to individualize the microcapsules and despise image artefacts. Subsequently, images containing microcapsules and different aggregates per microcapsule were processed with various *Fiji* tools to separate them properly and then estimate the volume of fibronectin. Finally, using *Fiji*'s open source *plugin* "3D Objects Counter", fibronectin volume was estimated in each of the 3D cardiac tissue models. The results are presented as a ratio between the volume of fibronectin and the corresponding volume of the selected microcapsule, in both mono- and tricultures.

3.3.7. RT-qPCR: gene expression profiling

One, seven and fifteen days *post*-microencapsulation, alginate microbeads were dissolved with a chelating solution as indicated beforehand (consult **3.2**) and centrifuged at 300 x *g* for 5 min. Pellets were snap-frozen and kept at –80 ºC until RNA isolation.

Total RNA was extracted with *High Pure RNA Isolation Kit* (#11828665001, **Roche**), according to manufacturer's instructions. Before proceeding with cDNA synthesis, RNA concentration (ng/mL) and

purity (A_{260}/A_{280} and A_{260}/A_{230} absorbance ratios) were spectrophotometrically determined in a microvolume *UV-Vis* spectrophotometer (*NanoDrop™ 2000c*, ***Thermo Scientific***).

cDNA was synthesized from 80 ng of RNA per sample, using *Transcriptor High Fidelity cDNA Synthesis Kit* (#081955001, ***Roche***), following manufacturer's instructions. In brief, reverse transcription comprised: (i) an initial step of RNA secondary structures' denaturation, completed at 65 ºC (10 min), (ii) a reverse transcriptase incubation step, optimized for 55 ºC (30 min) and (iii) a final temperature-mediated enzyme inactivation step, at 85 ºC (5 min).

RT-qPCR relative quantification of gene expression was performed using *LightCycler® 480 Probes Master* (#04707494001, ***Roche***), following manufacturer's instructions. In short, a 10 µL reaction contained 2.5 µL cDNA template (undiluted), 0.5 µL *TaqMan® Gene Expression Assay* (20X concentrated), 5 µL *LightCycler® 480 Probes Master* (2X concentrated) and 2 µL water (PCR-grade). Amplification reactions were performed in a 384 well plate format using a *LightCycler® 480 Real-Time PCR System* (***Roche***). Threshold cycle values (C_T) were determined using *LightCycler® 480 Software*, *v.1.5* (***Roche***). Data were analysed using the $2^{-\Delta\Delta CT}$ method for relative gene expression quantification, as described by **Livak and Schmittgen (2001)**[188], and consist of technical triplicates. Variations in relative expression were normalized to *GAPDH* and *RPLP0* housekeeping genes as internal controls.

All information regarding *TaqMan® Gene Expression Assays*, used in RT-qPCR gene expression analysis, is displayed in **Annex 1.2**, **Table S3**.

3.3.8. Structural and ultrastructural assessment

3.3.8.1. Structural: histological/histochemical-based methods

At the start and endpoint (1 and 15 days after microencapsulation, respectively) of the microencapsulated 3D hiPSC-CM mono- and 3D hiPSC-CM/ECMC triculture cardiac tissue models, culture samples were collected and fixed as previously described (consult **3.3.6**). Fixed cells were washed twice with DPBS and stored at 4 ºC, until histochemical staining.

Alginate microcapsules were pelleted, embedded in 2% (w/v) high melting temperature agarose (***Lonza***), dehydrated in a graded series of alcohols and then embedded in paraffin wax (***Merck Millipore***).

Paraffin blocks were sectioned (3 µm thickness) on a rotary microtome (*RM 2135*, ***Leica***) for Hematoxylin and Eosin (H&E; ***Sigma-Aldrich***), Toluidine Blue (TB; ***EMS***), Masson Trichrome with Aniline Blue (MT; ***IHC WORLD***, Woodstock, MD, USA), Picrosirius Red (PSR; ***Polysciences Europe GmbH***, Eppelheim, Germany) and Periodic Acid-Schiff (PAS; ***Sigma-Aldrich***) histochemical staining, following manufacturer's instructions.

Histological images were digitalized in a *NanoZoomer SQ* whole slide scanner (***Hamamatsu Photonics***) and viewed with *NDP view* software (*NDP.view*, *v.2.3*, ***Hamamatsu Photonics***). *Fiji* was used to linear brightness and contrast adjustments[185].

3.3.8.2. Structural: scanning electron microscopy (SEM)

At the endpoint (15 days after microencapsulation) of the microencapsulated 3D hiPSC-CM mono- and 3D hiPSC-CM/ECMC triculture cardiac tissue models, culture samples were collected and fixed as previously described (consult **3.3.6**). Fixed cells were washed twice with DPBS (***Thermo Fisher Scientific***) and stored at 4 ºC until preparation for scanning electron microscopy (SEM).

After washes with *Milli-Q* water and further dehydration, samples were dried in adhesive carbon tabs (12mm, ***Agar Scientific***), developed to eliminate background noise from SEM imaging. Before

visualization, an Au/Pd film of 15 nm was deposited to avoid charging effects. Surface and cross-section SEM observations were carried out using a scanning electron microscopy workstation (***Carl Zeiss AURIGA CrossBeam***, FIB-SEM).

3.3.8.3. Ultrastructural: transmission electron microscopy (TEM)

At the start and endpoint (1 and 15 days after microencapsulation, respectively) of the microencapsulated 3D hiPSC-CM mono- and 3D hiPSC-CM/ECMC triculture cardiac tissue models, culture samples were collected and fixed as previously described (consult **3.3.6**). Fixed cells were washed twice with DPBS and stored at 4 °C until preparation for transmission electron microscopy (TEM).

A second fixation was performed using 2% (v/v) paraformaldehyde (***EMS***) and 2.5% (v/v) glutaraldehyde (***Polysciences***) in 0.1M phosphate buffer (PB), for 1 hour at 4 °C. Cells were washed three times with PB and then were embedded in 2% low melting point agarose (***OmniPur***) for further processing.

Post fixation was achieved with 1% osmium tetroxide (w/v) (***EMS***) in 0.1M PB, for 30 min at 4 °C, in the dark. After two washes with 0.1 M PB and two washes with distilled water, samples were incubated with 1% aqueous tannic acid (w/v) (***EMS***) for 20 min at 4 °C. After five washes with distilled water, samples were contrasted with 0.5% aqueous uranyl acetate (w/v) for 1h at 4 °C, in the dark. Afterwards, they were washed three times with distilled water, dehydrated in a graded series of ethanol (30%, 50%, 75% at 4 °C, 90%, 100%) and embedded in *EMbed-812 epoxy resin* (***EMS***). Ultrathin sections of the 3D cardiac tissue models were cut on a ultramicrotome (*EM UC7*, ***Leica***), using a diamond knife. Sections were collected on grids coated with 1% (w/v) *formvar* (***Agar Scientific***) in chloroform (***VWR***) and stained with 1% (w/v) uranyl acetate and Reynolds lead citrate, for 5 minutes each. Images were acquired on a transmission electron microscope (*H-7650*, ***Hitachi***) at 100 keV, equipped with a *XR41M* mid mount *AMT* digital camera.

3.3.8.3.1. Quantification of ultrastructural features

Sarcomere length was estimated by measuring two parallel segments, per sarcomere, joining adjacent Z lines. **Sarcomere angle dispersion** was determined as previously described by **Correia *et al.* (2017)**[84]. In brief, sarcomeric alignment is defined as the inverse of the magnitude of angle dispersion (*SEM* of sarcomere angles), meaning that a low angle dispersion specifies a high degree of alignment. *SEM* of sarcomere angles, σ_M, was calculated by the quotient between the standard deviation of the distribution of sarcomere angles' means, σ, and the square root of the number of sarcomeres, *√N*: $\sigma_M = \frac{\sigma}{\sqrt{N}}$. *SEM* stands for standard error of the mean. Measurements were performed in *Fiji* open source software[185].

3.3.9. Functional assessment: live cell calcium imaging

Live cell calcium imaging was used to evaluate intracellular Ca^{2+} spontaneous and pharmacologically induced-transients, in 3D hiPSC-CM mono- and 3D hiPSC-CM/ECMC tricultures, at the endpoint of the models. Live cell calcium imaging workflow is schematically represented in **Fig.3.2**.

The technique was performed using the *Fluo-4 Direct™ Calcium Assay Kit* (***Thermo Fisher Scientific***), according to the manufacturer's instructions. In brief, alginate microbeads were transferred onto *µ-Slide 4 Well* (***Ibidi***). Subsequently, they were incubated with 1:2 calcium indicator fluorescent dye *Fluo-4 Direct™ calcium assay reagent* (***Thermo Fisher Scientific***; diluted in a 1:1 mixture of *RPMI/B27-ins* and *ECGM2*), for 45 min at 37 °C, followed by 15 min at *RT*. *Fluo-4* exhibits excitation at 494 nm and emission at 516 nm and its fluorescence intensity, at 494 nm, is 100-fold enhanced upon Ca^{2+} binding. After two

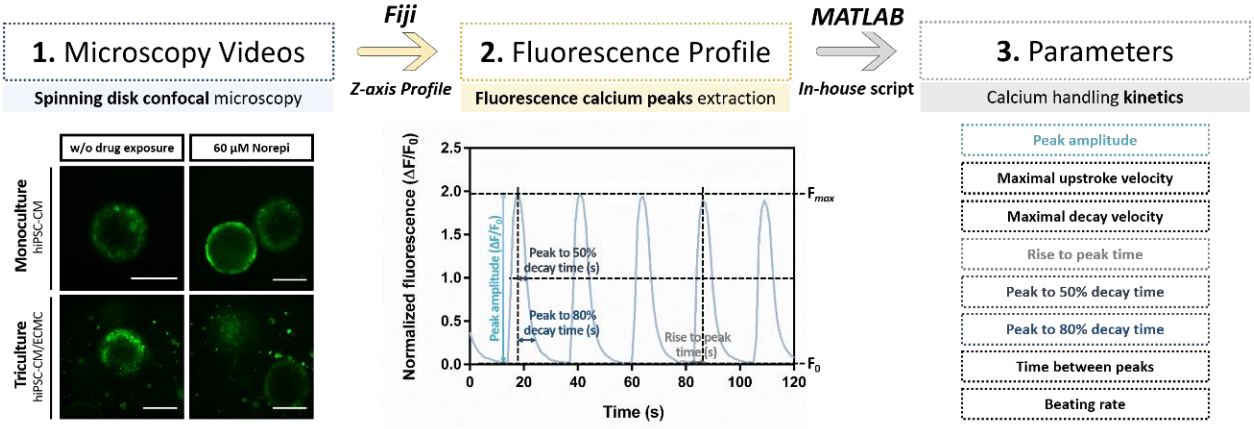

Figure 3.2 | Schematic workflow of live cell calcium imaging: video acquisition and data processing.

1. *Microscopy Videos*: Cardiac tissue models were imaged using a spinning disk confocal microscope (*system*: ***Revolution XD***, ***Andor***; *microscope*: ***Eclipse Ti-E***, ***Nikon***; *confocal scanner*: ***CSU-X1***, ***Yokogawa***) and 30 sec videos were recorded through *Micro-Manager 1.4* software (consult **Annex 5**, **5.2. *List of videos: spinning disk confocal microscopy***, **Fig.S12**).

2. *Fluorescence Profile*: Fluorescence peaks were extracted from a manually selected whole mount spheroid and then generated by the *Fiji* open source software "Z-axis Profile" plot tool.

3. *Parameters*: Using an *in-house* developed *MATLAB* (version ***R2016a***, ***MathWorks***) script, which has as input *Fiji* results, the different parameters of calcium handling kinetics are then returned.

more washes with the culture media mixture, cardiac tissue models were analysed either alone or in the presence of different cardioactive drugs.

In these pharmacological tests, they were incubated with the target compounds for approximately 5 min before acquisition. Specifically, pharmacological responses of hiPSC-CM, in both mono- and triculture models, exposed to 60 µM norepinephrine (β_1-adrenergic receptor agonist; norepinephrine bitartrate, ***Sigma-Aldrich***), 40 µM heptanol (gap junction uncoupler; ***Sigma-Aldrich***), 4 µM propranolol (β-blocker; propranolol hydrochloride, ***Sigma-Aldrich***) and, finally, 4 µM propranolol and thereafter 60 µM norepinephrine, were evaluated.

Optical recordings of intracellular Ca^{2+} transients were acquired using a spinning disk confocal microscope (*system*: ***Revolution XD***, ***Andor***; *microscope*: ***Eclipse Ti-E***, ***Nikon***; *confocal scanner*: ***CSU-X1***, ***Yokogawa***) and 30 sec videos were recorded through *Micro-Manager 1.4* software (**Fig.3.2**, *left panel*).

Fluorescence peaks were extracted from a manually selected whole mount spheroid and then generated by the *Fiji* open source software "Z-axis Profile" plot tool (**Fig.3.2**, *middle panel*). Using an *in-house* developed *MATLAB* (version ***R2016a***, ***MathWorks***) script, which has as input *Fiji* results, the different parameters of calcium kinetics are then returned (**Fig.3.2**, *right panel*), *viz*. peak amplitude (ΔF/F0), maximal upstroke velocity (ΔF/F0/s), maximal decay velocity (ΔF/F0/s), rise to peak time (s), peak to 50% decay time (s), peak to 80% decay time (s). The remaining parameters analysed for calcium kinetics – time between peaks (s) and beating rate (beats/min) – were analysed manually afterwards.

3.3.10. Biomaterial mechanobiological characterization: atomic force microscopy (AFM)

AFM-based mechanical dynamic characterization was performed to compare the mechanobiological behaviour of the hydrogel-based *scaffold* (in the absence of cells), mono- and triculture, 15 days after microencapsulation. Samples were collected and fixed as indicated beforehand (consult **3.3.6**). Fixed samples were washed twice with DPBS and stored at 4 °C, until AFM analyses.

Alginate microcapsules were embedded in 2% (w/v) high melting temperature agarose (***Lonza***), forming a thin film, which was hydrated immediately prior to AFM acquisitions.

AFM measurements were performed in an AFM system (*MFP-3D Stand Alone*, ***Asylum Research***) operated in alternate contact mode (AC mode). For measurements in native conditions (*i.e.* liquid

environment), two types of commercially available AFM probes were used: *BL-AC40TS* (f_0 = 110 kHz; k = 0.09 N/m; ***Olympus Micro Cantilevers***) and *AC240TS* (f_0 = 70 kHz; k = 1.7 N/m; ***Olympus Micro Cantilevers***); for measurements in air, only *AC160TS* (f_0 = 300 kHz; k = 26 N/m; ***Olympus Micro Cantilevers***) was used. Images were plane-fitted prior to reproduction. *Gwyddion*, an open-source software programme (*Gwyddion*, *v.2.51*, http://gwyddion.net), was used to analyse and construct AFM 2D and 3D images (*e.g*. topographical or phasing imaging). Using AFM images, by measuring two perpendicular diameters, per pore, the biomaterial-*scaffold* average pore diameter was estimated.

Force spectroscopy mode-atomic force microscopy (FS-AFM) curve acquisition was performed in liquid, relying on the same probes. The resulting curves were analysed using ***Asylum Research***'s software packages installed in *IGOR Pro* software (***WaveMetrics***) and, at least, three capsules per condition were considered. Via FS-AFM, relevant biomechanical parameters, that can be correlated with a remodelling of cardiac microenvironment, were also quantified – Young's modulus, stiffness, hardness and adhesion – for the biomaterial-based *scaffold* and for mono- and triculture models (endpoint quantification).

3.4. Cardiotoxicity assays with chemotherapeutic drugs

Doxorubicin (cardiotoxic anthracycline, *MW*: 579,980 g/mol; *doxorubicin hydrochloride*, ***MedChem Express***) and paclitaxel (cardiotoxic taxane, *MW*: 853,906 g/mol; *Taxol®*, ***Paclitaxel Farmoz***) were dissolved in stock solutions (10 mg/mL and 6 mg/mL, respectively) and were serially diluted (final concentrations: 0.1, 0.5, 1, 5, 10, 50 and 100 µM).

At the endpoint, samples of the microencapsulated 3D hiPSC-CM mono- and 3D hiPSC-CM/ECMC triculture cardiac tissue models were dispensed into 96-well plates and incubated with 1X *PrestoBlue™ Cell Viability Reagent* (diluted in a 1:1 mixture of *RPMI/B27-ins* and *ECGM2*) for 3h at 37 ºC, with gentle agitation, in the dark. As described earlier (consult **3.3.2**), fluorescence was measured at the excitation and emission wavelengths of 560 and 590 nm, correspondingly. This timepoint was considered as the 0h. Then, the exhausted culture medium, containing *PrestoBlue™*, was removed and the samples were incubated with serial dilutions of the anticancer drugs (doxorubicin and paclitaxel, diluted in a 1:1 mixture of *RPMI/B27-ins* and *ECGM2* containing 1X *PrestoBlue™ Cell Viability Reagent*), for 72h at 37 ºC, with gentle agitation, in the dark. Fluorescence was read again, as previously described. 72 and 0h fluorescence intensity values (*RFU*, relative fluorescence units) were initially normalized per spheroid. Final *RFU* values are the quotient between 72 and 0h (untreated controls). Analyses consisted of three technical replicas. Controls (subtracted from the mean of the three technical replicas) were also read, at 72 and 0h, and correspond to 1X *PrestoBlue™* diluted in the culture media mixture.

3.5. Upscaling the 3D cardiac tissue models to stirred-tank bioreactors

At day 7, hiPSC-CM were harvested and dissociated as indicated earlier (consult **3.1.2**).

hiPSC-CM (100 x 10^6 cell) were then inoculated in a 200 mL (*inoculum*: 0.5 x 10^6 cell/mL) software-controlled stirred-tank bioreactor (*DasGip cellferm-pro bioreactor system*, ***Eppendorf AG***, Hamburg, Germany) (**Fig.3.3**). Culture conditions were set to maintain cells under 3% pO_2 (15% of air with 21% of oxygen; atmospheric hypoxic environment), 37 ºC and an initial stirring rate of 60 or 80 rpm (explained below). Two independent bioreactor experiments were performed, with the aim of optimizing the aggregation of hiPSC-CM in STBRs (preliminary results). In the first, perfusion operation mode was activated at day 10, with a dilution rate of 0.30 day^{-1}. Stirring rate was originally set to 60 rpm and, at day 9, was increased to 70 rpm and thus maintained until day 18. In the second, perfusion was started at day

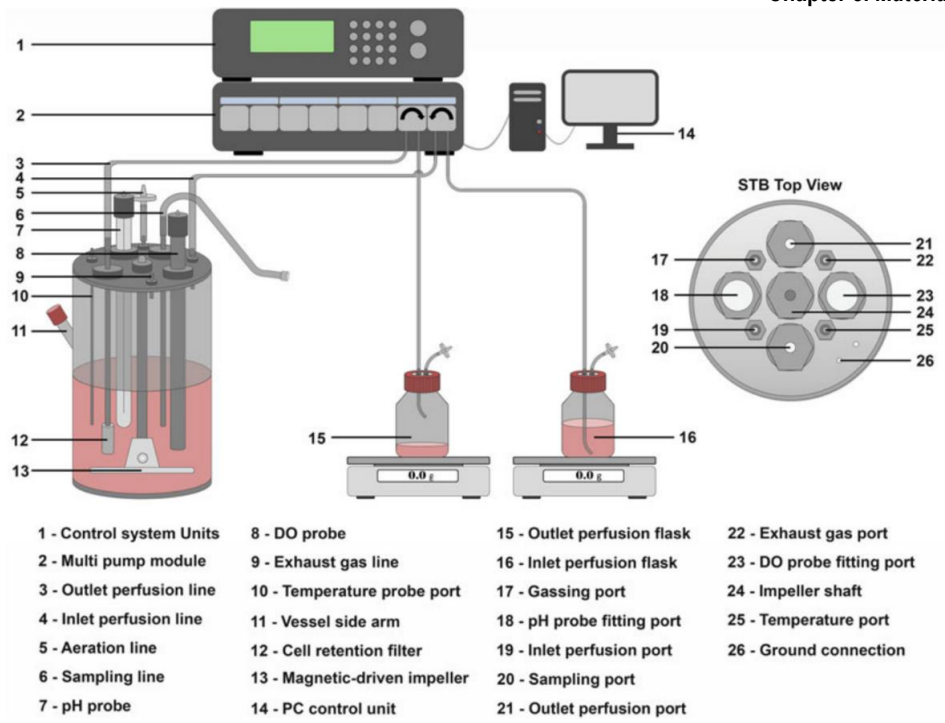

Figure 3.3 | Schematic illustration of the STBR apparatus used for hiPSC-CM aggregation (from day 7 to day 18), operating under perfusion mode [reproduced from **Simão *et al.* (2016)**[226].

9, with the aforementioned dilution rate. Stirring rate was initially set to 80 rpm and, at day 11, was increased to 90 rpm and thus maintained until day 18 (*BR culture time*: 12 days; day 7 to 18).

At day 18 of hiPSC-CM differentiation, 3D hiPSC-CM spheroids were collected from the STBR and approximately 14 x 10^6 cells were dispersed in 3 mL of the 1.1% (w/v) alginate equimolar mixture (consult **3.2**), dissolved in NaCl 0.9% (w/v) solution (***Merck Millipore***). Then, spheroids were microencapsulated either alone (3D hiPSC-CM monocultures), or together with hiPSC-ECMC (3D hiPSC-CM/ECMC tricultures), differentiated in parallel as described in **3.1.3**, in a 1:2 ratio (about 28 x 10^6 ECMC), for an approximate total of 42 x 10^6 CM/ECMC, following the procedure described in **3.2**.

Finally, re-inoculation in two similar bioreactor vessels (working volume: 250 mL; *DASbox*, ***Eppendorf AG***, Hamburg, Germany) was performed: one of them was inoculated with the monoculture microcapsules, whilst the other with the triculture ones. As a *proof-of-concept*, 3D cardiac tissue models were both maintained in culture for only 6 days (*post*-microencapsulation).

FDA-PI live-dead double staining, spheroid and microcapsule concentration, distribution of spheroids per microcapsule, spheroid and microcapsule size determination, flow cytometry of the starting populations and immunofluorescence (in monolayers and in whole capsules) were determined as previously described for the primary models established in shake flask (consult **3.3**).

3.6. Statistical analysis

Statistical analyses were performed using *GraphPad Prism* version 6 (***GraphPad Software***). Data are mean ± standard deviation (SD) or mean ± standard error of the mean (SEM). The test statistics used to infer statistical differences between groups, as well as the number of biological independent experiments and technical replicates performed, are indicated in the figure captions of the section 4. *Results and Discussion* and in *Annex*. The significance level (*alpha* value) was fixed at 0.05 with a 95% confidence interval (CI). Statistical significance was defined based on *p*-value, *P* (*ns* – not significant, *$P \leq 0.05$, ***$P \leq 0.001$, ****$P \leq 0.0001$). Asterisks (*) denote significant differences. Whenever no statistical significance relationship is indicated in the graphs, consider it as *ns* – not significant, $P > 0.05$. All results will be exhibited with four significant figures.

4. Results and Discussion

4.1. Steps toward microencapsulation: experimental strategy, culture monitoring and phenotypic assessment, before microencapsulation

A 3D triculture cardiac tissue model, completely hiPSC-derived, was implemented. For this, a two-step strategy, based on (i) two separate hiPSC differentiations, toward CM or non-myocytes (endothelial and mesenchymal cells), encompassing (ii) a subsequent microencapsulation step in a biocompatible hydrogel, was employed. This experimental strategy is schematically summarized in **Fig.4.1**.

Also, this type of dual strategy has already been used in our group (*e.g.* cancer 3D models)[178,179,182,189], yet never in the cardiac context. Accordingly, the model we are describing arises as a whole new concept.

The use of *AggreWell*™ plates was the primary strategy chosen for generating 3D hiPSC-CM spheroids, because it offers the benefit of obtaining spheroids with a very reduced size dispersion (**Fig.4.2*e***; average spheroid diameter at day 18, prior to microencapsulation: 142.1 ± 26, 24 µm), as well as high cell viabilities, as can be seen in the FDA-PI live/dead double staining (**Fig.4.2*d***). In addition, it is a user-friendly and standardized approach, consistent with high-throughput assays[1,79,91]. A uniform average spheroid diameter is indispensable for maintaining comparable mass and oxygen diffusional gradients between spheroids under similar culture conditions and, particularly, for ensuring reproducibility and a low *batch-to-batch* variability, for instance, in high-throughput screening (HTS) assays[190]. Spheroids with diameters greater than 400-500 µm, typically lead to the formation of necrotic centres in their *core*, owing to oxygen and/or nutrients deprivation of the inner cells[190].

With regard to other aggregation methods, such as those in stirred tank bioreactors, average spheroid diameter dispersion may be a very difficult factor to control, as will be demonstrated in section **4.9**.

In parallel, at day 5 of hiPSC-CM differentiation (corresponding to day 0 of hiPSC-ECMC differentiation), the second differentiation was started (**Fig.4.1**, *bottom*), in 2D monolayer co-culture conditions.

The principle is similar to that of the myocyte differentiation, aiming for the initial formation/polarization of cardiac mesoderm, so as to engender the various types of cells of the cardiovascular system (consult **1.2.3**). The focal difference will be the induction of endothelial and mesenchymal lineages through VEGF supplementation, which is one of the main factors responsible for initiating and regulating angiogenesis[191]. Furthermore, it has been widely reported in the literature that VEGF has the ability to induce differentiation into ECs[55,99,100,110].

hiPSC phenotype before differentiations (**Fig.4.2*a***) and those of hiPSC-cardiac derivatives (hiPSC-CM's in **Fig.4.2*b*** and hiPSC-ECMC's in **Fig.4.2*c***), at the end of the differentiation/prior to microencapsulation, was routinely determined via flow cytometry. Unsurprisingly, hiPSC exhibited common pluripotency/stemness-related markers (**Fig.4.2*a***; $OCT4^+$: 64.16 ± 5.459, $SSEA\text{-}4^+$: 91.90 ± 5.233 and $TRA\text{-}1\text{-}60^+$: 88.20) and absence of early differentiation markers (**Fig.4.2*a***; *SSEA-1*: 0).

At day 15 of hiPSC-CM differentiation, spheroids displayed a phenotype agreeing with the differentiation protocol used[83,84], explicitly an expression of CM markers larger than 75% (**Fig.4.2*b***, 3D hiPSC-CM, pink, black stripes; $SIRP\alpha/\beta^+$: 83.13 ± 3.635, $cTnT^+$: 76.60 and $VCAM\text{-}1^+$: 73.23 ± 6.746). A 2D cell control (**Fig.4.2*b***, 2D hiPSC-CM, pale pink, black dots) was also maintained for comparison with 3D hiPSC spheroid differentiation (consult **3.1.2.2**); however, at day 15, there was no significant statistical difference in SIRPα/β and VCAM-1's expressions between 2D and 3D (**Fig.4.2*b***, 2D hiPSC-CM and 3D hiPSC-CM; $P > 0.05$, *ns*).

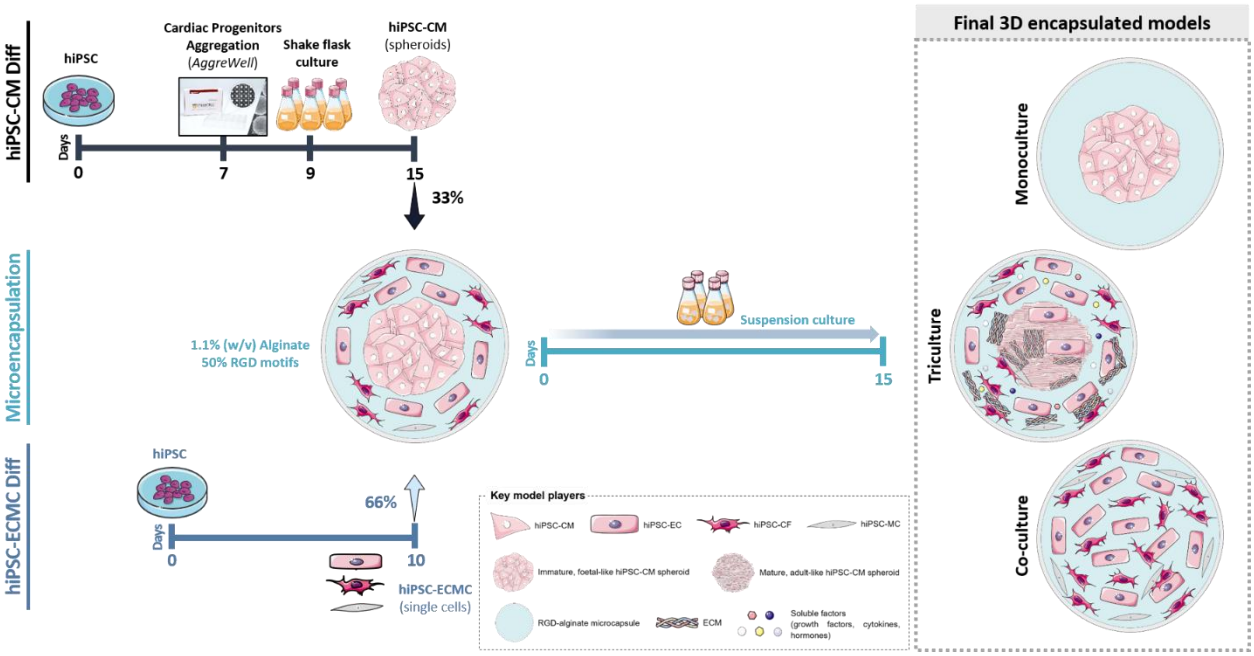

Figure 4.1 | Experimental strategy – *in vitro* reconstruction of the *in vivo* heart microenvironment.

Schematic illustration of the **culture strategy** for the **final 3D triculture** hiPSC-derived **cardiac** tissue **model**, as well as for the 3D mono- and co-culture models. Defined cardiovascular cell populations (hiPSC-CM spheroids and hiPSC-ECMC) were systematically differentiated from hiPSC. Representations of the models are not to scale. The key model players are also exhibited.

With respect to the non-myocyte hiPSC-ECMC phenotype, evaluated at day 10 (day 15 of hiPSC-CM differentiation), it can be concluded that this differentiation consistently generates (data from four biologically independent experiments) a mixture of approximately 25% of ECs (**Fig.4.2*c***; $CD31^+$: 28.55 ± 7.033 and VE-$cadherin^+$: 19.87 ± 5.759), as demonstrated by the EC surface markers CD31 and VE-cadherin, whereas the remaining 75% express concomitantly Vimentin and α-SMA, (**Fig.4.2*c***; $Vimentin^+$: 89.98 ± 2.445 and α-SMA^+: 34.98 ± 16.55), probably corresponding to cells of a mesenchymal lineage.

Almost 90% of the cells in the mixed ECMC population express Vimentin, which clearly reveals the prevalence of MCs, with only about 35% of cells expressing α-SMA, a marker for CFs and VSMCs[192]. For simplicity, we will always refer to a mesenchymal population, which most likely will not be pure; as such, we may even be in the presence of a "quadriculture" cell-based model, in which, along with CMs, there are also ECs, CFs and VSMCs. Identification of the mesenchymal subpopulations is also hampered by the fact that there are no fully specific markers for CFs or VSMCs[29,36,192–195].

These FC results correspond to all the cell populations used to develop the models that will be discussed afterwards (consult **List of Models**).

To further characterize the ECMC phenotype, the expression of specific markers for ECs (VE-cadherin) together with MC markers (Vimentin, α-SMA or DDR2) was evaluated by immunofluorescence of the ECMC monolayers (**Fig.4.2*f***). Nevertheless, it was not possible to draw much more conclusions than those already gotten via FC, namely the presence of an endothelial population (VE-$cadherin^+$) and a larger mesenchymal population, which expresses Vimentin or DDR2, but does not express VE-cadherin.

Lastly, both hiPSC-CM spheroids and hiPSC-ECMC single cells were microencapsulated in biocompatible hydrogel scaffold (composed of a 1:1 mixture of conventional non-RGD alginate and RGD peptide-coupled alginate), which provides a 3D controllable, inert and chemically defined microenvironment (unlike, for instance, *Matrigel*) for the cells to physically attach and communicate. 3D hiPSC-derived cardiac tissue models were then kept in shake flask culture for, at least, 15 days (**Fig.4.1**).

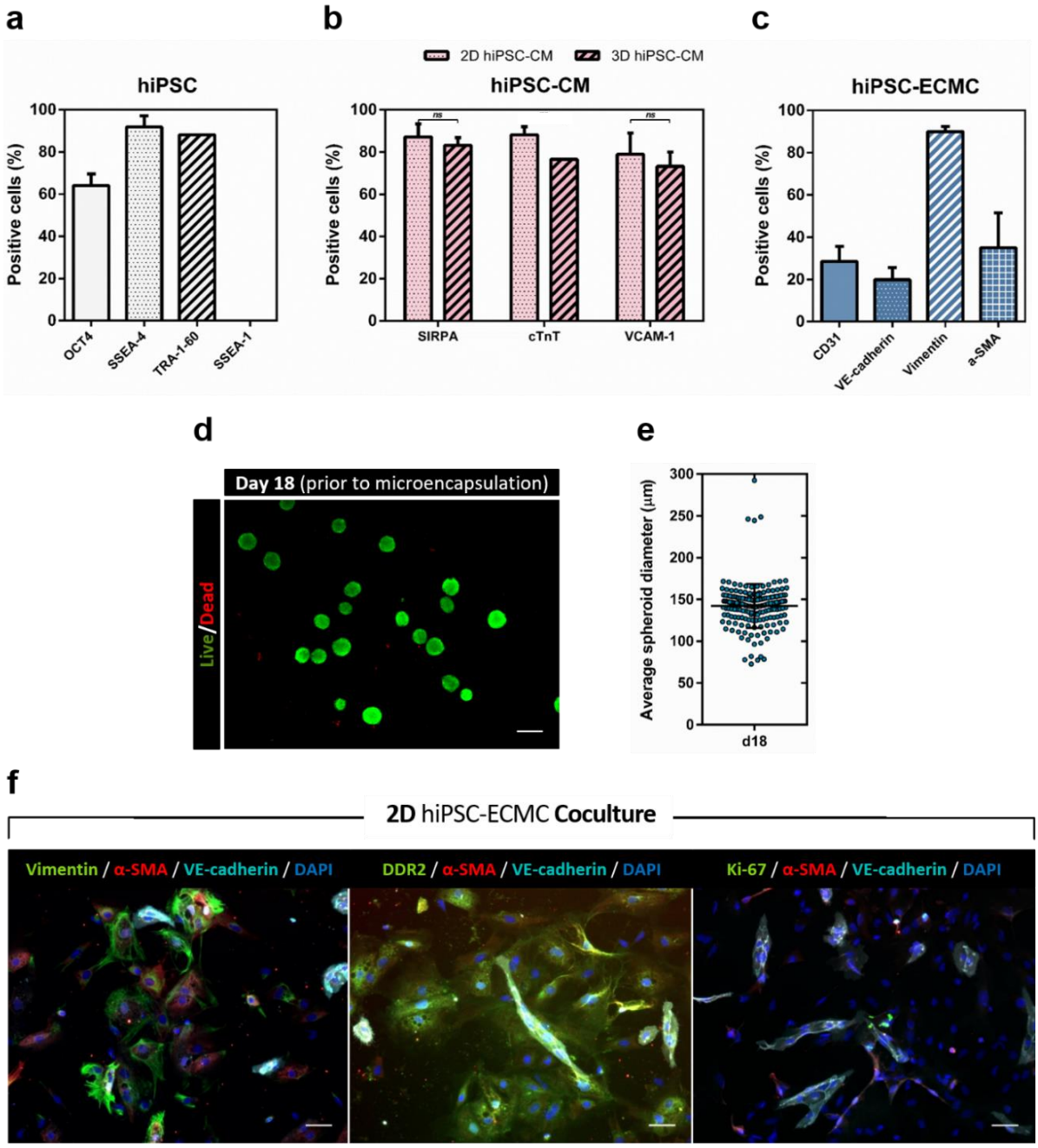

Figure 4.2 | Monitoring and phenotypic characterization of hiPSC and hiPSC-derived cultures, before differentiation and prior to microencapsulation, respectively. **(*a*-*c*)** hiPSC and hiPSC-based cultures – hiPSC-CM and hiPSC-ECMC – **flow cytometry phenotypic characterization**. Data are mean ± SD from two independent experiments (n = 2), for hiPSC and hiPSC-CM **(*a*-*b*)**, and four (n = 4), concerning hiPSC-ECMC **(*c*)**. **(*a*)** Percentage of positive **hiPSC** for the expression of common **pluripotency** stem cell markers (Oct-4, SSEA-4 and TRA-1-60) and spontaneous **differentiation** ones (SSEA-1), before differentiations. **(*b*)** Percentage of positive **hiPSC-CM** for SIRPα/β, VCAM-1 and cTnT **cardiac** specific markers, at day 15, prior to microencapsulation, in 2D monolayer (2D hiPSC-CM, control condition; pale pink, **black dots**) and 3D spheroid (3D hiPSC-CM; pink, **black stripes**) cultures. Ordinary two-way ANOVA analysis with Sidak's *post hoc* test for multiple comparisons (*ns* – not significant, $P > 0.05$). **(*c*)** Percentage of positive **hiPSC-ECMC** for CD31 and VE-cadherin **endothelial** specific markers and Vimentin and α-SMA **mesenchymal** markers, at day 10, prior to microencapsulation. **(*d*)** Evaluation of **hiPSC-CM spheroids viability**, through a **live/dead assay**, at day 18, prior to microencapsulation (**Model #1-*a*–MCT-SF**). Spheroids were stained with **FDA** (fluorescein diacetate) – **live** cells, **green**, and **PI** (propidium iodide) – **dead** cells, **red**. Scale bar, 200 µm. **(*e*)** Scatter dot plot displaying the **hiPSC-CM average spheroid diameter**, at day 18, prior to microencapsulation. Line at mean with SD. Data are mean ± SD from one independent experiment (**Model #1-*a*–MCT-SF**) (n = 92 spheroids). **(*f*)** **Wide-field immunofluorescence** microscopy representative images of the **2D hiPSC-ECMC co-culture**, at day 10, prior to microencapsulation. 2D hiPSC-ECMC immunostained for the **endothelial** marker **VE-cadherin** (**cyan**) and for the **mesenchymal** markers **Vimentin** (**green**), **α-SMA** (**red**) and **DDR2** (**green**). **Proliferative** cells labelled for **Ki-67** (**green**). Nuclei were counterstained with **DAPI** (**blue**). Scale bars, 50 µm.

Therefore, a heterotypic 3D hiPSC-CM/ECMC triple cardiac tissue model, encompassing the three aforementioned cardiac populations, in a cellular ratio (**Fig.4.1**) of around 33% hiPSC-CM spheroids to 66% hiPSC-ECMC (*i.e*. 1 CM to 2 ECMCs), microencapsulated in this alginate hydrogel (consult **3.2**), was generated (**Fig.4.1**, *right*, *dashed text box*). This cell ratio was selected in order to mimic the numbers of the different cardiac populations in the adult human heart, according with **Bergmann *et al*. (2015)**'s studies (for further detail, consult **1.1.2.4**). 3D hiPSC-CM monocultures (only spheroids microencapsulated) and 3D hiPSC-ECMC co-cultures (microencapsulated hiPSC-ECMC monolayers) were also established (**Fig.4.1**, *right*, *dashed text box*) and in depth characterized for comparison with the triculture model, as will be demonstrated throughout this section.

hiPSC-CM spheroids viability characterization (**Fig.S1*a*** for **Model #1-*b*–MCT-SF**; and **Fig.S1*b*** for **Pilot Model–M-SF**), likewise evaluated via live/dead assays, as well as their average diameter (**Fig.S1*c*** for both **Model #1-*b*–MCT-SF** and **Pilot Model–M-SF**), concerning to two more independent experiments, are compiled in **Annex 2.1**. **Model #1-*b*–MCT-SF** is a biological replicate of **Model #1-*a*–MCT-SF** (**Fig.4.2*d*** and **Fig.4.2*e***), whilst **Pilot Model–M-SF** consisted of a study in which only monocultures were microencapsulated and it was a relevant first step for the transition to the heterotypic triculture model (for supplementary information about the mentioned models, consult **List of Models**).

Again, these results demonstrate a high cell viability of the cardiac spheroids (**Fig.S1*a*** and **Fig.S1*b***) and a slightly higher average spheroid diameter (221.6 ± 55.15) before microencapsulation, conferring reproducibility and validating the chosen aggregation method.

4.2. After microencapsulation scenario: cell viability, metabolic activity and model monitoring and characterization

4.2.1. A heterotypic cellular crosstalk between hiPSC-CM and hiPSC-EC favours the survival of hiPSC-EC in the triculture model

Owing to the fact that the different cell populations – myocytes and nonmyocytes – are compartmentalized in close proximity within the biomaterial-based construct, one of the central hypotheses of this study is that a heterotypic crosstalk, mimicking certain features of the myocardium-endocardium interactions taking place in the human heart[17,25,26,28] (consult **1.1.2** and **1.1.2.1**), would be established, especially amongst hiPSC-CM and hiPSC-ECs, in the 3D triculture model.

Consequently, it is expected that there is a higher survival of hiPSC-EC in the triculture model, where they are in close contact with hiPSC-CM, instead of the coculture model. In both, hiPSC-EC are in the presence of hiPSC-MC, at a similar ratio and culture circumstances.

In order to substantiate our hypothesis, a qualitative assessment of the microencapsulated 3D hiPSC-derived cardiac tissue models' cell viability (**Model #1-*a*–MCT-SF**) over time (days 0, 1, 7, and 15 *post*-microencapsulation) was performed using the FDA-PI live/dead assay (**Fig.4.3*a***).

In **Fig.4.3*a*** it is possible to perceive that 3D hiPSC-CM monoculture and 3D hiPSC-CM/ECMC triculture conditions sustain a high cell viability during 15 days of culture. However, when looking at the 3D hiPSC-ECMC model, we can observe that, at days 0 and 1, hiPSC-ECMC display high viabilities (**Fig.4.3*a***, *Coculture*); however, from day 7 (**Fig.4.3*a***, *Coculture*, *red boxes*), the cells begin to die, as shown by the intensification in PI's red staining, with this tendency being extended until day 15.

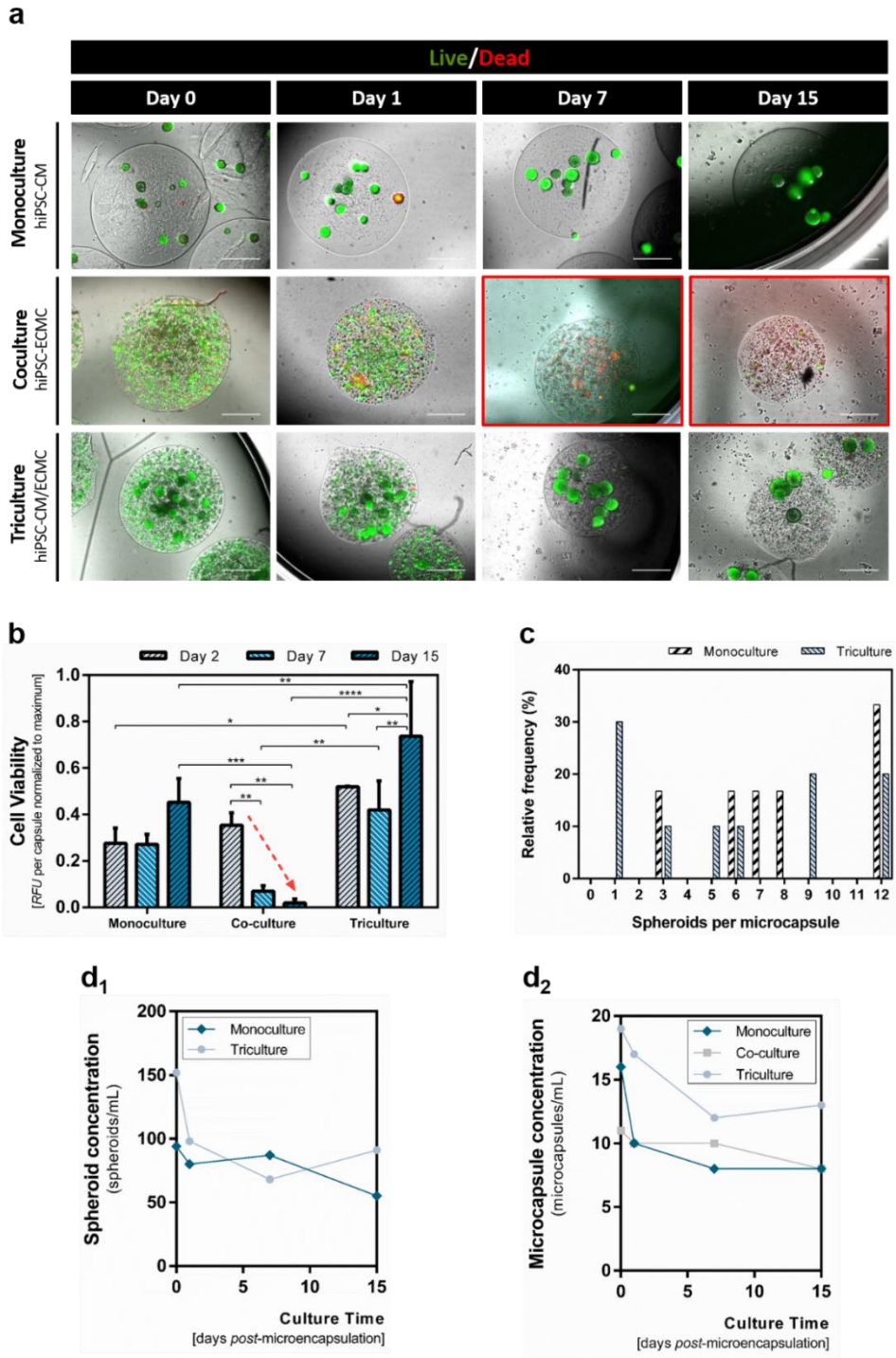

Figure 4.3 | hiPSC-ECMC are not capable to survive in the absence of hiPSC-CM, denoting positive evidence of heterotypic cellular communication in the triple model (Model #1-*a*–MCT-SF). (***a***) Qualitative assessment of 3D hiPSC-based cardiac tissue models' (hiPSC-CM mono-, hiPSC-ECMC co- and hiPSC-CM/ECMC triculture) **cell viability over time** (*from left to right*: 0, 1, 7 and 15 days after microencapsulation), cultured under similar circumstances. **Highlighted** (**red boxes**): co-culture on days 7 and 15, *post*-microencapsulation. Cultures were stained with **FDA** (fluorescein diacetate) – **live** cells, **green**, and **PI** (propidium iodide) – **dead** cells, **red**. Scale bars, 500 µm. (***b***) **Cell viability quantification** in the different 3D cultures, **throughout** the culture **time** (days 2, 7, and 15 *post*-microencapsulation), using a ***PrestoBlue*** resazurin–based dye assay. Data are mean ± SD from one independent experiment and consist of three technical replicates (n = 3). Ordinary two-way ANOVA analysis with Tukey's *post hoc* test for multiple comparisons (*$P \leq 0.05$, **$P \leq 0.01$, ***$P \leq 0.001$, ****$P \leq 0.0001$). Fluorescence intensity values (*RFU*, relative fluorescence units) were normalized to the number of capsules, counted per well, and to the maximum of fluorescence intensity, verified in the three timepoints considered. Excitation and emission wavelengths were 560 and 590 nm, respectively; gain was 176. (***c***) **Spheroids per microcapsule distribution**, in mono- and triculture, 1 day after microencapsulation. (***d***) Characterization of the behaviour of the encapsulated models in terms of (***d*$_1$**) **spheroid** (mono- and triculture) and (***d*$_2$**) **microcapsule** (mono-, co- and triculture) **concentration**, **over time** (0, 1, 7 and 15 days after microencapsulation).

This result seems to be in line with hypothesis put forward: hiPSC-EC are communicating with hiPSC-CM, in the triple model, and this communication is vital for their survival, since, in the coculture, they do not subsist in CMs absence.

Aiming to validate these results, we quantified cell viability over time (days 2, 7, and 15 *post*-microencapsulation) using *PrestoBlue*™ resazurin-based dye assay (for further detail, consult **3.3.2**), as shown in **Fig.4.3*b***.

At day 2, both 3D mono- and coculture cardiac models exhibit comparable metabolic activities (**Fig.4.3*b***, *Monoculture* and *Coculture*), with the triculture demonstrating higher values (**Fig.4.3*b***, Monoculture *vs*. Triculture at day 2, *****). Nonetheless, at day 7, as hypothesized and in agreement with live/dead results (**Fig.4.3*a***), there is an sudden decrease (**Fig.4.3*b***, indicated by the red down arrow) in metabolic activity in the coculture model (day 2 *vs*. day 7, ******), extendable until day 15 (day 2 *vs*. day 15, ******). Hence, we ended up focusing on mono- and triculture models: the coculture, as will be realized, was then abandoned in many of the performed characterizations.

Regarding the remaining models, monoculture maintains its metabolic activity over the 15 days (there are no significant statistical differences in monoculture over this period; **Fig.4.3*b***), whereas the triculture, from day 7 to 15, discloses a significant increase of metabolic activity (**Fig.4.3*b***, day 7 *vs*. day 15, ******).

Thus, it should be emphasized that, at day 15 (endpoint), the triculture model displays a metabolic activity significantly higher than that of its control counterparts (**Fig.4.3*b***, Triculture *vs*. Monoculture at day 15, ****** and Triculture *vs*. Coculture, ********), which may be linked with hiPSC-ECMC proliferation in this model.

Spheroids per microcapsule distribution (**Fig.4.3*c***) at day 1 *post*-microencapsulation, as well as the behaviour of the encapsulated models (**Fig.4.3*d***), in terms of spheroid (**Fig.4.3d_1**) and microcapsule (**Fig.4.3d_2**) concentration over time (0, 1, 7 and 15 days after microencapsulation), were also evaluated.

These results reveal the absence of empty capsules (**Fig.4.3*c***); nevertheless, a wide dispersion of spheroids per microcapsule is verified (**Fig.4.3*c***). This may be due to the fact that in **Model #1-*a*–MCT-SF** the average microcapsule diameter is much higher (1546 ± 62.05 µm, instead of 700-800 µm, for the remaining models, as shown in **Annex 2.2**, **Table S4** and **Fig.S2**), thereby tolerating the storing of a bigger number of spheroids per microcapsule.

This could be a disadvantageous factor when using this sort of models for high-throughput drug screening assays, which require fairly standardized responses[21,22,190]. The way to circumvent this obstacle will be, prior to the incubation of a given compound, counting the number of microcapsules and corresponding spheroids, in each well, and carry out a subsequent normalization.

Concerning the models' behaviour, it is possible to notice that both spheroid (**Fig.4.3d_1**) and microcapsule concentrations (**Fig.4.3d_2**) slightly decrease at day 1 *post*-encapsulation, and then remain constant until day 15, indicating the stability of the engineered cardiac models. This initial decrease may be explained by a certain adaptation of the cell populations in the first days of culture (**Fig.4.3d_1**) and by the mechanical disruption of some microcapsules during the microencapsulation and succeeding inoculation step in shake flasks (**Fig.4.3d_2**).

4.2.2. Depending on the RGD peptide-coupled alginate proportion, RGD motifs exert agonist or antagonistic effects on hiPSC-EC

To study the impact of the scaffold's RGD motifs on cell survival and proliferation (for further detail, consult **1.3.3.2.3**), a new *batch* was generated (**Model #1-*b*–MCT-SF**), in which, in addition to the

mentioned models (mono-, co- and triculture, microencapsulated in a mixture containing 50% RGD peptide-coupled alginate), the new ones were established in 100% RGD peptide-coupled alginate.

Pursuing a similar strategy, the same trend was detected for the replicates of the previous *batch* (**Fig.4.4*a***, $Monoculture_{50}$, $Coculture_{50}$, $Triculture_{50}$), in which the viability of mono- and tricultures was maintained over the culture time, whilst the coculture's noticeably decreases after day 7 *post*-microencapsulation (**Fig.4.4*a***, $Coculture_{50}$).

Increasing RGD peptide-coupled alginate proportion does not appear to impact the survival of monocultures, which continuously maintain a high cell viability, regardless of whether they are encapsulated in a peptide-modified scaffold with 50% or 100% RGD motifs (**Fig.4.4*a***, $Monoculture_{50}$ and $Monoculture_{100}$). Though, contrariwise to what would be expected, when using a scaffold consisting solely of 100% RGD peptide-coupled alginate, it is found that the co-culture's cell death tendency, on days 7 and 15, is now also extended to the triculture model (**Fig.4.4*a***, $Coculture_{50}$, $Coculture_{100}$ and $Triculture_{100}$).

Hence, we can conclude that increasing RGD peptide-coupled alginate ratio up to 100% in the microcapsule scaffold does not entail benefits for hiPSC-ECMC and is even detrimental, since it inhibits the heterotypic crosstalk in the triple model.

Albeit RGD (*arginine-glycine-aspartate* peptide sequence) is one of the most regularly found binding motifs attached to scaffolds[116,131], because of its ability to ultimately lead to the initiation of cell signalling for survival and proliferation[116,131], there is some disagreement regarding some of the its functions. **Maubant *et al*. (2018)**'s study[196], examining the impact of non-peptide mimetic RGD on human endothelial cells, demonstrates that these motifs, in addition to the declared agonist functions, may also exert an antagonistic activity, inducing detachment, caspases activation and apoptosis in HUVECs[196]. On the other hand, **Matsuki *et al*. (2018)**[197] also demonstrated that RGD peptides, at high concentrations, may exert an antagonistic effect, inducing apoptosis, via direct activation of caspase-3[197]. This leads us to conclude about the existence of an hypothetical threshold concentration (which will probably depend on the RGD-modified material), from which there is a modification in the nature of the promoted effects.

Moreover, a 50% RGD peptide-coupled alginate appears to be ideal to promote an agonist effect of hiPSC-EC survival, in the triple model (**Fig.4.4*a***).

The metabolic activity of the biological replicas of the models shown in **Fig.4.3*b*** (50% RGD peptide-coupled alginate) was also evaluated (**Fig.4.4*b***), at days 7 and 14 *post*-microencapsulation, with similar results to those previously attained (**Fig.4.3*b***). In these models, microcapsules with approximately half of the size (**average microcapsule diameter**: 832.7 ± 28.30 µm; consult **Annex 2.2**, **Table S4** and **Fig.S2**) were obtained, which allowed a more compact spheroid per microcapsule distribution (**Fig.4.4*c***), but also led to the existence of more empty microcapsules.

Model behaviour's results also corroborate the inefficiency of the scaffold formed by 100% RGD-peptide coupled alginate in encapsulating the triple model, with extremely low values of spheroid and microcapsule concentrations (**Fig.4.4*d*$_1$**, *Triculture-100*: 1.500 ± 0.7071 spheroids/mL; and **Fig.4.4*d*$_2$**, *Triculture-100*: 9.000 ± 1.414 microcapsules/mL).

Pilot experiment's (**Pilot Model–M-SF**) results, relating to cell viability, metabolic activity, spheroid distribution per microcapsule and concentration of spheroids and microcapsules, are shown in **Annex 2.2**, **Fig.S3**. The microcapsule average diameters resulting from the different experiments (**Pilot Model–M-SF**, **Model #1-*a*–MCT-SF**, **Model #1-*b*–MCT-SF** and **Model #2-*b*–MT-BR-2**) is compiled in **Annex 2.2**, **Table S4** and **Fig.S2**.

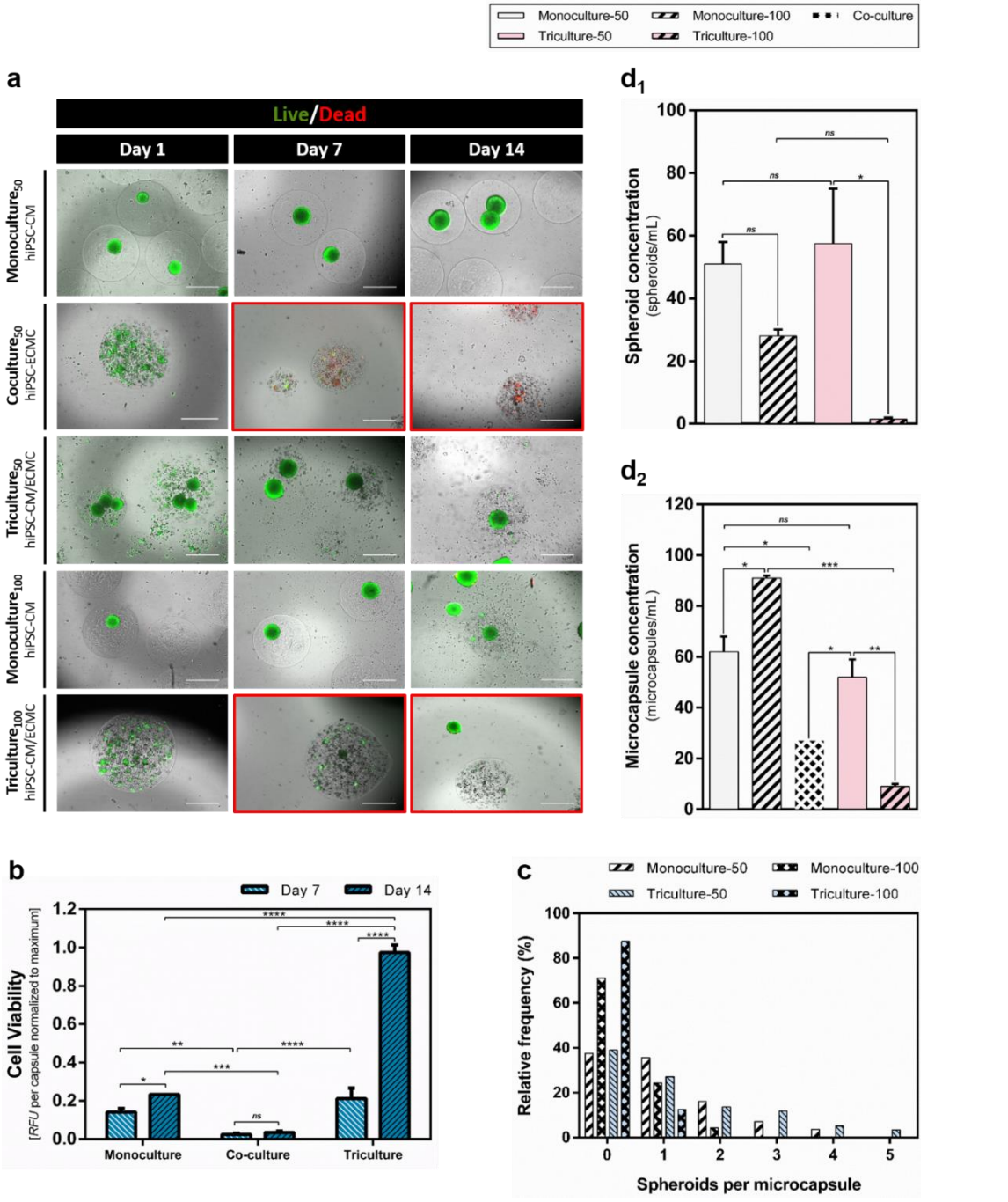

Figure 4.4 | Increasing RGD peptide-coupled alginate proportion up to 100% in the microcapsule scaffold does not entail benefits for hiPSC-ECMC, inhibiting heterotypic communication in the triple model (Model #1-*b*–MCT-SF). **(*a*)** Qualitative assessment of 3D hiPSC-based cardiac tissue models' (with 50 or 100% of RGD peptide-coupled alginate) **cell viability over time** (*from left to right*: 0, 1 and 14 days after microencapsulation), cultured under similar conditions. **Highlighted** (**red boxes**): co-culture$_{50}$ and triculture$_{100}$ on days 7 and 14, *post*-microencapsulation. Cultures were stained with **FDA** (fluorescein diacetate) – **live** cells, **green**, and **PI** (propidium iodide) – **dead** cells, **red**. Scale bars, 500 µm. **(*b*)** **Cell viability quantification** in the different 3D models **over time** (days 7 and 14 *post*-microencapsulation), using a ***PrestoBlue*** resazurin–based dye assay. Data are mean ± SD from one independent experiment and consist of three technical replicates (n = 3). Ordinary two-way ANOVA analysis with Tukey's and Sidak's *post hoc* tests for multiple comparisons (*$P \leq 0.05$, **$P \leq 0.01$, ***$P \leq 0.001$, ****$P \leq 0.0001$). Fluorescence intensity values (*RFU*, relative fluorescence units) were normalized per capsule and to the maximum of fluorescence intensity. Excitation and emission wavelengths were 560 and 590 nm, respectively; gain was 176. **(*c*)** **Spheroids per microcapsule distribution**, in mono- and tricultures (50 and 100% of RGD peptide-coupled alginate), 1 day after microencapsulation. **(*d*)** Characterization of the behaviour of the encapsulated models, in terms of **(d_1) spheroid** (monocultures and tricultures) and **(d_2) microcapsule concentration** (monocultures, co-culture and tricultures). Error bars are mean ± *SEM* from one independent experiment, corresponding to the mean values of days 1, 7 and 14, *post*-microencapsulation (n = 3). Ordinary one-way ANOVA analysis with Tukey's *post hoc* test for multiple comparisons (*ns* – not significant, *$P \leq 0.05$, **$P \leq 0.01$, ***$P \leq 0.001$).

4.3. RT-qPCR gene expression profiling unveils the first evidences of cardiac maturation

One way to circumvent hiPSC-CM immaturity is to create *in vitro* co-culture models comprising myocytes and non-myocytes (consult **1.3.1** and **1.3.2**). Hence, another hypothesis to be tested would be that hiPSC-CM would disclose a more advanced maturation stage in the triculture model.

So, to investigate this hypothesis, we compared the expression of a broad panel of genes in mono- and triculture cardiac tissue models. Specifically, we quantified, via RT-qPCR, the relative expression of (**Figs.4.5*a-i***) key structural genes involved in sarcomere assembly (*MYL2*, *MYL7*, *MYH7*, *MYH6*, *TNNI3* and *TNNI1*) and (**Fig.4.5*j*** and **Fig.4.5*k***) ion channels (*L*-type calcium: *CACNA1C* and sodium: *SCN5A*), over time. Expression ratios for gene isoforms associated with an adult/definitive ventricular phenotype, *viz*. *MYL2/MYL7*, *MYH7/MYH6* and *TNNI3/TNNI1* (**Figs.4.5*c,f,i***, correspondingly) were also evaluated.

Gene expression profiling revealed positive evidence of cardiac maturation over time in both 3D hiPSC-CM mono- and 3D hiPSC-CM/ECMC triculture.

MYL2 (**Fig.4.5*a***), *MYH7* (**Fig.4.5*d***) and *TNNI3* (**Fig.4.5*g***) (isoforms more expressed in mature CMs) revealed an upregulated gene expression over the course of 15 days. Gene expression of the mature isoforms, at day 7, with the exception of *MYL2* (**Fig.4.5*a***, Monoculture *vs*. Triculture, ******), revealed no differences between mono- and triculture, which indicates that 7 days in culture are not sufficient for hiPSC-ECMC to cause significant differences in hiPSC-CM maturation, in the triple model. At day 15, there are significant differences between the two models in the expression of all the adult isoforms (**Figs.4.5*a,d,g***; *MYL2*: ********, *MYH7*: ******** and *TNNI3*: ********).

Conversely, changes in fetal isoforms were also observed: *MYL7* (**Fig.4.5*b***), *MYH6* (**Fig.4.5*e***) and *TNNI3* (**Fig.4.5*h***) maintained their expression approximately constant over the 15 days in the monoculture model, whereas, contrariwise to what would be expected, in the triculture model seems to exist a tendency of upregulation of these isoforms over time.

Therefore, to inspect whether or not there were differences in the maturation of hiPSC-CM between the two cardiac models, we decided to look at the expression ratios between adult and fetal isoforms (**Figs.4.5*c,f,i***; *MYL2/MYL7*, *MYH7/MYH6* and *TNNI3/TNNI1*).

Altogether, these ratios demonstrate a clear increase in expression at day 15, compared to day 7, indicative of cardiac maturation in both models over time and symbolizing chief structural changes associated with progression of heart development and *fetal-to-postnatal* transition[25,53,144]. Furthermore, *MYL2/MYL7* (**Fig.4.5*c***, Triculture *vs*. Monoculture, ********) and *TNNI3/TNNI1* (**Fig.4.5*i***, Triculture *vs*. Monoculture, ********) denote, at day 15, evidence of a more developed maturity stage of hiPSC-CM in the triple model. However, *MYH7/MYH6* (**Fig.4.5*f***) seems to indicate the opposite.

Giacomelli *et al*. (2017)[53] also obtained similar results, namely the upregulation of sarcomeric structural genes (*e.g*. *MYL2*, *TNNT2* and *ACTN2*), increased *MYL2/MYL7* ratio and upregulation of ion channel genes (*e.g*. *SCN5A* and *CACNA1C*) in cardiac microtissues (MTs) composed of hPSC-CM and hPSC-EC, compared to those composed only of hiPSC-CM monocultures[53].

Finally, the expression of transcripts of calcium (**Fig.4.5*j***, *CACNA1C*) and sodium (**Fig.4.5*k***, *SCN5A*) cardiac ion channels was also evaluated. Gene expression analysis, at day 15, agrees with the hypothesis of a higher maturation stage in the triple model (**Fig.4.5*j***, *CACNA1C*: ******** and **Fig.4.5*k***, *SCN5A*: *****).

These results are in line with those of **Vuorenpää *et al*. (2017)**[30], which also demonstrate an increased expression of *SCN5A* and *CACNA1C*, between days 7 and 18, in hPSC-CM cultured in the presence of a vascular-like network formed by human foreskin fibroblasts and HUVECs, in comparison to CMs alone[30]. In addition, as demonstrated by **Burridge *et al*. (2014)**[126], the expression of *CACNA1C* was shown to be

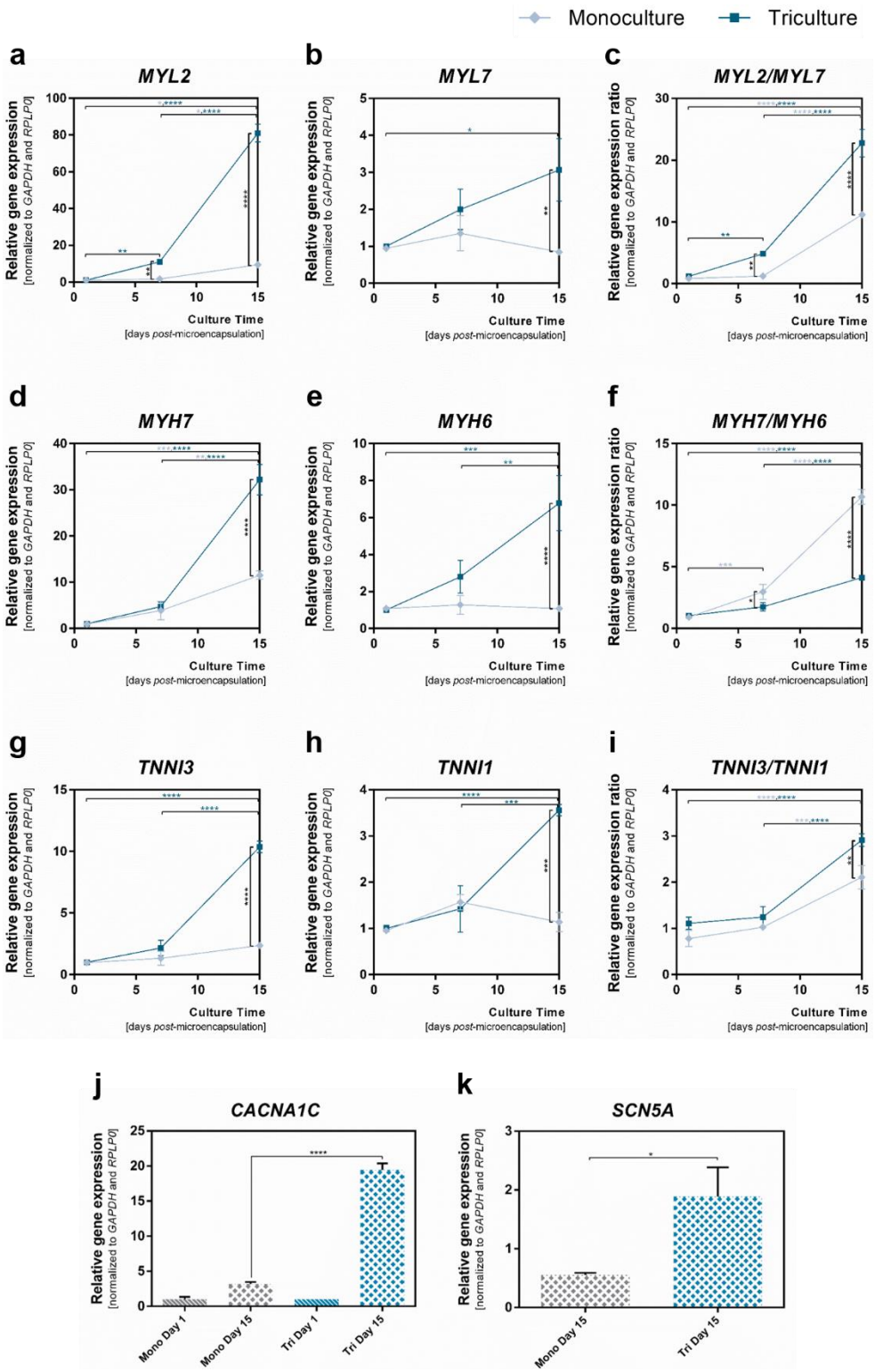

Figure 4.5 | RT-qPCR gene expression analysis discloses evidence of cardiac maturation over time, in both mono- and triculture cardiac tissue models (Model #1-*a*–MCT-SF). RT-qPCR gene expression analysis for **(*a-i*)** key **sarcomeric genes** (myosins: *MYL2*, *MYL7*, *MYH7* and *MYH6*; and troponins: *TNNI3* and *TNNI1*) and **(*j-k*) ion channels** (*CACNA1C* and *SCN5A*), in 3D hiPSC-CM **mono-** and 3D hiPSC-CM/ECMC **triculture**, **over time** (***a-i***: 1, 7 and 15 days *post*-microencapsulation; and ***j***: 1 and 15 days *post*-microencapsulation) and **(*k*)** 15 days *post*-microencapsulation. **(*c, f, i*)** Expression **ratios** for gene isoforms linked with an adult/definitive ventricular phenotype: *MYL2/MYL7*, *MYH7/MYH6* and *TNNI3/TNNI1*, correspondingly. Data are mean ± SD from one independent experiment and consist of technical triplicates (n = 3). Ordinary one-way ANOVA analysis with Tukey's *post hoc* test for multiple comparisons (*$P \leq 0.05$, **$P \leq 0.01$, ***$P \leq 0.001$, ****$P \leq 0.0001$). Colour code of the asterisks indicates the experimental group. All values are normalized to *GAPDH* and *RPLP0* housekeeping genes as internal controls. *Monoculture*: normalization to monoculture on day 1; *triculture*: normalization to triculture on day 1.

increased in hPSC-CM in co-culture with hPSC-EC and human amniotic mesenchymal stem cells (hAMSCs) [126]. Higher expression of *SCN5A* is achieved, for instance, in hPSC-CM matured by electrical stimulation, with a higher expression of *SCN5A* being therefore concerted with a more mature phenotype[198].

Still, further characterization is needed for us to be able to accurately state that, in fact, hiPSC-CM are in a more mature stage in the triculture model.

4.4. Imaging-based phenotypic platform

To in depth characterize the morphology, cellular architecture and phenotype of the different populations involved in both mono- and triculture cardiac models, as well as to provide insight into the conjecture of a more advanced hiPSC-CM maturation stage in the triculture, an extensive imaging-based phenotypic platform has been implemented.

4.4.1. Confocal immunofluorescence in cryosections discloses novel evidences of hiPSC-CM maturation and cardiac microenvironment remodelling in the triculture

At the endpoint, both 3D hiPSC-CM mono- and 3D hiPSC-CM/ECMC triculture were evaluated for the expression of cardiac (**Fig.4.6**; cTnT, sarcomeric α-actinin and titin), cardiac maturation (**Fig.4.7**, Cx43, MLC-2*a* and MLC-2*v*), cytoskeletal (**Fig.4.6**; F-actin), ECM (**Fig.4.8**, collagen type I, collagen type IV and fibronectin), endothelial (**Annex 3.1**, **Fig.S4**; CD31) and mesenchymal (**Annex 3.1**, **Fig.S4**; Vimentin, α-SMA and DDR2), and cell polarity (**Annex 3.1**, **Fig.S5**; ZO-1) and proliferation (**Annex 3.1**, **Fig.S5**; Ki-67) proteins.

Confocal analysis (for further detail, **1.5.5.1**) of cryosections demonstrate that, at day 15, cardiac spheroids express specific structural cardiac markers, *viz*. cTnT, sarcomeric α-actinin and titin, both in mono- (**Fig.4.6*a***) and triculture (**Fig.4.6*b***). F-actin staining displays assembly of an organized and striated myofibrillary structure, typical of developed sarcomeres in both models (**Fig.4.6*a*** and **Fig.4.6*b***; observe insets). Based on the confocal immunofluorescence images and using only these markers, it was not possible to distinguish differences in the maturation level of hiPSC-CM spheroids from the two models. This analysis has been complemented with a quantitative ultrastructural characterization, via transmission electron microscopy (results presented in section **4.5**).

In order to complement the discussed RT-qPCR gene expression results (consult **4.3**), Cx43 expression (component of gap junctions; **Fig.4.7**), as well as MLC-2*a*'s (encoded by *MYL7*, representing an immature ventricular/atrial/nodal CM phenotype; **Fig.4.7**) and MLC-2*v*'s (encoded by *MYL2*, indicating a definitive ventricular phenotype; **Fig.4.7**) were similarly assessed.

Although quantifications of confocal images have not been carried out (given that they derive from 10 µm's cryosections and the corresponding reconstructions are laborious and difficult), Cx43 appears to be overexpressed in the triculture, meaning an increase in cell-cell contacts and occasionally formation of larger junctional plates (**Fig.4.7*b***).

Moreover, this protein, in the triple model, is consistently distributed in the periphery of the cells (**Fig.4.7*b***; observe insets), while, in monoculture, it seems to present a more arbitrary and disorganized pattern (**Fig.4.7*a***, observe insets). Together with RT-qPCR results, this could symbolize another indication of a higher maturation of triculture's cardiac spheroids. Regarding the expression of MLC-2*a* and MLC-2*v* (fetal and adult isoform, respectively), it was not possible to perceive substantial differences between the two cardiac models (**Fig.4.7*a*** and **Fig.4.7*b***).

Interestingly, when evaluating the expression of ECM proteins (**Fig.4.8**), hiPSC-CM/ECMC, in the triple model, seem to produce greater amounts of ECM proteins (**Fig.4.8*b***, collagen type I, collagen type IV and fibronectin; observe insets), than hiPSC-CM in monoculture (**Fig.4.8*a***; observe insets).

This arises as another hint of heterotypic cellular communication in the triculture model.

In this particular case, hiPSC-MC (*e.g*. CFs) may play a key role in the production of these proteins, inducing a remodelling within the scaffold (replicated cardiac microenvironment), via self-produced ECM. Hence, we demonstrate that alginate microcapsules allow the accumulation of collagen type I and IV, forming collagen fibres that are interspersed in the spheroids (**Fig.4.8*a*** and **Fig.4.8*b***; observe insets), and

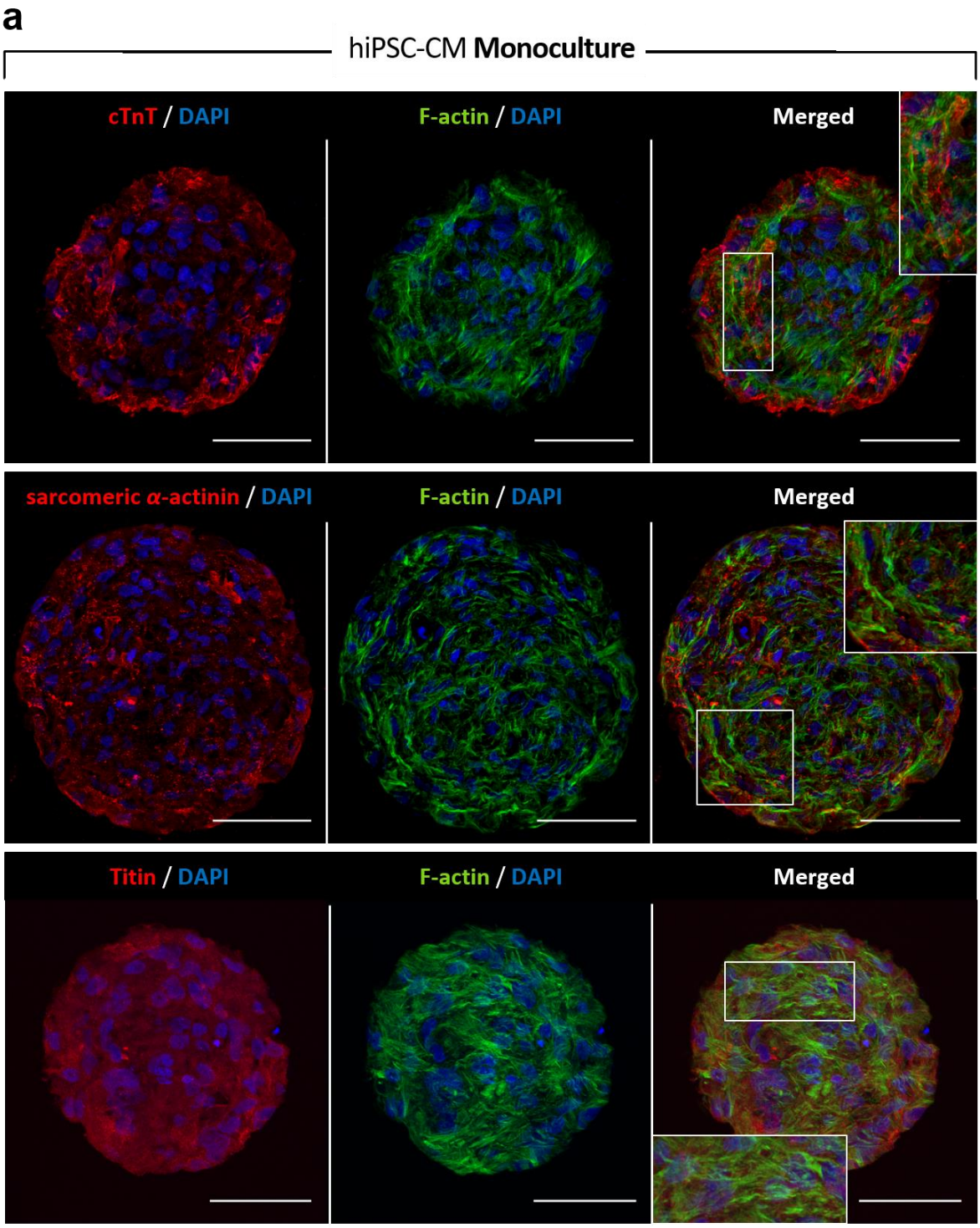

Figure continues on the following page

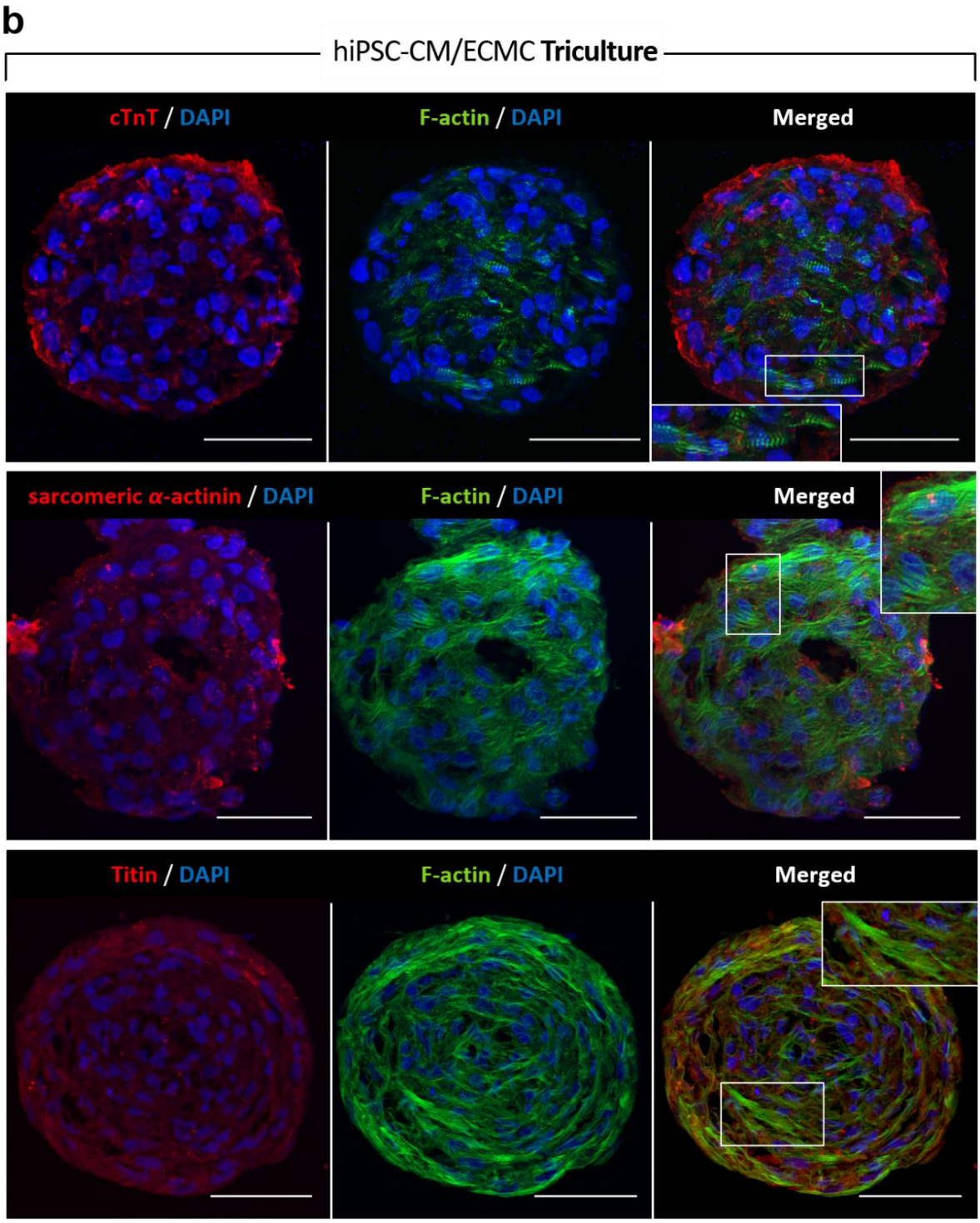

Figure 4.6 | Mono- and triculture confocal imaging-based phenotypic characterization: cardiac markers (Model #1-*a*–MCT-SF). **(*a*-*b*)** Confocal immunofluorescence microscopy of 3D hiPSC-CM mono- **(*a*)** and 3D hiPSC-CM/ECMC triculture **(*b*)** microcapsules, in 10 µm thick cryosections, at the **endpoint** of the models (day 15 *post*-microencapsulation), in similar culture circumstances. Data are representative maximum intensity z-projections from one independent experiment. Mono- **(*a*)** and triculture **(*b*)** immunostained (*from left to right*) for the **cardiac markers** **cTnT**, **sarcomeric α-actinin** and **titin** (**red**), and for **F-actin** (**phalloidin**, **green**). Nuclei were counterstained with **DAPI** (**blue**). **(*a*-*b*)** Insets indicate high magnification images of the corresponding white rectangles. All images acquired with a 63x 1.3*NA* (consult **List of Abbreviations and Conventions**) oil immersion objective (***Leica Microsystems***). Scale bars, 50 µm.

fibronectin (very notorious in the triculture; **Fig.4.8*b***), mimicking a tissue-like architecture and contributing to cardiac remodelling within the capsules. Changes in matrix structural components

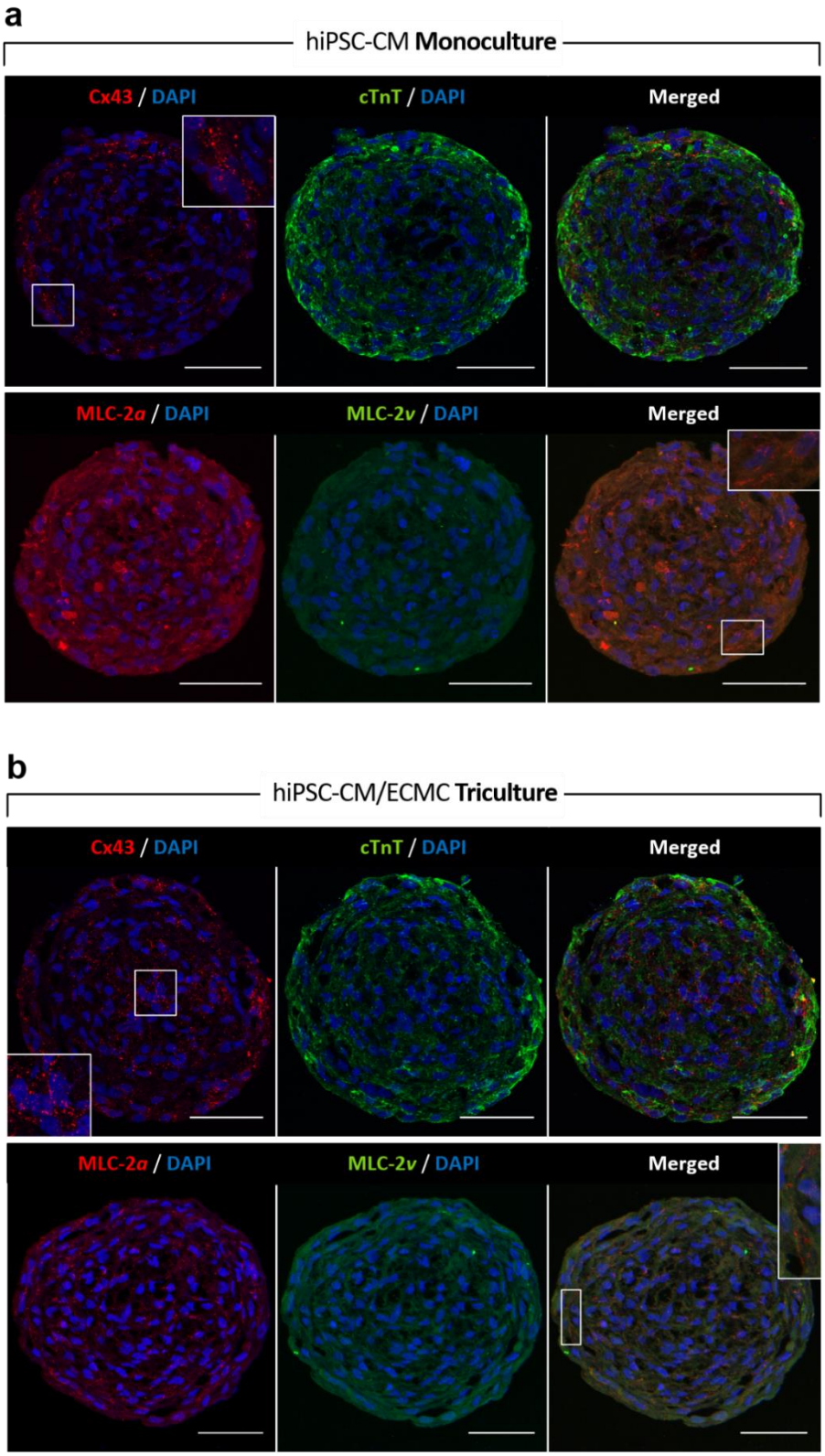

Figure 4.7 | Mono- and triculture confocal imaging-based phenotypic characterization: cardiac maturation markers (Model #1-*a*–MCT-SF). (*a*-*b*) Confocal immunofluorescence microscopy of 3D hiPSC-CM mono- (***a***, *upper panel*) and 3D hiPSC-CM/ECMC triculture (***b***, *lower panel*) microcapsules, in 10 µm thick cryosections, at the **endpoint** of the models (day 15 *post*-microencapsulation), in similar culture circumstances. Data are representative maximum intensity z-projections from one independent experiment. Mono- (***a***, *upper panel*) and triculture (***b***, *lower panel*) immunostained (*from left to right*) for **gap junctions** (**Cx43**, **red**) and for **immature ventricular**/atrial/nodal CM phenotype (**MLC-2*a***, **red**), and for **cTnT** and for **definitive ventricular** phenotype (**MLC-2*v***, **green**). Nuclei were counterstained with **DAPI** (**blue**). **(*a*-*b*)** Insets indicate high magnification images of the corresponding white rectangles. All images acquired with a 63x 1.3*NA* oil immersion objective (***Leica Microsystems***). Scale bars, 50 µm.

(collagen type I, collagen type IV and fibronectin) are, however, verified in both cardiac models (**Fig.4.8*a*** and **Fig.4.8*b***).

Garzoni *et al*. (2009)[114] obtained similar results: expression of sarcomeric tropomyosin, Cx43, collagen type IV, fibronectin and laminin, using a 3D model of CM spheroids supplemented either with ECs or bone marrow-derived mesenchymal stroma cells[114].

Looking at **Fig.S4** (**Annex 3.1**), it is possible to detect an endothelial population (hiPSC-EC), through CD31, and a mesenchymal one (hiPSC-MC), via Vimentin, α-SMA and DDR2 stainings, yet in a very reduced

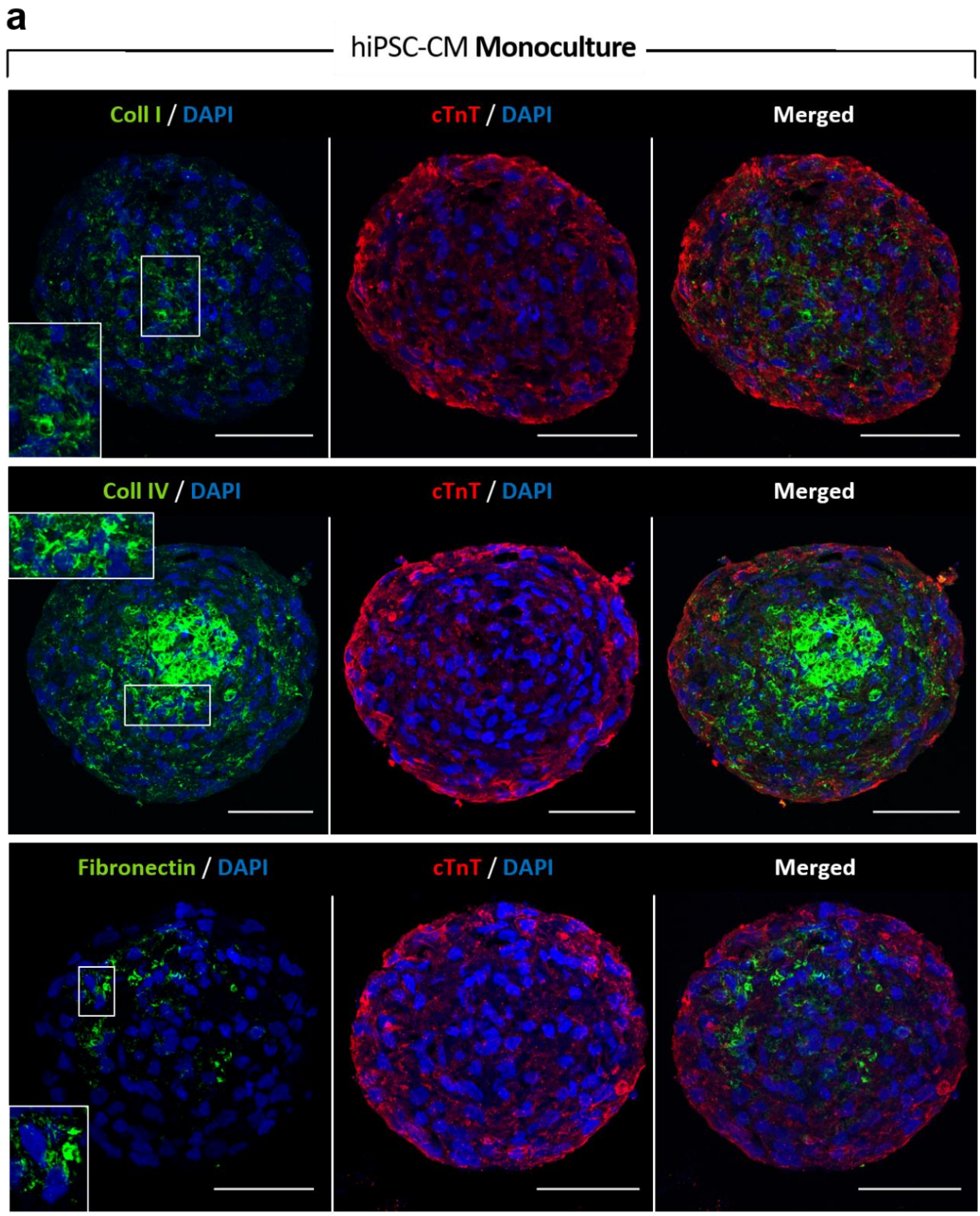

Figure continues on the following page

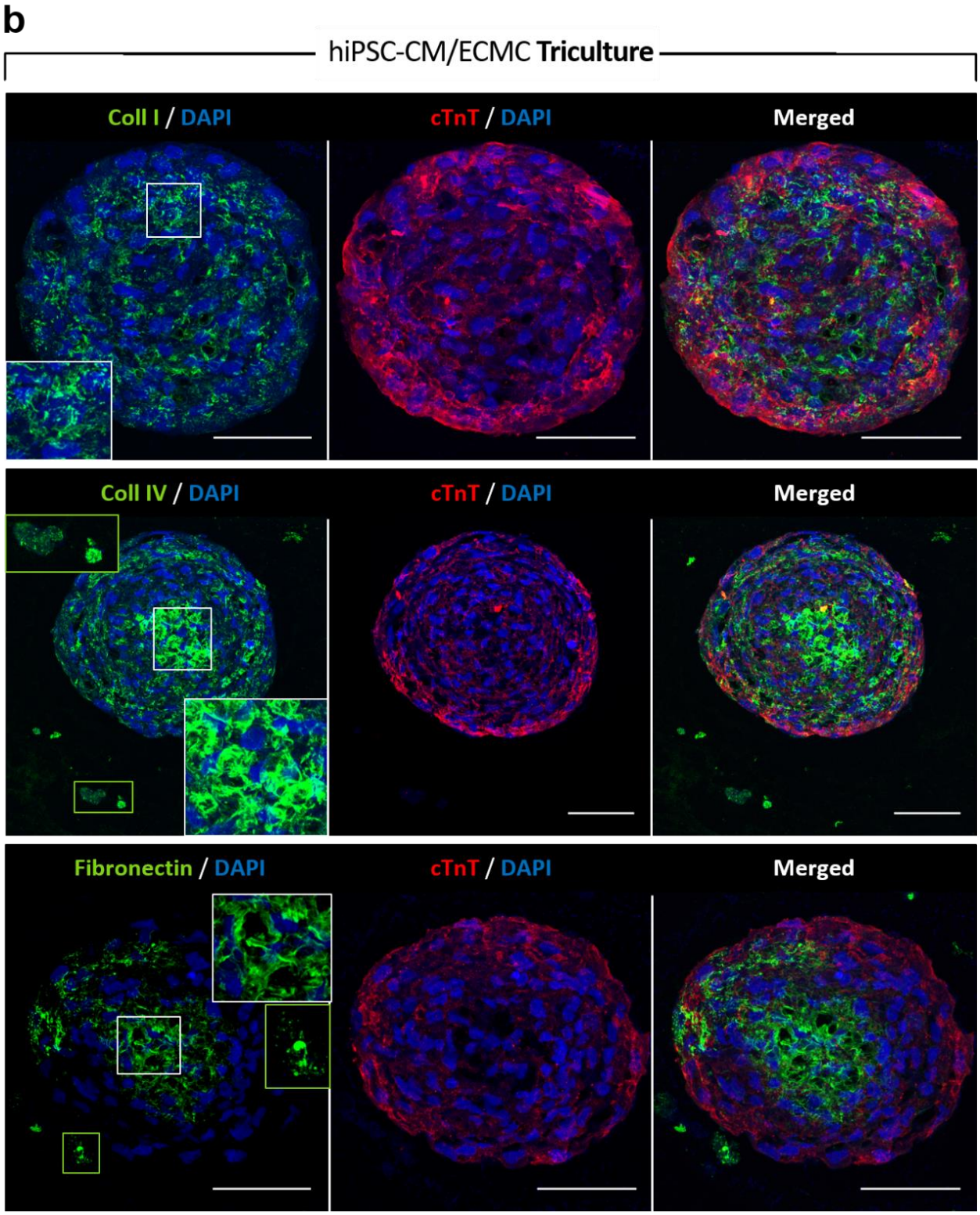

Figure 4.8 | hiPSC-CM/ECMC, in the triple model, appear to produce greater amounts of extracellular matrix proteins than hiPSC-CM alone (Model #1-*a*–MCT-SF). **(*a*-*b*)** Confocal immunofluorescence microscopy of 3D hiPSC-CM mono- **(*a*)** and 3D hiPSC-CM/ECMC triculture **(*b*)** microcapsules, in 10 µm thick cryosections, at the **endpoint** of the models (day 15 *post*-microencapsulation), in similar culture circumstances. Data are representative maximum intensity z-projections from one independent experiment. Mono- **(*a*)** and triculture **(*b*)** immunostained (*from left to right*) for the **ECM proteins** collagen type I, collagen type IV and fibronectin (green) and for **cTnT** (**red**). Nuclei were counterstained with **DAPI** (**blue**). **(*a*-*b*)** Insets indicate high magnification images of the corresponding white or green rectangles. All images acquired with a 63x 1.3*NA* oil immersion objective (*Leica Microsystems*). Scale bars, 50 µm.

proportion relative to hiPSC-CM spheroids. So, we realized that, in the triculture model, due to (i) the nature of the chosen scaffold and (ii) the immunofluorescence procedure itself, in which cryosections with a very reduced thickness (10 µm) are subjected to several washing steps (for further detail, consult **3.3.6.2**), hiPSC-ECMC (single cells) were lost during the washes. Accordingly, we decided to adapt *in toto* immunofluorescence protocols that allowed us to study whole microcapsules, while maintaining their integrity.

Furthermore, it also seems that some that some of the hiPSC-EC (**Annex 3.1**, **Fig.S4**; CD31, observe inset of the corresponding green rectangle) and hiPSC-MC (**Annex 3.1**, **Fig.S4**; DDR2, observe insets of the corresponding white rectangles) have migrated from the peripheral space, around the spheroids, to their *core*. Noteworthy, *α*-SMA and Vimentin also seem to be more pronounced in the triculture model, which is in line with the hypothesis of a hiPSC-MC-induced remodelling of the cardiac microenvironment.

Expression of ZO-1 and Ki-67 was also evaluated for the two cardiac models and the results are exhibited in **Annex 3.1**, **Fig.S5**. Again, there seems to be a greater expression of ZO-1 (a tight junction-associated protein) in the triculture model (**Annex 3.1**, **Fig.S5**; ZO-1), which together with the upregulation of Cx43 (**Fig.4.7*b***), indicates an increase in cell-cell contacts, correlated with cardiac maturation. There is no evidence of proliferative cells inside the spheroids (**Annex 3.1**, **Fig.S4**; Ki-67), since hiPSC-CM exhibit a post-mitotic state[199,200].

4.4.2. Whole mount immunofluorescence is consistent with an overexpression of ECM proteins in the triple model

4.4.2.1. Multiphoton microscopy

Using multiphoton microscopy (for further detail, consult **1.5.5.2**), whole capsules of the mono- and triculture models were also evaluated for the expression of cardiac (**Fig.S6**; cTnT and sarcomeric *α*-actinin) and cardiac maturation (**Fig.S7**; MLC-2*a* and MLC-2*v*) markers, with similar conclusions to those obtained in cryosections (**Fig.4.6** and **Fig.4.7**). Partial 3D volume reconstructions (3D projects) were created using this technique (**Annex 3.3**, **3D Projects 1–12**). Multiphoton imaging-based phenotypic characterization of whole monocultures for the pilot experiment (**Pilot Model-M-SF**) is compiled in **Annex 3.2**, **Fig.S8**.

Multiphoton 3D projects have turned out to be quite useful to confirm the hypothesis hitherto postulated: there is, in fact, an increased production of ECM proteins by hiPSC-CM/ECMC, in the triple model (**Fig.4.9*b***; collagen type I, collagen type IV and fibronectin; observe insets), when compared to hiPSC-CM monocultures (**Fig.4.9*a***).

4.4.2.2. Light-sheet fluorescence microscopy

Nevertheless, the utmost innovation in our imaging-based characterization, in comparison to that of similar models[53,114,115,124,201–204], comes from the use of light-sheet fluorescence microscopy, which allows us to get multi-views of the same sample, by rotating it, culminating in faithful and realistic 3D volume reconstructions that, lately, permit quantification of certain markers of interest (for further detail, consult **1.5.5.4**). Besides, there are no cases in the literature that report the use of LSFM to characterize this sort of cardiac models. Thus, this technique was used to image mono- and tricultures, with the specific aim of further characterizing the endothelial and mesenchymal populations, as exposed in **Fig.4.10*a***.

As predicted, the 3D reconstructions (**Annex 3.4**, **LSFM Movies 1–6**) exhibit a much more representative cellular ratio between hiPSC-CM spheroids and hiPSC-ECMC single cells in the triple model (**Fig.4.10*a***, *upper and middle panels*).

In addition, it is noticed that hiPSC-EC (**Fig.4.10*a***, *upper and middle panels*; CD31^{+} and VE-cadherin^{+}, green) and hiPSC-MC (**Fig.4.10*a***, *upper and middle panels*; α-SMA^{+} and Vimentin^{+}, red) are surrounding the spheroids; still, a proportion of hiPSC-EC have migrated in the capsule and were then internalized, which may be an indication of a rudimentary microvasculature-like structure within them[114].

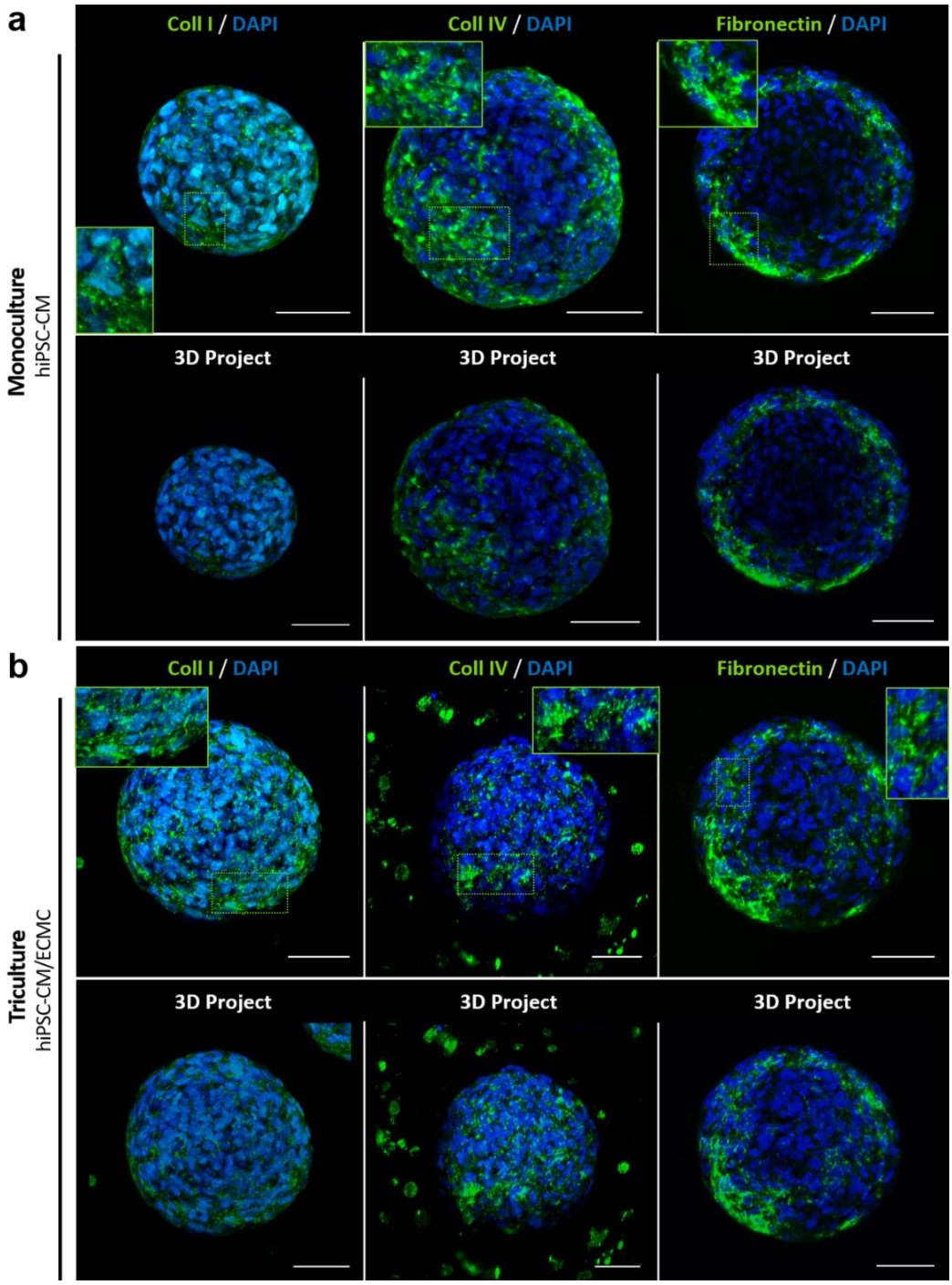

Figure 4.9 | Multiphoton 3D projects are consistent with a higher production of ECM proteins by hiPSC-CM/ECMC, in the triple model, when compared to hiPSC-CM monocultures (Model #1-*a*–MCT-SF).

Multiphoton immunofluorescence microscopy of whole mount microencapsulated 3D hiPSC-CM mono- (***a***, *upper panel*) and 3D hiPSC-CM/ECMC triculture (***b***, *lower panel*), in similar culture circumstances, at **day 15** *post*-microencapsulation. Data are representative maximum intensity z-projections and 3D projects (consult **Annex 3.3**, **3D Projects 7–12**) from one independent experiment. Mono- (***a***, *upper panel*) and triculture (***b***, *lower panel*) immunostained (*from left to right*) for the **ECM proteins collagen type I**, **collagen type IV** and **fibronectin** (**green**). Nuclei were counterstained with **DAPI** (**blue**). (***a-b***) Insets indicate high magnification images of the corresponding green dotted rectangles. All images acquired with a 40x 0.8*NA* water immersion objective (***Olympus***), adding an optical zoom up to 2.5x; total magnification: up to 100x. Scale bars, 50 µm.

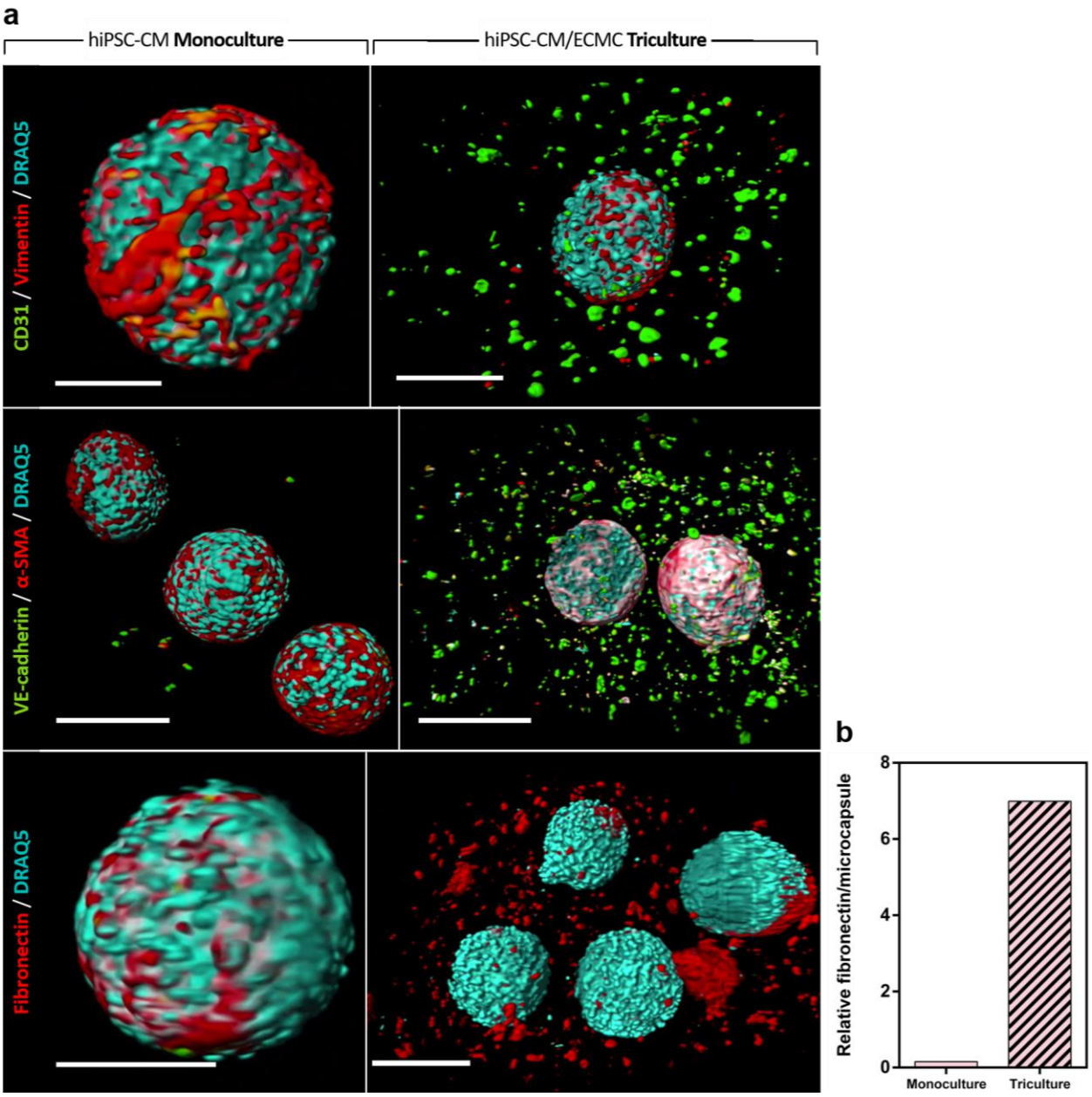

Figure 4.10 | Light-sheet imaging-based phenotypic *in toto* characterization of whole mount mono- and tricultures (Model #1-*α*–MCT-SF). (*a*) Light-sheet immunofluorescence microscopy of the whole mount microencapsulated cardiac tissue models: 3D hiPSC-CM mono- (*left panel*) and 3D hiPSC-CM/ECMC triculture (*right panel*), in similar culture circumstances, at day 15 *post*-microencapsulation. Data are 3D volume reconstructions of the whole models (consult **Annex 3.4**, **LSFM Movies 1–6**), along eight different angles per sample (0º to 360º), with an incremental step of 45º, from one independent experiment. Mono- (*left panel*) and triculture (*right panel*) immunostained (*from top to bottom*) for the **endothelial** cell surface **markers** **CD31** (**green**) and **VE-cadherin** (**green**), for the **mesenchymal markers** **Vimentin** (**red**), **α-SMA** (**red**) and for the **ECM protein** **fibronectin** (**red**). Nuclei were counterstained with **DRAQ5** (**cyan**). All images acquired with a 16x 0.8*NA* water immersion objective (***Nikon***), placed perpendicularly to the excitation plane. Scale bars, 100 µm. **(*b*) LSFM-based quantification of the total fibronectin volume per microcapsule, in mono- and tricultures, at day 15 *post*-microencapsulation.**

On the other hand, it seems that hiPSC-MC (conceivably CFs) are adjacent to the hiPSC-EC, along the rudimentary microvasculature that has formed within the spheroids or, alternatively, in monolayer, together with hiPSC-EC (giving structural support) and around the spheroids (consult **LSFM Movies 1–4**).

These findings demonstrate the feasibility of an *in vitro* 3D triculture cardiac tissue model, fully derived from hiPSC, in which spheroids and monolayers are established within a confined biomaterial.

The deposition of ECM proteins, specifically fibronectin, was also evaluated via LSFM (**Fig.4.10*a***, *lower panel*; and **Fig.4.10*b***). An extensive fibronectin network, reminiscent of a tissue-like architecture, was found in the triculture (**Fig.4.10*a***, *lower panel*, *right*). In monocultures (**Fig.4.10*a***, *lower panel*, *left*), it is also possible to observe fibronectin deposited on the spheroids, as described beforehand for confocal immunofluorescence in cryosections (**Fig.4.8*a***).

A 45.6-fold increase in relative fibronectin expression was found in tricultures, at day 15, compared to monocultures (**Fig.4.10*b***). Although the quantification methods are still being optimized (consult **3.3.6.3.4**), fibronectin's upregulation in the triculture is evident.

A higher deposition of fibronectin in the triple model (hiPSC-ECMC-mediated) may be due to an increase in cell-cell interactions (heterotypic communication), leading to the hypothesized remodelling of the cardiac microenvironment[205], which, in turn, favours important cell-ECM interactions. *In vivo*, fibronectin is expressed during early development and in adult heart, increasing enormously following injury[205,206].

Taken together, these data demonstrate that the 3D hiPSC-CM/ECMC triculture mimics certain cellular and molecular features of the composition of human heart tissue.

4.5. Structural and ultrastructural assessment

4.5.1. Ultrastructural analysis shows improved sarcomere length and myofibrillar alignment in the triculture model

Relevant ultrastructural elements of mono- and triculture models were analysed via transmission electron microscopy (TEM). To follow up the results and provide insight into the anatomy of the cardiac sarcomere, a simplified diagram is shown in **Fig.4.11*a***.

Specifically, at the ultrastructural level, it is possible to observe, in both cardiac models, at the endpoint (**Fig.4.11*b***), registers of highly organized sarcomeres, displaying aligned myofibrils, Z lines, gap junctions connecting adjacent hiPSC-CM and density of mitochondria (**Fig.4.11*b***; observe insets). These features were not observed at the beginning of both models (1 day after microencapsulation; **Fig.4.12**), meaning a dramatic structural maturation over time, from day 1 to day 15.

At day 1, disorganized and forming sarcomeres (with chaotic myofibrillar alignment and split Z lines), as well as shorter and few gap junctions were detected (**Fig.4.12**; observe insets). There do not seem to be noteworthy differences in the density or mitochondrial area between days 1 and 15. Moreover, as would be expected, at day 1, there are no significant ultrastructural differences between mono- and triculture, since in the triple model the three populations were in close contact for a very short period of time, scarce to induce notorious ultrastructural changes in hiPSC-CM.

At day 15, (**Model #1-*a*-MCT-SF; Fig.4.11*c*** and **Fig.4.11*d***; **Annex 4.1**, **Table S5**), sarcomere length (**Fig.4.11*c***; **Annex 4.1**, **Table S5**) and sarcomere angle dispersion (**Fig.4.11*d***; **Annex 4.1**, **Table S5**) were evaluated.

The resting sarcomere length increased significantly from 1.433 ± 0.1907 µm, in the monoculture, to 1.521 ± 0.1342 µm, in the triple model (**Fig.4.11*c*** and **Annex 4.1**, **Table S5**; ** P = 0.0047). Although triculture's value is still lower than those of other studies reported in the literature: 2.2 µm in **Ronaldson-Bouchard *et al*. (2018)**'s[207] and 1.81 µm in **Lundy *et al*. (2012)**'s[208], both with late stage, adult human ventricular myocytes, is an important indication of a structural maturation in the triculture model.

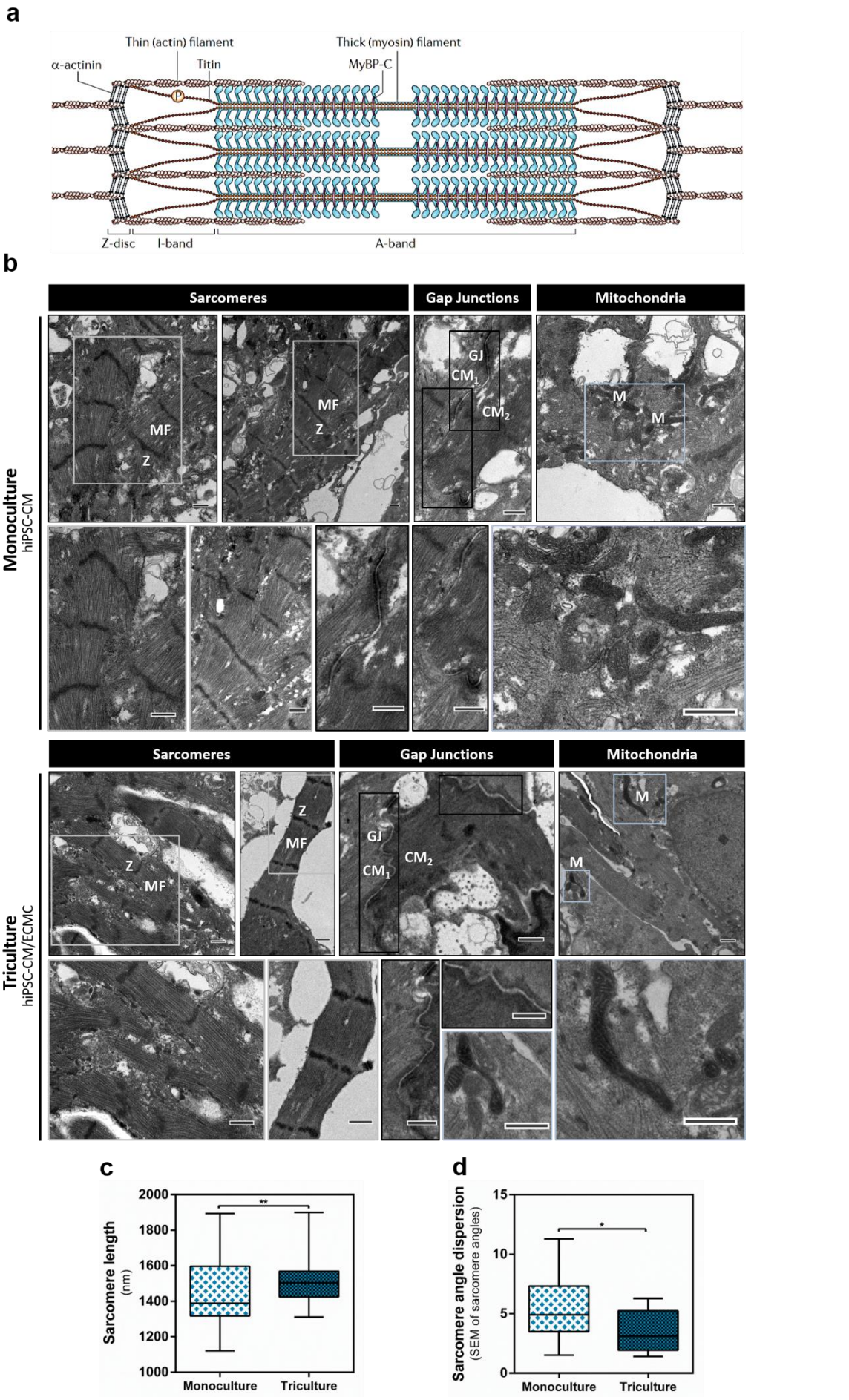

Figure's caption is shown on the following page

Figure 4.11 | 15 days after microencapsulation, hiPSC-CM, in the triple model, reveal enhanced ultrastructure properties, compared to those displayed in the monocultures, suggestive of cardiac maturation (Model #1-*a*–MCT-SF). (***a***) **Simplified diagram of cardiac sarcomere anatomy** [reproduced from **Hwang and Sikes (2015)**[150]]. Sarcomere is the **functional** contractile **unit** in heart cardiomyocytes. **Thin** filaments, constituted by **actin**, are anchored in the Z-disc (or Z-line) and form momentary sliding **interactions** with **thick** filaments, composed mainly of **myosin**. Each of the thick filaments is bounded by six parallel thin filaments. Through *α*-actinin, the latter form crosslinking networks between adjacent sarcomeres, at the Z-disc. In addition to the **Z-disc**, **I-band** and **A-band** are relevant ultrastructural properties defined by their components (actin, myosin and cytoskeleton proteins) and appearance in polarized light. Through microscopy, it can be observed that the **darker A-band** matches up to the thick filament, whereas the **lighter I-band** is crossed by the six thin filaments and the analogous six titin proteins. (***b***) Representative **TEM** micrographs of 3D hiPSC-CM **mono-** and 3D hiPSC-CM/ECMC **triculture** cardiac tissue models, at **day 15** *post*-microencapsulation. Registers of **sarcomeres**, displaying aligned **myofibrils** (**MF**) and organized **Z-discs** (**Z**), **gap junctions** (**GJ**) connecting neighbouring hiPSC-CMs (denoted as $\mathbf{CM_1}$ and $\mathbf{CM_2}$) and density of **mitochondria** (**M**). Insets indicate high magnification images of the corresponding **grey**, **black** or **cyan** rectangles. Scale bars, 500 nm (in both figures and magnifications). (***c-d***) Quantification of ultrastructural features: (***c***) **sarcomere length** (n = 40-52 sarcomeres; two-tailed Mann–Whitney nonparametric test, $^{**}P = 0.0047$) and (***d***) **sarcomere angle dispersion** (n = 8-15 sarcomeres; two-tailed unpaired t-student test ($^{*}P = 0.0379$), in mono- and triculture, at day 15 post-microencapsulation. (***c-d***) Data are mean ± SD from one independent experiment.

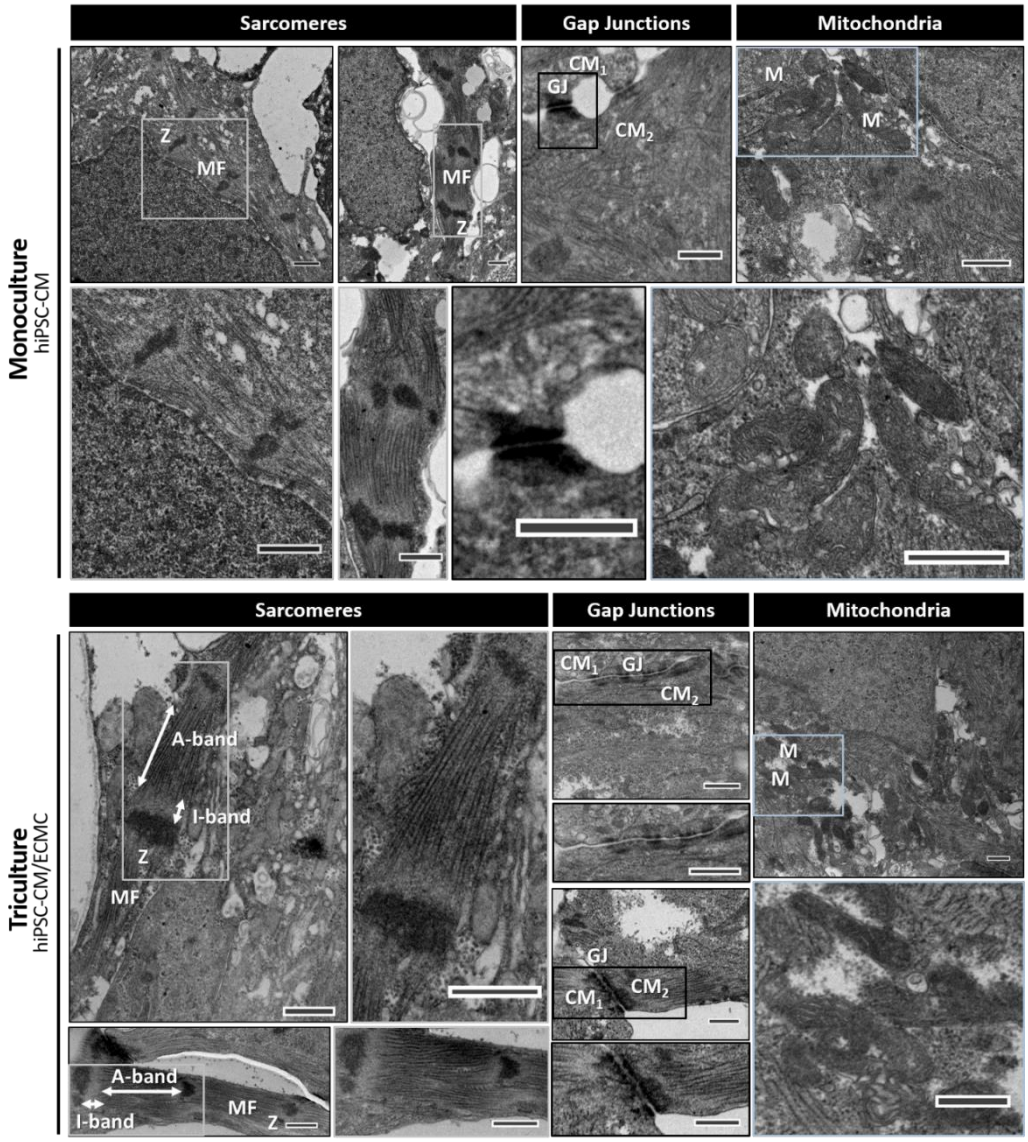

Figure 4.12 | Ultrastructural characterization of mono- and triculture, 1 day after microencapsulation (Model #1-*a*–MCT-SF). Representative **TEM** micrographs of 3D hiPSC-CM **mono-** (*upper panel*) and 3D hiPSC-CM/ECMC **triculture** (*lower panel*) cardiac tissue models, at **day 1** *post*-microencapsulation. Registers of **sarcomeres**, displaying misaligned **myofibrils** (**MF**) and split **Z-discs** (**Z**), as well as **A-** and **I-bands**, smaller **gap junctions** (**GJ**) connecting neighbouring hiPSC-CMs (denoted as $\mathbf{CM_1}$ and $\mathbf{CM_2}$) and density of **mitochondria** (**M**). Insets indicate high magnification images of the corresponding **grey**, **black** or **cyan** rectangles. Scale bars, 500 nm (in both figures and magnifications).

The sarcomeric myofibrillar alignment was also found to be significantly higher in the triculture model, as shown by the reduction in sarcomere angle dispersion (**Fig.4.11*d*** and **Annex 4.1**, **Table S5**; decrease of 5.535 ± 3.419, in mono-, to 3.039 ± 1.589, in triculture; * $P = 0.0379$).

The increase in anisotropic alignment in the triple model, supported by the apparent upregulation of Cx43 and ZO-1 in this model (consult **4.1.1**), is a further indication of an enhanced triculture's structural maturity[25,84,144,207–209].

Altogether, TEM data show that, over 15 days, there were noticeable ultrastructural changes in both models, consistent with cardiac maturation and, particularly, with a more advanced hiPSC-CM maturation stage in the triple model.

Despite these evident ultrastructural changes, we failed to identify any clear T-tubule formation or presence of multinucleation, losing, at the ultrastructural level, to other models, in which it was possible to reach more advanced stages of maturation[207].

TEM micrographs for a biologically independent experiment (**Model #1-*b*–MCT-SF**), at the beginning (**Fig.S9**) and endpoint (**Fig.S10**) of both mono- and triculture cardiac tissue models, are also exhibited in **Annex 4.1**, validating the results discussed in this topic.

4.5.2. Histological/histochemical-based characterization

To characterize spheroids' structure and morphology, we performed histological analysis of paraffin sections of mono- and triculture cardiac tissue models, from two separate experiments, at the endpoint (15 or 14 days after microencapsulation; **Fig.4.13**). Pilot experiment's histological characterization, involving only microencapsulated monocultures, is accessible in **Annex 4.2**, **Fig.S11**.

H&E histological stain allows us to observe nuclei, in purple tones (stained by hematoxylin, which binds to negatively charged nucleic acids, due to its basic nature/positive charge; **Fig.4.13** and **Annex 4.2**, **Fig.S11**), along with eosinophilic structures, *viz*. cytoplasm and extracellular proteins, in pale pink (labelled by eosin, since it is acidic/negatively charged and, therefore, binds to acidophilic substances, for instance side chains of positively charged amino acids; **Fig.4.13** and **Annex 4.2**, **Fig.S11**).

Via PAS stain, we detected the presence of glycoproteins (pink) in both mono- (**Fig.4.13** and **Annex 4.2**, **Fig.S11**) and tricultures (**Fig.4.13**).

Being a basic dye, Toluidine Blue (TB) binds to nucleic acids, labelling nuclei and heteropolysaccharides, such as glycosaminoglycans (GAGs). There were no differences between mono- and tricultures (**Fig.4.13** and **Annex 4.2**, **Fig.S11**), which in line with our expectations, as an increase in GAG content (*e.g*. chondroitin sulfates, hyaluronic acid or heparin) in the adult human heart is associated with pathophysiological processes of heart muscle injury[210,211].

Interestingly, we found the existence of lumens and deposition of fibrillar type I collagen within the spheroids, confirmed by H&E (**Fig.4.13** and **Annex 4.2**, **Fig.S11**; pale pink) and Masson Trichrome (MT, **Fig.4.13*a***; blue) stains. Particularly, MT seems to indicate a higher ECM production in **Model #1-*a*-MCT-SF** (**Fig.4.13*a***; blue) compared to **Model #1-*b*-MCT-SF** (**Fig.4.13*b***) and **Pilot Model-M -SF** (**Annex 4.2**, **Fig.S11**. It should be also noted that single cells (hiPSC-ECMC) are rarely found in the histological sections (3 µm thickness), which is explained by the fact that they are lost during the sectioning procedure.

The fact that the spheroids' structure is not entirely compact is another technical obstacle to the implementation of microscopy techniques (consult **1.5.5.4**), owing to the increased light scattering[162,163,165,166,169,180]. However, as aforesaid, immunofluorescence (cryosections combined with *in*

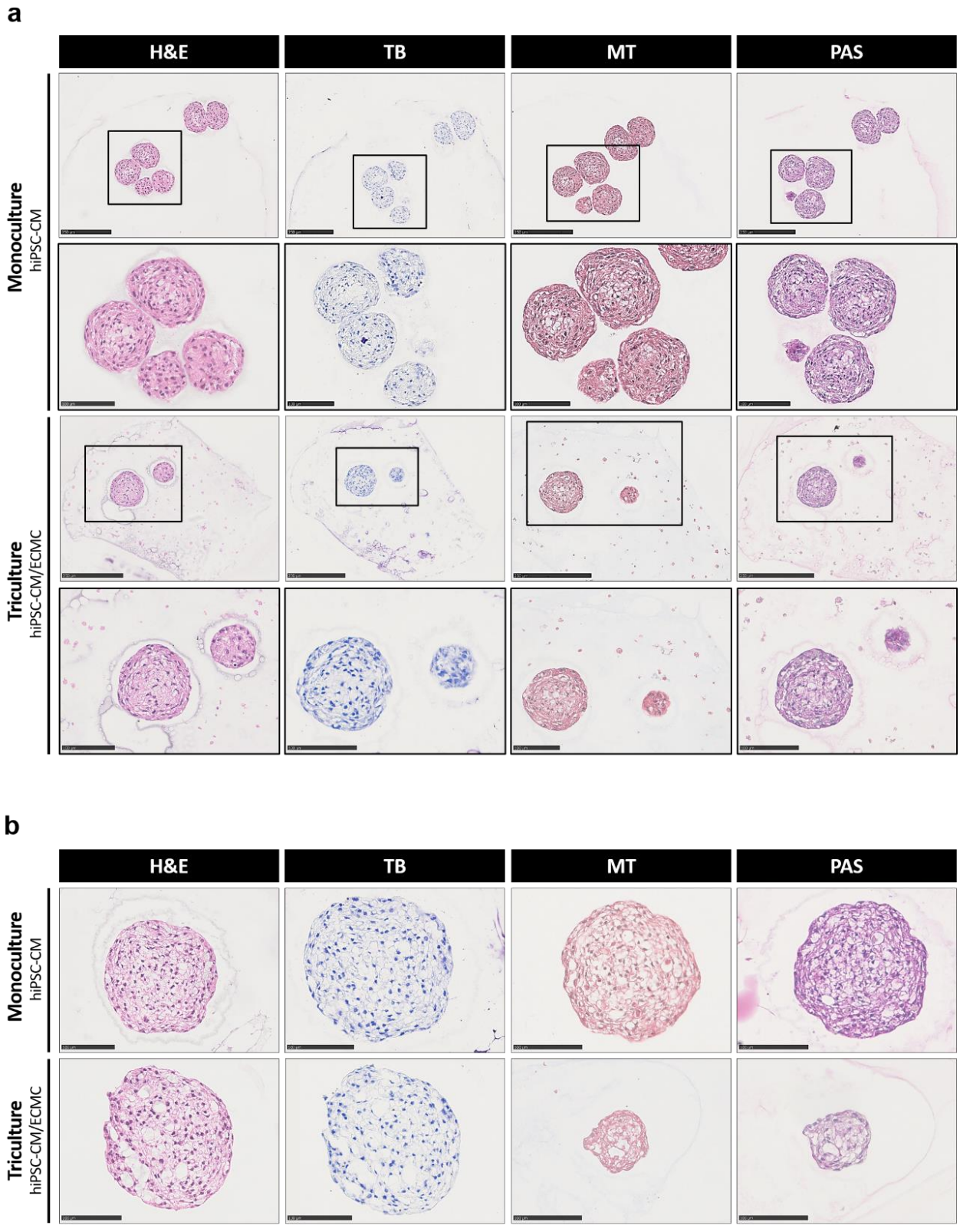

Figure 4.13 | Histochemistry and morphology analysis of mono- and tricultures from two separate experiments (Model #1-*a*–MCT-SF and Model #1-*b*–MCT-SF). (*a*-*b*) Histochemistry characterization of 3 µm thick paraffin sections of 3D hiPSC-CM **mono-** and 3D hiPSC-CM/ECMC **triculture** microcapsules, taken at the **endpoint** of the models (days 15 and 14 *post*-microencapsulation, respectively) and stained for **H&E**, **TB**, **MT** and **PAS**. Data are representative images from two independent experiments: (***a***, *upper panel*, Model #1-*a*–MCT-SF) and (***b***, lower *panel*, Model #1-*b*–MCT-SF). **(*a*)** Insets indicate high magnification images of the corresponding black rectangles. **Abbreviations** (*from top to bottom*): **Hematoxylin** and Eosin (**H&E**), **Toluidine Blue** (**TB**), **Masson Trichrome** w/ Aniline Blue (**MT**) and **Periodic Acid-Schiff** (**PAS**). **(*a*)** Scale bars, 250 µm; 100 µm in high magnification images. **(*b*)** Scale bars, 100 µm (in all images).

toto protocols; consult **4.4.1**) has proved to be a much more robust technique for determining ECM levels and visualizing single cells.

In addition to detecting a collagen content much smaller than those noticed via immunofluorescence, MT (**Fig.4.13**) and PSR (**Annex 4.2**, **Fig.S11**) stains did not distinguish it between mono- and tricultures.

Nonetheless, Picrosirius Red (PSR) (**Annex 4.2**, **Fig.S11**) is a relevant method, given that it allows the quantification of fibrillar type I and III collagens, via polarization microscopy[212,213] . This method was used only in the pilot experiment's monocultures (**Annex 4.2**, **Fig.S11**), as a routine characterization, since a broad microscopy-based phenotypic characterization toolbox and, particularly, that involving LSFM (consult **4.4.2.2**), which allows very faithful quantifications, was implemented later.

Finally, several cardiac models reported the use of some of these stains with analogous results. **Figtree *et al.* (2017)**[204] demonstrated an increased ECM deposition, via PSR stain, in cardiac spheroids used to model cardiac fibrosis[204]. **Siang Ong *et al.* (2017)**[214] showed the presence of collagen (via H&E and MT), indicating the deposition of ECM after printing of 3D cardiac patches, created from spheroids containing hiPSC-CM, hiPSC-EC and hiPSC-FB[214].

4.6. Functional evaluation: live cell calcium imaging

To determine the functionality and maturity of the Ca^{2+} handling apparatus of hiPSC-CM, in both mono- and tricultures, intracellular Ca^{2+} spontaneous and pharmacologically induced-transients, from two independent experiments (**Figs.4.14–4.17**), were recorded at the endpoint of the models. For the values of the different parameters of calcium handling kinetics, along with a list of selected videos, consult **Annex 5.1**, **Table S6** and **Table S7**, and **Annex 5.2**, **Fig.S12**, respectively.

4.6.1. Assessment of spontaneous whole spheroid intracellular Ca^{2+} transients

Whole spheroid intracellular Ca^{2+} spontaneous transients were observed in both models, indicating the presence of a functional hiPSC-CM calcium handling machinery (**Fig.4.14**, *mono*- and *triculture*; and **Fig.4.15*a*$_1$**, **Fig.4.15*b*$_1$**).

Looking at **Fig.4.14**, in comparison with monoculture, hiPSC-CM triculture's spontaneous calcium releases exhibited significantly higher peak to 50% (***; **Fig.4.14*f*** and **Annex 5.1**, **Table S6**) and to 80% (**; **Fig.4.14*g*** and **Annex 5.1**, **Table S6**) decay times and greater time between peaks (***; **Fig.4.14*h*** and **Annex 5.1**, **Table S6**), *i.e*. reduction of the beating rates (*; **Fig.4.14*i*** and **Annex 5.1**, **Table S6**). There were no significant statistical differences, from mono- to triculture, in the other parameters of calcium handling kinetics (*ns*; peak amplitude, upstroke velocity and rise to peak time; **Fig.4.14*b***, **Fig.4.14*c*** and **Fig.4.14*e***, correspondingly), with the exception of the decay velocity, which disclosed a significant reduction in triculture (*; **Fig.4.14*d*** and **Annex 5.1**, **Table S6**).

Taken together, **Model #1-*a*-MCT-SF**'s results (**Fig.4.14**, **Fig.4.15** and **Annex 5.1**, **Table S6**) showed slower calcium handling kinetics in the triculture model (**Fig.4.14*a***), as evidenced by the significant decrease in beating rate, from mono- to triculture (*; **Fig.4.14*i*** and **Annex 5.1**, **Table S6**), which may be correlated with a more mature Ca^{2+} handling apparatus in this model[96,152,215,216].

Also, in this experiment, we sought to investigate the pharmacological response profile of the human engineered cardiac tissues to a β_1-adrenergic receptor agonist (norepinephrine, 60 μM) (**Figs.4.14*b–i*** and **Fig.4.15**).

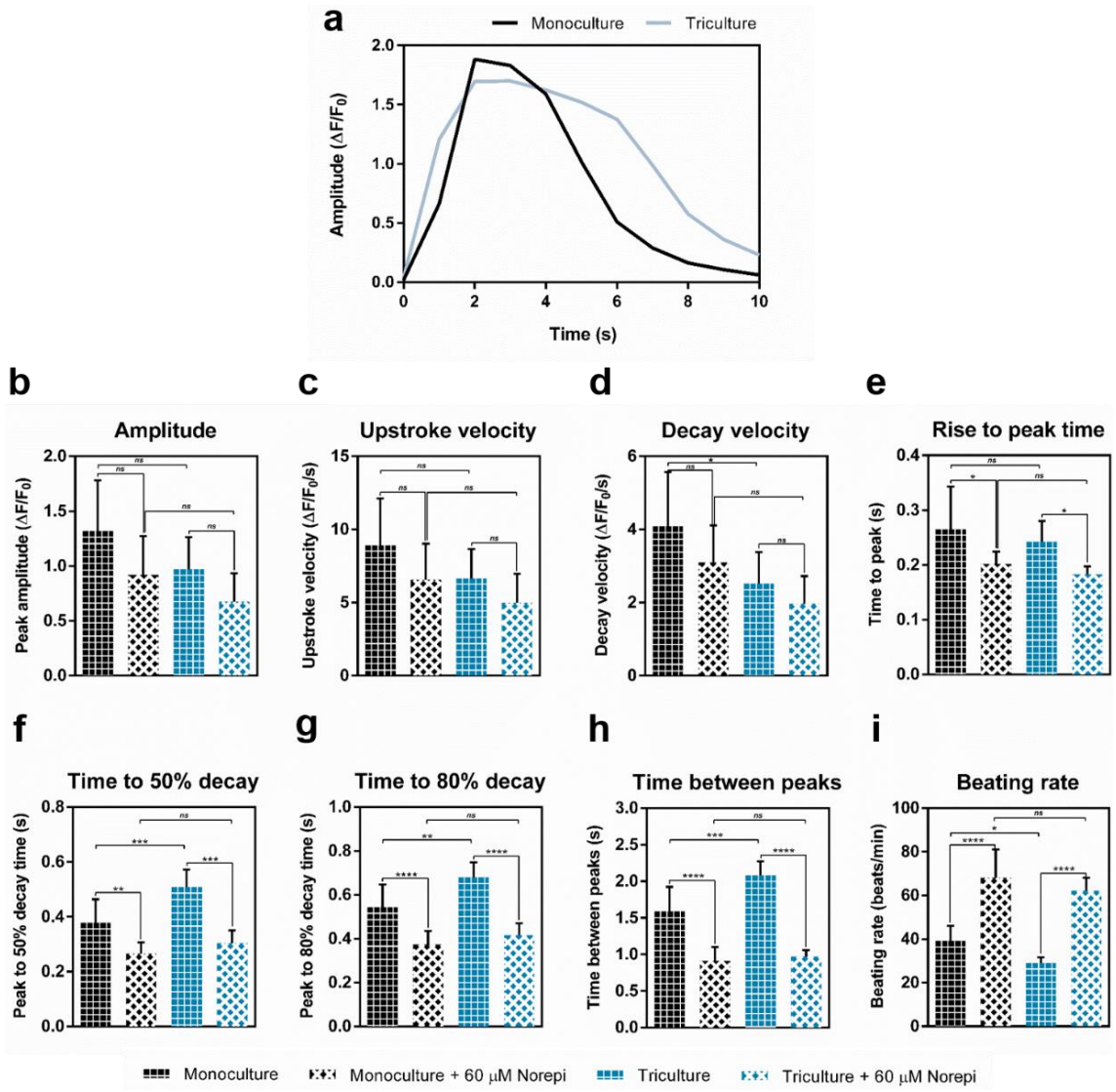

Figure 4.14 | Impact of a β1-adrenergic receptor agonist (norepinephrine) on hiPSC-CM functionality, in both mono- and tricultures, assessed by live cell calcium imaging (Model #1-*a*–MCT-SF). (***a***) Representative **tracing** of **calcium transients** (*upper panel*), in mono- and tricultures that weren't exposed to norepinephrine. (***b-i***) hiPSC-CM **calcium handling kinetics** (*lower panel*), in mono- and tricultures, in the absence and presence of 60 μM of norepinephrine. (***b***) **Amplitude**, (***c***) **upstroke** and (***d***) **decay velocities**, (***e***) **rise to peak time**, (***f***) **time** to **50%** and (***g***) **time** to **80% decay**, (***h***) **time between peaks** and (***i***) **beating rate**. Data are mean ± SD from one independent experiment. All kinetic parameters: *n* = 8-13. Ordinary one-way ANOVA analysis with Tukey's *post hoc* test for multiple comparisons (*ns* – not significant, **P* ≤ 0.05, ***P* ≤ 0.01, ****P* ≤ 0.001, *****P* ≤ 0.0001). All parameters refer to **15 days after microencapsulation**, for both mono- and triculture cardiac tissue models, under similar culture circumstances. **Abbreviations: *Norepi* –** Norepinephrine. **Caption:** *Mono-* and *Triculture* groups – conditions *w/o* drug exposure; *Monoculture + 60 μM Norepi* and *Triculture + 60 μM Norepi* – conditions exposed to norepinephrine.

Representative traces of Ca^{2+} transients in mono- and tricultures (**Fig.4.15**) revealed a comparable chronotropic response to norepinephrine, in both models, which translated into a significant decrease in rise to peak time (***** in both mono- and tricultures; **Fig.4.14*e*** and **Annex 5.1**, **Table S6**) and in peak to 50% (****** in mono- and ******* in tricultures; **Fig.4.14*f*** and **Annex 5.1**, **Table S6**) and to 80% (******** in both mono- and tricultures; **Fig.4.14*g*** and **Annex 5.1**, **Table S6**) decay times, in both mono- and tricultures; Fig.4.14g and Annex 5, Table S6) decay times; and, more importantly, a significant decrease in time between peaks (******** in both mono- and tricultures; **Fig.4.14*h*** and **Annex 5.1**, **Table S6**), meaning a matching increase in beating rate (******** in both mono - and tricultures; **Fig.4.14*i*** and **Annex 5.1**, **Table S6**).

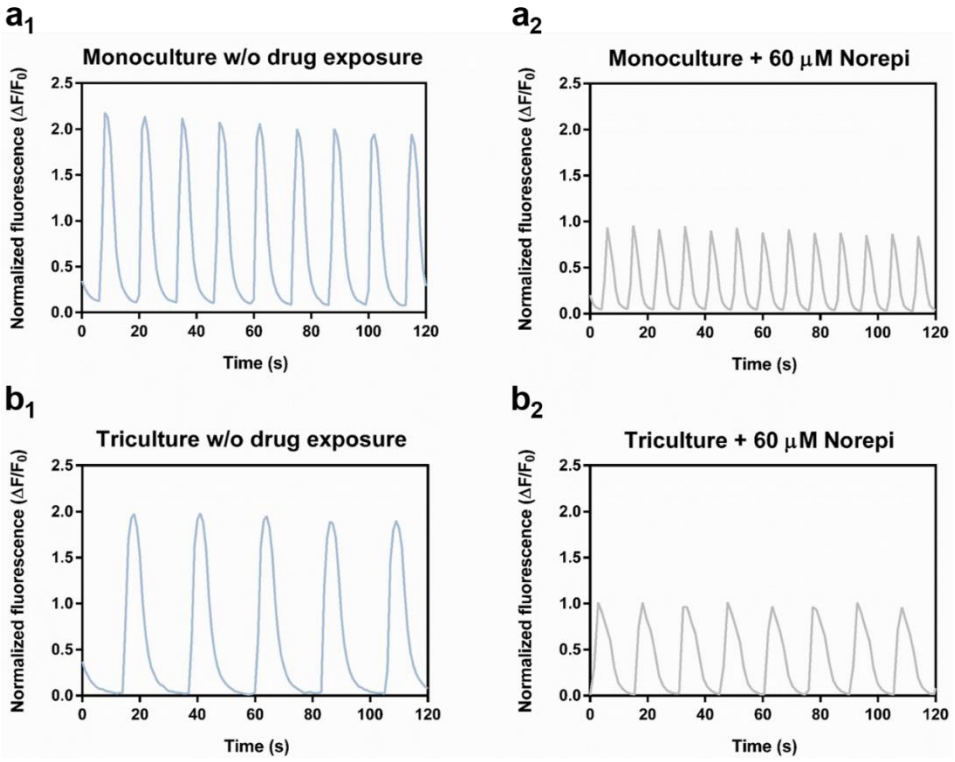

Figure 4.15 | hiPSC-CM revealed a positive chronotropic response to norepinephrine in mono- and triculture models (Model #1-*a*–MCT-SF). (***a*₁-*b*₂**) Representative **traces** of **Ca^{2+} transients** in mono- and tricultures, at **day 15** *post*-microencapsulation. (***a*₁, *b*₁**) (*Left panel*) **Ca^{2+} spontaneous release:** (***a*₁**) mono- and (***b*₁**) triculture *w/o* drug exposure. (***a*₂, *b*₂**) (*Right panel*) ***Norepi*-induced Ca^{2+} release:** (***a*₂**) mono- and (***b*₂**) triculture exposed to 60 μM of *norepi*. **Abbreviations: *Norepi* –** Norepinephrine.

The results obtained via exposure to norepinephrine are in line with those described in the literature for other α-[215] (*e.g.* phenylephrine) or β-adrenergic agonists[97,215] (*e.g.* isoproterenol), namely the shortening of the decay times[217] and the increased beating rates[97,215].

4.6.2. Evaluation of pharmacological responses to several cardioactive drugs

To assess the pharmacological and, in particular, the chronotropic responses (*i.e.* variations in the beating rate) of hiPSC-CM, in both mono- and tricultures, we treated the models with target cardioactive drugs, including 60 μM norepinephrine (β_1-adrenergic receptor agonist), 40 μM heptanol (gap junction uncoupler), 4 μM propranolol (non-selective β-blocker) and, finally, 4 μM propranolol and thereafter 60 μM norepinephrine. The concentrations tested are in the range reported by other studies as non-cytotoxic[97,215,218]. Exposure to cytotoxic chemotherapeutic drugs will be described in the ensuing topic. The mechanisms of action of the different cardioactive drugs tested are schematized in **Fig.4.17*a***.

Model #1-*b*-MCT-SF's calcium kinetic parameters, in the absence of pharmacological agents, show similar calcium kinetics (**Fig.4.17*a***) between both cardiac models, with a significant decrease, from mono- to triculture, in upstroke (****; **Fig.4.16*b*** and **Annex 5.1**, **Table S7**) and decay (***; **Fig.4.16*c*** and **Annex 5.1**, **Table S7**) velocities. There were no significant statistical differences, from mono- to triculture, in the other parameters of calcium kinetics (*ns*; peak amplitude, rise to peak time, peak to 50% and 80% decay time, time between peaks and beating rate; **Figs.4.16*b,e,f–i***, correspondingly). Hence, there does not appear to be significant differences in the maturation level amongst the two models.

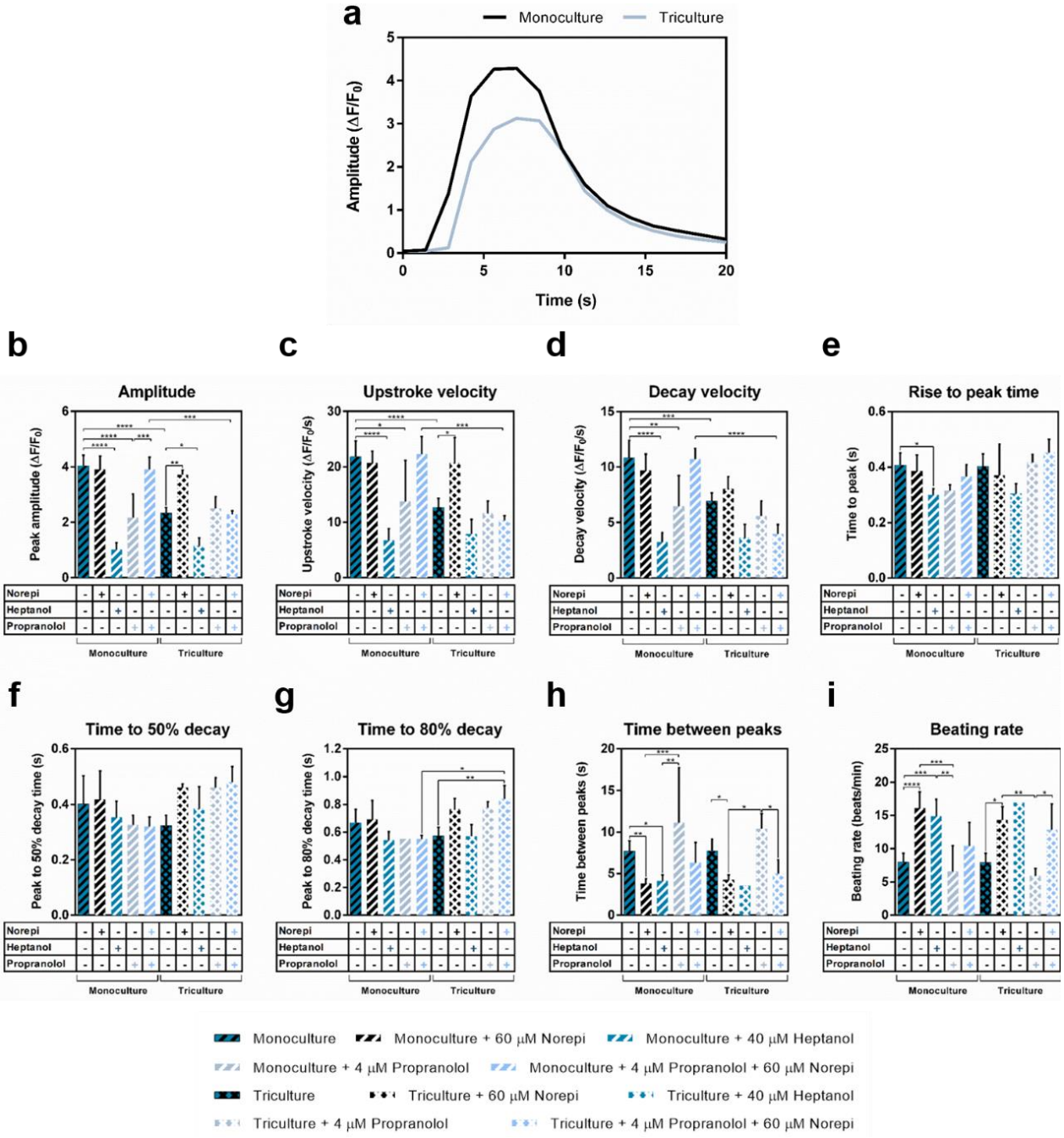

Figure 4.16 | hiPSC-CM, in both mono- and tricultures, have the ability to pharmacologically respond to different cardioactive drugs (norepinephrine, propranolol and heptanol) (Model #1-*b*–MCT-SF). (***a***) Representative **tracing** of **calcium transients** (*upper panel*), in mono- and tricultures *w/o* drug exposure. (***b-i***) hiPSC-CM **calcium handling kinetics** (*lower panel*), in mono- and tricultures, in the absence and presence of different cardioactive drugs. (***b***) **Amplitude**, (***c***) **upstroke** and (***d***) **decay velocities**, (***e***) **rise to peak time**, (***f***) **time** to **50%** and (***g***) **time** to **80% decay**, (***h***) **time between peaks** and (***i***) **beating rate**. Addition (+) and subtraction (-) signals (below the charts) indicate which drugs are present in a given combination (either in mono- or triculture). Data are mean ± SD from one independent experiment. All kinetic parameters: *n* = 2-8. Ordinary one-way ANOVA analysis with Tukey's *post hoc* test for multiple comparisons (**P* ≤ 0.05, ***P* ≤ 0.01, ****P* ≤ 0.001, *****P* ≤ 0.0001). All parameters refer to **14 days after microencapsulation**, for both mono- and triculture cardiac tissue models, under similar culture circumstances. **Abbreviations: *Norepi* –** Norepinephrine. **Caption:** *Mono-* and *Triculture* groups – conditions *w/o* drug exposure; *Monoculture + 60 μM Norepi* and *Triculture + 60 μM Norepi* – conditions exposed to the β_1-adrenergic receptor agonist, norepinephrine; *Monoculture + 40 μM Heptanol* and *Triculture + 40 μM Heptanol* – conditions exposed to the gap junction uncoupler, heptanol; *Monoculture + 4 μM Propranolol* and *Triculture + 4 μM Propranolol* – conditions exposed to the β-blocker, propranolol; and *Monoculture + 4 μM Propranolol + 60 μM Norepi* and *Triculture + 4 μM Propranolol + 60 μM Norepi* – conditions exposed to propranolol and thereafter to norepinephrine.

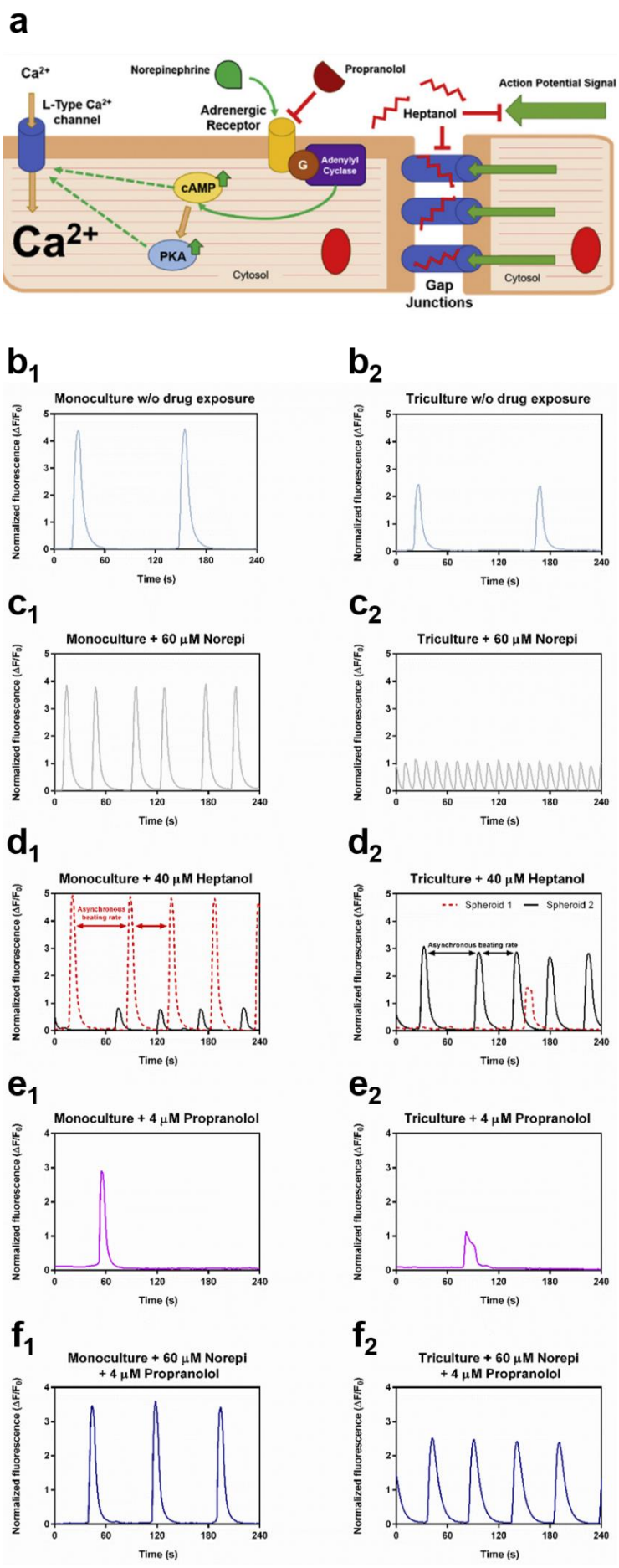

Figure 4.17 | Pharmacological responses of hiPSC-CM to different cardioactive compounds (norepinephrine, propranolol and heptanol), in mono- and triculture models (Model #1-*b*–MCT-SF). **(*a*) Scheme depicting the mechanisms of action of the cardioactive drugs tested: norepinephrine, propranolol and heptanol** [reproduced from Gouveia *et al.* (2017)[97]]. **(*b*$_1$-*f*$_2$)** Representative **traces** of **Ca^{2+} transients** in mono- and tricultures, at **day 14** *post*-microencapsulation. **(*b*$_1$, *b*$_2$) Ca^{2+} spontaneous release:** **(*a*$_1$)** mono- and **(*b*$_1$)** triculture *w/o* drug exposure. **(*c*$_1$, *c*$_2$) *Norepi*-induced positive chronotropic response:** **(*c*$_1$)** mono- and **(*c*$_2$)** triculture exposed to 60 µM of *norepi*. **(*d*$_1$, *d*$_2$) Heptanol-induced uncoupling of cardiac gap junctions:** **(*d*$_1$)** mono- and **(*d*$_2$)** triculture exposed to 40 µM of heptanol. **(*e*$_1$, *e*$_2$) Propranolol-mediated negative chronotropic response:** **(*e*$_1$)** mono- and **(*e*$_2$)** triculture exposed to 4 µM of propranolol. **(*f*$_1$, *f*$_2$) Propranolol and *norepi* dual response:** **(*f*$_1$)** mono- and **(*f*$_2$)** triculture exposed to 4 µM of propranolol and thereafter to 60 µM of norepinephrine. **Abbreviations: *Norepi*** – Norepinephrine.

As discussed for **Model #1-*a*-MCT-SF**, in **Model #1-*b*-MCT-SF**, hiPSC-CM revealed a positive chronotropic response to norepinephrine, in both models, evinced by the significant decrease in time between peaks (** in mono- and * in tricultures; **Fig.4.16*h***, **Figs.4.17*b*$_1$,*b*$_2$,*c*$_1$,*c*$_2$** and **Annex 5.1**, **Table S7**) and the agreeing increase of beating rate (**** in mono- and * in tricultures; **Fig.4.16*i***, **Figs.4.17*b*$_1$,*b*$_2$,*c*$_1$,*c*$_2$** and **Annex 5.1**, **Table S7**).

In addition, similarly to what has been described in the literature for β-adrenergic receptor repression[97], propranolol-mediated negative chronotropic response appears to occur in both cardiac models, although the differences were not statistically significant. Specifically, representative traces of Ca^{2+} transients in mono- and tricultures (**Figs.4.17*b*$_1$,*b*$_2$,*e*$_1$,*e*$_2$**) appear to indicate, as expected, results opposing to norepinephrine's: increase in time between peaks (**Fig.4.16*h*** and **Annex 5.1**, **Table S7**) and corresponding decrease in beating rate**s** (**Fig.4.16*i***, **Figs.4.17*b*$_1$,*b*$_2$,*e*$_1$,*e*$_2$** and **Annex 5.1**, **Table S7**).

Remarkably, the low frequency of beatings induced by propranolol is recovered by the addition of norepinephrine, that reinstates the basal beating rates (values of mono- and tricultures w/o drug exposure). Thus, we can say the combined responses of the antagonist followed by addition of the β_1-adrenergic receptor agonist turn out to have a null balance.

Propranolol and *norepi* dual response is characterized by a significant decrease in time between peaks (* in tricultures; **Fig.4.16*h*** and **Annex 5.1**, **Table S7**) and a matching increase in beating rates (* in tricultures; **Fig.4.16*i***, **Figs.4.17*b*$_1$,*b*$_2$,*f*$_1$,*f*$_2$** and **Annex 5.1**, **Table S7**). These tendencies were found in both models but were only statistically relevant for the triculture.

Lastly, upon the treatment with the cardiac gap junction uncoupler heptanol, hiPSC-CM, in both models, revealed asynchronous beating rates (**Figs.4.17*b*$_1$,*b*$_2$,*d*$_1$,*d*$_2$** and **Annex 5.1**, **Table S7**) with peak amplitudes significantly lower (**** in mono- and * in tricultures; **Fig.4.16*b***, **Figs.4.17*b*$_1$,*b*$_2$,*d*$_1$,*d*$_2$** and **Annex 5.1**, **Table S7**), when compared to the *w/o drug exposure* counterparts.

As shown by **Gouveia *et al*. (2017)** a low concentration of heptanol reduces the propagation of action potentials in hiPSC-CM[97]. Higher concentrations (not tested) would probably completely block the beating rates.

All told, these observations indicate that β-adrenergic receptors (through stimulation or repression) and gap junction proteins were appropriately expressed on both models; yet, with respect to the pharmacological responses, only a few significant differences, not necessarily suggestive of a higher cardiac maturation in the triculture, were found between the two cardiac models.

4.7. Functional evaluation: chemotherapeutic drug-induced cardiotoxicity

In clinical settings, a large majority of anticancer drugs may induce cell death of cardiomyocytes in some patients within hours of intravenous administration[11,21,22,219,220].

As a *proof-of-concept* that the 3D mono- and triculture cardiac tissue models' setup allow the study of the effect of cardiotoxic drugs, we challenged them with the anthracycline doxorubicin and the taxane paclitaxel, two chemotherapeutic drugs with widely reported cardiotoxicity[13,19,21].

hiPSC-CM survival upon doxorubicin or paclitaxel treatment was determined via FDA-PI live/dead double staining (**Fig.4.18*a***) and *PrestoBlue* resazurin-based dye assay (for metabolic activity quantification; **Fig.4.18*b***). To this end, hiPSC-CM in, both mono- and tricultures, were exposed to an increasing concentration gradient, in the micromolar range (0 – *Control*, 1, 10 and 100 μM), using single dosing (exposure at the endpoint of both models for of 72-hour duration).

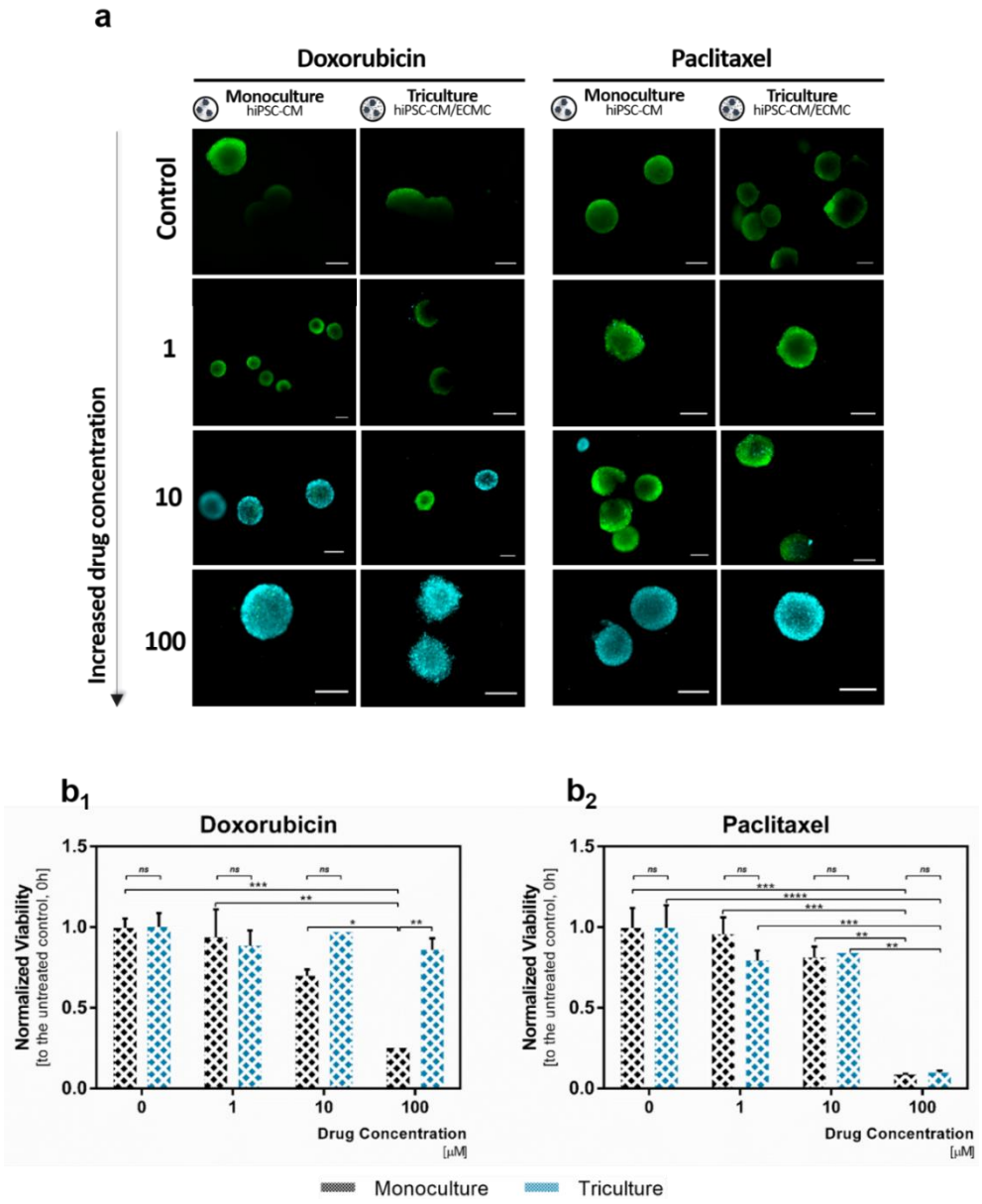

Figure 4.18 | 72-hour treatment of hiPSC-CM, in mono- and triculture cardiac tissue models, with increasing doses of cardiotoxic anticancer drugs (doxorubicin and paclitaxel) (Model #1-*b*–MCT-SF). (*a*) Assessment of 3D hiPSC-CM **mono-** and 3D hiPSC-CM/ECMC **triculture** cardiac tissue models' **cell viability**, through a **live/dead** assay, after **72 h** of exposure (corresponding to day 17 *post*-microencapsulation) to **cardiotoxic anticancer drugs** (**doxorubicin** and **paclitaxel**) (*from left to right*: doxorubicin and paclitaxel-induced cardiotoxicity, in mono- and tricultures, respectively; *from top to bottom*: *control* condition, indicating 0 μM, and increasing drug concentrations). Cultures were stained with **FDA** (fluorescein diacetate) – **live** cells, **green**, and **TO-PRO-3 Iodide** – **dead** cells, **cyan**. Scale bars, 200 μm. **(*b*)** Effect of **doxorubicin** (**b_1**) and **paclitaxel** (**b_2**) (**72-hour** treatment) on hiPSC-CM **viability**, in **mono-** and **triculture** models, using a ***PrestoBlue*** resazurin–based dye assay. Data are mean ± *SEM* from one independent experiment and consist of three technical replicates ($n = 3$). Ordinary two-way ANOVA analysis with Tukey's and Sidak's *post hoc* tests for multiple comparisons (*ns* – not significant, $^*P \leq 0.05$, $^{**}P \leq 0.01$, $^{***}P \leq 0.001$, $^{****}P \leq 0.0001$). 72 and 0 h fluorescence intensity values (*RFU*, relative fluorescence units) were initially normalized per spheroid. Final *RFU* values are the quotient between 72 and 0 h (untreated controls). Excitation and emission wavelengths were 560 and 590 nm, respectively; gain was 176.

As a result, doxorubicin and paclitaxel induced cell death (as seen by the intensification in TO-PRO-3's cyan staining) in a dose-dependent manner (**Fig.4.18*a***). Besides, FDA-PI results also show us that, after a 72h exposure at a concentration of 100 μM, cell viability was reduced to practically zero (**Fig.4.18*a***), given that all the spheroids express TO-PRO-3.

Nonetheless, when metabolic activity is evaluated, the results appear to differ from those of FDA-PI (**Fig.4.18*b*$_1$**; triculture condition).

PrestoBlue's results confirm that doxorubicin significantly reduced the cell viability in the monoculture in a dose-dependent manner. Furthermore, at a 100 µM concentration, only approximately 25% of hiPSC-CM remained viable in this model (**Fig.4.18*b*$_1$**; monoculture condition). However, contrariwise to FDA-PI assessment, *PrestoBlue*'s demonstrate that 100 µM (highest concentration tested) is not sufficient to induce substantial cardiotoxicity effects in triculture's hiPSC-CM. There were no statistically significant differences in the concentrations studied (**Fig.4.18*b*$_1$**; triculture condition). This could be owing to a cardioprotective effect of the non-myocyte populations (*e.g.* hiPSC-EC) on hiPSC-CM[25,28,35,53], nevertheless we have not conducted any study to show that this is indeed the case.

On the other hand, the fact that we are working with encapsulated models and in a 3D configuration translates, in practical terms, into extra diffusion barriers and a higher cellular organization level, which may cause us to adopt, in the future, a wider range of concentrations. Several studies have been reporting that concentrations of anticancer drugs in the micromolar and nanomolar range are sufficient to perceive appreciable effects on cell viability[22,219–224]. However, these values are usually related to hiPSC-CM monolayers[219,221] or even to co-cultures[22], but in a 2D configuration[22].

Paclitaxel-induced cardiotoxicity was obvious and translated into a significant decrease in cell viability while drug concentration increased (**Fig.4.18*b*$_2$**; mono- and tricultures). Also, the results seem to follow those of the FDA-PI (**Fig.4.18*a***, Paclitaxel). At a concentration of 100 µM, hiPSC-CM display a viability of about 9%, in the monoculture, and approximately 10%, in the triculture. For each pair of concentrations, no significant differences, between mono- and tricultures, were detected.

Overall, these findings are still very premature and lack validation, but the generated models demonstrate potential to be applied in the *in vitro* screening of chemotherapeutic drugs. In the future, these results may be complemented with gene expression profiling of relevant biomarkers, ATP levels determination, proteomics/metabolomics or live cell calcium imaging in which these drugs are used in non-cytotoxic concentrations.

4.8. Hydrogel-based scaffold characterization

4.8.1. FS-AFM mechanobiological properties indicate a dynamic remodelling of the cardiac microenvironment in the triple model

RGD-peptide coupled alginate microcapsules' mechanobiological properties were studied using atomic force microscopy (AFM) in three distinct conditions: (i) scaffold alone (in the absence of cells), (ii) construct encapsulating monocultures or (iii) construct encapsulating tricultures, as depicted in **Fig.4.19*a***.

AFM 2D and 3D phase (**Fig.4.19*b*** and **Annex 6**, **Fig.S13*a***, for high magnification images) and topographical imaging (**Fig.4.19*c*** and **Annex 6**, **Fig.S13*b***, for high magnification images) evidenced an alginate porous surface structure, displaying some inhomogeneity, primarily in the microcapsule constructs containing mono- and tricultures (**Fig.4.19** and **Annex 6**, **Fig.S13**, for high magnification images; *mono-* and *triculture* conditions), which appears to be a first signal that *cell-to-scaffold* contacts do indeed exist. Also, these contacts may play a key role in biomaterial composition changes. Moreover, resorting to AFM images, a microcapsule average pore diameter, corresponding to 579.6 ± 137.0 nm (**Fig.4.19*e*** and **Annex 6**, **Table S8**) was determined.

Furthermore, to provide insight into these *cell-to-scaffold* contacts, a set of relevant biomechanical parameters, correlated with a makeover of the cardiac microenvironment[108,159], was quantified via Force

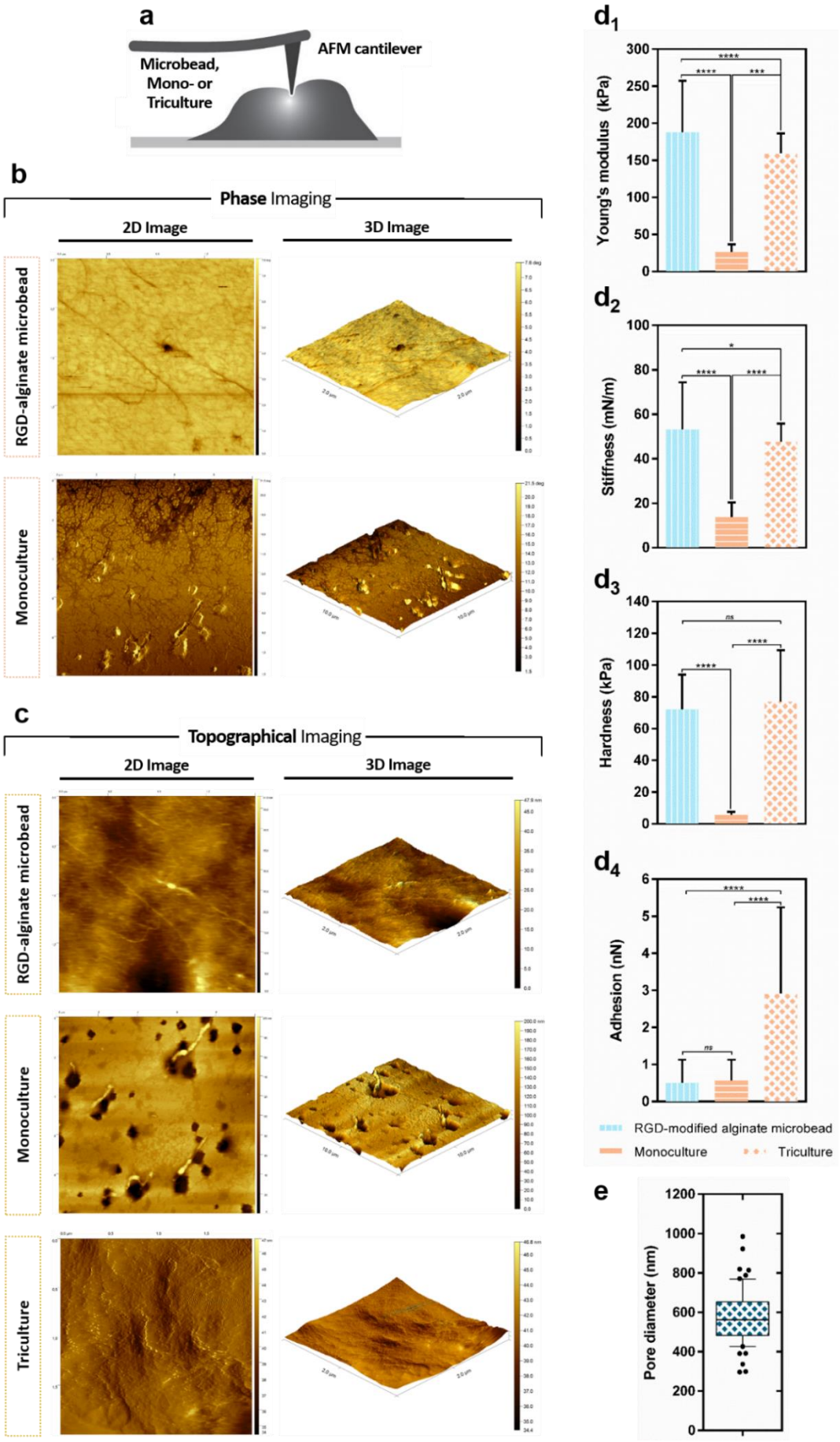

Figure's caption is shown on the following page

Figure 4.19 | FS-AFM characterization of the microcapsule *scaffold*, as well as the 3D cardiac cell-based models, biomechanical behaviour. (*a*) Scheme illustrating the contact between AFM cantilever tip and empty RGD-alginate microbead, mono- or triculture, resulting in a given measurement of force [adapted from **Liu *et al*. (2012)**[159]]. **(*b-c*) AFM 2D** and **3D images** (*left panel*) of **RGD-alginate microbead**, **mono-** and **triculture** (wet scanning), referring to the **endpoint** of the models (days 15 or 14 *post*-microencapsulation). **(*b*)** AFM 2D and 3D **phase imaging** of RGD-alginate microbead and monoculture. **(*c*)** AFM 2D and 3D **topographical imaging** of RGD-alginate microbead, mono- and triculture. **(*b-c*)** A scan area of 4 μm^2 (*size*: 2 x 2 µm), for RGD-alginate microbead and triculture, and 100 μm^2 (*size*: 10 x 10 µm), regarding monoculture, were used. For high magnification images, consult **Annex 6**, **Fig.S13**). **(d_1-d_4) FS-AFM**-based **mechanobiological properties** (*right panel*) of the **microbead *scaffold*** and **mono-** and **triculture** cardiac tissue models (**endpoint** quantification). **(d_1) Young's modulus** (n = 63-80), **(d_2) Stiffness** (n = 63-80), **(d_3) Hardness** (n = 71-81) and **(d_4) Adhesion** (n = 69-77)**.** Data are mean ± SD from one independent experiment (**Pilot Model–M-SF**), for RGD-alginate microbead, and two (**Model #1-*a*–MCT-SF** and **Model #1-*b*–MCT-SF**), for mono- and triculture. Ranked one-way ANOVA analysis (Kruskal-Wallis nonparametric test) with Dunn's *post hoc* test for multiple comparisons (*ns* – not significant, *$P \leq 0.05$, ***$P \leq 0.001$, ****$P \leq 0.0001$). **(*e*)** Boxplot representing the biomaterial **pore diameter** (n = 61). *Whiskers*: 10-90 percentile. *Outliers*: plotted as discrete points. Data are mean ± SD from two independent experiments (**Pilot Model–M-SF Model** and **Model #1-*a*–MCT-SF**).

Spectroscopy mode-AFM (**FS-AFM**), for the scaffold alone and for mono- and triculture cardiac tissue models (endpoint quantification) (**Figs.4.19d_1–d_4**; Young's modulus, stiffness, hardness and adhesion, correspondingly). The values obtained for these parameters are summarized in **Annex 6**, **Table S8**.

The calcium alginate microcapsule biomaterial alone demonstrated a Young's modulus (also known as elastic modulus) corresponding to 188.0 ± 69.38 kPa, significantly higher than that of both cardiac models (****; **Fig.4.19d_1** and **Annex 6**, **Table S8**).

Considering that Young's modulus measures an object's resistance to being deformed elastically (*i.e*. non-permanently), this seems to indicate that the microenvironment in the presence of the cells is less stiff, when compared to the biomaterial alone. In addition, in comparison to monoculture, **triculture's** Young's modulus is significantly higher (***; **Fig.4.19d_1** and **Annex 6**, **Table S8**; *triculture*: 159.3 ± 27.27 kPa and *monoculture*: 26.24 ± 10.44 kPa), which is consistent with a remodelling of the cardiac microenvironment from mono- to triculture, with the latter exhibiting a less plastic (*i.e*. stiffer) microenvironment. This can be explained by the fact that non-myocyte populations (mostly hiPSC-MC and, in particular, CFs) contribute to a higher ECM production in the tricultures, as proved earlier (consult **4.4.2**). In this context, **Stevens *et al*. (2009)** showed that the stiffness of multicellular cardiac patches derived from hESC-CM, MEFs and HUVECs was 4-fold higher than those composed of CMs only[115], which matches our results.

Given that Young's modulus is a measure of stiffness, stiffness' results (**Fig.4.19d_2**) exhibit a pattern consistent with those discussed so far: (i) microcapsule scaffold alone exhibited a significantly superior stiffness compared to mono- and triculture values (53.12 ± 21.29 mN/m, **** *vs*. mono and * *vs*. triculture; **Fig.4.19d_2** and **Annex 6**, **Table S8**); and (ii) significantly higher triculture's stiffness, in comparison to that of the monoculture (****; **Fig.4.19d_2** and **Annex 6**, **Table S8**; *triculture*: 47.79 ± 8.074 mN/m and *monoculture*: 13.63 ± 6.653 mN/m).

Hardness' results also showed a similar tendency, without significant differences between the scaffold and the triple model (*ns*; **Fig.4.19d_3** and **Annex 6**, **Table S8**). Besides, monoculture's hardness is lower than the rest (5,737 ± 1,718 kPa; **** *vs*. both RGD-modified alginate microbead and triculture; **Fig.4.19d_3** and **Annex 6**, **Table S8**).

Noteworthy, the **adhesion** between the AFM tip and the biomaterial in the triple model (although with some dispersion of adhesion values) was significantly higher when compared to the others (2,913 ± 2,326 nN, **** *vs*. both RGD-modified alginate microbead and monoculture ; **Fig.4.19d_3** and **Annex 6**, **Table S8**), which is consistent with the hypothesized remodelling of the cardiac microenvironment from mono- to triculture. A higher adhesion may also be owing to the interaction of CFs with the scaffold via RGD motifs.

In sum, our hydrogel-based scaffold seems to be suitable to recapitulate the human heart microenvironment[23], since hPSC-CM maturation is favoured on substrates with an elasticity within the same order of magnitude as that of the human cardiac muscle (Young's modulus of 10-15 kPa)[14,23,25].

4.8.2. Biomaterial ultrastructure and spheroids structure

TEM imaging was conducted in order to characterize the ultrastructure of the scaffold microcapsule in the absence of cells.

TEM micrographs (**Fig.4.20*a*** and **Fig.4.20*a*$_1$**) demonstrate that RGD-peptide coupled alginate hydrogels are mesh-like, fibrous networks with a nanosized pore structure, agreeing with AFM results (**Fig.4.19*e***). This TEM pattern is similar to that found by **Hsiong *et al*. (2008)** in RGD-modified alginate disks[148].

On the other hand, to complement the structure and ultrastructure results obtained for hiPSC-CM spheroids (consult **4.5**), scanning electron microscopy (SEM) was employed.

The spheroids exhibit a solid and compact structure, as well as a topography with some heterogeneity (**Fig.4.20*b***), in which *cell-to-cell* contacts can be discerned in higher magnification images (**Fig.4.20*b*$_1$**). This topography is similar to those observed by **Horton and Auguste (2012)** on spheroids with ECM deposited on their surface[225], demonstrating that the ours are surrounded by an outer layer of ECM, agreeing with the performed immunofluorescence characterizations (consult **4.4.2**).

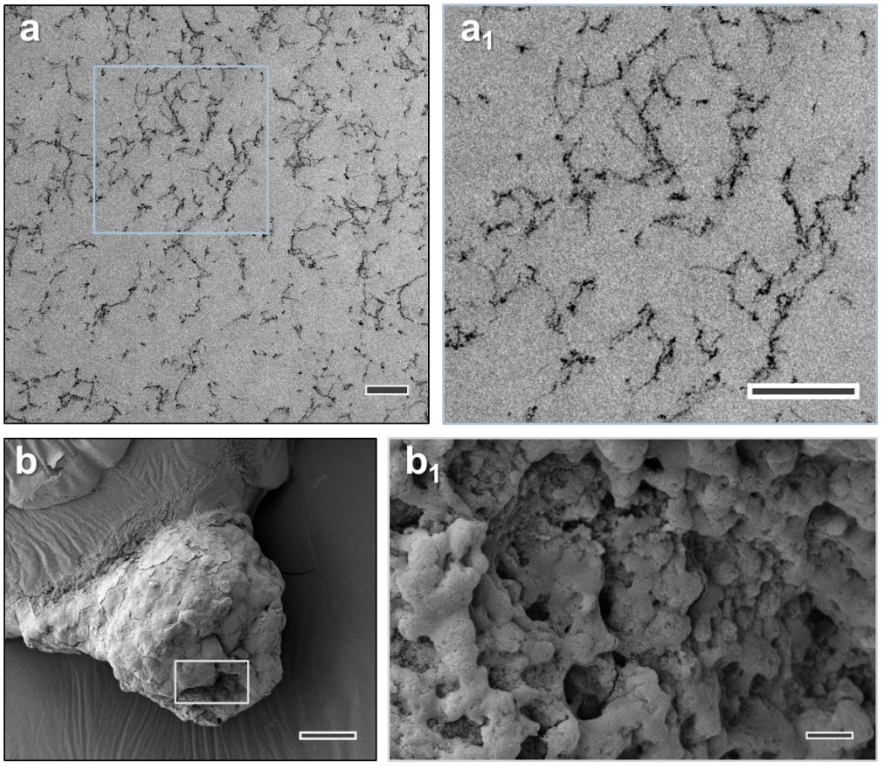

Figure 4.20 | Biomaterial ultrastructure and hiPSC-CM spheroids structure characterization. (*a*-*a*$_1$) Representative **TEM** micrographs (*upper panel*) of an **empty RGD-modified calcium alginate microbead** (**50%** of **RGD** peptide-coupled alginate), at **day 15** *post*-microencapsulation. **(*b*-*b*$_1$)** Representative **SEM** micrographs (*lower panel*) of a **hiPSC-CM spheroid**, at **day 15** after microencapsulation. **(*a*$_1$, *b*$_1$)** Insets indicate high magnification images of the corresponding cyan or grey rectangles. **(*a*-*a*$_1$)** *TEM*: Scale bars, 500 nm (in both images). **(*b*-*b*$_1$)** *SEM*: Scale bars, 50 µm; 500 nm in high magnification images.

4.9. Scalability approaches using stirred-tank bioreactors

To perform the upscaling of the 3D cardiac tissue models (consult **3.5**), a *proof-of-concept*, using, as a culture system, small-scale stirred-tank bioreactors (STBRs), operating in perfusion, was carried out.

As illustrated in **Fig.4.21*a***, the pursued strategy is, in all respects, similar to that hitherto described (consult **4.1**), including a first aggregation step, in which hiPSC-CM are inoculated as a single cell suspension, with the aim of forming cardiac spheroids (**Fig.4.21*a***). Nevertheless, the aggregation process,

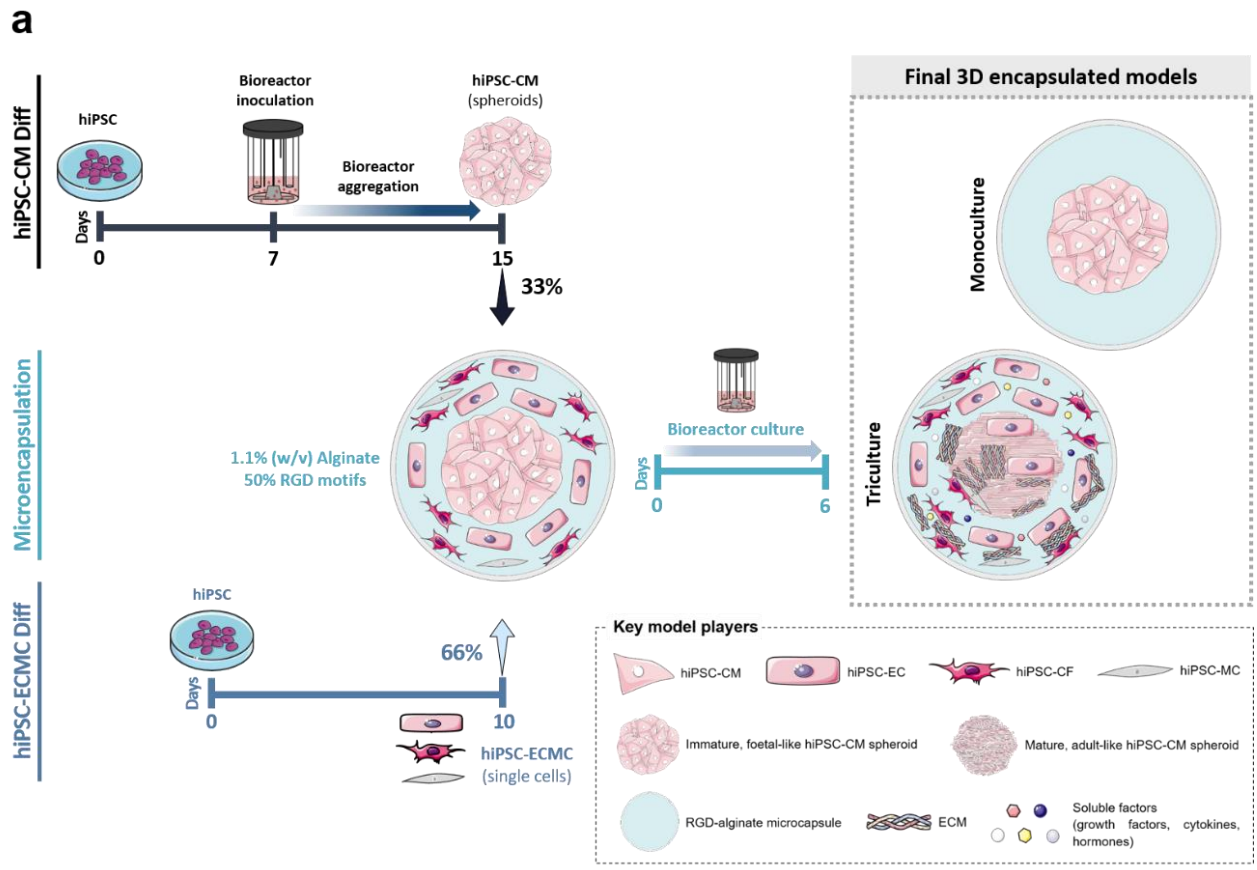

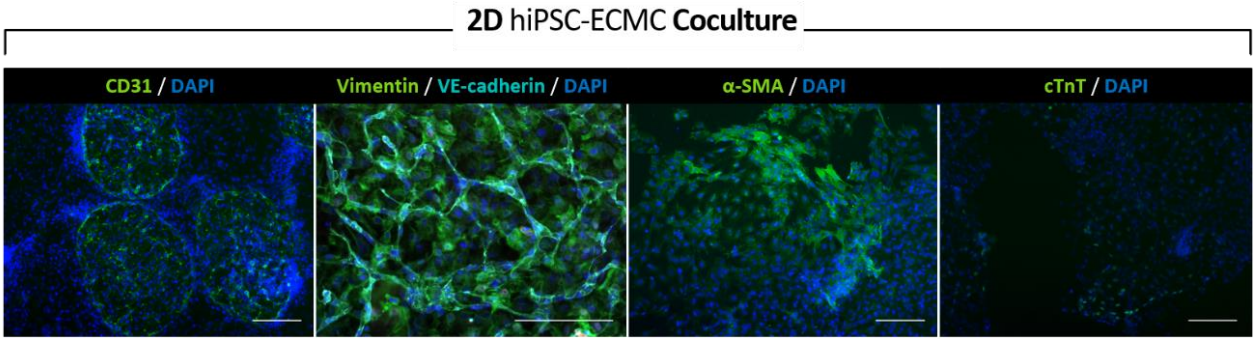

Figure 4.21 | Bioreactor experimental strategy and phenotypic characterization of the 2D hiPSC-ECMC co-culture, prior to microencapsulation. (***a***) Schematic overview of the **bioreactor culture strategy** (*upper panel*) for obtaining the **final 3D triculture** hiPSC-derived **cardiac** tissue **model**, as well as for the 3D monoculture control. Defined cardiovascular cell populations (hiPSC-CM spheroids and hiPSC-ECMC) were systematically differentiated from hiPSC. Representations of the models are not to scale. The key model players are also exhibited. (***b***) **Wide-field immunofluorescence** microscopy representative images (*lower panel*) of the **2D hiPSC-ECMC co-culture**, at day 10, prior to microencapsulation. 2D hiPSC-ECMC immunostained (*from left to right*) for the **endothelial** markers **CD31** (**green**) and **VE-cadherin** (**cyan**), for the **mesenchymal** markers **Vimentin** and **α-SMA** (**green**) and for the cardiac marker **cTnT** (**green**), as negative control. Nuclei were counterstained with **DAPI** (**blue**). Scale bars, 200 μm.

in view of a more straightforwardly scalable and reproducible process[51,139,226], was done in STBRs (**Fig.4.21*a***).

Subsequently, it was further possible to carry out the microencapsulation step, in one (**Model #2-*b*-MT-BR-2**) of the two bioreactor independent experiments performed, producing microencapsulated mono- and tricultures (**Fig.4.21*a***, *right*), under conditions analogous to those described in **3.2** and **4.1**. Owing to the fact that this was still an opening study, in which the focal goal was to increase the scale of the previously established models and not properly study the differences between mono- and tricultures, the 3D cardiac tissue models were only kept in culture for 6 days (**Fig.4.21*a***)

In the same way to what has been demonstrated beforehand (consult **4.1** and **Fig.4.2*f***), 2D hiPSC-ECMC co-culture phenotype was assessed via immunofluorescence, prior to microencapsulation (**Fig.4.21*b***). The results were similar to those already attained, which attests the robustness of hiPSC-ECMC differentiation process: (i) presence of an endothelial population (CD-31$^+$ and VE-cadherin$^+$; **Fig.4.21*b***) and, (ii) in greater number, a mesenchymal one (Vimentin$^+$ and α-SMA$^+$; **Fig.4.21*b***). Neither hiPSC-EC nor hiPSC-MC express cTnT (negative control) cardiac marker, proving the absence of hiPSC-CM in culture (**Fig.4.21*b***).

Noteworthy, the FC results, shown in **4.2**, **Figs.4.2*a-c*** (hiPSC before differentiations, as well as hiPSC-CM and hiPSC-ECMC, prior to microencapsulation, correspondingly), already include the bioreactor experiments.

4.9.1. hiPSC-CM aggregation dynamics in STBRs

hiPSC-CM aggregation profile in STBRs, concerning two biologically independent experiments (**Model #2-*a*–BR-1** and **Model #2-*b*–MT-BR-2**; for further detail, consult **List of Models**), was studied in terms of cell viability (FDA-PI live/dead assay; **Figs.4.22*a,c***, *left panel*) and spheroid size (**Figs.4.22*b,d***, *right panel*), from day 7 (inoculation) until day 18 (last day prior to microencapsulation).

Albeit hiPSC-CM spheroids have remained viable during the culture time (**Fig.4.22*a***), in the case of the first experiment (**Model #2-*a*–BR-1**) it is possible to note a low cell density (**Fig.4.22*a***), reduced average spheroid diameters (*e.g*. 97.58 ± 40.32 µm at day 18; **Fig.4.22*b***) and a high size dispersion (**Fig.4.22*b***).

As discussed in **4.1**, the difficulty in controlling spheroid size dispersion is the main drawback of STBRs, in comparison to *AggreWell*™ plates, which allow the generation of hiPSC-CM with a very reproducible size. We attempted to mitigate this factor by adjusting the stirring rate (shown in FDA-PI images; **Figs.4.22*a,c***, *left panel*), in order to control the aggregation process and maintain an average spheroid diameter as homogeneous as possible: in the case of **Model #2-*a*–BR-1**, stirring rates between 60 and 70 *rpm*, together with a dilution rate of 0.30 day^{-1} (consult **Annex 7**, **Table S9**), were found to be inadequate to uphold an homogeneous spheroid size.

On the basis of these first results, a new *batch* (**Model #2-*b*-MT-BR-2**) was carried out, in which higher stirring rates, between 80 and 90 *rpm*, were used, while the dilution rate was maintained (consult **Annex 7**, **Table S9**). This gave rise to a noticeable increase in cell density over time, without compromising spheroid viability (**Fig.4.22*b***), and led to higher average spheroid diameters (*e.g*. 132.2 ± 52.80 µm at day 18, **Fig.4.22*d***). However, there was still a high size dispersion (**Fig.4.22*b***), so the process still lacks some optimization.

Cell concentration, over the 12 days of aggregation (from day 7 to day 18) shows a comparable profile in both experiments, with a decrease in cell concentration in the first days of aggregation (days 7 and 8), which later stabilized until day 18 (**Fig.4.23*a***). These results agree with those of FDA-PI, displaying a 6.75-

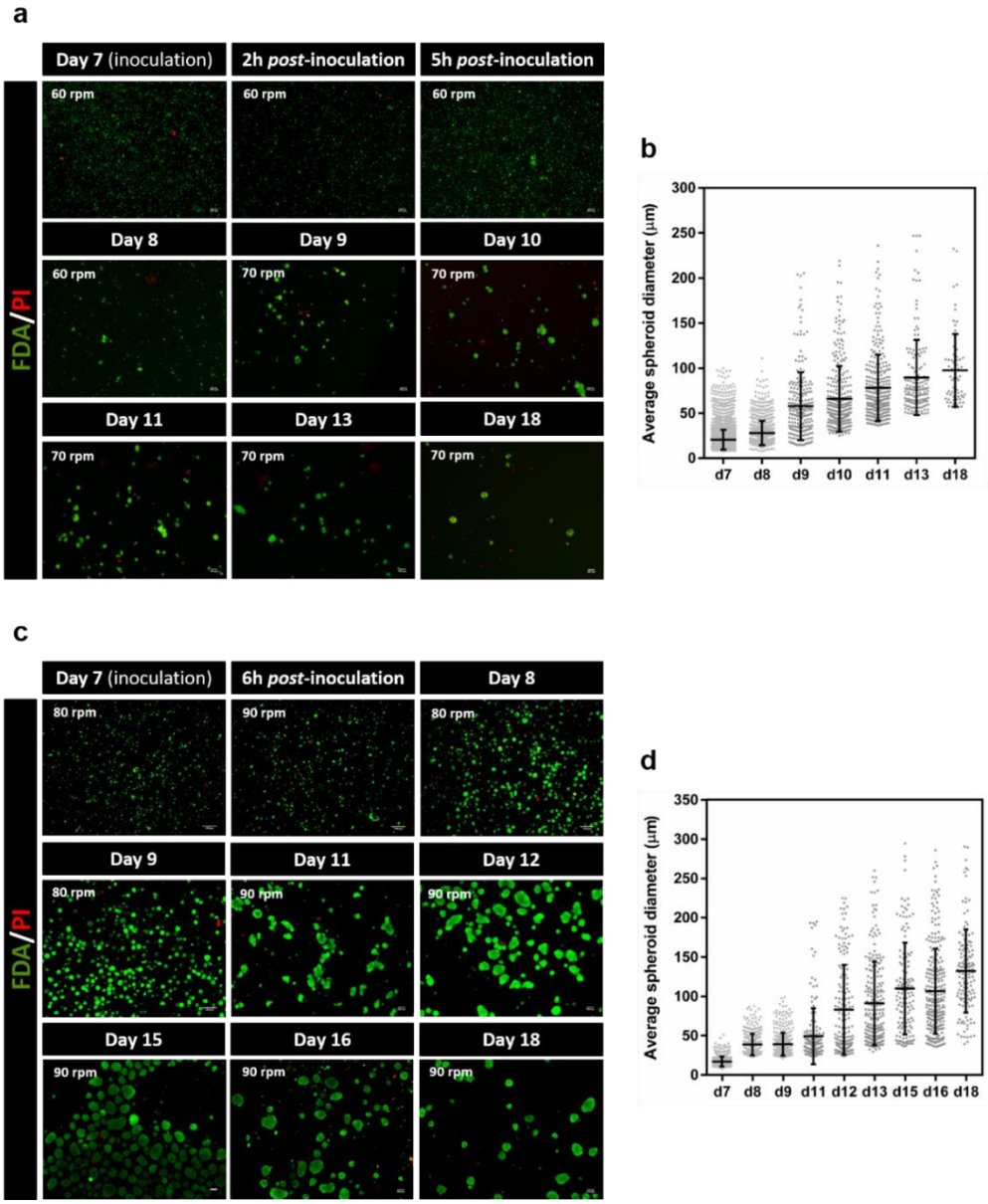

Figure 4.22 | Comparison of hiPSC-CM aggregation profile in stirred-tank bioreactors, from day 7 to day 18: cell viability and spheroid size (Model #2-*a*–BR-1 and Model #2-*b*–MT-BR-2). (***a***, ***c****, left panel*) Evaluation of **hiPSC-CM spheroids viability** in **stirred-tank bioreactors**, through a **live/dead assay**, throughout the culture time (**day 7 to day 18**, prior to microencapsulation)**.** **(*a*)** Perfusion operation mode was activated at day 10, with a dilution rate of 0.30 day^{-1}. Stirring rate was originally set to 60 rpm and, at day 9, was increased to 70 rpm and thus maintained until day 18. **(*c*)** Perfusion operation mode was started at day 9, with the aforesaid dilution rate. Stirring rate was initially set to 80 rpm and, at day 11, was increased to 90 rpm and thus maintained until day 18. (***b***, ***d****, right panel*) Scatter dot plots displaying the **hiPSC-CM average spheroid diameter**, over time (**day 7 to day 18**, prior to microencapsulation). Line at mean with SD. Data are mean ± SD from two bioreactor independent experiments: (***a***, ***b***, **Model #2-*a*–BR-1**) and (***c***, ***d***, **Model #2-*b*–MT-BR-2**) ($n \geq 67$ spheroids). Colour changes from light to dark grey, in the scatter dot plots, symbolise an increase in stirring rates.

fold increase in cell density in **Model #2-*b*-MT-BR-2**, at day 18, when compared to its counterpart (*BR-1*: 0.040 x 10^6 cell/ mL and *BR -2*: 0.27 x 10^6 cell/ mL; **Fig.4.23*a***).

Interestingly, spheroid concentration (**Fig.4.23*b***) appears to be the same at day 18 (*BR-1* and *BR-2*: 0.077 x 10^6 spheroids/mL; Fig.4.23b and Annex 7, Table S9) in both the models, indicating that *BR-2*'s spheroids are actually more compact (*i.e*. made up of a larger number of hiPSC-CM). Moreover, hiPSC-CM cell counts over time show that, in *BR-2*, hiPSC-CM exhibit a cell viability significantly higher than in *BR-1*

(96.68 ± 1.838%; * *vs*. BR-2; **Fig.4.23*c***). Some of the parameters related to the aggregation profiles in STBR, regarding the aforesaid experiments, are compiled in **Annex 7**, **Table S9**.

Hence, by joining all these results, *BR-2* experiment was the chosen to proceed to the microencapsulation step.

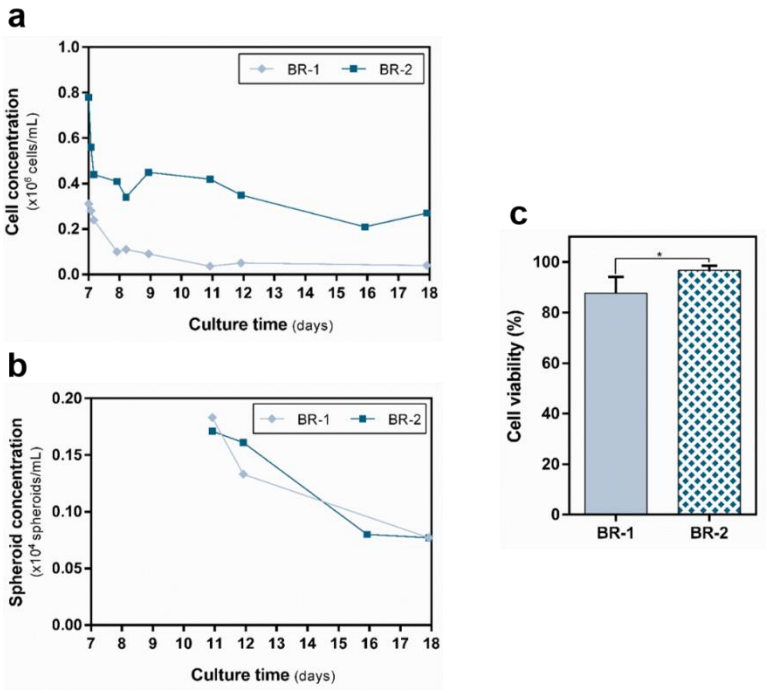

Figure 4.23 | hiPSC-CM cell and spheroid concentration profiles, as well as cell viability, over 12 days of aggregation (Model #2-*a*–BR-1 and Model #2-*b*–MT-BR-2). (***a-b***) Characterization of **hiPSC-CM** (***a***) **cell** and (***b***) **spheroid concentration** profiles along **12 days** of aggregation (day 7 to day 18, prior to microencapsulation). (***c***) **hiPSC-CM cell viability** prior to microencapsulation. Error bars are mean ± SD from one bioreactor independent experiment and refer to cell viability values calculated over the time of the aggregation process (*n* = 4-6). Two-tailed Mann–Whitney nonparametric test (*P = 0.0107). Model #2-*a*–BR-1 and Model #2-*b*–MT-BR-2 denote two independent bioreactor experiments. (*in the charts*: simply referred to as *BR-1* and *BR-2*).

4.9.2. Towards 3D microencapsulated mono- and triculture cardiac tissue models in STBRs

In **Fig.4.24*a*** it can be seen that the microencapsulated monoculture and triculture conditions remain viable for 6 days of culture. Nonetheless, the cell viability is inferior to that observed in the corresponding models established in shake flask (consult **4.2**) and, particularly, some cell death, mainly in the tricultures, can be perceived (**Fig.4.24*a***, *triculture*). Once again, a substantial spheroid size dispersion within the microcapsules may explain this factor.

Spheroids per microcapsule distribution (**Fig.4.24*b***) on microencapsulation day, reveals a content of 0 to 6 spheroids per microcapsule, in monoculture, and 0 to 5, in triculture, with the majority of the capsules encapsulating 2 spheroids **Fig.4.24*b***). These values demonstrate a more shortened distribution than some of the experiments performed on shake flask (consult **4.2.1**, **Fig.4.3*c***). In addition, average microcapsule diameter values, concerning **Model #2-*b*-MT-BR-2** (817.5 ± 41.52 µm) were likewise compiled in **Annex 2.2**, **Table S4** and **Fig.S2**.

Model behaviour's results show that triculture's spheroid (**Fig.4.24*c***) and microcapsule (**Fig.4.24*d***) concentrations are significantly lower than those of the monocultures (* *vs*. monocultures; **Fig.4.24*c*** and **Fig.4.24*d***) . The very low density of spheroids and microcapsules can be explained due to some technical problems that have occurred during the microencapsulation process, which still requires an additional optimization.

Finally, the phenotype of monoculture's cardiac spheroids was evaluated via confocal immunofluorescence in cryosections (**Fig.4.24*e***). At the endpoint (6 days after microencapsulation), confocal analysis demonstrates the expression of specific structural cardiac markers, *viz*. cTnT and sarcomeric *α*-actinin (**Fig.4.24*e***). Furthermore, it is possible to distinguish a striated pattern, typical from the sarcomeric myofibrillar structure (**Fig.4.24*e***; observe insets). Besides, it appears that, at day 6, the

spheroids do not express *Nkx*2-5 (one of the earliest markers of cardiac lineage, typically expressed in CPCs)[227].

To sum up, the work presented in this last topic discloses that STBRs can be used as a technological platform to generate hiPSC-CM spheroids; yet, there is still a way to go when it comes to optimizing this system to support the microencapsulated 3D cardiac tissue models.

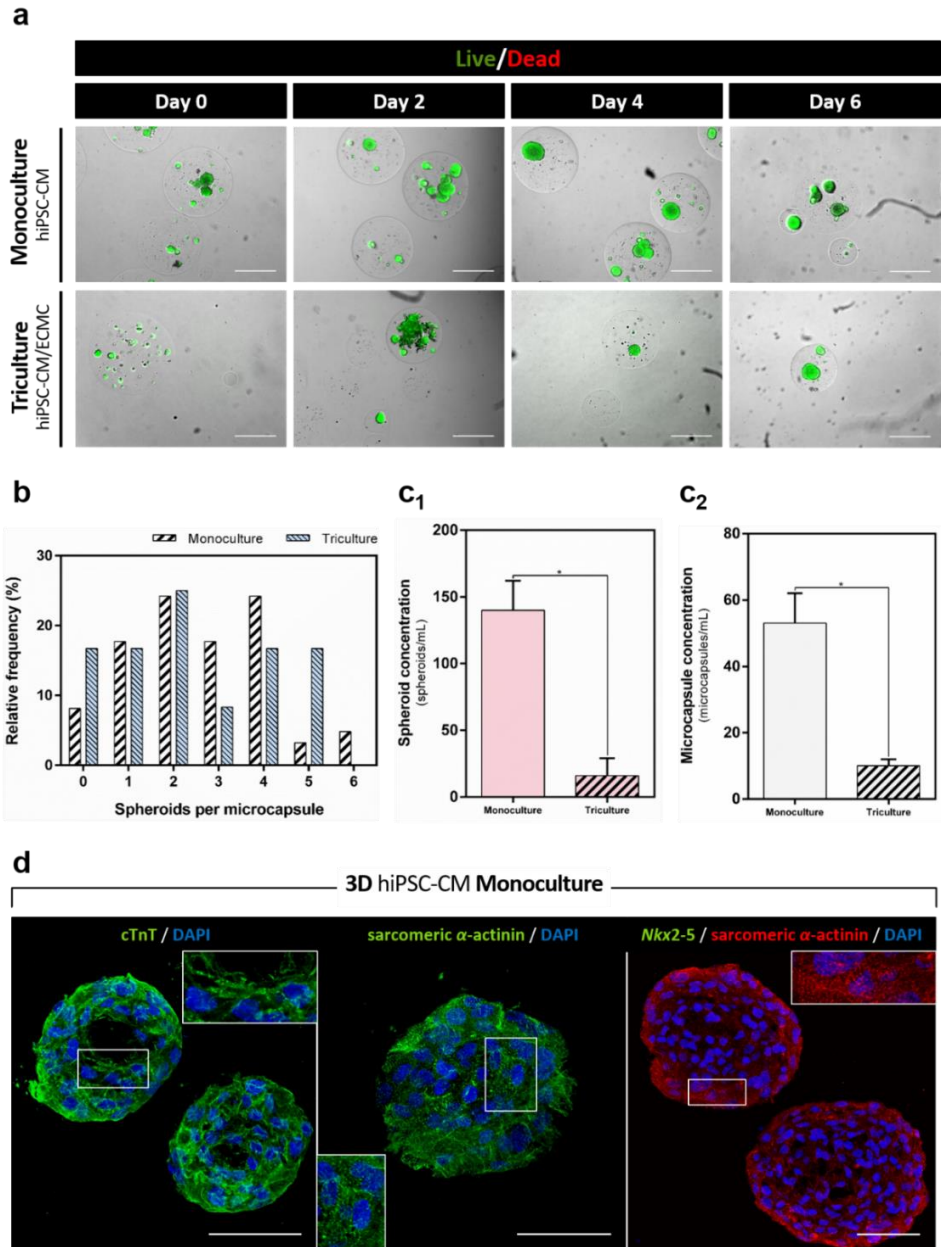

Figure 4.24 | Towards mono- and triculture cardiac tissue models using small scale stirred-tank bioreactors: cell viability, model monitoring and phenotypic characterization (Model #2-*b*–MT-BR-2). (***a***) Qualitative assessment of 3D hiPSC-derived cardiac tissue models' (hiPSC-CM mono- and hiPSC-CM/ECMC triculture) **cell viability over time** (*from left to right*: 0, 2, 4 and 6 days after microencapsulation), cultured under similar circumstances. Cultures were stained with **FDA** (fluorescein diacetate) – **live** cells, **green**, and **PI** (propidium iodide) – **dead** cells, **red**. Scale bars, 500 µm. (***b***) **Spheroids per microcapsule distribution**, in mono- and triculture, on the **day of microencapsulation** (day 0). (***c***) Characterization of the behaviour of the encapsulated models, in terms of (***c*$_1$**) **spheroid** and (***c*$_2$**) **microcapsule concentration**, in both mono- and tricultures. Error bars are mean ± *SEM* from one independent experiment, corresponding to the mean values of days 0 and 6, *post*-microencapsulation (n = 2). Two-tailed Mann–Whitney nonparametric test (*$P \leq 0.05$). (***d***) **Confocal immunofluorescence microscopy** of 3D microencapsulated hiPSC-CM **monocultures**, in 12 µm thick cryosections, at the **endpoint** of the model (**day 6** *post*-microencapsulation). Data are representative maximum intensity z-projections from one independent experiment. hiPSC-CM spheroids immunostained (*from left to right*) for the **cardiac markers** **cTnT** and **sarcomeric α-actinin** (**green**), and also for ***Nkx*2-5** (**green**) and **sarcomeric α-actinin** (**red**). Nuclei were counterstained with **DAPI** (**blue**). Scale bars, 50 µm.

5. Concluding Remarks and Outlook

In this work, **3D** mono- and **triculture cardiac microtissues**, that recapitulate *in vitro* certain features of the *in vivo* human heart microenvironment, have been developed, in a high throughput fashion.

The use of highly competent protocols for the **differentiation** of **hiPSC** toward **myocytes** (hiPSC-CM) and **non-myocytes** (hiPSC-EC and hiPSC-MC), coupled with the **microencapsulation technology**, using a biocompatible hydrogel, resulted in a robust system, fully hiPSC-derived and amenable for medium- to large-scale production.

Specifically, employing **human cell sources** to attain the various cardiac populations allows to mimic the **heterotypic cellular crosstalk** inherent to the human heart, whereas the RGD peptide-modified **hydrogel** provides a 3D controllable, inert and chemically **defined microenvironment** (advantageous when compared to undefined animal-derived preparations, *e.g*. *Matrigel* or collagen mixtures) for the cells to physically attach and communicate.

3D mono- and triculture human EHTs were successively microencapsulated and maintained in culture for a minimum of 15 days, with high cellular viabilities, which were confirmed via FDA-PI live/dead and *PrestoBlue*™ assays. Furthermore, early on, several cues of a heterotypic cellular communication in the triculture model were evident: noteworthy, hiPSC-ECMC, did not survive in the 3D coculture model, in the absence of hiPSC-CM.

In addition to the cellular crosstalk, another aspect explored in this work was **hiPSC-CM maturation**, studied through comparison between structure, ultrastructure, gene and protein expression, calcium kinetics, responsiveness to cardiac affinity and cardiotoxic chemotherapeutic drugs, and mechanobiological behaviour, amid mono- and tricultures.

After only **15 days** of culture, **gene expression profiling**, **imaging-based phenotypic characterization** and **ultrastructure analysis** exposed clear evidence of a **structural maturation over time** in both models: (i) upregulation of *MYL2*, *MYH7* and *TNNI3* adult sarcomeric gene isoforms and increased *MYL2/MYL7*, *MYH7/MYH6* and *TNNI3/TNNI1* gene expression ratios, (ii) extremely organized ultrastructure (not observed at the beginning); and others consistent with a more **advanced maturation stage** in **triculture** at **day 15**, in comparison to its counterpart: (i) increased *MYL2/MYL7* and *TNNI3/TNNI1*'s gene expression ratios, together with the upregulation of calcium (*CACNA1C*) and sodium (*SCN5A*) cardiac ion channels, (ii) apparent overexpression of gap junction proteins (Cx43 and ZO-1; confocal microscopy), (iii) enlarged production of ECM proteins (collagen type I, collagen type IV and fibronectin; confocal, multiphoton and LSFM) and (iv) significant improvement in sarcomere length and sarcomeric myofibrillar alignment.

Particularly, through a LSFM-based quantification of 3D volume reconstructions of the microcapsules, we determined a 45.6-fold increase in relative fibronectin expression in tricultures, at day 15, compared to monocultures.

Moreover, we have also demonstrated that our models have the ability to **support hiPSC-CM functionality** and **contractility**. Live cell calcium imaging demonstrated slower calcium handling kinetics in the triculture model, as evidenced by the significant decrease in beating rates, from mono- to triculture, which may be correlated with a more mature Ca^{2+} handling apparatus in this model. Exposure to cardioactive drugs (norepinephrine, heptanol and propranolol) was likewise evaluated, with hiPSC-CM, in both mono- and tricultures, demonstrating chronotropic typical responses, indicating that β-adrenergic receptors and gap junction proteins were properly expressed on these models. Following the functional characterization, cardiotoxicity findings demonstrated that doxorubicin significantly reduced the cell

viability in the monoculture, in a dose-dependent manner, whilst paclitaxel presented a similar, but more sensitive response, encompassing both mono- and triculture.

The **mechanobiological performance** of the **biomaterial** was studied using **AFM**. Our scaffold proved **suitable** to **recapitulate** the **heart microenvironment**, since it exhibited a Young's modulus within the same order of magnitude of human cardiac muscle's[14,23,25]. Also, **FS-AFM** provided insight into changes occurring within the scaffold (due to *cell-to-cell* and *cell-to-scaffold* contacts), by quantifying relevant biomechanical parameters (Young's modulus, stiffness, hardness and adhesion), suggestive of a hiPSC-ECMC-induced **remodelling** of the **cardiac microenvironment** in **triculture**.

Finally, a *proof-of-concept* has established that it is conceivable to carry out the upscaling of the 3D cardiac models using perfusion STBRs, although the bioprocess still lacks optimization.

Altogether, we can conclude that the **developed EHTs** are a **step forward** in the study of **heterotypic cellular communication** between myocytes and non-myocytes and **cardiomyocyte maturation**, being compatible with medium- to large-scale production and **high-throughput** compliances, required in preclinical and clinical settings.

To finish, it would be interesting to develop a **more robust** and standardized **cardiotoxicity platform** (resorting to both cardiotoxic and cardioprotective agents). Another of the future prospects of this work will be to **build** a **disease model**, entirely based on patient-specific hiPSC, using a methodology and characterization toolbox similar to those settled. Furthermore, to reliably mimic *in vitro* the *in vivo* heart microenvironment the construct should ideally include all the critical cardiac cells beyond CMs and ECs. Certainly, **increasing the complexity** of our **triculture format** via inclusion of other cardiac cell types (*e.g*. pericytes and smooth muscle cells) and complex 3D architectures will be explored to further improve the model.

6. Notes and References

§ It should be noted that this dissertation is drawn up in British English.

§§ Abbreviations and conventions are fully listed in the section *List of Abbreviations and Conventions.*

[1] **Di Baldassarre, A., *et al.*** Human-Induced Pluripotent Stem Cell Technology and Cardiomyocyte Generation: Progress and Clinical Applications. *Cells* **7,** 48 (2018).

[2] **Devalla, H.D., & Passier, R.** Cardiac differentiation of pluripotent stem cells and implications for modeling the heart in health and disease. *Sci Transl Med* **10,** 1–14 (2018).

[3] **Feric, N.T., & Radisic, M.** Maturing human pluripotent stem cell-derived cardiomyocytes in human engineered cardiac tissues. *Adv. Drug Deliv. Rev.* **96,** 110–134 (2016).

[4] **Keung, W., *et al.*** Developmental cues for the maturation of metabolic, electrophysiological and calcium handling properties of human pluripotent stem cell-derived cardiomyocytes. *Stem Cell Res. Ther.* **5,** 1–11 (2014).

[5] **Ghiroldi, A., *et al.*** Regenerating the human heart: direct reprogramming strategies and their current limitations. *Basic Res. Cardiol.* **112,** 1–14 (2017).

[6] **Moran, A.E., *et al.*** Temporal Trends in Ischemic Heart Disease Mortality in 21 World Regions, 1980 to 2010 The Global Burden of Disease 2010 Study. *Circulation* **129,** 1483–1492 (2014).

[7] **Ryan, A.J., *et al.*** Towards 3D in vitro models for the study of cardiovascular tissues and disease. *Drug Discov. Today* **21,** 1437–1445 (2016).

[8] **Cambria, E., *et al.*** Translational cardiac stem cell therapy: advancing from first-generation to next-generation cell types. *npj Regen. Med.* **2,** 1–10 (2017).

[9] **Kempf, H., *et al.*** Large-scale production of human pluripotent stem cell derived cardiomyocytes. *Adv. Drug Deliv. Rev.* **96,** 18–30 (2016).

[10] **Brandão, K.O., *et al.*** Human pluripotent stem cell models of cardiac disease: from mechanisms to therapies. *Dis. Model. Mech.* **10,** 1039–1059 (2017).

[11] **Magdy, T., *et al.*** Validating the pharmacogenomics of chemotherapy-induced cardiotoxicity: What is missing? *Pharmacol. Ther.* **168,** 113–125 (2016).

[12] **Chaudhari, U., *et al.*** Metabolite signatures of doxorubicin induced toxicity in human induced pluripotent stem cell-derived cardiomyocytes. *Amino Acids* **49,** 1955–1963 (2017).

[13] **Csapo, M., & Lazar, L.** Chemotherapy-Induced Cardiotoxicity: Pathophysiology and Prevention. *Clujul Med.* **87,** 135–142 (2014).

[14] **Mathur, A., *et al.*** In vitro cardiac tissue models: Current status and future prospects. *Adv. Drug Deliv. Rev.* **96,** 203–213 (2016).

[15] **Wang, F., *et al.*** Is Human-induced Pluripotent Stem Cell the Best Optimal? *Chin. Med. J. (Engl).* **131,** 852–856 (2018).

[16] **Ferri, N., *et al.*** Drug attrition during pre-clinical and clinical development: Understanding and managing drug-induced cardiotoxicity. *Pharmacol. Ther.* **138,** 470–484 (2013).

[17] **Vunjak Novakovic, G., *et al.*** Myocardial Tissue Engineering: In Vitro Models. *Cold Spring Harb. Perspect. Med.* **4,** 1–15 (2014).

[18] **Zeevi-Levin, N., *et al.*** Cardiomyocytes derived from human pluripotent stem cells for drug screening. *Pharmacol. Ther.* **134,** 180–188 (2012).

[19] **Cross, M.J., *et al.*** Physiological, pharmacological and toxicological considerations of drug-induced structural cardiac injury. *Br. J. Pharmacol.* **172,** 957–974 (2015).

[20] **Magdy, T., & Burridge, P.W.** The future role of pharmacogenomics in anticancer agent-induced cardiovascular toxicity. *Pharmacogenomics* **19,** 79–82 (2018).

[21] **Magdy, T., *et al.*** Human Induced Pluripotent Stem Cell (hiPSC)-Derived Cells to Assess Drug Cardiotoxicity: Opportunities and Problems. *Annu. Rev. Pharmacol. Toxicol.* **58,** 83–103 (2018).

[22] **Sharma, A., *et al.*** High-throughput screening of tyrosine kinase inhibitor cardiotoxicity with human induced pluripotent stem cells. *Sci Transl Med* **9,** 1–13 (2017).

[23] **Kofron, C.M., & Mende, U.** In vitro models of the cardiac microenvironment to study myocyte and non-myocyte crosstalk: bioinspired approaches beyond the polystyrene dish. *J. Physiol.* **595,** 3891–3905 (2017).

[24] **Dostal, D., *et al.*** Cardiac fibroblast physiology and pathology. *Compr. Physiol.* **5,** 887–909 (2015).

[25] **Dunn, K.K., & Palecek, S.P.** Engineering Scalable Manufacturing of High-Quality Stem Cell-Derived Cardiomyocytes for Cardiac Tissue Repair. *Front. Med.* **5,** 1–18 (2018).

[**26**] **Brutsaert, D.L.** Cardiac Endothelial-Myocardial Signaling: Its Role in Cardiac Growth, Contractile Performance, and Rhythmicity. *Physiol. Rev.* **83,** 59–115 (2003).

[**27**] **Harvey, P.A., & Leinwand, L.A.** Cellular mechanisms of cardiomyopathy. *J. Cell Biol.* **194,** 355–365 (2011).

[**28**] **Tian, Y., & Morrisey, E.E.** Importance of myocyte-nonmyocyte interactions in cardiac development and disease. *Circ. Res.* **110,** 1023–1034 (2012).

[**29**] **Ayoubi, S., *et al.*** Human induced pluripotent stem cell-derived vascular smooth muscle cells: differentiation and therapeutic potential. *Cardiovasc. Res.* **113,** 1282–1293 (2017).

[**30**] **Vuorenpää, H., *et al.*** Maturation of human pluripotent stem cell derived cardiomyocytes is improved in cardiovascular construct. *Cytotechnology* **69,** 785–800 (2017).

[**31**] **Lee, J.H., *et al.*** Human Pluripotent Stem Cell-Derived Atrial and Ventricular Cardiomyocytes Develop from Distinct Mesoderm Populations. *Cell Stem Cell* **21,** 179–194 (2017).

[**32**] **Sirabella, D., *et al.*** "The state of the heart": Recent advances in engineering human cardiac tissue from pluripotent stem cells. *Exp. Biol. Med.* **240,** 1008–1018 (2015).

[**33**] **Chen, H., *et al.*** Harnessing cell pluripotency for cardiovascular regenerative medicine. *Nat. Biomed. Eng.* **2,** 392–398 (2018).

[**34**] **Xin, M., *et al.*** Mending broken hearts: Cardiac development as a basis for adult heart regeneration and repair. *Nat. Rev. Mol. Cell Biol.* **14,** 529–541 (2013).

[**35**] **Lim, S.L., *et al.*** Cardiac endothelium-myocyte interaction: Clinical opportunities for new heart failure therapies regardless of ejection fraction. *Eur. Heart J.* **36,** 2050–2060 (2015).

[**36**] **Souders, C.A., *et al.*** Cardiac fibroblast: The renaissance cell. *Circ. Res.* **105,** 1164–1176 (2009).

[**37**] **Condorelli, G., *et al.*** Cardiomyocytes induce endothelial cells to trans-differentiate into cardiac muscle: Implications for myocardium regeneration. *Proc. Natl. Acad. Sci.* **98,** 10733–10738 (2001).

[**38**] **Hsieh, P.C.H., *et al.*** Endothelial-Cardiomyocyte Interactions in Cardiac Development and Repair. *Annu. Rev. Physiol.* **68,** 51–66 (2006).

[**39**] **Zhang, Y., *et al.*** Endothelial cells regulate cardiac myocyte reorganisation through β1-integrin signalling. *Cell. Physiol. Biochem.* **35,** 1808–1820 (2015).

[**40**] **Talman, V., & Kivelä, R.** Cardiomyocyte — Endothelial Cell Interactions in Cardiac Remodeling and Regeneration. *Front. Cardiovasc.* **5,** 1–8 (2018).

[**41**] **Noireaud, J., & Andriantsitohaina, R.** Recent insights in the paracrine modulation of cardiomyocyte contractility by cardiac endothelial cells. *Biomed Res. Int.* **2014,** 1–10 (2014).

[**42**] **d'Avenia, M., *et al.*** A novel MIR-371a-5p-mediated pathway, leading to BAG3 upregulation in cardiomyocytes in response to epinephrine, is lost in Takotsubo cardiomyopathy. *Cell Death Dis.* **6,** 1–10 (2015).

[**43**] **Wadugu, B., & Kuhn, B.** The role of neuregulin/ErbB2/ErbB4 signaling in the heart with special focus on effects on cardiomyocyte proliferation. *AJP Hear. Circ. Physiol.* **302,** 2139–2147 (2012).

[**44**] **Grego-Bessa, J., *et al.*** Notch Signaling Is Essential for Ventricular Chamber Development. *Dev. Cell* **12,** 415–429 (2007).

[**45**] **Itoh, N., *et al.*** Roles of FGF Signals in Heart Development, Health, and Disease. *Front. Cell Dev. Biol.* **110,** 1–11 (2016).

[**46**] **Yang, X., *et al.*** Fibroblast Growth Factor Signaling in the Vasculature. *Curr Atheroscler Rep.* **17,** 1–17 (2015).

[**47**] **Anderson, R.H., *et al.*** Cardiac anatomy revisited. *J. Anat.* **205,** 159–177 (2004).

[**48**] **Zhou, P., & Pu, W.T.** Recounting cardiac cellular composition. *Circ. Res.* **118,** 368–370 (2016).

[**49**] **Bergmann, O., *et al.*** Dynamics of Cell Generation and Turnover in the Human Heart. *Cell* **161,** 1566–1575 (2015).

[**50**] **Banerjee, I., *et al.*** Determination of cell types and numbers during cardiac development in the neonatal and adult rat and mouse. *Am. Physiol.* **293,** 1883–1891 (2007).

[**51**] **Serra, M., *et al.*** Process engineering of human pluripotent stem cells for clinical application. *Trends Biotechnol.* **30,** 350–359 (2012).

[**52**] **Serra, M., *et al.*** Microencapsulation technology: A powerful tool for integrating expansion and cryopreservation of human embryonic stem cells. *PLoS One* **6,** 1–13 (2011).

[**53**] **Giacomelli, E., *et al.*** Human heart disease: lessons from human pluripotent stem cell-derived cardiomyocytes. *Cell. Mol. Life Sci.* **74,** 3711–3739 (2017).

[**54**] **Abecasis, B., *et al.*** Expansion of 3D human induced pluripotent stem cell aggregates in bioreactors: Bioprocess intensification and scaling-up approaches. *J. Biotechnol.* **246,** 81–93 (2017).

[**55**] **Josowitz, R., *et al.*** Induced pluripotent stem cell-derived cardiomyocytes as models for genetic cardiovascular disorders. *Curr. Opin. Cardiol.* **26,** 223–229 (2011).

[**56**] **Karakikes, I., *et al.*** Human Induced Pluripotent Stem Cell-Derived Cardiomyocytes: Insights into Molecular, Cellular, and

Functional Phenotypes. *Circ. Res.* **117,** 80–88 (2015).

[**57**] **Le, T.Y.L., *et al.*** New Developments in Cardiac Regeneration. *Hear. Lung Circ.* **26,** 316–322 (2017).

[**58**] **Fortier, L.A.** Stem cells: Classifications, controversies, and clinical applications. *Vet. Surg.* **34,** 415–423 (2005).

[**59**] **Kalra, K., & Tomar, P.** Stem Cell: Basics, Classification and Applications. *Am. J. Phytomdicine Clin. Ther.* **2,** 919–930 (2014).

[**60**] **Alvarez, C. V., *et al.*** Defining stem cell types: Understanding the therapeutic potential of ESCs, ASCs, and iPS cells. *J. Mol. Endocrinol.* **49,** 89–111 (2012).

[**61**] **Poh, Y.-C., *et al.*** Generation of organized germ layers from a single mouse embryonic stem cell. *Nat. Commun.* **5,** 4000 (2014).

[**62**] **Takahashi, K., *et al.*** Induction of Pluripotent Stem Cells from Adult Human Fibroblasts by Defined Factors. *Cell* **131,** 861–872 (2007).

[**63**] **Martin, G.R.** Isolation of a pluripotent cell line from early mouse embryos cultured in medium conditioned by teratocarcinoma stem cells. *Proc. Natl. Acad. Sci. U. S. A.* **78,** 7634–7638 (1981).

[**64**] **Evans, M.J., & Kaufman, M.H.** Establishment in culture of pluripotential cells from mouse embryos. *Nature* **292,** 154–156 (1981).

[**65**] **Takahashi, K., & Yamanaka, S.** A decade of transcription factor-mediated reprogramming to pluripotency. *Nat. Rev. Mol. Cell Biol.* **17,** 183–93 (2016).

[**66**] **Takahashi, K., & Yamanaka, S.** Induction of Pluripotent Stem Cells from Mouse Embryonic and Adult Fibroblast Cultures by Defined Factors. *Cell* **126,** 663–676 (2006).

[**67**] **Yamanaka, S.** Strategies and New Developments in the Generation of Patient-Specific Pluripotent Stem Cells. *Cell Stem Cell* **1,** 39–49 (2007).

[**68**] **Reubinoff, B.E., *et al.*** Embryonic stem cell lines from human blastocysts: somatic differentiation in vitro. *Nat. Biotechnol.* **18,** 399–404 (2000).

[**69**] **Burridge, P.W., *et al.*** Modeling Cardiovascular Diseases with Patient-Specific Human Pluripotent Stem Cell-Derived Cardiomyocytes. *Methods Mol. Biol.* **1353,** 119–130 (2016).

[**70**] **Thomson, J.A., *et al.*** Embryonic Stem Cell Lines Derived from Human Blastocysts. *Science* **82,** 1145–1148 (1998).

[**71**] **Kropp, C., *et al.*** Impact of Feeding Strategies on the Scalable Expansion of Human Pluripotent Stem Cells in Single-Use Stirred Tank Bioreactors. *Stem Cells Transl. Med.* **5,** 1289–1301 (2016).

[**72**] **Olmer, R., *et al.*** Suspension Culture of Human Pluripotent Stem Cells in Controlled, Stirred Bioreactors. *Tissue Eng. Part C Methods* **18,** 772–784 (2012).

[**73**] **Kropp, C., *et al.*** Progress and challenges in large-scale expansion of human pluripotent stem cells. *Process Biochem.* **59,** 244–254 (2017).

[**74**] **Yu, J., *et al.*** Induced Pluripotent Stem Cell Lines Derived from Human Somatic Cells. *Science (80-.).* **318,** 1917–1920 (2007).

[**75**] **Zwi-Dantsis, L., & Gepstein, L.** Induced pluripotent stem cells for cardiac repair. *Cell. Mol. Life Sci.* **69,** 3285–3299 (2012).

[**76**] **Burridge, P.W., *et al.*** Production of de novo cardiomyocytes: Human pluripotent stem cell differentiation and direct reprogramming. *Cell Stem Cell* **10,** 16–28 (2012).

[**77**] **Simão, D., *et al.*** Functional metabolic interactions of human neuron-astrocyte 3D in vitro networks. *Sci. Rep.* **6,** 1–12 (2016).

[**78**] **Kehat, I., & Kenyagin-Karsenti, D.** Human embryonic stem cells can differentiate into myocytes with structural and functional properties of cardiomyocytes. *J. Clin. Invest.* **108,** 407–414 (2001).

[**79**] **Lewandowski, J., *et al.*** Techniques for the induction of human pluripotent stem cell differentiation towards cardiomyocytes. *J Tissue Eng Regen Med.* **11,** 1658–1674 (2016).

[**80**] **Mummery, C., *et al.*** Differentiation of Human Embryonic Stem Cells to Cardiomyocytes: Role of Coculture With Visceral Endoderm-Like Cells. *Circulation* **107,** 2733–2740 (2003).

[**81**] **Laflamme, M.A., *et al.*** Cardiomyocytes derived from human embryonic stem cells in pro-survival factors enhance function of infarcted rat hearts. *Nat. Biotechnol.* **25,** 1015–1024 (2007).

[**82**] **Lian, X., *et al.*** Directed cardiomyocyte differentiation from human pluripotent stem cells by modulating Wnt/β-catenin signaling under fully defined conditions. *Nat. Protoc.* **8,** 162–175 (2013).

[**83**] **Correia, C., *et al.*** 3D aggregate culture improves metabolic maturation of human pluripotent stem cell derived cardiomyocytes. *Biotechnol. Bioeng.* **115,** 630–644 (2018).

[**84**] **Correia, C., *et al.*** Distinct carbon sources affect structural and functional maturation of cardiomyocytes derived from human pluripotent stem cells. *Sci. Rep.* **7,** 1–17 (2017).

[**85**] **Burridge, P.W., *et al.*** Chemically defned generation of human cardiomyocytes. *Nat. Methods* **11,** 855–860 (2014).

[**86**] **Tohyama, S., *et al.*** Distinct metabolic flow enables large-scale purification of mouse and human pluripotent stem cell-derived cardiomyocytes. *Cell Stem Cell* **12,** 127–137 (2013).

[**87**] **Elliott, D.A., *et al.*** NKX2-5eGFP/w hESCs for isolation of human cardiac progenitors and cardiomyocytes. *Nat. Methods* **8,** 1037–1040 (2011).

[**88**] **Dubois, N.C., *et al.*** SIRPA is a specific cell-surface marker for isolating cardiomyocytes derived from human pluripotent stem cells. *Nat. Biotechnol.* **29,** 1011–1018 (2011).

[**89**] **Kamps, J.A., & Krenning, G.** Micromanaging cardiac regeneration: Targeted delivery of microRNAs for cardiac repair and regeneration. *World J. Cardiol.* **8,** 163–179 (2016).

[**90**] **Spater, D., *et al.*** How to make a cardiomyocyte. *Development* **141,** 4418–4431 (2014).

[**91**] **Mummery, C.L., *et al.*** Differentiation of human embryonic stem cells and induced pluripotent stem cells to cardiomyocytes: A methods overview. *Circ. Res.* **111,** 344–358 (2012).

[**92**] **Rajala, K., *et al.*** Cardiac differentiation of pluripotent stem cells. *Stem Cells Int.* **2011,** 1–13 (2011).

[**93**] **Cao, N., *et al.*** Ascorbic acid enhances the cardiac differentiation of induced pluripotent stem cells through promoting the proliferation of cardiac progenitor cells. *Cell Res.* **22,** 219–236 (2012).

[**94**] **Iglesias-García, O., *et al.*** Neuregulin-1β Induces Mature Ventricular Cardiac Differentiation from Induced Pluripotent Stem Cells Contributing to Cardiac Tissue Repair. *Stem Cells Dev.* **24,** 484–496 (2015).

[**95**] **Li, S., *et al.*** Calcium signalling of human pluripotent stem cell-derived cardiomyocytes. *J. Physiol.* **591,** 5279–5290 (2013).

[**96**] **Itzhaki, I., *et al.*** Calcium handling in human induced pluripotent stem cell derived cardiomyocytes. *PLoS One* **6,** 1–12 (2011).

[**97**] **Gouveia, P.J., *et al.*** Flexible nanofilms coated with aligned piezoelectric microfibers preserve the contractility of cardiomyocytes. *Biomaterials* **139,** 213–228 (2017).

[**98**] **Rana, P., *et al.*** Characterization of human-induced pluripotent stem cell-derived cardiomyocytes: Bioenergetics and utilization in safety screening. *Toxicol. Sci.* **130,** 117–131 (2012).

[**99**] **Olmer, R., *et al.*** Differentiation of Human Pluripotent Stem Cells into Functional Endothelial Cells in Scalable Suspension Culture. *Stem Cell Reports* **10,** 1–16 (2018).

[**100**] **Lee, S., *et al.*** Generation of Human Pluripotent Stem Cell-derived Endothelial Cells and Their Therapeutic Utility. *Curr Cardiol Rep.* **20,** 1–7 (2018).

[**101**] **Palpant, N.J., *et al.*** Generating high-purity cardiac and endothelial derivatives from patterned mesoderm using human pluripotent stem cells. *Nat. Protoc.* **12,** 15–31 (2017).

[**102**] **Tan, J.Y., *et al.*** Efficient Derivation of Lateral Plate and Paraxial Mesoderm Subtypes from Human Embryonic Stem Cells Through GSKi-Mediated Differentiation. *Stem Cells Dev.* **22,** 1893–1906 (2013).

[**103**] **Orlova, V. V., *et al.*** Functionality of endothelial cells and pericytes from human pluripotent stem cells demonstrated in cultured vascular plexus and zebrafish xenografts. *Arterioscler. Thromb. Vasc. Biol.* **34,** 177–186 (2014).

[**104**] **Patsch, C., *et al.*** Generation of vascular endothelial and smooth muscle cells from human pluripotent stem cells. *Nat. Cell Biol.* **17,** 994–1003 (2015).

[**105**] **Hirt, M.N., *et al.*** Cardiac tissue engineering : State of the art. *Circ. Res.* **114,** 354–367 (2014).

[**106**] **Nishimura, K., *et al.*** Type 3 iodothyronine deiodinase is expressed in human induced pluripotent stem cell derived cardiomyocytes. *Life Sci.* **203,** 276–281 (2018).

[**107**] **Parikh, S.S., *et al.*** Thyroid and Glucocorticoid Hormones Promote Functional T-Tubule Development in Human-Induced Pluripotent Stem Cell-Derived Cardiomyocytes. *Circ. Res.* **121,** 1323–1330 (2017).

[**108**] **Pesl, M., *et al.*** Atomic force microscopy combined with human pluripotent stem cell derived cardiomyocytes for biomechanical sensing. *Biosens. Bioelectron.* **85,** 751–757 (2016).

[**109**] **Pesl, M., *et al.*** Phenotypic assays for analyses of pluripotent stem cell–derived cardiomyocytes. *J. Mol. Recognit.* **30,** 1–14 (2017).

[**110**] **Giacomelli, E., *et al.*** Three-dimensional cardiac microtissues composed of cardiomyocytes and endothelial cells co-differentiated from human pluripotent stem cells. *Development* **144,** 1008–1017 (2017).

[**111**] **Vuorenpää, H., *et al.*** Novel in vitro cardiovascular constructs composed of vascular-like networks and cardiomyocytes. *Vitr. Cell. Dev. Biol. - Anim.* **50,** 275–286 (2014).

[**112**] **Fennema, E., *et al.*** Spheroid culture as a tool for creating 3D complex tissues. *Trends Biotechnol.* **31,** 108–115 (2013).

[**113**] **Günter, J., *et al.*** Microtissues in Cardiovascular Medicine: Regenerative Potential Based on a 3D Microenvironment. *Stem Cells Int.* **2016,** 1–20 (2016).

[**114**] **Garzoni, L.R., *et al.*** Dissecting coronary angiogenesis: 3D co-culture of cardiomyocytes with endothelial or mesenchymal cells. *Exp. Cell Res.* **315,** 3406–3418 (2009).

[**115**] **Stevens, K.R., *et al.*** Physiological function and transplantation of scaffold-free and vascularized human cardiac muscle tissue. *Proc. Natl. Acad. Sci.* **106,** 16568–16573 (2009).

[**116**] **Shachar, M., *et al.*** The effect of immobilized RGD peptide in alginate scaffolds on cardiac tissue engineering. *Acta Biomater.* **7,** 152–162 (2011).

[**117**] **Ellis, B.W., *et al.*** Human IPSC-derived myocardium-on-chip with capillary-like flow for personalized medicine. *Biomicrofluidics* **11,** 1–18 (2017).

[**118**] **Nguyen, D.C., *et al.*** Microscale generation of cardiospheres promotes robust enrichment of cardiomyocytes derived from human pluripotent stem cells. *Stem Cell Reports* **3,** 260–268 (2014).

[**119**] **Beauchamp, P., *et al.*** Development and Characterization of a Scaffold-Free 3D Spheroid Model of Induced Pluripotent Stem Cell-Derived Human Cardiomyocytes. *Tissue Eng. Part C Methods* **21,** 852–861 (2015).

[**120**] **Richards, D.J., *et al.*** Nanowires and electrical stimulation synergistically improve functions of hiPSC cardiac spheroids. *Nano Lett.* **16,** 4670–4678 (2016).

[**121**] **Tan, Y., *et al.*** Silicon nanowire-induced maturation of cardiomyocytes derived from human induced pluripotent stem cells. *Nano Lett.* **15,** 2765–2772 (2015).

[**122**] **Ou, D.B., *et al.*** Three-dimensional co-culture facilitates the differentiation of embryonic stem cells into mature cardiomyocytes. *J. Cell. Biochem.* **112,** 3555–3562 (2011).

[**123**] **Godier-Furnémont, A.F.G., *et al.*** Composite scaffold provides a cell delivery platform for cardiovascular repair. *Proc. Natl. Acad. Sci. U. S. A.* **108,** 7974–9 (2011).

[**124**] **Narmoneva, D.A., *et al.*** Endothelial cells promote cardiac myocyte survival and spatial reorganization: Implications for cardiac regeneration. *Circulation* **110,** 962–968 (2004).

[**125**] **Masumoto, H., *et al.*** The myocardial regenerative potential of three-dimensional engineered cardiac tissues composed of multiple human iPS cell-derived cardiovascular cell lineages. *Sci. Rep.* **6,** 1–10 (2016).

[**126**] **Burridge, P.W., *et al.*** Multi-cellular interactions sustain long-term contractility of human pluripotent stem cell-derived cardiomyocytes. *Am. J. Transl. Res.* **6,** 724–735 (2014).

[**127**] **Caspi, O., *et al.*** Tissue engineering of vascularized cardiac muscle from human embryonic stem cells. *Circ. Res.* **100,** 263–272 (2007).

[**128**] **Colombo, M., & Bianchi, A.** Click chemistry for the synthesis of RGD-Containing integrin ligands. *Molecules* **15,** 178–197 (2010).

[**129**] **Jia, J., *et al.*** Development of peptide-functionalized synthetic hydrogel microarrays for stem cell and tissue engineering applications. *Acta Biomater.* **45,** 110–120 (2016).

[**130**] **Dawson, J., *et al.*** Collagen scaffolds with or without the addition of RGD peptides support cardiomyogenesis after aggregation of mouse embryonic stem cells. *Vitr. Cell. Dev. Biol. - Anim.* **47,** 653–664 (2011).

[**131**] **Gandaglia, A., *et al.*** Cardiomyocytes *In Vitro* Adhesion Is Actively Influenced by Biomimetic Synthetic Peptides for Cardiac Tissue Engineering. *Tissue Eng. Part A* **18,** 725–736 (2012).

[**132**] **Ott, H.C., *et al.*** Perfusion-decellularized matrix: Using nature's platform to engineer a bioartificial heart. *Nat. Med.* **14,** 213–221 (2008).

[**133**] **Guyette, J.P., *et al.*** Bioengineering Human Myocardium on Native Extracllular Matrix. *Circ. Res.* **118,** 56–72 (2016).

[**134**] **Hinton, T.J., *et al.*** Three-dimensional printing of complex biological structures by freeform reversible embedding of suspended hydr(1) Hinton, T. J.; Jallerat, Q.; Palchesko, R. N.; Park, J. H.; Grodzicki, M. S.; Shue, H.-J.; Ramadan, M. H.; Hudson, A. R.; Feinberg, A. W. Thr. *Sci Adv.* **1,** 1–10 (2015).

[**135**] **Zhang, Y.S., *et al.*** Bioprinting 3D microfibrous scaffolds for engineering endothelialized myocardium and heart-on-a-chip. *Biomaterials* **110,** 45–59 (2016).

[**136**] **Kempf, H., *et al.*** Cardiac differentiation of human pluripotent stem cells in scalable suspension culture. *Nat. Protoc.* **10,** 1345–1361 (2015).

[**137**] **Kempf, H., *et al.*** Controlling expansion and cardiomyogenic differentiation of human pluripotent stem cells in scalable suspension culture. *Stem Cell Reports* **3,** 1132–1146 (2014).

[**138**] **Murry, C.E., *et al.*** Regeneration Gaps. Observations on Stem Cells and Cardiac Repair. *J. Am. Coll. Cardiol.* **47,** 1777–1785 (2006).

[**139**] **Correia, C., *et al.*** Combining Hypoxia and Bioreactor Hydrodynamics Boosts Induced Pluripotent Stem Cell Differentiation Towards Cardiomyocytes. *Stem Cell Rev. Reports* **10,** 786–801 (2014).

[**140**] **King, J.A., & Miller, W.M.** Bioreactor development for stem cell expansion and controlled differentiation. *Curr. Opin. Chem. Biol.* **11,** 394–398 (2007).

[**141**] **Dos Santos, F.F., *et al.*** Bioreactor design for clinical-grade expansion of stem cells. *Biotechnol. J.* **8,** 644–654 (2013).

[**142**] **Jenkins, M.J., & Farid, S.S.** Human pluripotent stem cell-derived products: Advances towards robust, scalable and cost-effective manufacturing strategies. *Biotechnol. J.* **10,** 83–95 (2015).

[**143**] **Fridley, K.M., *et al.*** Hydrodynamic modulation of pluripotent stem cells. *Stem Cell Res. Ther.* **3,** 1–9 (2012).

[**144**] **Denning, C., *et al.*** Cardiomyocytes from human pluripotent stem cells: From laboratory curiosity to industrial biomedical platform. *Biochim. Biophys. Acta - Mol. Cell Res.* **1863,** 1728–1748 (2016).

[**145**] **Angst, B.D., *et al.*** Dissociated spatial patterning of gap junctions and cell adhesion junctions during postnatal differentiation of ventricular myocardium. *Circ. Res.* **80,** 88–94 (1997).

[**146**] **Masuda, H., *et al.*** Ultrastructure of endothelial cells under flow alteration. *Microsc. Res. Tech.* **60,** 2–12 (2003).

[**147**] **Hess, M.W., *et al.*** 3D Versus 2D Cell Culture: Implications for Electron Microscopy. *Methods Cell Biol.* **96,** 649–670 (2010).

[**148**] **Hsiong, S.X., *et al.*** AFM imaging of RGD presenting synthetic extracellular matrix using gold nanoparticles. *Macromol. Biosci.* **8,** 469–477 (2008).

[**149**] **Correia, C., *et al.*** Effective Hypothermic Storage of Human Pluripotent Stem Cell-Derived Cardiomyocytes Compatible With Global Distribution of Cells for Clinical Applications and Toxicology Testing. *Stem Cells Transl. Med.* **5,** 658–669 (2016).

[**150**] **Hwang, P.M., & Sykes, B.D.** Targeting the sarcomere to correct muscle function. *Nat Rev Drug Discov.* **14,** 313–328 (2015).

[**151**] **Zhang, X.H., *et al.*** Ca2+signaling in human induced pluripotent stem cell-derived cardiomyocytes (iPS-CM) from normal and catecholaminergic polymorphic ventricular tachycardia (CPVT)-afflicted subjects. *Cell Calcium* **54,** 57–70 (2013).

[**152**] **Lee, Y.-K., *et al.*** Calcium Homeostasis in Human Induced Pluripotent Stem Cell-Derived Cardiomyocytes. *Stem Cell Rev. Reports* **7,** 976–986 (2011).

[**153**] **Bers, D.M.** Calcium Cycling and Signaling in Cardiac Myocytes. *Annu. Rev. Physiol.* **70,** 23–49 (2008).

[**154**] **Seok, H., *et al.*** Comparable calcium handling of human iPSC-derived cardiomyocytes generated by multiple laboratories. *J. Mol. Cell. Cardiol.* **85,** 79–88 (2015).

[**155**] **Kaestner, L., *et al.*** Genetically encoded Ca2+ indicators in cardiac myocytes. *Circ. Res.* **114,** 1623–1639 (2014).

[**156**] **Vahabi, S., *et al.*** Atomic force microscopy application in biological research: A review study. *Iran. J. Med. Sci.* **38,** 76–83 (2013).

[**157**] **Wang, J., *et al.*** Atomic force microscope study of tumor cell membranes following treatment with anti-cancer drugs. *Biosens. Bioelectron.* **25,** 721–727 (2009).

[**158**] **Carvalho, F.A., & Santos, N.C.** Atomic force microscopy-based force spectroscopy - Biological and biomedical applications. *IUBMB Life* **64,** 465–472 (2012).

[**159**] **Liu, J., *et al.*** Atomic force mechanobiology of pluripotent stem cell-derived cardiomyocytes. *PLoS One* **7,** 1–7 (2012).

[**160**] **Lieu, D.K., *et al.*** Absence of Transverse Tubules Contributes to Non-Uniform Ca $^{2+}$ Wavefronts in Mouse and Human Embryonic Stem Cell–Derived Cardiomyocytes. *Stem Cells Dev.* **18,** 1493–1500 (2009).

[**161**] **Thorn, K.** A quick guide to light microscopy in cell biology. *Mol. Biol. Cell* **27,** 219–222 (2016).

[**162**] **Pampaloni, F., *et al.*** High-resolution deep imaging of live cellular spheroids with light-sheet-based fluorescence microscopy. *Cell Tissue Res.* **352,** 161–177 (2013).

[**163**] **Pampaloni, F., *et al.*** The third dimension bridges the gap between cell culture and live tissue. *Nat. Rev. Mol. Cell Biol.* **8,** 839–845 (2007).

[**164**] **Smyrek, I., & Stelzer, E.H.K.** Quantitative three-dimensional evaluation of immunofluorescence staining for large whole mount spheroids with light sheet microscopy. *Biomed. Opt. Express* **8,** 484 (2017).

[**165**] **Gualda, E.J., *et al.*** Imaging of human differentiated 3D neural aggregates using light sheet fluorescence microscopy. *Front. Cell. Neurosci.* **8,** 1–10 (2014).

[**166**] **Pampaloni, F., *et al.*** Light sheet-based fluorescence microscopy (LSFM) for the quantitative imaging of cells and tissues. *Cell Tissue Res.* **360,** 129–141 (2015).

[**167**] **Gualda, E.J., *et al.*** Three-dimensional imaging flow cytometry through light-sheet fluorescence microscopy. *Cytom. Part A* **91,** 144–151 (2017).

[**168**] **Ficher, R.S., *et al.*** Microscopy in 3D: a biologist's toolbox. *Trends Cell Biol.* **21,** 682–691 (2009).

[**169**] **Verveer, P.J., *et al.*** High-resolution three-dimensional imaging of large specimens with light sheet-based microscopy. *Nat. Methods* **4,** 311–313 (2007).

[**170**] **Helmchen, F., & Denk, W.** Deep tissue two-photon microscopy. *Nat. Methods* **2,** 932–940 (2005).

[**171**] **Wolf, K., *et al.*** Collagen-based cell migration models in vitro and in vivo. *Semin. Cell Dev. Biol.* **20,** 931–941 (2009).

[**172**] **Campagnola, P.J., & Loew, L.M.** Second-harmonic imaging microscopy for visualizing biomolecular arrays in cells, tissues

and organisms. *Nat. Biotechnol.* **21,** 1356–1360 (2003).

[**173**] **Andresen, V., *et al.*** Infrared multiphoton microscopy: subcellular-resolved deep tissue imaging. *Curr. Opin. Biotechnol.* **20,** 54–62 (2009).

[**174**] **Abadi, P.P.S.S., *et al.*** Engineering of Mature Human Induced Pluripotent Stem Cell-Derived Cardiomyocytes Using Substrates with Multiscale Topography. *Adv. Funct. Mater.* **28,** 1–11 (2018).

[**175**] **Weber, M., & Huisken, J.** Light sheet microscopy for real-time developmental biology. *Curr. Opin. Genet. Dev.* **21,** 566–572 (2011).

[**176**] **Piccinini, F., *et al.*** ReViMS: Software tool for estimating the volumes of 3-D multicellular spheroids imaged using a light sheet fluorescence microscope. *Biotechniques* **63,** 227–229 (2017).

[**177**] **Rebelo, S.P., *et al.*** Three-dimensional co-culture of human hepatocytes and mesenchymal stem cells: improved functionality in long-term bioreactor cultures. *J. Tissue Eng. Regen. Med.* **11,** 2034–2045 (2017).

[**178**] **Rebelo, S.P., *et al.*** 3D-3-culture: A tool to unveil macrophage plasticity in the tumour microenvironment. *Biomaterials* **163,** 185–197 (2018).

[**179**] **Estrada, M.F., *et al.*** Modelling the tumour microenvironment in long-term microencapsulated 3D co-cultures recapitulates phenotypic features of disease progression. *Biomaterials* **78,** 50–61 (2016).

[**180**] **Gualda, E.J., *et al.*** SPIM-fluid: open source light-sheet based platform for high-throughput imaging. *Biomed. Opt. Express* **6,** 4447–4456 (2015).

[**181**] **Stock, K., *et al.*** Capturing tumor complexity in vitro: Comparative analysis of 2D and 3D tumor models for drug discovery. *Sci. Rep.* **6,** 1–15 (2016).

[**182**] **Rebelo, S.P., *et al.*** HepaRG microencapsulated spheroids in DMSO-free culture: novel culturing approaches for enhanced xenobiotic and biosynthetic metabolism. *Arch. Toxicol.* **89,** 1347–1358 (2015).

[**183**] **Jones, K.H., & Senft, J.A.** An improved method to determine cell viability by simultaneous staining with fluorescein diacetate-propidium iodide. *J. Histochem. Cytochem.* **33,** 77–79 (1985).

[**184**] **Ross, D.D., *et al.*** Estimation of Cell Survival by Flow Cytometric Quantification of Fluorescein Diacetate / Propidium Iodide Viable Cell Number Estimation of Cell Survival by Flow Cytometric Quantification of Fluorescein. *Cancer Res.* **49,** 3776–3782 (1989).

[**185**] **Schindelin, J., *et al.*** Fiji: An open-source platform for biological-image analysis. *Nat. Methods* **9,** 676–682 (2012).

[**186**] **Gualda, E.J., *et al.*** OpenSpinMicroscopy: An open-source integrated microscopy platform. *Nat. Methods* **10,** 599–600 (2013).

[**187**] **Huisken, J., *et al.*** Optical Sectioning Deep inside Live Embryos by Selective Plane Illumination Microscopy. *Science (80-.).* **305,** 1007–1009 (2004).

[**188**] **Livak, K.J., & Schmittgen, T.D.** Analysis of relative gene expression data using real-time quantitative PCR and the 2-ΔΔCT method. *Methods* **25,** 402–408 (2001).

[**189**] **Santo, V.E., *et al.*** Adaptable stirred-tank culture strategies for large scale production of multicellular spheroid-based tumor cell models. *J. Biotechnol.* **221,** 118–129 (2016).

[**190**] **Mehta, G., *et al.*** Opportunities and Challenges for use of Tumor Spheroids as Models to Test Drug Delivery and Efficacy. *J. Control Release* **164,** 192–204 (2012).

[**191**] **Wang, N., *et al.*** Vascular endothelial growth factor stimulates endothelial differentiation from mesenchymal stem cells via Rho/myocardin-related transcription factor-A signaling pathway. *Int. J. Biochem. Cell Biol.* **45,** 1447–1456 (2013).

[**192**] **Latif, N., *et al.*** Expression of smoothmuscle cellmarkers and co-activators in calcified aortic valves. *Eur. Heart J.* **36,** 1335–1345 (2015).

[**193**] **Ivey, M.J., & Tallquist, M.D.** Defining the Cardiac Fibroblast. *Circ. J.* **80,** 2269–2276 (2016).

[**194**] **Camelliti, P., *et al.*** Structural and functional characterisation of cardiac fibroblasts. *Cardiovasc. Res.* **65,** 40–51 (2005).

[**195**] **Sebastião, M.J., *et al.*** Unveiling Human Cardiac Fibroblast Membrane Proteome. *Proteomics* **18,** 1–8 (2018).

[**196**] **Maubant, S., *et al.*** Blockade of alpha v beta3 and alpha v beta5 integrins by RGD mimetics induces anoikis and not integrin-mediated death in human endothelial cells. *Blood* **108,** 3035–3044 (2006).

[**197**] **Matsuki, K., *et al.*** RGD peptide-induced cell death of chondrocytes and synovial cells. *J. Orthop. Sci.* **13,** 524–532 (2008).

[**198**] **Chan, Y.-C., *et al.*** Electrical Stimulation Promotes Maturation of Cardiomyocytes Derived from Human Embryonic Stem Cells. *J. Cardiovasc. Transl. Res.* **6,** 989–999 (2013).

[**199**] **Leri, A., *et al.*** Origin of Cardiomyocytes in the Adult Heart Annarosa. *Circ. Res.* **116,** 150–166 (2014).

[**200**] **Dätwyler, D.A., *et al.*** Reactivation of the mitosis-promoting factor in postmitotic cardiomyocytes. *Cells Tissues Organs* **175,** 61–71 (2003).

[**201**] **Hussain, A., *et al.*** Functional 3-D cardiac co-culture model using bioactive chitosan nanofiber scaffolds. *Biotechnol.*

Bioeng. **110,** 637–647 (2013).

[**202**] **Nakane, T., *et al.*** Impact of Cell Composition and Geometry on Human Induced Pluripotent Stem Cells-Derived Engineered Cardiac Tissue. *Sci. Rep.* **7,** 1–13 (2017).

[**203**] **Polonchuk, L., *et al.*** Cardiac spheroids as promising in vitro models to study the human heart microenvironment. *Sci. Rep.* **7,** 1–12 (2017).

[**204**] **Figtree, G.A., *et al.*** Vascularized Cardiac Spheroids as Novel 3D in vitro Models to Study Cardiac Fibrosis. *Cells Tissues Organs* **204,** 191–198 (2017).

[**205**] **Konstandin, M.H., *et al.*** Fibronectin is Essential for Reparative Cardiac Progenitor Cell Response Following Myocardial Infarction. *Circ. Res.* **113,** 1–23 (2013).

[**206**] **Van Dijk, A., *et al.*** Accumulation of fibronectin in the heart after myocardial infarction: A putative stimulator of adhesion and proliferation of adipose-derived stem cells. *Cell Tissue Res.* **332,** 289–298 (2008).

[**207**] **Ronaldson-bouchard, K., *et al.*** Advanced maturation of human cardiac tissue grown from pluripotent stem cells. *Nature* 1–18 (2018).

[**208**] **Lundy, S.D., *et al.*** Structural and Functional Maturation of Cardiomyocytes Derived From Human Pluripotent Stem Cells. *Stem Cells Dev.* 1–47 (2012).

[**209**] **Narita, H., *et al.*** Engraftment and morphological development of vascularized human iPS cell-derived 3D-cardiomyocyte tissue after xenotransplantation. *Sci. Rep.* **7,** 1–9 (2017).

[**210**] **Drobnik, J., *et al.*** Temporary augmentation of glycosaminoglycans content in the heart after left coronary artery ligation. *Pathophysiology* **11,** 35–39 (2004).

[**211**] **Lucas, A., & Wakefield, D.** Glycosaminoglycans (GAGs) in Cardiovascular Disease: Searching for the Sweet Spot. *J. Clin. Exp. Cardiolog.* **07,** 1–3 (2016).

[**212**] **Vogel, B., *et al.*** Determination of collagen content within picrosirius red stained paraffin-embedded tissue sections using fluorescence microscopy. *MethodsX* **2,** 124–134 (2015).

[**213**] **Lattouf, R., *et al.*** Picrosirius Red Staining: A Useful Tool to Appraise Collagen Networks in Normal and Pathological Tissues. *J. Histochem. Cytochem.* **62,** 751–758 (2014).

[**214**] **Ong, C.S., *et al.*** Biomaterial-Free Three-Dimensional Bioprinting of Cardiac Tissue using Human Induced Pluripotent Stem Cell Derived Cardiomyocytes. *Sci. Rep.* **7,** 1–11 (2017).

[**215**] **Han, J., *et al.*** Cell alignment induced by anisotropic electrospun fibrous scaffolds alone has limited effect on cardiomyocyte maturation. *Stem Cell Res.* **16,** 740–750 (2016).

[**216**] **Argenziano, M., *et al.*** Electrophysiologic Characterization of Calcium Handling in Human Induced Pluripotent Stem Cell-Derived Atrial Cardiomyocytes. *Stem Cell Reports* **10,** 1867–1878 (2018).

[**217**] **Shinnawi, R., *et al.*** Monitoring human-induced pluripotent stem cell-derived cardiomyocytes with genetically encoded calcium and voltage fluorescent reporters. *Stem Cell Reports* **5,** 582–596 (2015).

[**218**] **Maddah, M., *et al.*** A non-invasive platform for functional characterization of stem-cell-derived cardiomyocytes with applications in cardiotoxicity testing. *Stem Cell Reports* **4,** 621–631 (2015).

[**219**] **Zhao, L., & Zhang, B.** Doxorubicin induces cardiotoxicity through upregulation of death receptors mediated apoptosis in cardiomyocytes. *Sci. Rep.* **7,** 1–11 (2017).

[**220**] **Takeda, M., *et al.*** Development of In Vitro Drug-Induced Cardiotoxicity Assay by Using Three-Dimensional Cardiac Tissues Derived from Human Induced Pluripotent Stem Cells. *Tissue Eng. Part C Methods* **24,** 56–67 (2017).

[**221**] **Louisse, J., *et al.*** Assessment of acute and chronic toxicity of doxorubicin in human induced pluripotent stem cell-derived cardiomyocytes. *Toxicol. Vitr.* **42,** 182–190 (2017).

[**222**] **Maillet, A., *et al.*** Modeling Doxorubicin-Induced Cardiotoxicity in Human Pluripotent Stem Cell Derived-Cardiomyocytes. *Sci. Rep.* **6,** 1–13 (2016).

[**223**] **Holmgren, G., *et al.*** Expression profiling of human pluripotent stem cell-derived cardiomyocytes exposed to doxorubicin-Integration and visualization of multi-omics data. *Toxicol. Sci.* **163,** 182–195 (2018).

[**224**] **Lu, H.F., *et al.*** Engineering a functional three-dimensional human cardiac tissue model for drug toxicity screening. *Biofabrication* **9,** 1–16 (2017).

[**225**] **Horton, R.E., & Auguste, D.T.** Synergistic effects of hypoxia and extracellular matrix cues in cardiomyogenesis. *Biomaterials* **33,** 6313–6319 (2012).

[**226**] **Simão, D., *et al.*** Perfusion Stirred-Tank Bioreactors for 3D Differentiation of Human Neural Stem Cells. *Methods Mol. Biol.* **1502,** 129–142 (2016).

[**227**] **Behrens, A.N., *et al.*** Nkx2-5 Mediates Differential Cardiac Differentiation Through Interaction with Hoxa10. *Stem Cells Dev.* **22,** 2211–2220 (2013).

Annex

Annex 1 | Supplement to *Materials and Methods*.

1.1 | Immunofluorescence phenotypic characterization.

A comprehensive list of primary and secondary antibodies and counterstains used in immunofluorescence characterizations (2D, cryosections and whole microcapsules) is compiled in **Annex 1.1**. Reference and supplier, host species, clonality, epitope localization and isotype and dilution and analytical method are also specified (**Table S1** and **Table S2**).

Table S1. Summary of primary antibodies and counterstains used in immunofluorescence characterizations.

Antibody description[a]	Reference and Supplier	Host species	Clonality	Epitope localization and Isotype	Dilution and Analytical method[b]
Anti-cardiac troponin T	*MS-295-P1* (*Thermo Fisher Scientific*)	Mouse	Monoclonal (13-11)	Intracellular (IgG1)	1:200 (*CLSM*) 1:100 (*MPLCM*)
Anti-sarcomeric α-actinin	*A7811* (*Sigma-Aldrich*)	Mouse	Monoclonal (EA-53)	Intracellular (IgG1)	1:200 (*CLSM*) 1:100 (*MPLCM*)
Anti-titin	*sc-271946* (*Santa Cruz Biotechnology*)	Mouse	Monoclonal (E-2)	Intracellular (IgG1)	1:200 (*CLSM*)
Anti-connexin 43	*C6219* (*Sigma-Aldrich*)	Rabbit	Polyclonal	Intracellular (IgG)	1:400 (*CLSM*)
Anti-MLC-2*v* – PE conjugate	*130-106-133* (*Miltenyi Biotec*)	Mouse	Monoclonal (REA401)	Intracellular (IgG1k)	1:10 (*CLSM* and *MPLCM*)
Anti-MLC-2*a*	*sc-66967* (*Santa Cruz Biotechnology*)	Rabbit	Polyclonal	Intracellular (IgG)	1:50 (*CLSM* and *MPLCM*)
Anti-*Nkx*2-5	*sc-8697* (*Santa Cruz Biotechnology*)	*Goat*	Polyclonal	Intracellular (IgG)	1:100 (*CLSM*) 1:50 (*MPLCM*)
Anti-phalloidin – *AlexaFluor*® 488 conjugate	*A12379* (*Thermo Fisher Scientific*)	*Amanita phalloides*	*n.a.**	Intracellular (F-actin, cytoskeleton)	1:100 (*CLSM*)
Anti-collagen I	*ab34710* (*abcam*)	Rabbit	Polyclonal	Extracellular (IgG)	1:100 (*CLSM* and *MPLCM*)
Anti-collagen IV	*ab6586* (*abcam*)	Rabbit	Polyclonal	Extracellular (IgG)	1:100 (*CLSM* and *MPLCM*)
Anti-fibronectin	*ab2413* (*abcam*)	Rabbit	Polyclonal	Extracellular (IgG)	1:100 (*CLSM*, *MPLCM* and *LSFM*)

Anti-CD31	*M0823* (*Agilent Technologies/DAKO*)	Mouse	Monoclonal (JC70A)	Membrane (IgG1)	1:50 (*CLSM* and *LSFM*)
Anti-VE-cadherin	*AF938* (*R&D Systems*)	Goat	Polyclonal	Membrane (IgG)	1:13 (*CLSM* and *LSFM*)
Anti-α-smooth muscle actin	*M085129-2* (*Agilent Technologies/DAKO*)	Mouse	Monoclonal (1A4)	Intracellular (IgG2a)	1:100 (*CLSM*) 1:50 (*LSFM*)
Anti-vimentin	*ab16700* (*abcam*)	Rabbit	Monoclonal (v9)	Intracellular (IgG1)	1:100 (*CLSM* and *LSFM*)
Anti-DDR2	*ABIN2158508* (*antibodies-online*)	Rabbit	Polyclonal	Membrane (IgG2a)	1:200 (*CLSM*)
Anti-ZO-1	*40-2200* (*Thermo Fisher Scientific*)	Rabbit	Polyclonal	Intracellular (IgG)	1:100 (*CLSM*)
Anti-Ki-67	*ab16667* (*abcam*)	Rabbit	Monoclonal (SP6)	Intracellular (IgG)	1:100 (*CLSM*)
DAPI	*D3571* (*Thermo Fisher Scientific*)	*n.a.*	*n.a.*	Nuclei	1:1000 (*2D IF* and *MPLSM*)
DRAQ5	*4084S* (*Cell Signalling Technology*)	*n.a.*	*n.a.*	Nuclei	1:1000 (*LSFM*)
TO-PRO-3 Iodide	*T3605* (*Thermo Fisher Scientific*)	*n.a.*	*n.a.*	Nuclei	1:500 (*LSFM*)

[a] Only **primary antibodies** and **counterstains** (DAPI, DRAQ5 and TO-PRO-3 Iodide), used in immunofluorescence microscopy, are listed.

[b] The abbreviation in parentheses (italic) symbolises the imaging method in which a given identified antibody was used: **CLSM – Confocal** Laser Scanning Microscopy, **MPLSM – Multiphoton** Laser Scanning Microscopy and **LSFM – Light Sheet** Fluorescence Microscopy (consult List of Abbreviations and Conventions). **CLSM** was used in the context of **cryosections** immunofluorescence and **MPLSM** and **LSFM** in order to perform **whole-mount** immunofluorescence (with whole microcapsules). Conventional **Widefield Fluorescence** Microscopy was used as a routine technique and also in the characterization of 2D cell cultures, prior to microencapsulation. **2D IF** refers 2D Immunofluorescence.

* *n.a.* stands for not applicable.

Table S2. Summary of secondary antibodies used in immunofluorescence characterizations.

Antibody description[a]	Reference	Supplier	Host species	Clonality	Dilution and Analytical method[b]
Chicken anti-goat IgG *AlexaFluor®* 488	*A21467*	*Thermo Fisher Scientific*	Chicken	Polyclonal	1:500 (*CLSM*) 1:200 (*LSFM*)
Goat anti-mouse IgG *AlexaFluor®* 488	*A11001*	*Thermo Fisher Scientific*	Goat	Polyclonal	1:500 (*CLSM*) 1:200 (*MPLCM* and *LSFM*)
Goat anti-rabbit IgG *AlexaFluor®* 488	*A11008*	*Thermo Fisher Scientific*	Goat	Polyclonal	1:500 (*2D IF* and *CLSM*) 1:200 (*MPLCM* and *LSFM*)
Rabbit anti-mouse IgG *AlexaFluor®* 594	*A11062*	*Thermo Fisher Scientific*	Rabbit	Polyclonal	1:500 (*CLSM*) 1:200 (*LSFM*)
Goat anti-rabbit IgG *AlexaFluor®* 594	*A11037*	*Thermo Fisher Scientific*	Goat	Polyclonal	1:500 (*CLSM*) 1:200 (*MPLCM* and *LSFM*)
Goat anti-mouse IgG *AlexaFluor®* 594	*A11005*	*Thermo Fisher Scientific*	Goat	Polyclonal	1:500 (*2D IF* and *CLSM*)
Donkey anti-goat IgG *AlexaFluor®* 647	*A21447*	*Thermo Fisher Scientific*	Donkey	Polyclonal	1:500 (*2D IF* and *CLSM*)

[a] Only **secondary antibodies**, used in immunofluorescence microscopy, are listed.

[b] The abbreviation in parentheses (italic) symbolises the imaging method in which a given identified antibody was used: **CLSM – Confocal** Laser Scanning Microscopy, **MPLSM – Multiphoton** Laser Scanning Microscopy and **LSFM – Light Sheet** Fluorescence Microscopy (consult List of Abbreviations and Conventions). **2D IF** refers 2D Immunofluorescence.

1.2 | RT-qPCR: gene expression profiling.

Table S3. Summary of *TaqMan® Gene Expression Assays* used in RT-qPCR gene expression analysis.

Gene designation[a]	Probe reference[b]	Label[c]	Amplicon length (bp)	Function
MYL2	Hs00166405_m1	FAM-MGB	98	Structural
MYL7	Hs00221909_m1	FAM-MGB	58	Structural
MYH7	Hs01110632_m1	FAM-MGB	73	Structural
MYH6	Hs01101425_m1	FAM-MGB	67	Structural
TNNI3	Hs00165957_m1	FAM-MGB	93	Structural
TNNI1	Hs00913333_m1	FAM-MGB	77	Structural
CACNA1C	Hs00167681_m1	FAM-MGB	103	Ion channel
SCN5A	Hs00165693_m1	FAM-MGB	85	Ion channel
GAPDH	Hs99999905_m1	FAM-MGB	122	Housekeeping
RPLP0	Hs99999902_m1	FAM-MGB	105	Housekeeping

[a] ***MYL2*** – myosin regulatory light chain 2, encoding the ventricular/cardiac muscle protein isoform (frequently referred to as MLC-2*v*), ***MYL7*** – myosin regulatory light chain 7, encoding the atrial protein isoform (frequently referred to as MLC-2*a*), ***MYH7*** – myosin heavy chain 7, encoding the cardiac *beta*-myosin heavy chain protein isoform (frequently referred to as MHC-β), ***MYH6*** – myosin heavy chain 6, encoding the cardiac *alpha*-myosin heavy chain protein isoform (frequently referred to as MHC-α), ***TNNI3*** – troponin I3, encoding the cardiac muscle isoform (frequently referred to as cTnI), ***TNNI1*** – troponin I1, encoding the slow skeletal muscle isoform (frequently referred to as ssTnI), ***CACNA1C*** – calcium, L-type voltage-gated channel, *alpha* 1C subunit, encoding the calcium channel $Ca_v1.2$, ***SCN5A*** – sodium voltage-gated channel, *alpha* subunit 5, encoding the cardiac sodium channel $Na_v1.5$, ***GAPDH*** – glyceraldehyde-3-phosphate dehydrogenase and ***RPLP0*** – ribosomal protein lateral stalk subunit P0 (consult List of Abbreviations and Conventions).

[b] *TaqMan* probes were purchased from *Thermo Fisher Scientific*.

[c] The 5' terminus of the probe is labelled with FAM (6-carboxyfluorescein), the fluorochrome. MGB stands for minor groove binder.

Annex 2 | Establishment of fully hiPSC-derived hydrogel-based 3D cardiac tissue models.

2.1 | Characterization before microencapsulation: cell viability and spheroid size.

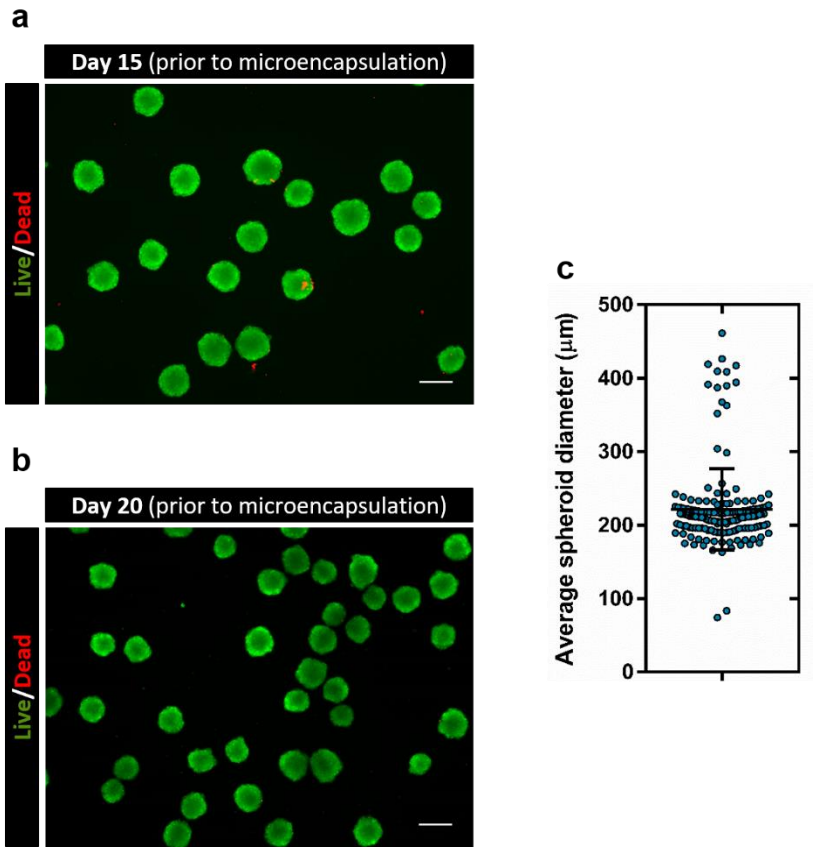

Figure S1 | Culture monitoring before microencapsulations: cell viability and spheroid size (Model #1-*b*–MCT-SF and Pilot Model–M-SF).

(***a-b***) Evaluation of **hiPSC-CM spheroids viability**, through a **live/dead assay**, at **days 15** (***a***) and **20** (***b***), prior to microencapsulation (**Model #1-*b*–MCT-SF** and **Pilot Model–M-SF**, respectively). Spheroids were stained with **FDA** (fluorescein diacetate) – **live** cells, **green**, and **PI** (propidium iodide) – **dead** cells, **red**. Scale bars, 200 µm.

(***c***) Scatter dot plot exhibiting the **hiPSC-CM average spheroid diameter**, at day prior to microencapsulation. Line at mean with SD. Data are mean ± SD from two independent experiments (**Model #1-*b*–MCT-SF** and **Pilot Model–M-SF**) (n = 91 spheroids).

2.2 | Characterization after microencapsulation: average microcapsule diameter, cell viability, metabolic activity and model monitoring and characterization.

Table S4. Average microcapsule diameter resulting from different experiments (Pilot Model–M-SF, Model #1-*a*–MCT-SF, Model #1-*b*–MCT-SF and Model #2-*b*–MT-BR-2)

Experiment designation	Average microcapsule diameter[a] (µm)
Pilot Model–M-SF	767.5 ± 27.43
Model #1-*a*–MCT-SF	1546 ± 62.05
Model #1-*b*–MCT-SF	832.7 ± 28.30
Model #2-*b*–MT-BR-2	817.5 ± 41.52

[a] Data are mean ± SD. Each one of the data sets matches to an individual experiment, accounting for a total of four independent experiments (Pilot Model–M-SF, Model #1-*a*–MCT-SF, Model #1-*b*–MCT-SF and Model #2-b–MT-BR-2). $n \geq 30$ microcapsules. Statistically significant differences between experiments were assessed through an **ordinary one-way ANOVA analysis** with **Tukey's** *post hoc* test for multiple comparisons (****$P \leq 0.0001$). Asterisks (*) denote significant differences. Whenever no statistical significance relationship is indicated in the graphs, consider it as *ns* – not significant, $P > 0.05$.

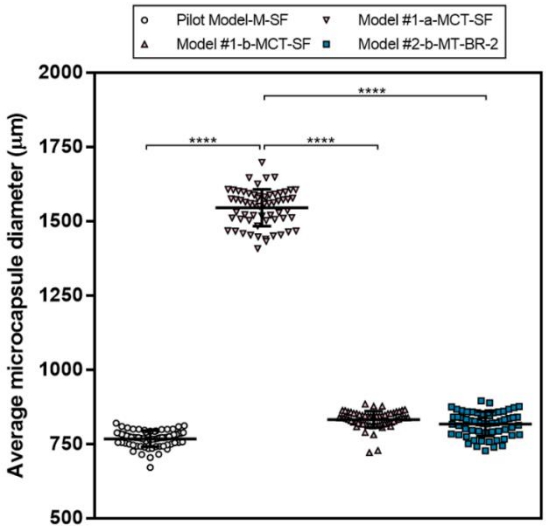

Figure S2 | Average microcapsule diameter resulting from four separate experiments (Pilot Model–M-SF, Model #1-*a*–MCT-SF, Model #1-*b*–MCT-SF and Model #2-*b*–MT-BR-2). Scatter dot plot displaying the **average microcapsule diameter**. Line at mean with SD. Data are mean ± SD. Each one of the data sets matches to an individual experiment, accounting for a total of four independent experiments ($n \geq 30$ microcapsules). Ordinary one-way ANOVA analysis with Tukey's *post hoc* test for multiple comparisons (****$P \leq 0.0001$). Whenever no statistical significance relationship is indicated in the graphs, consider it as *ns* – not significant, $P > 0.05$.

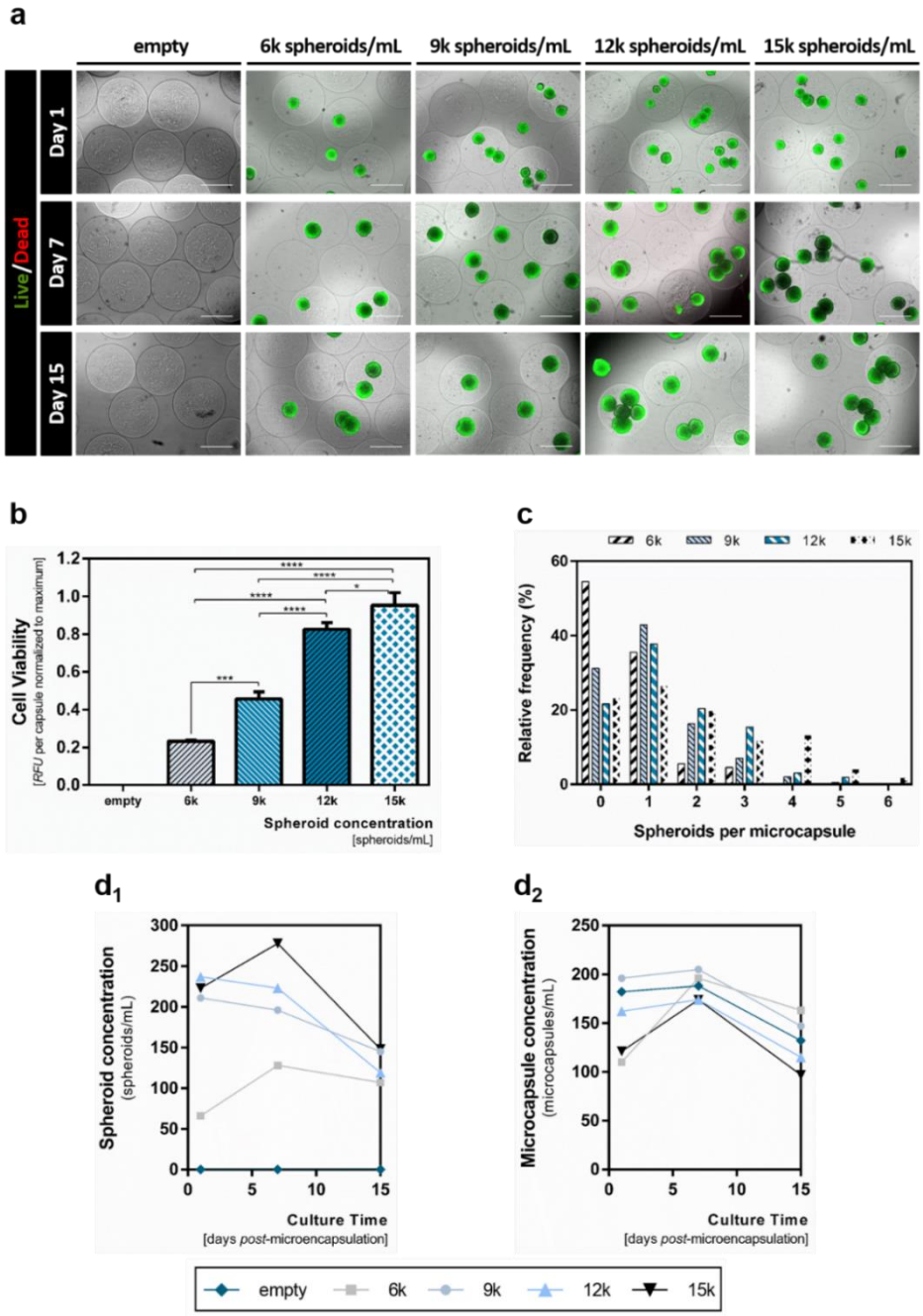

Figure's caption is shown on the following page

Figure S3 | Pilot experiment, which led to the microencapsulation of only hiPSC-CM monocultures: cell viability, metabolic activity and model monitoring and characterization (Pilot Model–M-SF). **(*a*)** 3D hiPSC-CM **monoculture** cardiac tissue **models' cell viability over time**, cultured under similar circumstances (*from left to right*: empty microcapsules and **increasing concentrations** of **spheroids**, per mL of alginate; *from top to bottom*: 1, 7 and 15 days after microencapsulation). Monocultures were stained with **FDA** (fluorescein diacetate) – **live** cells, **green**, and **PI** (propidium iodide) – **dead** cells, **red**. Scale bars, 500 µm. **(*b*)** 3D monocultures **metabolic activity quantification** at day 15 *post*-microencapsulation, using a ***PrestoBlue*** resazurin–based dye assay. Data are mean ± SD from one independent experiment and consist of three technical replicates (n = 3). Ordinary one-way ANOVA analysis with Tukey's *post hoc* test for multiple comparisons (*$P \leq 0.05$, ***$P \leq 0.001$, ****$P \leq 0.0001$). Fluorescence intensity values (*RFU*, relative fluorescence units) were normalized per capsule and to the maximum of fluorescence intensity. Excitation and emission wavelengths were 560 and 590 nm, respectively; gain was 165. **(*c*) Spheroids per microcapsule distribution**, in monocultures, 1 day after microencapsulation. **(*d*)** Monocultures' characterization in terms of **(d_1) spheroid** and **(d_2) microcapsule concentration**, **over time** (1, 7 and 15 days after microencapsulation).

Annex 3 | Microscopy-based phenotypic platform.

3.1 | Confocal immunofluorescence in cryosections.

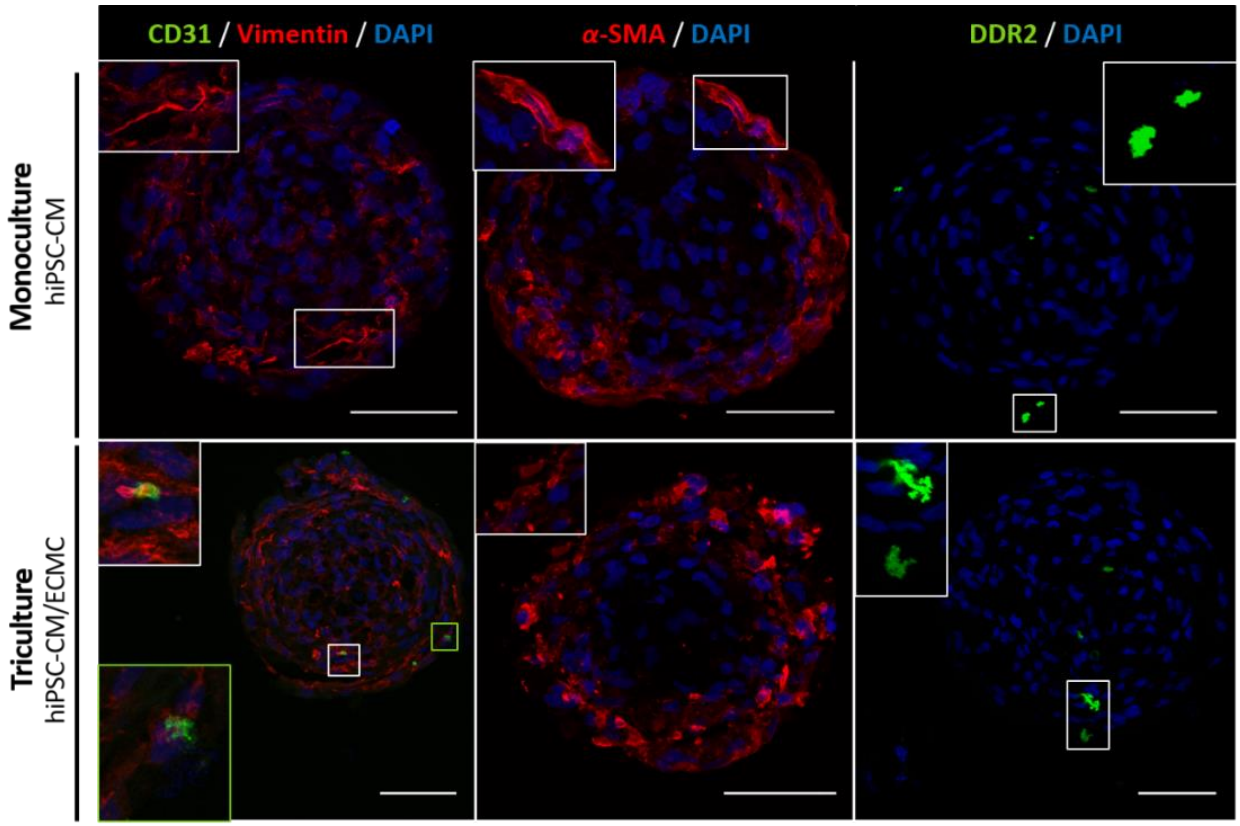

Figure S4 | Mono- and triculture confocal imaging-based phenotypic characterization: endothelial and mesenchymal markers (Model #1-*α*–MCT-SF). Confocal immunofluorescence microscopy of 3D hiPSC-CM mono- (*upper panel*) and 3D hiPSC-CM/ECMC triculture (*lower panel*) microcapsules, in 10 µm thick cryosections, at the **endpoint** of the models (day 15 *post*-microencapsulation), in similar culture circumstances. Data are representative maximum intensity z-projections from one independent experiment. Mono- (*upper panel*) and triculture (*lower panel*) immunostained (*from left to right*) for the **endothelial** cell surface **marker** **CD31** (**green**) and for the **mesenchymal markers** **Vimentin** (**red**), ***α*-SMA** (**red**) and **DDR2** (**green**). Nuclei were counterstained with **DAPI** (**blue**). Insets indicate high magnification images of the corresponding white or green rectangles. All images acquired with a 63x 1.3*NA* (consult **List of Abbreviations and Conventions**) oil immersion objective (***Leica Microsystems***). Scale bars, 50 µm.

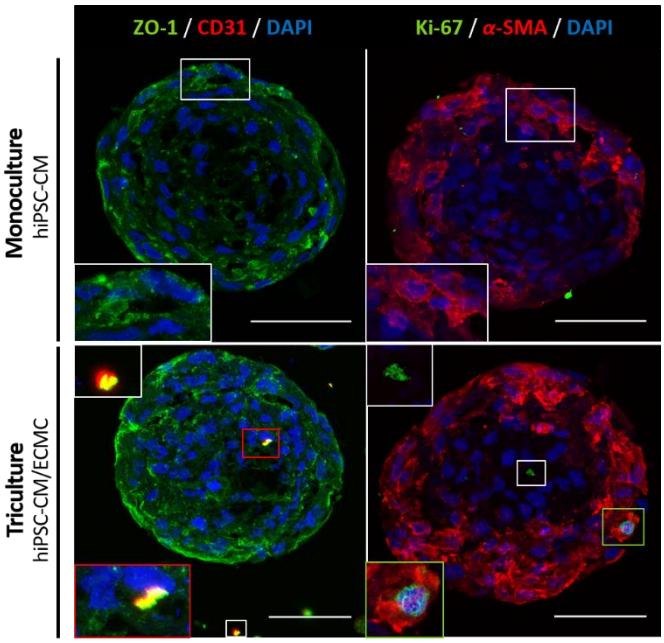

Figure S5 | Mono- and triculture confocal imaging-based phenotypic characterization: cell polarity and proliferation (Model #1-*α*–MCT-SF).
Confocal immunofluorescence microscopy of 3D hiPSC-CM mono- (*upper panel*) and 3D hiPSC-CM/ECMC triculture (*lower panel*) microcapsules, in 10 µm thick cryosections, at the **endpoint** of the models (day 15 *post*-microencapsulation), in similar culture circumstances. Data are representative maximum intensity z-projections from one independent experiment. Mono- (*upper panel*) and triculture (*lower panel*) immunostained (*from left to right*) for the **polarity marker** ZO-1 (green) and for **CD31** (**red**), and similarly for the **proliferation marker** Ki-67 (green) and for ***α*-SMA** (**red**). Nuclei were counterstained with **DAPI** (**blue**). Insets indicate high magnification images of the corresponding white, red or green rectangles. All images acquired with a 63x 1.3*NA* oil immersion objective (*Leica Microsystems*). Scale bars, 50 µm.

3.2 | Whole mount immunofluorescence.

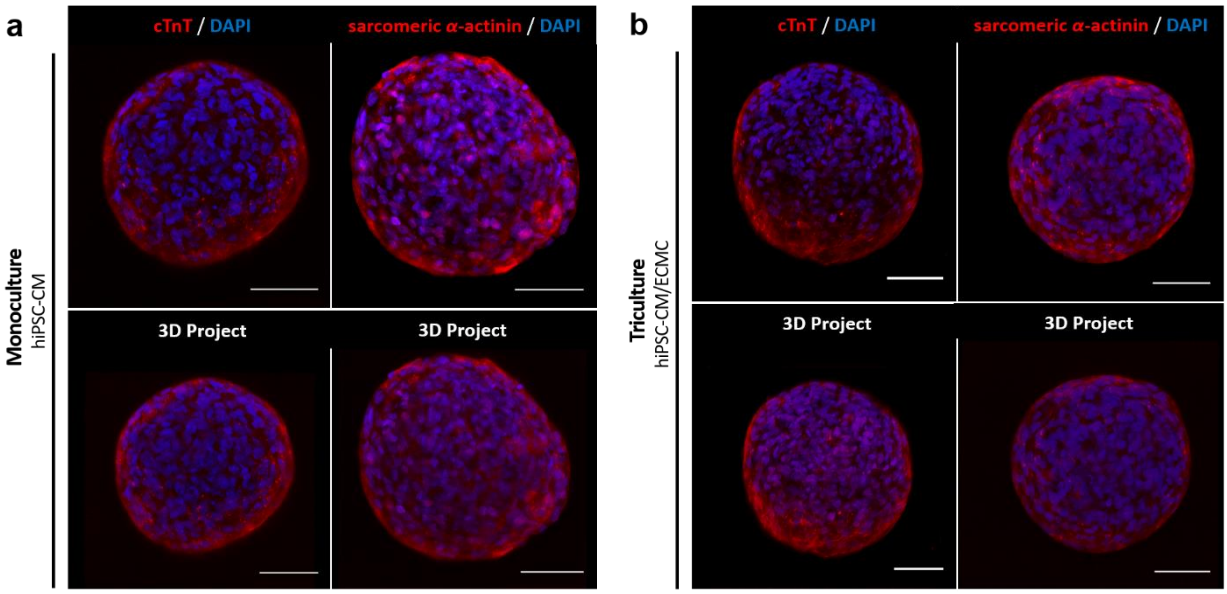

Figure S6 | Multiphoton imaging-based phenotypic characterization of whole mount mono- and tricultures: cardiac markers (Model #1-*α*–MCT-SF). Multiphoton immunofluorescence microscopy of whole mount microencapsulated 3D hiPSC-CM mono- (***a***, *upper panel*) and 3D hiPSC-CM/ECMC triculture (***b***, *lower panel*), in similar culture circumstances, at **day 15** *post*-microencapsulation. Data are representative maximum intensity z-projections and 3D projects (consult **Annex 3.3**, **3D Projects 1**–**4**) from one independent experiment. Mono- (***a***, *upper panel*) and triculture (***b***, *lower panel*) immunostained (*from left to right*) for the **cardiac markers** **cTnT** and **sarcomeric *α*-actinin** (**red**). Nuclei were counterstained with **DAPI** (**blue**). All images acquired with a 40x 0.8*NA* water immersion objective (*Olympus*), adding an optical zoom up to 2.5x; total magnification: up to 100x. Scale bars, 50 µm.

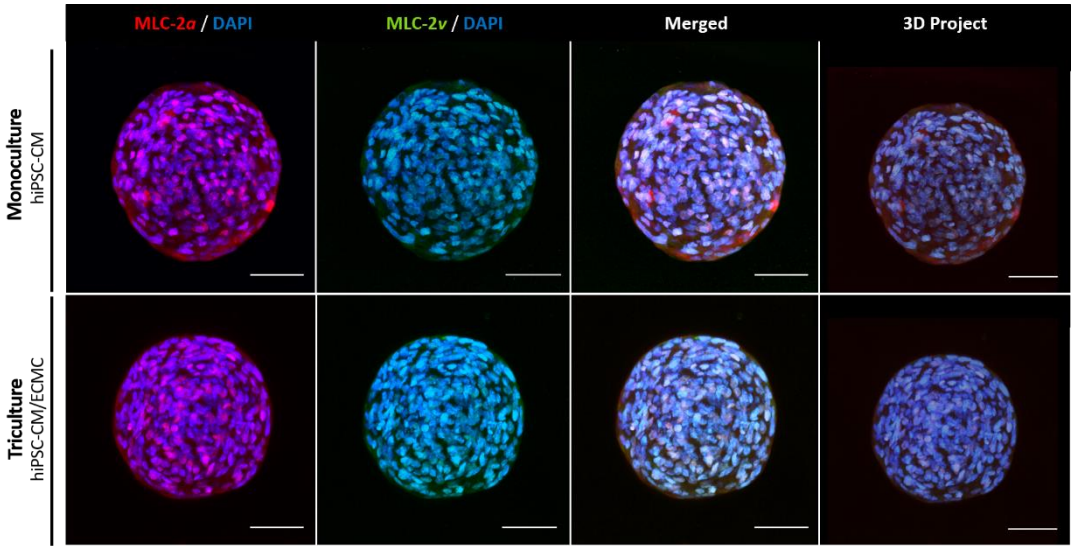

Figure S7 | Multiphoton imaging-based phenotypic characterization of whole mount mono- and tricultures: cardiac maturation markers (Model #1-*α*–MCT-SF). Multiphoton immunofluorescence microscopy of whole mount microencapsulated 3D hiPSC-CM mono- (*upper panel*) and 3D hiPSC-CM/ECMC triculture (*lower panel*), in similar culture circumstances, at **day 15** *post*-microencapsulation. Data are representative maximum intensity z-projections and 3D projects (consult **Annex 3.3**, **3D Projects 5** and **6**) from one independent experiment. Mono- (*upper panel*) and triculture (*lower panel*) immunostained (*from left to right*) for **immature ventricular**/atrial/nodal CM phenotype (**MLC-2*a***, **red**), and for **definitive ventricular** phenotype (**MLC-2*v***, **green**). Nuclei were counterstained with **DAPI** (**blue**). All images acquired with a 40x 0.8*NA* water immersion objective (***Olympus***), adding an optical zoom up to 2.5x; total magnification: up to 100x. Scale bars, 50 µm.

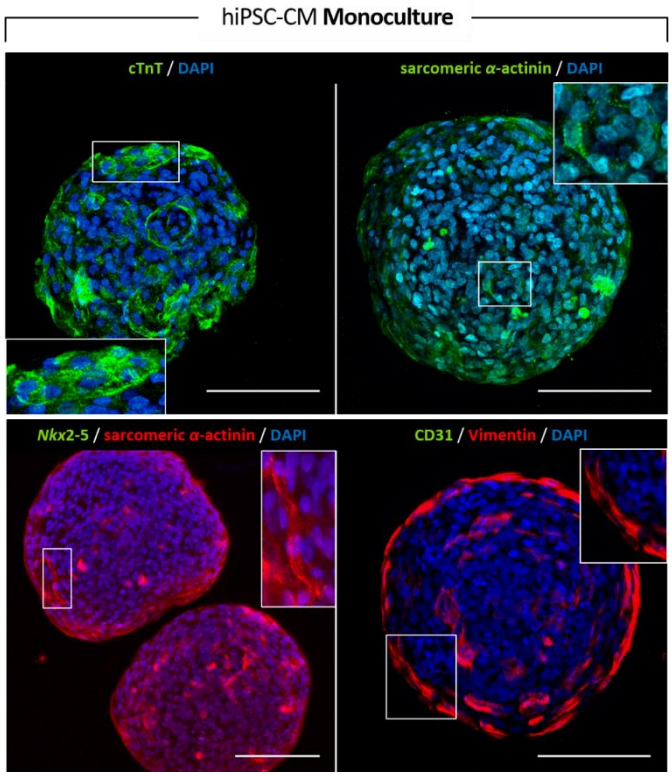

Figure S8 | Multiphoton imaging-based phenotypic characterization of whole mount monocultures (Pilot Model–M-SF). Multiphoton immunofluorescence microscopy of whole mount microencapsulated 3D hiPSC-CM monocultures, at **day 15** *post*-microencapsulation. Data are representative maximum intensity z-projections from one independent experiment. hiPSC-CM spheroids immunostained (*from left to right*) for the **cardiac markers** **cTnT** and ***Nkx*2-5** (**green**), **sarcomeric *α*-actinin** (**red**) and **sarcomeric *α*-actinin** (**green**), and also for the **endothelial** cell surface **marker** **CD31** (**green**) and for the **mesenchymal marker** **Vimentin** (**red**). Nuclei were counterstained with **DAPI** (**blue**). Insets indicate high magnification images of the corresponding white rectangles. All images acquired with a 40x 0.8*NA* water immersion objective (***Olympus***), adding an optical zoom up to 2.5x; total magnification: up to 100x. Scale bars, 100 µm.

3.3 | Multiphoton imaging-based phenotypic characterization: movies list.

A list of short **3D project** movies (**3D Projects 1–12**), that were constructed from z-stacks, acquired in the context of **multiphoton** immunofluorescence microscopy (in addition to the maximum intensity z-projections), is compiled in **Annex 3.3**. Movies relate to **mono-** and **triculture whole mount** microcapsules, at **day 15** *post*-microencapsulation, labelled for **cardiac** markers (cTnT and sarcomeric *α*-actinin), **cardiac maturation** markers (MLC-2*a* and MLC-2*v*) and **ECM proteins** (collagen type I, collagen type IV and fibronectin).

All the abovementioned materials, contained in this attachment, will be **digitally provided**.

3D Project 1 (*.gif* format) | 3D hiPSC-CM monoculture immunostained for cTnT (red) and counterstained with DAPI (blue).

3D Project 2 (*.gif* format) | 3D hiPSC-CM/ECMC triculture immunostained for cTnT (red) and counterstained with DAPI (blue).

3D Project 3 (*.gif* format) | 3D hiPSC-CM monoculture immunostained for sarcomeric *α*-actinin (red) and counterstained with DAPI (blue).

3D Project 4 (*.gif* format) | 3D hiPSC-CM/ECMC triculture immunostained for sarcomeric *α*-actinin (red) and counterstained with DAPI (blue).

3D Project 5 (*.gif* format) | 3D hiPSC-CM monoculture immunostained for MLC-2*a* (red) and MLC-2*v* (green), and counterstained with DAPI (blue).

3D Project 6 (*.gif* format) | 3D hiPSC-CM/ECMC triculture immunostained for MLC-2*a* (red) and MLC-2*v* (green), and counterstained with DAPI (blue).

3D Project 7 (*.gif* format) | 3D hiPSC-CM monoculture immunostained for the collagen type I (green) and counterstained with DAPI (blue).

3D Project 8 (*.gif* format) | 3D hiPSC-CM/ECMC triculture immunostained for the collagen type I (green) and counterstained with DAPI (blue).

3D Project 9 (*.gif* format) | 3D hiPSC-CM monoculture immunostained for the collagen type IV (green) and counterstained with DAPI (blue).

3D Project 10 (*.gif* format) | 3D hiPSC-CM/ECMC triculture immunostained for the collagen type IV (green) and counterstained with DAPI (blue).

3D Project 11 (*.gif* format) | 3D hiPSC-CM monoculture immunostained for the fibronectin (green) and counterstained with DAPI (blue).

3D Project 12 (*.gif* format) | 3D hiPSC-CM/ECMC triculture immunostained for the fibronectin (green) and counterstained with DAPI (blue).

3.4 | Light-sheet imaging-based phenotypic characterization: movies list.

A list of **3D volume reconstructions** (**LSFM Movies 1–6**), obtained via LSFM, is likewise compiled in **Annex 3.4**. These materials will also be digitally provided.

LSFM Movie 1 (*.avi* format) | 3D hiPSC-CM monoculture immunostained for CD31 (green) and Vimentin (red), and counterstained with DRAQ5 (cyan).

LSFM Movie 2 (*.avi* format) | 3D hiPSC-CM/ECMC triculture immunostained for CD31 (green) and Vimentin (red), and counterstained with DRAQ5 (cyan).

LSFM Movie 3 (*.avi* format) | 3D hiPSC-CM monoculture immunostained for VE-cadherin (green) and *α*-SMA (red), and counterstained with DRAQ5 (cyan).

LSFM Movie 4 (*.avi* format) | 3D hiPSC-CM/ECMC triculture immunostained for VE-cadherin (green) and *α*-SMA (red), and counterstained with DRAQ5 (cyan).

LSFM Movie 5 (*.avi* format) | 3D hiPSC-CM monoculture immunostained for fibronectin (green) and counterstained with DRAQ5 (cyan).

LSFM Movie 6 (*.avi* format) | 3D hiPSC-CM/ECMC triculture immunostained for fibronectin (green) and counterstained with DRAQ5 (cyan).

Annex 4 | Structural and ultrastructural assessment.

4.1 | Ultrastructural: transmission electron microscopy (TEM).

Table S5. Mono- and triculture cardiac tissue models ultrastructural features – sarcomere length and sarcomere angle dispersion – at day 15 *post*-microencapsulation.

3D cardiac tissue model	Sarcomere length[a] (nm)	Sarcomere angle dispersion[b] (*SEM* of sarcomere angles)
hiPSC-CM Monoculture	1433 ± 190.7[‡1]	5.535 ± 3.419[‡2]
hiPSC-CM/ECMC Triculture	1521 ± 134.2[‡1]	3.039 ± 1.589[‡2]

[a] Sarcomere length – Data are mean ± SD from one independent experiment (Model #1-*α*–MCT-SF). *n* = 40-52 sarcomeres. **Statistically significant differences between *Mono-* and *Triculture* were assessed through a two-tailed Mann–Whitney nonparametric test (**P = 0.0047). [b] Sarcomere angle dispersion – Data are mean ± SD from one independent experiment (Model #1-*α*–MCT-SF). *n* = 8-15 sarcomeres. *Statistically significant differences between mono- and triculture were assessed through a two-tailed unpaired *t*-student test (*P = 0.0379). Asterisks (*) denote significant differences.

[‡1] Sarcomere length was estimated by measuring two parallel segments, per sarcomere, joining adjacent Z lines.

[‡2] *SEM* of sarcomere angles, σ_M, was calculated by the quotient between the standard deviation of the original distribution of sarcomere angles' means, σ, and the square root of the number of sarcomeres, *VN*: $\boldsymbol{\sigma_M = \frac{\sigma}{\sqrt{N}}}$. *SEM* stands for *standard error of the mean*.

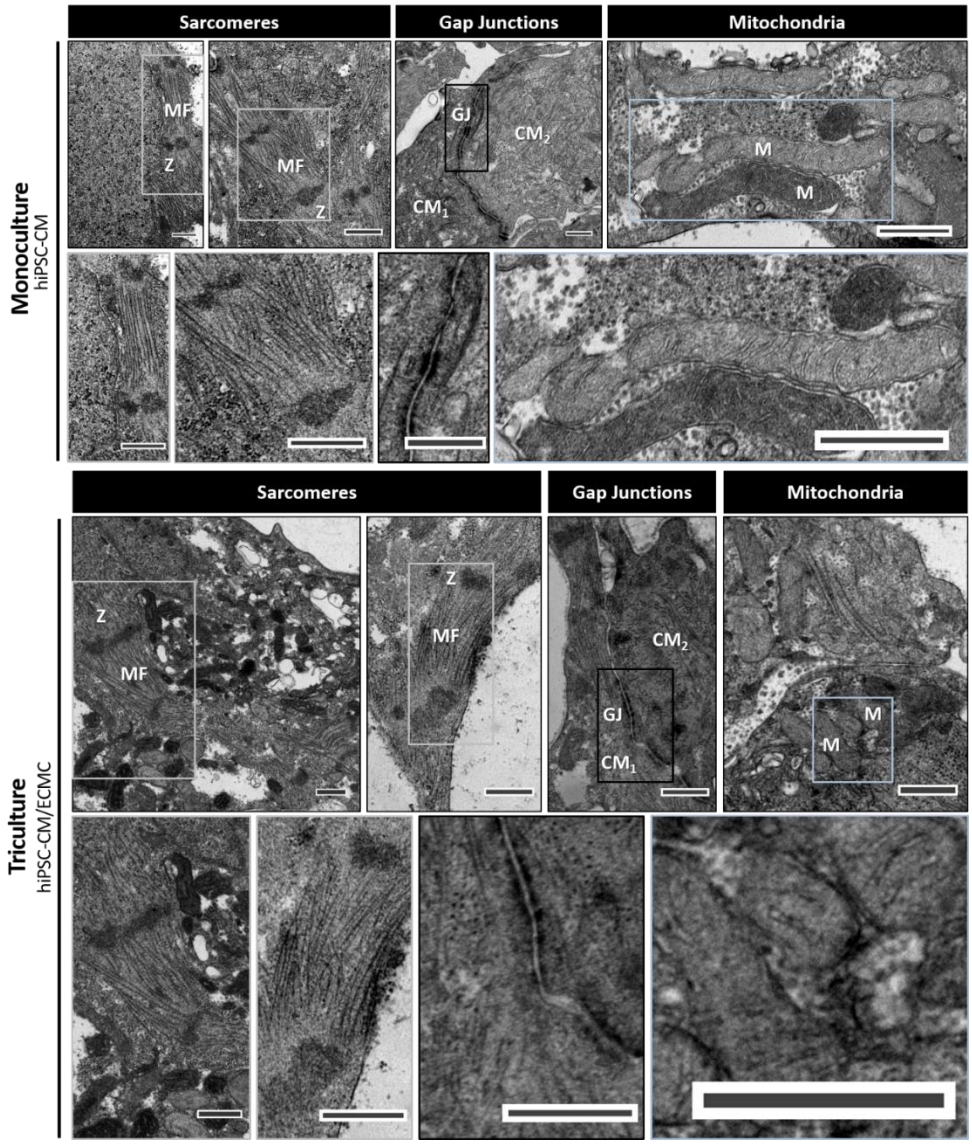

Figure's caption is shown on the following page

Figure S9 | Ultrastructural characterization of mono- and triculture, 1 days after microencapsulation (Model #1-*b*–MCT-SF). Representative **TEM** micrographs of 3D hiPSC-CM **mono-** (*upper panel*) and 3D hiPSC-CM/ECMC **triculture** (*lower panel*) cardiac tissue models, at **day 1** *post*-microencapsulation. Registers of sarcomeres, displaying misaligned myofibrils (MF) and split Z-discs (Z), shorter **gap junctions** (**GJ**) connecting neighbouring hiPSC-CMs (denoted as **CM_1** and **CM_2**) and density of mitochondria (M). Insets indicate high magnification images of the corresponding grey, **black** or cyan rectangles. Scale bars, 500 nm (in both figures and magnifications).

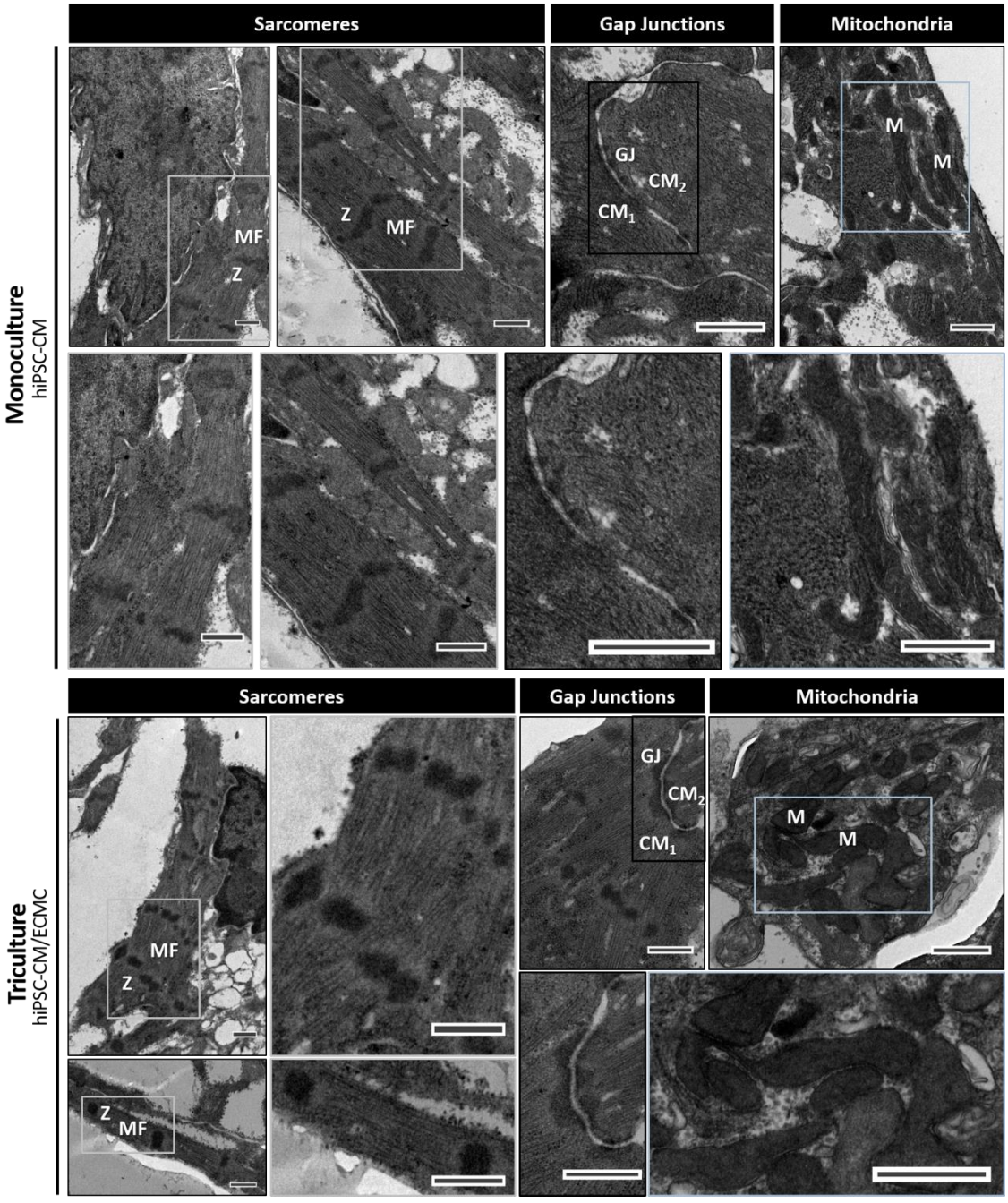

Figure S10 | Ultrastructural characterization of mono- and triculture, 14 days after microencapsulation (Model #1-*b*–MCT-SF). Representative **TEM** micrographs of 3D hiPSC-CM **mono-** (*upper panel*) and 3D hiPSC-CM/ECMC **triculture** (*lower panel*) cardiac tissue models, at **day 14** *post*-microencapsulation. Registers of sarcomeres, displaying aligned myofibrils (MF) and organized Z-discs (Z), **gap junctions** (**GJ**) connecting neighbouring hiPSC-CMs (denoted as **CM_1** and **CM_2**) and density of mitochondria (M). Insets indicate high magnification images of the corresponding grey, **black** or cyan rectangles. Scale bars, 500 nm (in both figures and magnifications).

4.2 | Structural: histological/histochemical-based characterization.

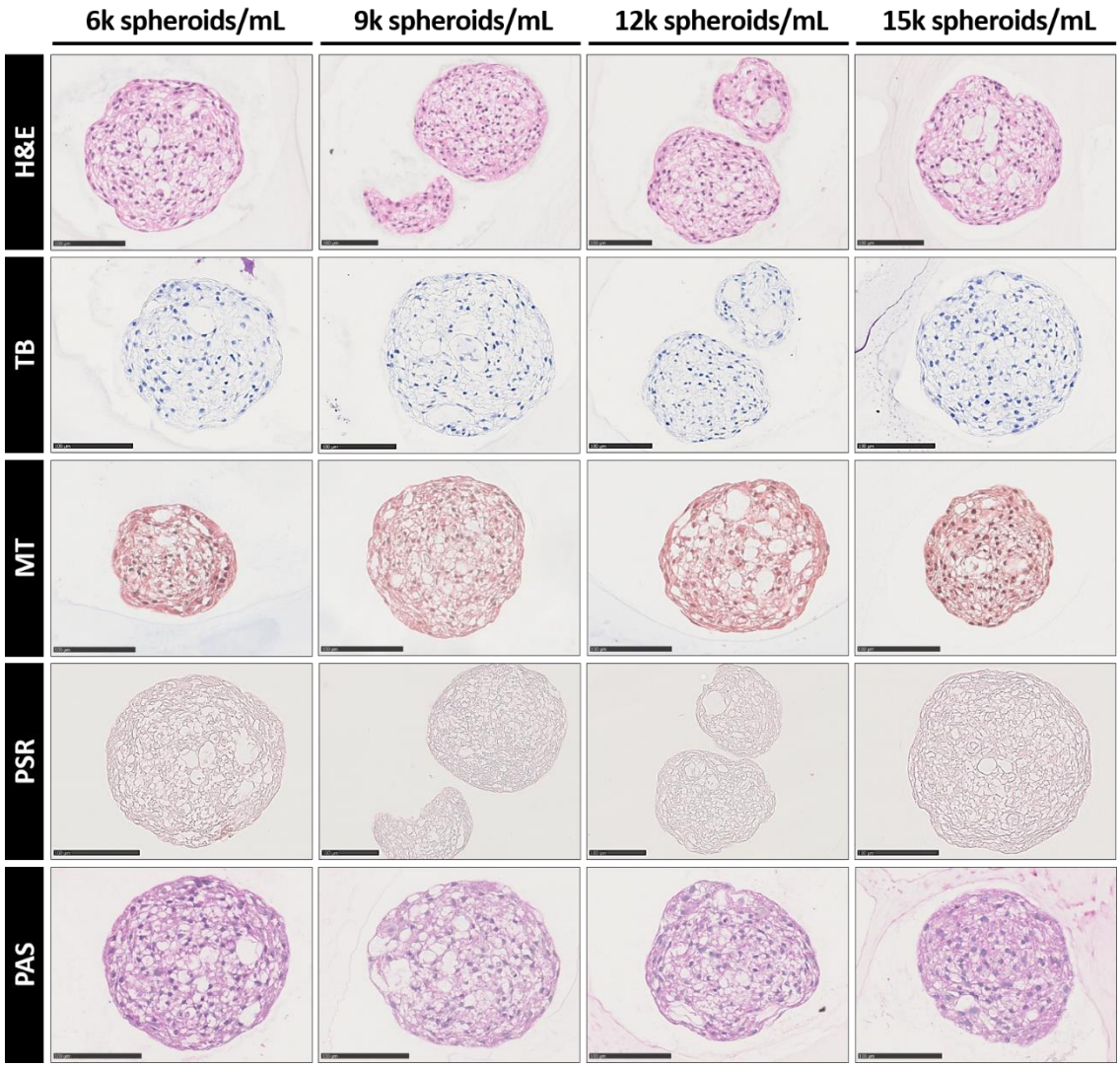

Figure S11 | Histochemistry and morphology analysis of 3D hiPSC-CM monocultures (Pilot Model–M-SF). Histochemistry characterization of 3 µm thick paraffin sections of 3D hiPSC-CM **monoculture** microcapsules (*from left to right*: increasing concentrations of spheroids, per mL of alginate), taken at **day 15** *post*-microencapsulation and stained for **H&E**, **TB**, **MT**, **PSR** and **PAS**. Data are representative images from one independent experiment. **Abbreviations** (*from top to bottom*): **Hematoxylin** and Eosin (**H&E**), **Toluidine Blue** (**TB**), **Masson Trichrome** w/ Aniline Blue (**MT**), Picrosirius Red (**PSR**) and **Periodic Acid-Schiff** (**PAS**). Scale bars, 100 µm.

Annex 5 | Functional evaluation: live cell calcium imaging.

5.1 | Calcium handling kinetic parameters.

Table S6. hiPSC-CM calcium transient kinetics in mono- and triculture and pharmacological response to a β_1-adrenergic receptor agonist, norepinephrine (60 µM), obtained by live cell calcium imaging.

Conditions [‡1]	Amplitude[a] ($\Delta F/F_0$)	Upstroke velocity[b] ($\Delta F/F_0$/s)	Decay velocity[c] ($\Delta F/F_0$/s)	Rise to peak time[d] (s)	Time to 50% decay[e] (s)	Time to 80% decay[f] (s)	Time between peaks[g] (s)	Beating rate[h] (beats/min)
Mono[‡2]	1.319 ± 0.4610	8.919 ± 3.199	4.085 ± 1.487	0.2650 ± 0.07801	0.3775 ± 0.08598	0.5438 ± 0.1023	1.589 ± 0.3353	39.04 ± 6.990
Mono + 60 µM *Norepi*	0.9185 ± 0.3527	6.556 ± 2.476	2.514 ± 0.8683	0.2015 ± 0.02267	0.2654 ± 0.04136	0.3731 ± 0.06277	0.9146 ± 0.1846	68.01 ± 13.10

Tri‡2	0.9700 ± 0.2947	6.666 ± 1.981	3.098 ± 1.010	0.2420 ± 0.03824	0.5080 ± 0.06460	0.6790 ± 0.06919	2.080 ± 0.1918	29.05 ± 2.522
Tri + 60 µM *Norepi*‡2	0.6725 ± 0.2614	4.978 ± 1.983	1.973 ± 0.7539	0.1825 ± 0.01488	0.3038 ± 0.04689	0.4163 ± 0.05344	0.9713 ± 0.08709	62.23 ± 5.794

a-h Data are mean ± SD from one independent experiment (Model #1-*a*–MCT-SF). **All kinetic parameters:** *n* = 8-13. Statistically significant differences between *Mono*, *Mono + 60 µM Norepi*, *Tri* and *Tri + 60 µM Norepi* groups were assessed through an **ordinary one-way ANOVA analysis** with **Tukey's** *post hoc* test for multiple comparisons (***ns*** – not significant, ***P* ≤ 0.05, ****P* ≤ 0.01, *****P* ≤ 0.001, ******P* ≤ 0.0001). Asterisks (*) denote significant differences.

‡1 These parameters refer to **15 days** after microencapsulation, for both mono- and triculture cardiac tissue models, under **similar culture circumstances**.

‡2 **Mono –** Monoculture, **Tri –** Triculture and ***Norepi –*** Norepinephrine (consult List of Abbreviations and Conventions).

Table S7. hiPSC-CM calcium transient kinetics in mono- and triculture and pharmacological responses to several cardioactive drugs, obtained by live cell calcium imaging.

Conditions ‡1	Amplitude[a] ($\Delta F/F_0$)	Upstroke velocity[b] ($\Delta F/F_0$/s)	Decay velocity[c] ($\Delta F/F_0$/s)	Rise to peak time[d] (s)	Time to 50% decay[e] (s)	Time to 80% decay[f] (s)	Time between peaks[g] (s)	Beating rate[h] (beats/min)
Mono‡2	4.049 ± 0.3713	21.83 ± 2.842	10.83 ± 1.586	0.4075 ± 0.04301	0.4013 ± 0.1012	0.6675 ± 0.09543	7.713 ± 1.215	7.966 ± 1.354
Mono + 60 µM *Norepi*	3.911 ± 0.4808	20.70 ± 2.112	9.685 ± 1.488	0.3863 ± 0.05655	0.4175 ± 0.1035	0.6900 ± 0.1372	3.800 ± 0.5801	16.11 ± 2.418
Mono + 40 µM Heptanol	1.023 ± 0.2406	6.743 ± 2.125	3.260 ± 0.8234	0.3000 ± 0.02160	0.3525 ± 0.05909	0.5425 ± 0.05852	4.125 ± 0.7295	14.88 ± 2.534
Mono + 4 µM *PPL*	2.175 ± 0.8415	13.83 ± 7.375	6.470 ± 2.772	0.3150 ± 0.02121	0.3250 ± 0.03536	0.5500 ± 0.01024	11.14 ± 6.597	6.540 ± 3.875
Mono + 4 µM *PPL* + 60 µM *Norepi*	3.913 ± 0.4332	22.35 ± 3.124	10.74 ± 0.9484	0.3667 ± 0.04163	0.3200 ± 0.03464	0.5500 ± 0.02646	6.300 ± 2.439	10.43 ± 3.541
Tri‡2	2.333 ± 0.1977	12.71 ± 1.586	6.925 ± 0.7212	0.4033 ± 0.04367	0.3233 ± 0.03615	0.5733 ± 0.05989	7.748 ± 1.402	7.942 ± 1.337
Tri + 60 µM *Norepi*‡2	3.720 ± 0.1697	20.73 ± 4.554	8.010 ± 1.146	0.3700 ± 0.1131	0.4600 ± 0.01414	0.7650 ± 0.07778	4.250 ± 0.6081	14.27 ± 2.051
Tri + 40 µM Heptanol	1.160 ± 0.2828	7.950 ± 2.602	3.610 ± 1.216	0.3050 ± 0.03536	0.3850 ± 0.07778	0.5700 ± 0.08485	3.540 ± 0.03267	16.94 ± 0.02963
Tri + 4 µM *PPL*‡2	2.503 ± 0.4252	11.62 ± 2.246	5.580 ± 1.340	0.4167 ± 0.02887	0.4600 ± 0.03606	0.7767 ± 0.04041	10.42 ± 1.790	5.890 ± 1.126
Tri + 4 µM *PPL* + 60 µM *Norepi*	2.290 ± 0.1300	10.40 ± 0.7711	3.977 ± 0.8334	0.4533 ± 0.04619	0.4800 ± 0.05568	0.8400 ± 0.09644	4.983 ± 1.669	12.88 ± 3.805

a-h Data are mean ± SD from one independent experiment (Model #1-*b*–MCT-SF). **All kinetic parameters:** *n* = 2-8. Statistically significant differences between *Mono*, *Mono + 60 µM Norepi*, *Mono + 40 µM Heptanol*, *Mono + 4 µM PPL*, *Mono + 4 µM PPL + 60 µM Norepi*, *Tri*, *Tri + 60 µM Norepi*, *Tri + 40 µM Heptanol*, *Tri + 4 µM PPL* and *Tri + 4 µM PPL + 60 µM Norepi* groups were assessed through an **ordinary one-way ANOVA analysis** with **Tukey's** *post hoc* test for multiple comparisons (***ns*** – not significant, ***P* ≤ 0.05, ****P* ≤ 0.01, *****P* ≤ 0.001, ******P* ≤ 0.0001). Asterisks (*) denote significant differences. Whenever no statistical significance relationship is indicated in the graphs, consider it as *ns* – not significant, *P* > 0.05.

‡1 These parameters refer to **14 days** after microencapsulation, for both mono- and triculture cardiac tissue models, under **similar culture circumstances**.

‡2 **Mono –** Monoculture, **Tri –** Triculture, ***Norepi –*** Norepinephrine and ***PPL –*** Propranolol and (consult List of Abbreviations and Conventions).

5.2 | List of videos: spinning disk confocal microscopy.

Videos refer to **hiPSC-CM spontaneous** Ca^{2+} **releases** (conditions *w/o* drug exposure) and to hiPSC-CM pharmacological **responses** to different **drugs** with **cardiac affinity**, specifically **norepinephrine**, **propranolol** and **heptanol**, in both mono- and triculture cardiac tissue models. Videos are from two independent experiments (**Model #1-*a*–MCT-SF** and **Model #1-*b*–MCT-SF**).

All the materials, contained in this attachment, will be **digitally provided**.

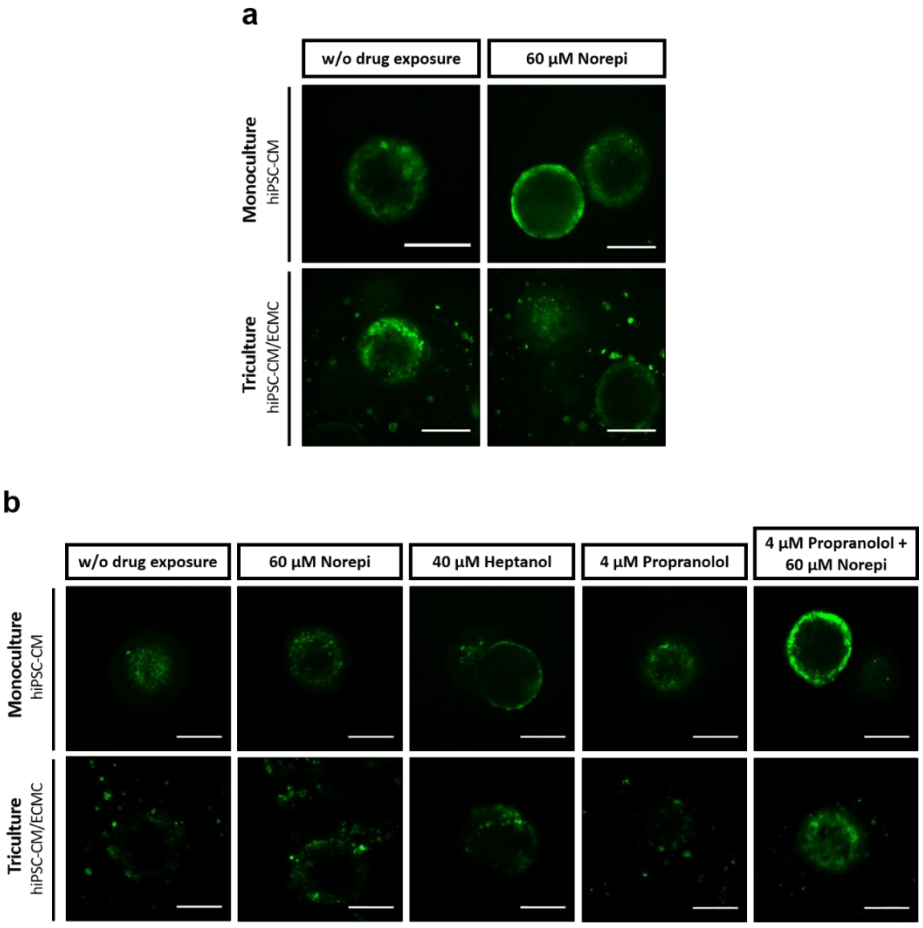

Figure S12 | Live cell calcium imaging microscopy videos from two separate experiments (Model #1-*a*–MCT-SF and Model #1-*b*–MCT-SF). Calcium imaging **spinning disk confocal** microscopy videos of 3D hiPSC-CM mono- and 3D hiPSC-CM/ECMC triculture cardiac tissue models, in similar culture circumstances, recorded at **day 15** *post*-microencapsulation. Videos show two distinct moments: i) ***resting*** (low intracellular Ca^{2+} concentration) and ii) ***depolarization*** (high intracellular Ca^{2+} concentration). Data are representative videos from two independent experiments: (***a***, *upper panel*, **Model #1-*a*–MCT-SF**) and (***b***, *lower panel*, **Model #1-*b*–MCT-SF**). All videos acquired with a 20x 0.75*NA* dry objective (***Nikon***). Scale bars, 200 µm.

Movie 1 (*.gif* format) | Ca^{2+} spontaneous releases in monoculture (monoculture w/o drug exposure), at day 15 *post*-microencapsulation (Model #1-*a*–MCT-SF).

Movie 2 (*.gif* format) | Ca^{2+} spontaneous releases in triculture (triculture w/o drug exposure), at day 15 *post*-microencapsulation (Model #1-*a*–MCT-SF).

Movie 3 (*.gif* format) | Monoculture exposed to 60 µM of *norepi*, at day 15 *post*-microencapsulation (Model #1-*a*–MCT-SF).

Movie 4 (*.gif* format) | Triculture exposed to 60 µM of norepi, at day 15 *post*-microencapsulation (Model #1-*a*–MCT-SF).

Movie 5 (*.gif* format) | Ca^{2+} spontaneous releases in monoculture (monoculture w/o drug exposure), at day 14 *post*-microencapsulation (Model #1-*b*–MCT-SF).

Movie 6 (*.gif* format) | Ca^{2+} spontaneous releases in triculture (triculture w/o drug exposure), at day 14 *post*-microencapsulation (Model #1-*b*–MCT-SF).

Movie 7 (*.gif* format) | Monoculture exposed to 60 µM of *norepi*, at day 14 *post*-microencapsulation (Model #1-*b*–MCT-SF).

Movie 8 (*.gif* format) | Triculture exposed to 60 µM of *norepi*, at day 14 *post*-microencapsulation (Model #1-*b*–MCT-SF).

Movie 9 (*.gif* format) | Monoculture exposed to 40 µM of heptanol, at day 14 *post*-microencapsulation (Model #1-*b*–MCT-SF).

Movie 10 (*.gif* format) | Triculture exposed to 40 µM of heptanol, at day 14 *post*-microencapsulation (Model #1-*b*–MCT-SF).

Movie 11 (*.gif* format) | Monoculture exposed to 4 µM of propranolol, at day 14 *post*-microencapsulation (Model #1-*b*–MCT-SF).

Movie 12 (*.gif* format) | Triculture exposed to 4 µM of propranolol, at day 14 *post*-microencapsulation (Model #1-*b*–MCT-SF).

Movie 13 (*.gif* format) | Monoculture exposed to 4 µM of propranolol and thereafter to 60 µM of norepinephrine (Model #1-*b*–MCT-SF).

Movie 14 (*.gif* format) | Triculture exposed to 4 µM of propranolol and thereafter to 60 µM of norepinephrine (Model #1-*b*–MCT-SF).

Annex 6 | Scaffold characterization: atomic force microscopy (AFM).

Table S8. FS-AFM-based mechanobiological properties of the biomaterial, mono- and triculture, at day 15 *post*-microencapsulation.

Conditions	Young's modulus[a] (kPa)	Stiffness[b] (mN/m)	Hardness[c] (kPa)	Adhesion[d] (nN)	Pore diameter[e] (nm)
RGD-alginate microbead	188.0 ± 69.38	53.12 ± 21.29	72.06 ± 21.82	0.5053 ± 0.6219	579.6 ± 137.0
Monoculture	26.24 ± 10.44	13.63 ± 6.653	5.737 ± 1.718	0.5743 ± 0.5503	
Triculture	159.3 ± 27.27	47.79 ± 8.074	77.07 ± 32.27	2.913 ± 2.326	

[a-d] Data are mean ± SD from one independent experiment (Pilot Model–M-SF), for RGD-alginate microbead, and two (Model #1-*a*–MCT-SF and Model #1-*b*–MCT-SF), for mono- and triculture. Young's modulus and Stiffness: n = 63-80, Hardness: n = 71-81 and Adhesion: n = 69-77. Statistically significant differences between *RGD-alginate microbead*, *Mono-* and *Triculture* groups were assessed through a ranked one-way ANOVA analysis (Kruskal-Wallis nonparametric test) with Dunn's *post hoc* test for multiple comparisons (***ns*** – not significant, ***$P \leq 0.05$, ****$P \leq 0.001$, *****$P \leq 0.0001$). Asterisks (*) denote significant differences.

[e] Data are mean ± SD from two independent experiments (Pilot Model–M-SF Model and Model #1-*a*–MCT-SF). n = 61.

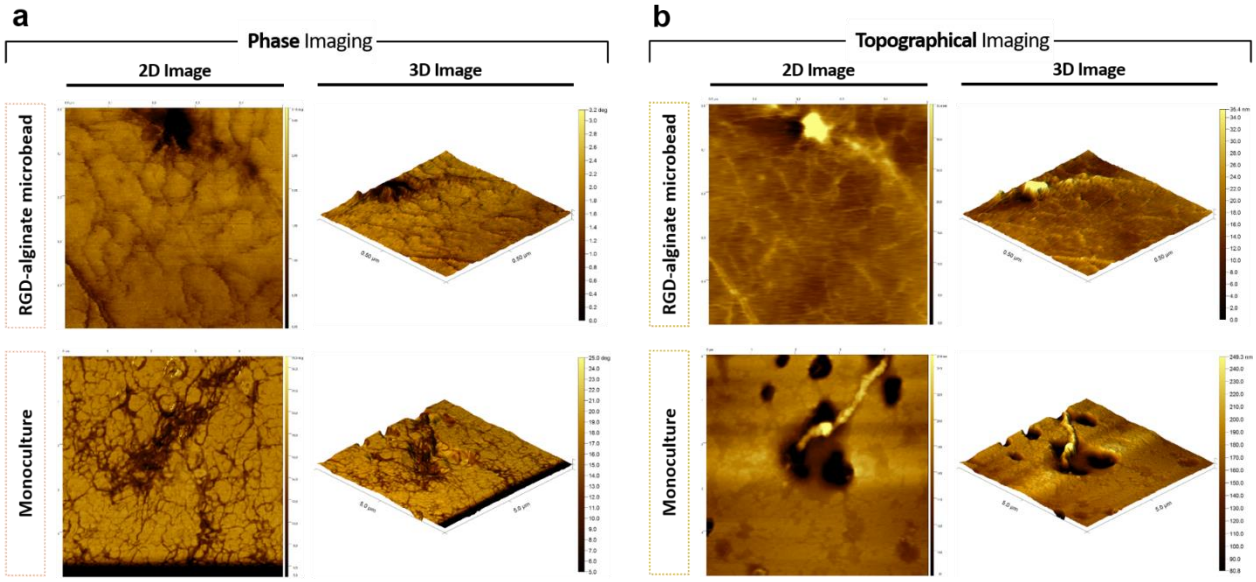

Figure S13 | AFM 2D and 3D imaging characterization of the microcapsule *scaffold* and 3D hiPSC-CM monoculture model (high magnifications). (*a*) AFM 2D and 3D **phase imaging** (*left panel*) of RGD-alginate microbead and monoculture. **(*b*)** AFM 2D and 3D **topographical imaging** (*right panel*) of the same groups. **(*a-b*)** A scan area of 0.25 µm² (*size*: 0.5 x 0.5 µm), for RGD-alginate microbead, and 25 µm² (*size*: 5 x 5 µm), for monoculture, were used. Data are representative images from one independent experiment (**Pilot Model–M-SF**), for RGD-alginate microbead, and two (**Model #1-*a*–MCT-SF** and **Model #1-*b*–MCT-SF**), for monoculture.

Annex 7 | Scalability approaches using stirred-tank bioreactors.

Table S9. Quantitative characterization of hiPSC-CM aggregation profile in stirred-tank bioreactors, from day 7 to day 18.

	Model #2-*a*–BR-1[a,*1]	Model #2-*b*–MT-BR-2[a,*1]
Working volume (mL)	200	200
Inoculum (x10^6 cell)	100	100
Inoculum concentration (x10^6 cell/mL)	0,31 (*0,5*)[*2]	0,78 (*0,5*)[*2]
Final cell concentration (x10^6 cell/mL)	0,04	0,27
Final spheroid concentration (x 10^4 spheroid/mL)	0,077	0,077
Stirring rate (rpm)	60 (d7-d8); 70 (d9-d18)	80 (d7-d10); 90 (d11-d18)

[a] Small-scale software-controlled stirred-tank bioreactors (***DasGip*** *cellferm-pro bioreactor system*, ***Eppendorf AG***, Hamburg, Germany).

[*1] **Other culture parameters: Temperature –** 37 °C, **Dissolved Oxygen (DO) –** 3% O_2 tension (15% of air with 21% of oxygen; **atmospheric hypoxia** environment), **Dilution Rate (DR) –** 0.30 day^{-1} and **Hydraulic Residence Time (HRT) –** 3,33 day. **Model #2-*a*–BR-1** and **Model #2-*b*–MT-BR-2** denote two independent bioreactor experiments. [*2] The number in parentheses (italic) represents the corresponding **theoretical inoculum concentrations**.